Study of the diffuse emissions with the H.E.S.S. experiment

Tania Garrigoux

To cite this version:

Tania Garrigoux. Study of the diffuse emissions with the H.E.S.S. experiment. Sciences of the Universe [physics]. Université Pierre et Marie Curie, 2015. English. NNT : . tel-01353854

HAL Id: tel-01353854
https://hal.science/tel-01353854

Submitted on 15 Aug 2016

THÈSE DE DOCTORAT
DE L'UNIVERSITÉ PIERRE ET MARIE CURIE
SORBONNE UNIVERSITÉS

présentée par

Tania Garrigoux

Pour obtenir le grade de

DOCTEUR ÈS SCIENCES
DE L'UNIVERSITÉ PIERRE ET MARIE CURIE

Spécialité :

Physique de l'Univers (STEP'UP - ED N° 560)

Étude des émissions diffuses avec l'expérience H.E.S.S.

M Pascal VINCENT Directeur de thèse

Soutenue le 18 mai 2015 devant le jury composé de:

MM	Jean-Pierre	LEES	Rapporteur
	Manel	MARTÍNEZ	Rapporteur
	Reynald	PAIN	Examinateur
	Pierre	SALATI	Examinateur
	Christian	STEGMANN	Examinateur
	Pascal	VINCENT	Invité

PhD THESIS
OF THE UNIVERSITÉ PIERRE ET MARIE CURIE
SORBONNE UNIVERSITÉS

presented by

Tania Garrigoux

Submitted in fulfillment of the requirements for the degree of

DOCTEUR ÈS SCIENCES
DE L'UNIVERSITÉ PIERRE ET MARIE CURIE

Specialty :

Physics of the Universe (STEP'UP - ED N° 560)

Study of the diffuse emissions with the H.E.S.S. experiment

Mr Pascal VINCENT Supervisor

Defended on May 18^{th} 2015 in front of the committee:

Mr	Jean-Pierre	LEES	Referee
	Manel	MARTÍNEZ	Referee
	Reynald	PAIN	Examiner
	Pierre	SALATI	Examiner
	Christian	STEGMANN	Examiner
	Pascal	VINCENT	Invited

Acknowledgements

I would like to thank the members of my committee, not only for accepting being part of it, but also for their patience and helpfulness in finding a date for my defense. Your comments and questions undoubtly helped improve the quality of this manuscript.

Merci à toi Pascal, pour m'avoir accompagnée dans cette aventure. Tu as su m'encadrer et me canaliser jusqu'au bout.

Merci à toutes les personnes du labo qui ont participé à créer une ambiance de travail à la fois agréable et efficace. Merci à Sophie, ma marraine, pour ses conseils et son écoute.

Je remercie le groupe HESS au sein duquel j'ai effectué ma recherche, parmi lesquels mes co-doctorants compagnons d'aventures, Camille et MattKieff (co-bureau), Mathieu, Raphael et Daniel.

Merci à mes autres collègues de bureau, Guigui et Aurélien. Merci à Guigui d'avoir été mon compagnon de nuits/soirées/week ends au labo, t'as grandement contribué à rendre cette période intense plus plaisante.

Merci à Miguel et Jules pour m'avoir accueillie pendant les derniers mois.

Je veux également remercier les équipes de monitorat, pour l'expérience très enrichissante qu'elles m'ont apporté, mais également pour leur prévenance.

I would like to thank the HESS collaboration as a whole for such an interesting working experience and every person with whom I had the pleasure to interact.

A big thank you to Markus, for his welcome and for being so understanding throughout my challenging first months in South Africa. Thanks to my friends, from the lab and from my neighborhood, Iurii and Dariya, Paul and Elize, Hassan, Burcu, Maryse, Mehdi, Isak and Hambe, Zorawar and all those that I probably forget, for all their support during that time.

Un grand merci à ma famille et amis, pour tout leur soutien au cours de ces longues années. À ma Nanounette, pour cette chouette collocation et tant de beaux échanges au quotidien (FCD!), Laet et Titi pour m'avoir accueillie et même parfois nourrie, mes co-bureau/co-doctorants/amis Camille et MattKieff, avec qui j'ai partagé tellement de choses, Ruby pour me permettre de me ressourcer dans un merveilleux environnement, Camcam pour son écoute, petite Alice pour nos psychanalyses, le groupe jeu pour ces journées de divertissement, que ce soit sportif ou en intérieur, Floflo pour sa joie et bonne humeur, Miguel pour son soutien pendant la dernière ligne droite, Jules et Kévin pour leur amitié témoignée pendant les pauses café mais aussi en dehors du labo, Geo et Diane pour ne pas m'avoir virée de leur mariage, Mat, Loulou, Pef, Fred, Ben, Antoine...

Thanks to all my friends en México, en France and around the world, as well as all the people I had the pleasure to connect with.

Gracias a mis witos y mi familia mexicana por estar siempre presentes a pesar de la distancia. Merci à Papa di et Mina pour leur soutien continu et pour avoir toujours cru en moi.

Gracias Agudita awada, Pistu y Piwa por aguantar todos mis caprichos. No lo habría logrado sin su apoyo incondicional. Et enfin un grand merci à mon Bidou, qui m'a fait la personne que je suis aujourd'hui.

Contents

List of figures

List of tables

Introduction

The area of astrophysics that studies the diffuse emissions, very energetic particles that travel through space and arrive on Earth from all directions, has seen an increasing rise of interest over the last decade. With the launch of satellites like Fermi and the ISS and with the significant improvement of ground-based gamma-ray astronomy, propelled by the emergence of Čerenkov instruments like the High Energy Stereoscopic System (H.E.S.S.), these radiations are more easily and precisely detected and studied than ever before. A new understanding of the distribution of matter and fields in the Galaxy becomes thus accessible, enriching our knowledge of the Galaxy and the Universe as a whole. Moreover, recent anomalies in the spectra of these emissions open the door to other areas of exotic physics, such as the subject of Dark Matter, which is believed to be present everywhere in the Universe but is only seen through its gravitational interaction with usual matter. The possibility that the anomalies in the characterization of the diffuse emissions are due to annihilating or decaying Dark Matter has added to the interest in the investigation of these type of emissions.

To introduce the context of this work, the second part of the document gives an overview of, on the one hand, the different types of active gamma-ray sources, as this work was performed in the framework of gamma-ray astronomy, and on the other, the diffuse emissions. The particle emission mechanisms, very different for both, are also described. Concerning the diffuse emissions, a brief summary of the previously obtained results, given by various experiments in similar energy domains, is included for later comparison. The implications in the topic of Dark Matter are also quickly described.

A drawback in ground-based gamma detection is the small window of observation in time and space. Observations can only take place during the night, when the moon is well below the horizon and the largest area which can be explored at a given time is less than 5° on a side. These limits push for an important observation strategy, so the focus will be on active astrophysical sources which are interesting for a wide variety of subjects. Hence, in the field of view, at least one such source will generally be present. Because the developed method aims at extracting the constituents of the diffuse emissions detected at very high energies ($E \gtrsim 100$ GeV) by the High Energy Stereoscopy System, the source region had to be excluded. The originality of this work lies in the fact that no cuts are applied on the data to select one particle or another, as is done in all previous studies. The analysis takes advantage of the development of the discriminant variables introduced in chapter 2. These discriminant variables are studied so as to determine the intervals and observation periods in which they can be used. They are then used to build probability density functions (PDFs) to separate the various components (hadrons, electrons and photons) in the background of the active source in the window of observation. The field of view of the active galactic nucleus PKS 2155-304 was used as a benchmark to obtain the concentrations of the different diffuse emissions. These can then be used to obtain an upper limit on the flux of the diffuse gamma emission. Chapter 5 deals with this aspect of the work.

Because the method is based on PDFs constructed without any cuts to eliminate particles, a difficulty arises when verifying its reliability. As already stated, the standard methods do require this type of data selection, so a direct comparison between standard methods and the developed one is not possible. This issue is adressed with the use of the astrophysical source. Indeed, both the standard and developed analyses can predict the number of photons in the source. However, because of the different data selection, the values differ. In chapter 6, a third way of making this calculation is introduced, consisting on the modelization of the source using the information carried by the point spread function (PSF) of the instrument. For point-like sources, it allows the estimation of the amount of photons collected in the acceptance map of the field of view centered on the targeted source, for a given set of cuts. The values obtained like this could therefore be compared to both the standards methods and the developed one, by applying the corresponding event selection, and thus act as a bridge for the comparison. In this fashion, the particle disentangling method based on the discriminant variables described in chapter 5 is validated, as well as the results it gives for the estimation of the different populations in the background region of PKS 2155-304. Furthermore, the behavior of the detector and its modelization could be studied with the work done on the PSF.

A second facet of this work, presented in the last chapter, was the reconstruction of the spectra for the diffuse emissions. A first idea was to use the concentrations and PDFs obtained in chapter 5, to construct the estimator of data component named X_{eff} and elaborate probabilities for each diffuse particle. In this way, each event will participate in different proportions to the spectrum of each diffuse emission. Once the spectra have been produced, their respective fits lead to the flux and spectral index of each type of particle, thus characterizing the diffuse emissions. Another way of obtaining the different spectra uses the built PDFs of chapter 5 to fit the data and obtain at the same time the concentrations of each type of particle and its weight in the general spectrum. The implementation of this unfolding technique, called *sPlot*, is described in the second part of the chapter.

This study is presented in the framework of the H.E.S.S. experiment, which consists of an array of five telescopes optimized for gamma-ray observation at very high energies. As all ground-based telescopes, it does not detect gamma-rays directly, for at these energies they immediately interact with the atmosphere. Instead, H.E.S.S. uses the properties of the shower of secondary particles induced by the primary particle when it first encounters the atmosphere to reconstruct its main characteristics. We will now describe the different ways of detecting gamma-rays. The focus being on the ground-based method, the particle's shower development in the atmosphere will be detailed. Then, the H.E.S.S. system will be introduced, as well as the particularities of the different ways of reconstructing events to identify the type of shower, primary particle and its parameters. Will also be introduced the different variables, assigned to each event, that will allow to discriminate between the different types of particles in the subsequent method.

Part I

Gamma-ray astronomy with the H.E.S.S. experiment

Chapter 1

Detecting gamma-rays

Sommaire

Several methods exist to detect gamma-rays, depending on their energy interval. At low energies (MeV - GeV), a direct detection is possible either at high altitudes or in space with satellites (EGRET, FERMI...). At higher energies, however, these are no longer contained in the fiducial volume of the detector and, in addition, the decrease of the flux requires too important collection surfaces to be sent to space, thus detection is only possible in an indirect way on Earth (H.E.S.S., MAGIC, VERITAS...). First is given a brief overview of different experiments that study gamma-rays, space borne or ground based. Then, the basic principles behind the detection technique for ground based telescopes is detailed, tackling the way particles interact with matter in the atmosphere to form air showers, with specific characteristics depending on the primary particle. The most significant feature is the emission of Čerenkov light, which is detected by Imaging Atmoshperic Čerenkov Telescopes such as H.E.S.S.

1.1 Gamma-ray detectors

Gamma-rays cover the energy domain above 100 keV. Because at these energies the radiation is absorbed by the Earth's atmosphere, its observation became possible in the 1960s, when detectors that could go above all or most of the atmosphere were first developed. Although balloon experiments can detect cosmic rays, historically their main results concern electrons and hadrons. Nowadays, their detection capabilities are very limited as compared to that of modern satellites and ground-based telescopes, which is essentially due to their short time of flight. Therefore, they were not included in the following overview.

1.1.1 Satellites

The first detection of extragalactic γ dates back to 1961, when the Explorer 11 satellite picked up 22 cosmic gamma-ray photons. However, the first significant gamma-ray emission from our galaxy was detected in 1967, with the launch of OSO-3 (Third Orbiting Solar Observatory). Later, SAS-2 (Small Astronomy Satellite 2) reveals for the first time an emission above 50 MeV from three pulsars, the Crab, Vela and Geminga [1]. The first catalog of very high energy sources, with 25 of them among the first extragalactic source: 3C 273, was given by the COS-B satellite (COsmic-ray Satellite [2]), which also mapped the diffuse gamma-ray emission, mainly concentrated in the galactic plane. A huge leap in gamma-ray astronomy came from the EGRET detector carried by the CGRO satellite (Compton Gamma Ray Observatory), which did a more complete mapping of the gamma-ray sky in the 100 MeV - 10 GeV range. With its surface detection and sensibility 10 to 20 times superior to those of previous instruments, EGRET was able to detect 271 sources above 100 MeV [3] (of which around 170 remain unidentified) and to study with a much better precision the galactic diffuse emission.

Launched in 2008, the Fermi satellite (formerly named GLAST for Gamma-ray Large Area Space Telescope) is the most recent gamma-ray satellite. It includes two scientific instruments: the Large Area Telescope (LAT) and the Gamma-ray Burst Monitor (GBM) (see figure 1.1). The LAT is an imaging gamma-ray detector with a field of view that encompasses about 20% of the sky, allowing it to observe the whole sky in three hours. Although it can reconstruct events up to ~1 TeV, it was initially planned to cover the range in energy from 30 MeV to 300 GeV. Its sensitivity is 10 times that of EGRET and its detection technique similar, based on the conversion of photons into electron-positron pairs which pass through interleaved layers of silicon microstrip detectors, leaving a distinct track. Then, the particles enter a calorimeter in which their energy can be measured. At high energies, the major constraint comes from LAT's lack of magnetic field, which limits the separation of the two conversion electrons and thus, their energy reconstruction. An important characteristic of the detector, is that it possesses an anti-coincidence system that allows to reject charged particles, hence discriminating between electrons and gamma. The performance of the LAT allowed to multiply by 7 the number of detected active sources, increasing it to a total of 1873 constituting the 2FGL catalog, seen figure 1.2. Moreover, the mapping of the gamma-ray sky by LAT shows much more precisely than EGRET the diffuse emission extending in the galactic plane and well above it (figure 1.3). The GBM (Gamma-ray Burst Monitor) is composed of 14 scintillation detectors aimed at detecting gamma-ray bursts from about 10 keV to around 30 MeV, across the whole sky. Its combination with the LAT provides a powerful tool to study Gamma-Ray Bursts (GRBs) and in only two years 491 were detected [4].

The Alpha Magnetic Spectrometer (AMS-02) on the International Space Station (ISS) is an experiment designed to measure cosmic rays at energies ranging between 0.5 to about 500 GeV. It was installed on May 19th, 2011 and in July 2012 had already recorded over 18 billion cosmic ray events. The module includes various detectors with different purposes. The energy of primary electrons, positrons and gamma passing through the detector is measured with the Electromagnetic Calorimeter (ECAL). This allows the distinction between hadrons and other particles. The ACC, or Anti-Coincidence Counter, is used as a veto for high inclination particles, which are not in the acceptance of the detector, and for secondary particles produced by the interaction of cosmic rays with the detector's environment. 80% of such particles are in this

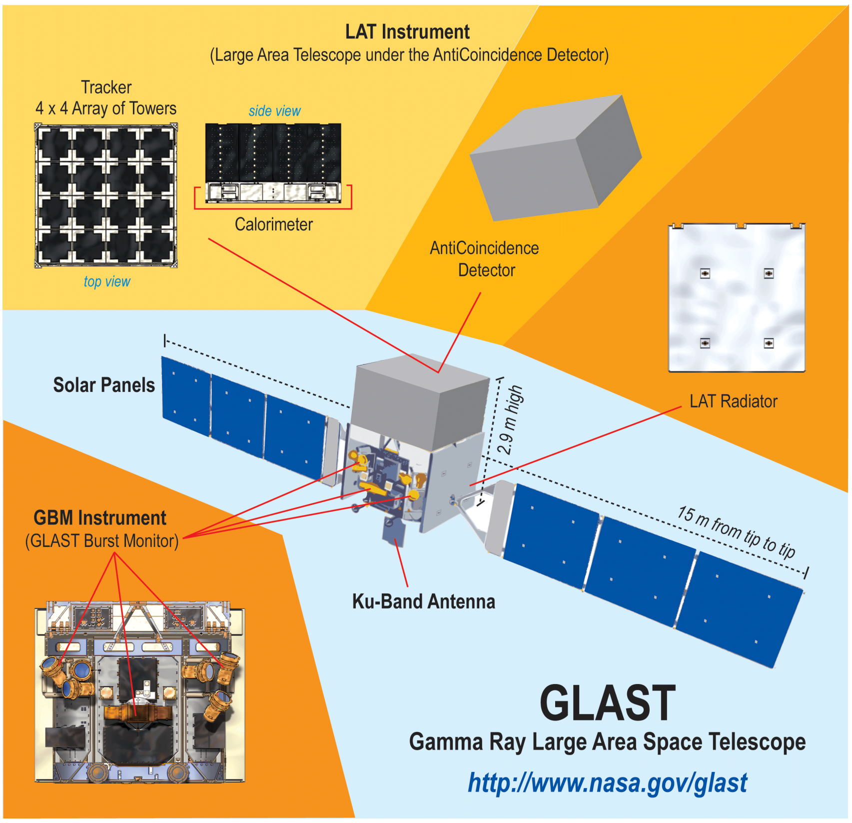

Figure 1.1: The Fermi satellite, with its two instruments: the LAT and the GBM. Credit: NASA E/PO, Sonoma State University, Aurore Simonnet.

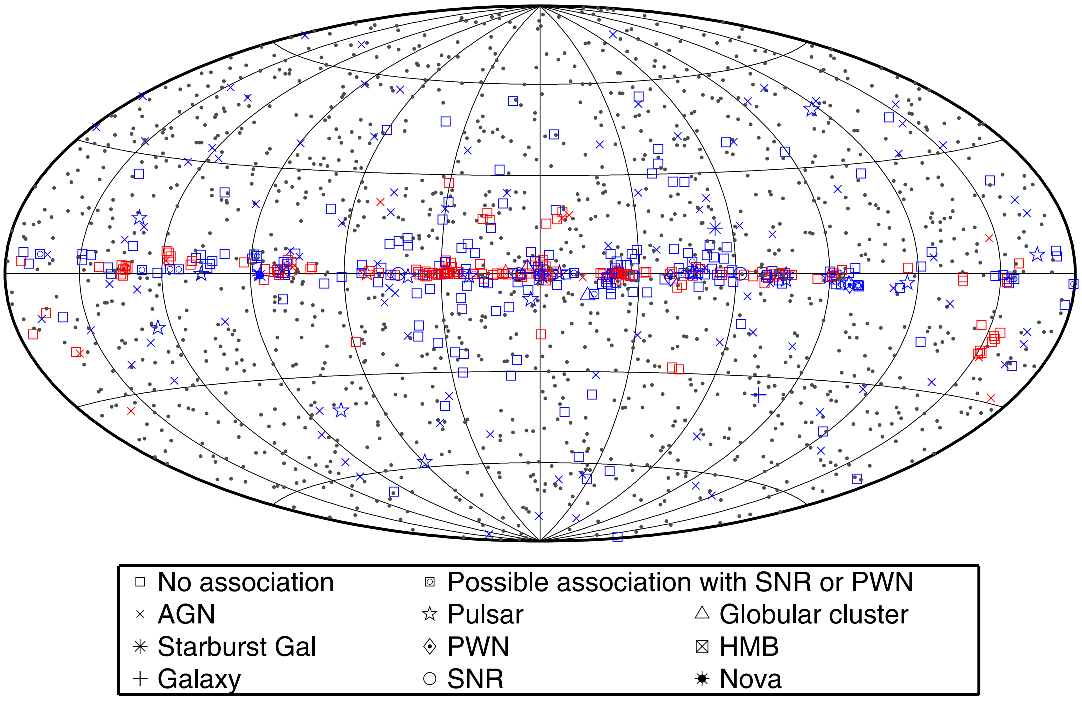

Figure 1.2: Fermi sources of the 2FGL catalog, taken from [5].

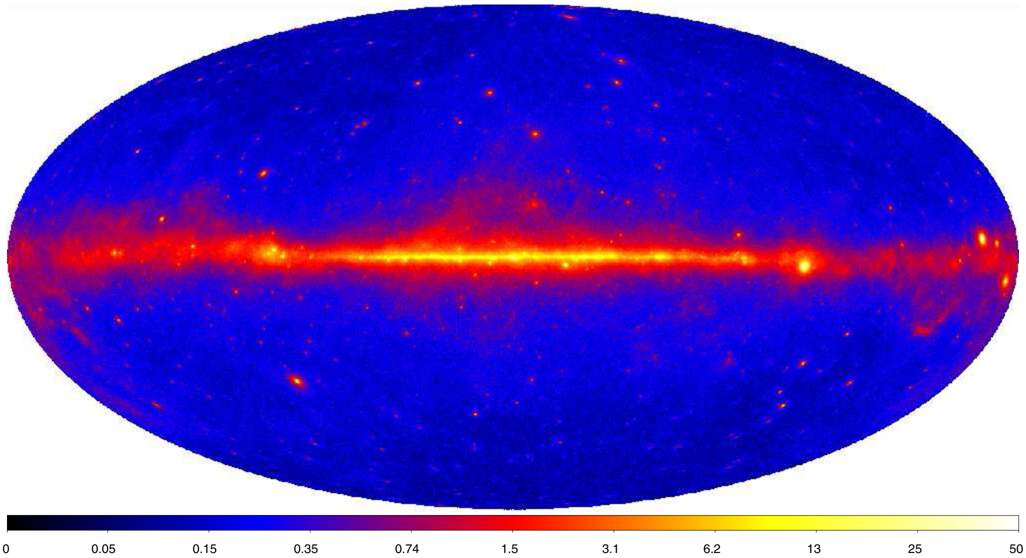

Figure 1.3: The galactic diffuse emission as seen by Fermi. The energy flux is given in the domain between 100 MeV and 10 GeV, in units of 10^{-7}erg cm^{-2} s^{-1} sr^{-1}. Credit [5].

way discarded. The Time of Flight (ToF) system serves as the first level trigger for charged particles, along with the ACC for particle selection depending on the arrival direction and ECAL for neutral particles. The ToF can give the direction (downstream or upstream) of the charged particles. The tracking system, consisting of a magnet and a silicon tracker, determine their absolute charge and momentum. This is achieved by tracking the curvature of the charged particle with a magnetic field. Thus, the combination of the ToF with the tracking system allow the measurement of the sign of the charge and the distinction between matter and antimatter. In this way, electrons and ions up to Z∼30 are identified. The Ring-Imaging Čerenkov Detector (RICH) can measure the velocity of incoming particles and, together with the tracking system, recognize elements until the iron (Z=26) as well as distinguish electrons from protons up to 15 GeV. The Transition Radiation Detector (TRD) can identify relativistic light particles by detecting the X-rays that charged particles emit in the subdetector. It allows the identification of electrons and positrons between 1 GeV and 100 GeV, as well as and efficient discrimination between e^+ or e^- and protons above 300 GeV. Concerning the gamma, the ECAL combined with the tracking system, the TRD, the RICH or the ToF acting as veto devices can separate them and measure their energy. Finally, a Star Tracker determines the orientation of the module in space and a GPS gives the precise time when a gamma-ray has arrived.

Although gamma-ray astronomy started with satellites, for photons above ∼100 GeV, their detection efficiency and resolution decreases very fast. This is due to the fact that fluxes of high energy particles are relatively weak, and therefore a collective surface area of around ~10^4 m^2 is necessary. However, the constraints on the size and weight of space satellites do not allow them to exceed 1 m^2. To study particles with this kind of energies, only ground based experiments can be used, which detect the particles indirectly, after their interaction with the atmosphere.

1.1.2 Ground based experiments

Very high-energy photons produce extensive showers of secondary particles in the atmosphere, as explained in detail in section 1.2. These are either directly observed by radiation encounters (see section 1.1.2.1) or are indirectly detected thanks to the Čerenkov photons emitted by the secondary particles (section 1.1.2.2), a phenomenon that happens when particles travel faster than light in the medium. The latter currently achieves the highest sensitivity.

1.1.2.1 Charged particle detectors

For a primary gamma ray of very high energy, of the order of 1 TeV or more, a more or less important amount of charged particles reaches the ground. They can be detected by scintillation detectors. However, their energy threshold remains quite high because at lower energies, the showers don't enter deep enough into the atmosphere and the density of charged particles at ground level are too low. So, one of the requirements is to be located at very high altitude, closer to the height of maximum development of the shower (which is higher for lower energy primary particles). The main advantages of this kind of detectors is, on the one hand, that they have a large field of view (above 1 sr) and on the other that they observe all the time, day and night. The drawbacks are their low angular and energy resolution and sensitivity, due to a significant cosmic ray irreducible background. Moreover, their energy threshold is quite high compared to other types of detectors.

The first charged particle detector that was sensitive enough to identify point-like sources was the Milagro gamma-ray observatory. It consisted of a 24-million liter water reservoir equipped with photomultipliers used to detect the Čerenkov emission of charged particles going through the water. The PMTs were arranged in two layers, one of which was used to reconstruct the direction of the air shower and its energy. The obtained angular resolution was of around 0.75°. The reconstruction technique relied principally on the measure of the relative arrival time of the air showers across the array, along with their number. A bottom layer of PMTs was used principally to reject hadronic background noise, by detecting mainly muons which can penetrate deeper into the water. The Milagro observatory was able to detect the Crab nebulae [6], blazar Markarian 421 and three extended sources in the galactic plane [7]. A new generation of experiments like HAWC (High-Altitude Water Cherenkov Observatory), uses techniques very similar to Milagro's. In HAWC's case, an extra PMT layer is added with a high quantic efficiency, so as to increase sensitivity at low energies. HAWC should be able to observe gamma-rays between 100 GeV, which represents a significant lower threshold than Milagro's at $\sim$1 TeV, and 100 TeV. HAWC's expected sensitivity is 15 times above Milagro's while covering 2/3 of the sky in 24 hours.

1.1.2.2 Imaging atmospheric Čerenkov telescopes

Imaging atmospheric Čherenkov telescopes are based on the imaging air Čherenkov technique. An incident high energy gamma ray, when entering the atmosphere high up, generates an air shower of secondary particles. The number of these reaches a maximum at a height of about 10 km, and the shower dies out deeper in the atmosphere. Since the charged shower particles move at a velocity above the speed of light in the medium, they emit Čherenkov radiation, a faint blue light, beamed around the direction of the incident primary particle. A telescope located somewhere within the roughly 250 m diameter light pool will reconstruct the air shower if its mirror area is large enough to collect enough photons. The acquired image shows the track of the air shower, which points back to the celestial object where the incident gamma ray originated. Moreover, the intensity of the image is related to the energy of the gamma ray and its shape allows to separate the well-collimated electromagnetic showers from the more diffuse hadronic ones. With a light density of about 100 photons/(m^2 TeV) in the 300 nm to 600 nm wavelength range, this kind of telescopes can only observe on moonless nights, when the background noise is lowest.

For the detection of TeV gamma-rays, IACTs have emerged as the most powerful instruments, considering their drastic improvement in the last decades. The Crab nebula gamma emission at TeV energies was first detected by the Whipple Observatory in 1989 using the imaging atmospheric Čerenkov technique and requiring 50h of observation time to achieve a 5σ significativity [8]. Later, in the 1990's, the HEGRA (High Energy Gamma Ray Astronomy) experiment [9] and CAT (Cherenkov Array at Themis) imaging telescope could detect this source with equal significativity in 15 mins. Now, the running Čerenkov experiments: VERITAS (Very Energetic Radiation Imaging Telescope Array System), MAGIC (Major Atmospheric Gamma-Ray Imaging Cherenkov telescope) and H.E.S.S. (High Energy Stereoscopic System), can detect a source with the strength of the Crab within a few minutes. In the case of H.E.S.S., it is within 30 sec and with an energy threshold of 100 GeV.

Among the dedicated Čerenkov imaging experiments that are still in operation, the two MAGIC telescopes are located in La Palma, Canary Islands. Each telescope has a large active mirror surface of 236 m^2. The assets of this experiment is its very low energy threshold (around 50 GeV) and its very fast pointing capability, both telescopes being able to reposition within 30 - 60 seconds to any sky position [11]. The latter allows the observation of transient events like GRBs and is achievable thanks to the light weight telescope frames made of carbon fiber tubes. As for VERITAS, it is composed of four 12 m in diameter telescopes yielding a field of view of 3.5° and an energy detection ranging from 100 GeV to 30 TeV [12]. Both of these experiments are in the northern hemisphere and have discovered 19 and 16 sources, respectively [1]. In the southern hemisphere, after the end of observations of CANGAROO III system, only the H.E.S.S. array observes. This experiment is described in detail in chapter 2 for its data is taken for the analysis presented in this work, which was done within the H.E.S.S. collaboration.

At low energies, however, gamma-ray observations are still limited by non-gamma-ray backgrounds (electrons and protons mainly) due to the small number of photons in the showers. At high energies, the number of primary photons decreases significantly. The next generation of ground based gamma-ray detectors will start with the construction of the CTA (Čerenkov Telescope Array) observatory (see [13]). With its low energy threshold, large effective areas (the array will cover about 1 km^2) and rapid slewing capabilities, CTA should be able to measure the spectra and variability of GRBs and Active Galactic Nuclei (AGNs) at energies from some tens of GeV to beyond 100 TeV, as well as boost the sample of the detection of the latter by about one order of magnitude. Furthermore, the increase in its angular resolution should allow to resolve the morphology of extended sources with a precision never obtained before. CTA will consist of two arrays of IACTs, one in each hemisphere, so as to be able to observe the entire sky. In the Northern Hemisphere, the main goal will be the study of extragalactic objects at lowest possible energies. The Southern Hemisphere's array, however, will have its emphasis on galactic sources, covering the whole range of energy. Construction is expected to start in 2018. An artist's impression of CTA can be found figure 1.4.

The success of the Čerenkov imaging technique even prompted the use of solar facilities to observe Čerenkov radiation. Fields of solar mirrors (known as heliostats) can collect and direct the Čerenkov light into special equipment that detect and record it via secondary optics and

---

[1] http://tevcat.uchicago.edu

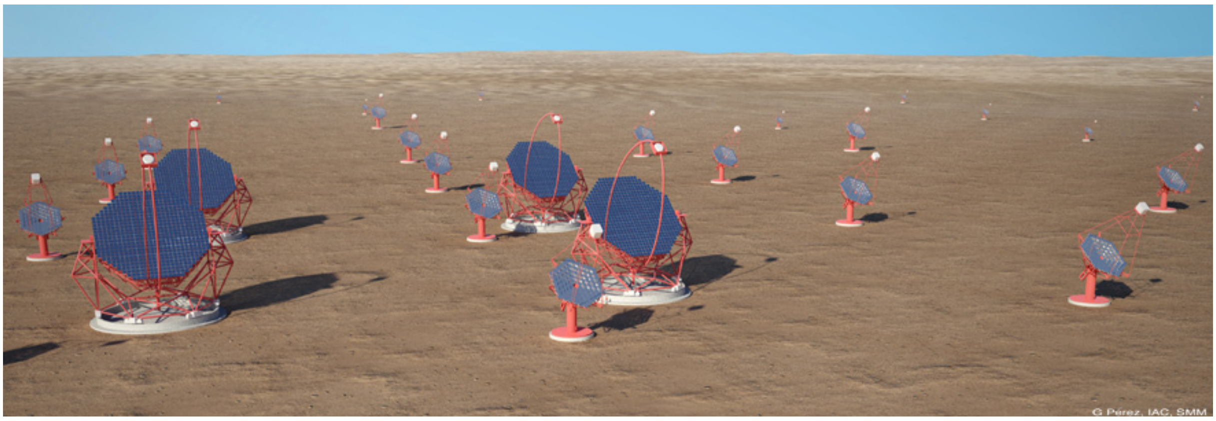

Figure 1.4: An artist's impression of the Čerenkov Telescope Array, the biggest future project for IACTs. Credit: https://www.cta-observatory.org/

PMTs. Examples are the CELESTE experiment at the Themis site in the French Pyrénées that converted a former solar electric plant [10] or STACEE (Solar Tower Atmospheric Cherenkov Effect Experiment) that used during night a solar thermal test facility in New Mexico. In addition, air showers can be detected with X-ray fluorescence, produced by the deexcitation of the molecules present in the atmosphere after their excitation by shower particles. As opposed to the Čerenkov light which is highly directional, this emission is isotropic. The well-known Pierre Auger observatory studying ultra-high-energy cosmic rays incorporates both fluorescence and Čerenkov detectors in a 3000 km^2 array. At those energies however, no gamma has been clearly identified.

1.2 Particles interacting with matter

When a very energetic particle enters the atmosphere, it will interact with it. In the case of electromagnetic particles, this happens almost immediately. Thus, the entry of an incident particle in the atmoshpere will produce an air shower of secondary particles that in turn interact, usually resulting in a combination of electromagnetic cascades and hadronic multiparticle production. The development of the air showers is described first. Then, two shower parameters important for the subsequent analysis are introduced in this section: the height of the maximum of the shower development and the first interaction point in the atmosphere.

1.2.1 Atmospheric shower development

Showers are commonly divided into two categories: the electromagnetic ones when the initial particle is an electron or a photon and the hadronic ones.

1.2.1.1 Electromagnetic showers

When gamma-rays enter the atmosphere, they interact with the atoms, mainly with the electromagnetic field of their nuclei, and convert into electron-positron pairs. In turn, these will emit a bremsstrahlung photon due to the nuclei's fields and the process will repeat itself with decreasing energy. This will occur until the energy of the electrons drops to a critical value, noted E_c, below which average energy losses due to ionization begin to exceed radiative losses. The development of the shower then stops. This explanation corresponds to a simplification introduced by Heitler (see figure 1.5) in which the bremsstrahlung and pair production will cause the formation of the shower, while the ionization of atoms will provoke its expiration.

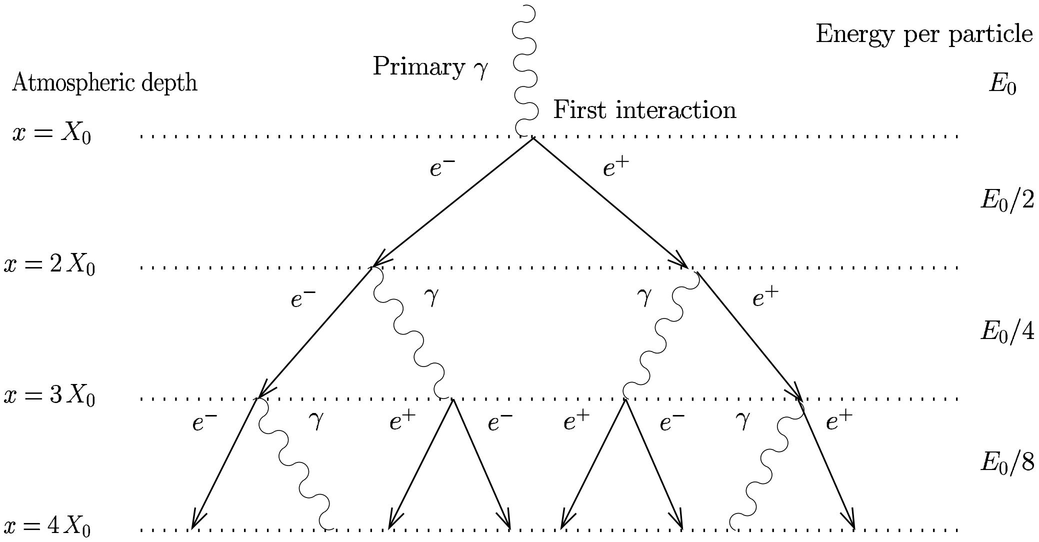

Figure 1.5: In the Heitler simplified model of electromagnetic showers, every radiation length X_0 there is either a pair production or a bremsstrahlung emission, in which each resulting particle has half the energy of the previous one.

The bremsstrahlung process induces an energy loss by distance x traveled through matter of density ρ:

$$-\left.\frac{dE}{dx}\right|_{rad} \approx \frac{\rho E}{X_0} \tag{1.1}$$

which integrated gives:

$$E(x) = E_0 \cdot e^{-\rho x/X_0} \tag{1.2}$$

where X_0 (expressed in g·cm^{-2}) is defined as the distance in which the electron looses $1-1/e \approx 63\%$ of its energy and given by:

$$\frac{1}{X_0} = 4\alpha N_A Z^2 r_e^2 \left[ln(183 Z^{-\frac{1}{3}}) + \frac{2}{9} \right] \tag{1.3}$$

with Z the charge number, N_A the Avogadro constant, r_e the classical electron radius and α the fine structure constant.

At high energies, the energy loss because of ionization for electrons is given by the Bethe-Bloch formula:

$$-\frac{dE}{dx} = 2\pi \frac{(\alpha hc)^2 N_A}{m_e c^2} \rho \frac{Z}{A} \left[ln \frac{4 m_e^2 c^4 \gamma^2 (\gamma - 1)}{I^2} - \frac{a}{2} - \frac{\delta}{2} \right] \propto lnE \tag{1.4}$$

where c is the speed of light, h the Planck constant, α the fine structure constant, m_e the electron rest mass, ρ the matter's density, Z and A the charge and molar mass numbers, γ the Lorentz factor, I the mean ionization potential, δ the density correction. Finally, a is a parameter with a value of 2.9 for positrons and 3.6 for electrons, since the Pauli exclusion principle will only apply on electrons, not allowing them to be in the same quantum state as the electron in the atom with which it is interacting.

The critical energy is obtained when the energy loss through bremsstrahlung equals the loss from ionization:

$$\frac{(dE/dx)_{rad}}{(dE/dx)_{ion}} = 1 \approx \frac{Z}{1600}\frac{E_c}{m_e} \Rightarrow E_c = \frac{817{,}6\ \text{MeV}}{Z} \tag{1.5}$$

Hence the critical energy also depends solely on the medium's parameters, and its value is $E_c = 83$ MeV in dry air.

For the pair production process, the attenuation of the intensity of the photon beam is given by:

$$I(x) = I(0)e^{-n\sigma_\pi x} \tag{1.6}$$

with n the atomic number density of the matter and σ_π the cross section for the interaction:

$$\sigma_\pi = \alpha r_e^2 Z^2 \left(\frac{28}{9} ln\left(183Z^{\frac{1}{3}}\right) - \frac{2}{27}\right) \sim \text{constant} \tag{1.7}$$

σ_π is independent of the energy and the only parameters are from the matter the photon is going though. One can write equation 1.6 as:

$$I(x) = I(0)e^{-\rho x/X_c} \tag{1.8}$$

with X_c the conversion length of the photon, by analogy with the X_0 of the electron (seen in equation 1.1). From the formulas 1.7 and 1.3, one can find that $X_c = \frac{9}{7}X_0$, which is why it is considered that there is a pair production or loss by bremsstrahlung every radiation length X_0 in the Heitler model, assuming that the energy is equally divided between the secondary particles after the passage of one length scale, as seen figure 1.5.

In the case of electromagnetic showers, the predominant process determining lateral shower development is multiple Coulomb scattering. Charged particles will be deflected during their whole path by the nuclei's electric fields. Although each will be a small-angle scatter, their accumulation leads to a deviation of the order of 1 degree. This Coulomb scattering distribution is well described by the theory of Molière, in which it is modelized by a Gaussian shape for small angles and by a Rutherford scattering at large angles, with longer tails than a Gaussian. The lateral spread of the shower is characterized by the Molière radius R_M (g$\cdot$ cm^{-2}), defined by the radius of a cylinder containing in average 90% of the energy of the shower. R_M is given by:

$$R_M = X_0 \frac{E_s}{E_c} \tag{1.9}$$

with E_s the scale energy:

$$E_s = m_e c^2 \sqrt{4\pi/\alpha} = 21{,}2052\ \text{MeV} \tag{1.10}$$

In the air, $R_M \approx$80 m at sea level.

1.2.1.2 Hadronic showers

Showers initiated by hadrons are fundamentally different from electromagnetic ones, for they can produce a wide variety of secondary particles, like smaller nuclei, hyperons, pions, kaons, muons and neutrinos, as well as the three in electromagnetic sub showers: electrons, positrons and photons. Some examples of decay processes of kaons that might result from hadrons interacting with the atmosphere are shown in 1.11 and 1.11, although pions are often directly produced. The π^0 decay into two gamma represents about one third of the energy of the hadronic cascade at each stage. So, the induced air shower will have two components: an electromagnetic and a hadronic one, the latter feeding the first via decay of neutral and charged mesons.

$$\begin{array}{rl} K_s^0 \rightarrow \pi^0\pi^0 & (30.69 \pm 0.05)\% \\ \searrow \pi^+\pi^- & (69.20 \pm 0.05)\% \\ K^\pm \rightarrow \pi^\pm\pi^0 & (20.66 \pm 0.08)\% \end{array} \tag{1.11}$$

$$\begin{array}{ll} \pi^0 \rightarrow 2\gamma & (98.823 \pm 0.034)\% \\ \pi^+ \rightarrow \mu^+\nu_\mu & (99.98770 \pm 0.00004)\% \\ \mu^+ \rightarrow e^+\nu_e\bar{\nu}_\mu & (\approx 100\%) \end{array} \tag{1.12}$$

A couple of characteristics of the hadronic showers' development allows to distinguish them from electromagnetic showers when looking at their image in the camera, as will be seen in section 2.2. Because the hadronic free path length is about 90 g·cm^{-2}, which is about three times the radiation length X_0, hadronic showers will develop much later. This, added to the fact that a significant fraction of the primary energy goes into long-lived muons and neutrinos, as well as nucleus interactions, results hadronic showers emitting less light than electromagnetic showers for the same primary's energy. Moreover, they will generally be accompanied by muons produced in the decay of charged pions, easy to identify in camera images. Their lateral extension will be dominated by inelastic scattering of the secondary particles sensitive to weak and strong interaction at extended target particles. The secondary particles will thus receive higher transverse momenta and the lateral development of the hadronic showers is much more pronounced than that of electromagnetic ones, induced by multiple Coulomb scattering. Finally, hadronic showers produce electromagnetic sub showers with very different intensities, causing large fluctuations that result in a wider spread of the arrival times of light at ground level. These complex multi-particle processes also leads to irregular shapes of the shower, as compared to electromagnetic ones. All these characteristics can be observed in figure 1.6.

It can be noted that the intensity of primary nucleons in the energy range from several GeV to somewhat beyond 100 TeV is given approximatively by [15]:

$$I_N(E) \approx 1.8 \times 10^4 (\frac{E}{1\ \mathrm{GeV}})^{-\alpha} \frac{\mathrm{nucleons}}{\mathrm{m}^2\ \mathrm{s\ sr\ GeV}} \tag{1.13}$$

where E is the energy-per-nucleon (including rest mass energy) and $\alpha (\equiv \gamma + 1) = 2.7$ is the differential spectral index of the cosmic ray flux and γ is the integral spectral index. Therefore, the flux of protons is around 79%, while that of Helium nuclei is about 70% of what is left, giving a total of $\sim 14\%$. Moreover, at equal energies, Helium nuclei will only produce half the light as protons (see simulations in [14]). Hence, they will represent only 10% of the detected light form hadronic showers. In the same way, the other elements are generally neglected, for their contributions are lowers than 1%.

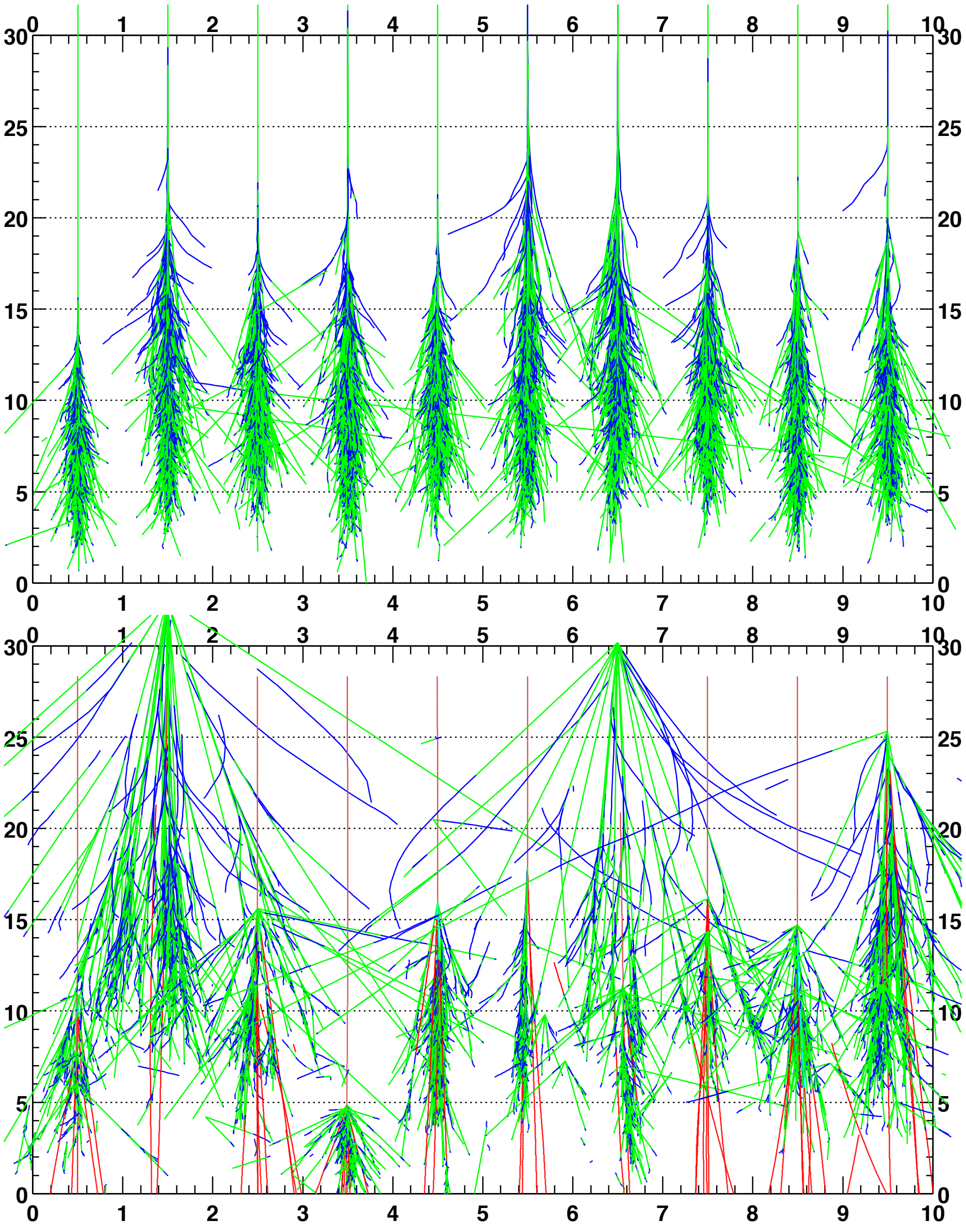

Figure 1.6: Comparison between ten electromagnetic (top) and hadronic (bottom) showers from 300 GeV primary particles. Photons are shown in green, electrons in blue and hadrons in red. The elecromagnetic showers have less fluctuations than hadronic ones and are much more similar to each other. Both axis are given in kilometers. The vertical scale gives the altitude with respect to sea level. Taken from [14]

1.2.2 Height of the maximum of shower development and first interaction point

The height of the maximum of shower development and the first point of interaction of the primary particle in the atmosphere are two important parameters that define a shower's development in the air. They are illustrated in figure 1.7.

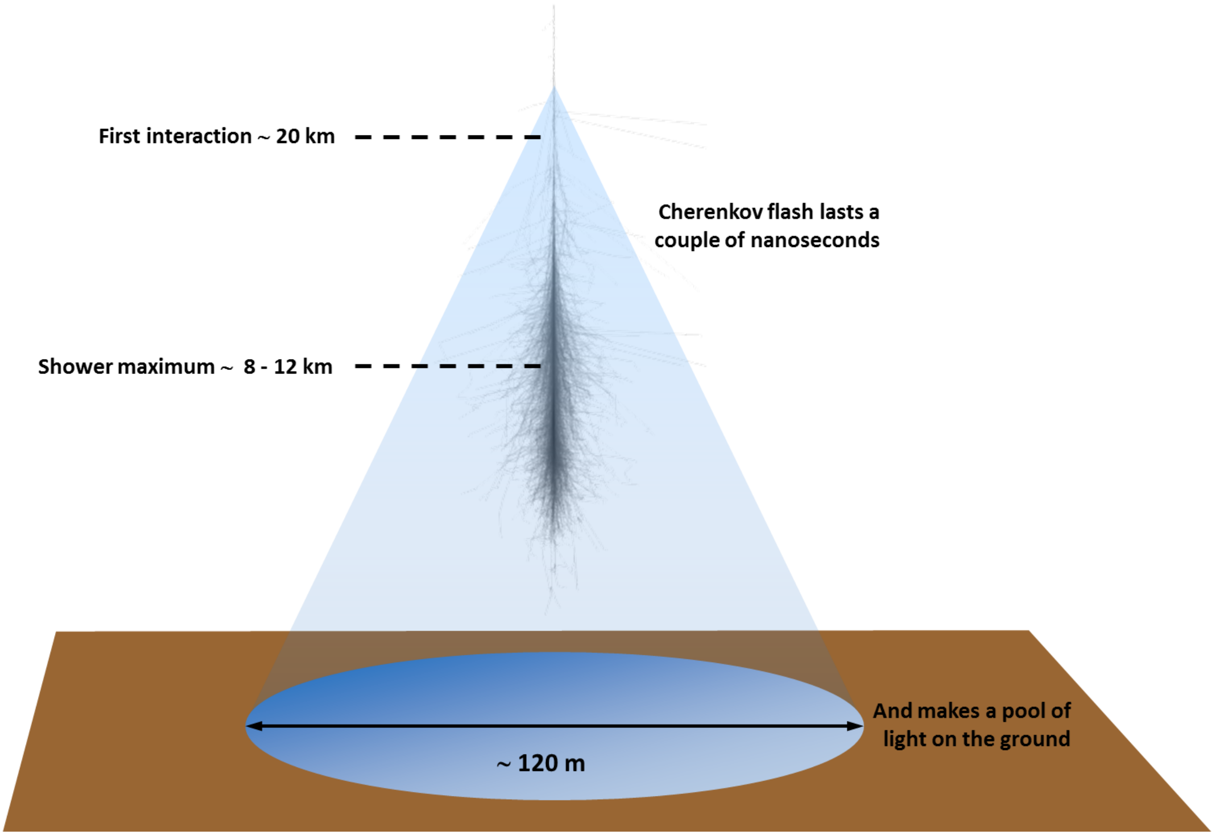

Figure 1.7: Maximum of shower development (altitude ~8-12 km) and first interaction point (altitude ~20 km). In blue can be seen the Čerenkov light emitted by the charged particles produced in the air shower and propagating in the atmosphere. Credit: M. Daniel

Even though the Heitler model does not capture accurately all details of electromagnetic showers, two important features of these are present: the maximum of shower development depends on the logarithm of the primary's energy E_0 and the number of particles at the shower maximum N_{max} is proportional to E_0. This can be simply calculated from the fact that after $n = x/X_0$ branchings, the shower has $N(x) = 2^{x/X_0}$ particles, each with an energy of $E(x) = E_0 \cdot 2^{-x/X_0}$. Here, x is the distance in g·cm^{-2} traveled by the particle along the shower axis. Then, the height of the maximum of the shower development X_{max} is given by:

$$E_0 \cdot 2^{-X_{max}/X_0} = Ec \Rightarrow X_{max} = \frac{ln(E_0/E_c)}{ln2} \cdot X_0 \tag{1.14}$$

With this expression, N_{max} can be computed as follows:

$$N_{max} = 2^{X_{max}/X_0} = \frac{E_0}{E_c} \tag{1.15}$$

However, there is a difference between electron and photon induced showers, that comes from the radiation length X_0 for electrons and the attenuation length for the photons X_c. These characterize their mean free path and hence their first point of interaction in the atmosphere and, as seen in section 1.2.1.1, $X_c = \frac{9}{7}X_0$. So the first point of interaction will also differ by about 20% Moreover, the position of the height of the maximum of the shower development t_{max}, expressed in radiation length units with respect to the first point of interaction, is parameterized [16] by $t_{max} = 1.0 \cdot ln(y) + C_j$ where $j = e, \gamma$ and $y = E/E_C$, where E is the energy of the incoming particle and the two C_j parameters varies from 0.5 to 1 depending on authors of the parameterization. At around 1 TeV, a value of t_{max} equal to 8.87 for electrons can be estimated from simulations and, consequently, a value between 9.37 and 9.87 for photons is expected. Besides the fact that they develop in average one radiation length higher in the atmosphere, due to the cumulated differences in the first point of interaction and height of the maximum of the shower development, the only difference electron induced showers have with respect to γ induced ones is that the primary electron already emits a Čerenkov radiation. In a homogeneous medium, both would be identical in every other way.

Nonetheless, the difference of about 22% in the first point of interaction has an influence on the development of the electromagnetic shower for gamma and electrons. Indeed, in a inhomogeneous medium, if the shower starts higher in the atmoshpere, the matter density will be lower and the shower will penetrate and develop more deeply into the atmosphere, as compared to one starting later. Hence, with their point of interaction deeper in the atmosphere, gamma showers won't develop as far as expected in a homogeneous medium. The opposite will be true for electrons. Therefore, the gap between their two t_{max} should be reduced. In a inhomogeneous medium, simulations are needed to know what to expect.

Concerning hadrons, because their mean free path is about 3 times the radiation length of electrons, as previously commented, the first point of interaction in the atmosphere will vary greatly, up to several tens of kilometers. In addition, the showers penetrate deeper into the atmosphere, and the X_{max} depth is in average larger. The relation that is usually given for hadrons is $t_{max} = 0.6 \cdot ln(E/X_h) + 8.1$, with X_h expressing their mean free path.

1.2.3 Atmospheric Čerenkov light

The Čerenkov effect is the equivalent of the sonic barrier but for light. Because most secondary particles in the air showers have ultra-relativistic speeds, these are larger than the local phase velocity of light. When this happens for a charged particle in a dielectric medium, an electromagnetic shock wave that takes the form of a light cone is emitted towards the front. The angle of this cone θ_c is given by:

$$\cos\theta_c = \tfrac{1}{n\beta} + \tfrac{\hbar k}{2p} \cdot \left(1 - \tfrac{1}{n^2}\right) \text{ (with } \beta = \tfrac{v}{c}\text{)}$$

with p the particle's momentum, k its wave vector, v its speed, and n the refractive index of the medium. Because the Čerenkov photons produced in this way have wavelengths in the blue-ultraviolet part of the spectrum, for which $k \ll p$, the relation can be written as follows:

$$\cos\theta_c \approx \tfrac{1}{n\beta} \approx \tfrac{1}{n} \text{ (for } \beta \approx 1\text{)}$$

θ_c is usually around 1° in the air. The Čerenkov photons, produced in this way, have wavelengths in the blue-ultraviolet part of the spectrum and are partially absorbed by the atmosphere. The spot at ground level has a typical radius of 120 m for an electromagnetic shower whose height of maximum development is located around 10 km, corresponding to a primary particle with an energy of the order of the TeV and a zenith angle of 0°. These characteristics are displayed in figure 1.7. The flash of Čerenkov light only lasts a few nanoseconds. The Čerenkov cone will be detected, allowing the identification and reconstruction of the primary particle's initial parameters. After cumulating all detected particles during a given observation time, a full sky map can be reconstructed, along with the targeted source(s) in the field of view.

Chapter 2

The High Energy Stereoscopic System

Sommaire

The data used in this work was taken by the H.E.S.S. telescopes, which are first described in a quick overview of their main features. Then, the reconstruction of the different characteristics of the air showers, as are the primary particle, their energy, incoming direction or first point of interaction in the atmosphere are introduced depending on the model used for reconstruction. Next is explained that although a good identification of the initial particle and, in this way, background rejection is achieved, further treatment of the obtained map of the sky is needed in standard analyses. Because the method developed in this work does not rely on cuts for selecting the particles but on the use of discriminant variables, several differences can be highlighted, which is the object of the last part in the "Shower reconstruction" section.

2.1 The H.E.S.S. experiment

2.1.1 General characteristics

Since the fall 2003, the High Energy Stereoscopic System (H.E.S.S.) [17] is devoted to the observations of high energy gamma rays, in the 100 GeV to a few tens of TeV energy range for the first phase and with a lower energy threshold, of about 20 GeV, for the second phase starting in July 2012. It enables scientists to explore gamma-ray sources with intensities at a level of a few thousandths of the flux of the Crab nebula (the brightest "steady" source of gamma rays in the sky mainly observable in the northern hemisphere). Its primary goal is to provide the experimental basis for an improved understanding of the acceleration, propagation and interactions of non-thermal populations of particles. The instrument consists of an array of five Imaging Atmospheric Čerenkov Telescopes (IACTs) situated in the Khomas Highland of Namibia, an area well known for its excellent optical quality. This southern location provides optimal conditions for observing the center of our Galaxy, a region full of high-energy sources as supernova remnants and pulsars, which are of significant interest for gamma-ray astronomy.

With a single telescope providing a single view of a shower, it is difficult to reconstruct the exact geometry of the air shower in space. To accomplish this, multiple telescopes are used which view the shower from different points and allow a stereoscopic reconstruction of the shower geometry, as will be detailed in section 2.2. The four telescopes corresponding to the phase I of the experiment (named CT1, CT2, CT3 and CT4) are 12 m in diameter, weighting around 60 tons, and are arranged in the form of a square 120 m on a side. This spacing is a compromise between the large base needed to provide views from each telescope different enough as to allow a good stereoscopic reconstruction, and the requirement that two or more telescopes detect the shower for, as seen in section 1.2.3, the Čereknov light pool is usually around 250 m in diameter.

While the first H.E.S.S. telescope began operation in Summer 2002, with the whole phase one array observing by December 2003, the fifth telescope (called CT5) was added at the center of this array for the second phase of the project in 2012. The aim is not only to lower the energy threshold as already mentioned, but also to increase the sensitivity and angular resolution - the pixelisation of CT5 is half that of the other telescopes - of the instrument, with more telescopes observing at the same time, an important feature as will be seen in section 2.2. With its 28m diameter, 614 m^2 collection area as compared to 108 m^2 for a phase 1 telescope, and 580 tons weight, CT5 is the largest IACT ever built on Earth. Nonetheless, its rotation speed is twice that of phase I telescopes. The simultaneous use of these two different types of telescopes, CT1-4 and CT5, H.E.S.S. II constitutes the first hybrid IACT array, and paves the way for future projects like CTA described in section 1.1.2.2. A photo of the array can be seen figure 2.1.

As for other large IACTs, for cost reasons H.E.S.S. telescopes' light reflectors are segmented into an array of individual mirror facets. Phase I telescopes have 382 of them, spherical, 60 cm in diameter, arranged in a Davies Cotton layout to limit the Coma aberrations (far from the optical axis). However, this will induce a higher spread of the arrival time of the photons to the camera. Thus, to minimize time dispersion which would be even more significant for the biggest telescope CT5, a parabolic arrangement was preferred for its 875 hexagonal facets of 90 cm size. Given the weight of the facets and the size of the dish, a cost-effective design of the structure which does not deform when moved in elevation due to gravity would be non-trivial. Therefore, H.E.S.S.' dish and reflector constitute a compromise between stiffness against weight and cost, yielding only uncritical deformations over the working range in elevation, as will be seen in section 2.1.5.1. Moreover, the space between the facets is minimised to make optimum use of the reflector area.

Figure 2.1: The H.E.S.S. site in Namibia. The four "small" telescopes arranged in a square constitute the first phase of the project, whereas the central fifth telescope is the latest addition to the experiment. Credit: C. Medina

Unlike other Čerenkov telescopes, the complete electronics for image digitization, readout and triggering is integrated into the camera body. This way, no signal transmission is needed, which can be a source of noise, bandwidth limitation, and cost. For this design, a high-performance cooling system is required, with fans distributed in the body of the camera, of which up to 240 (CT5) are for the frontal electronics. The temperature is controlled by 360 thermometers in this part of the camera. H.E.S.S. I cameras consist of 960 pixels of small size (0.16°) so as to resolve the details in the Čerenkov images of air showers it detects and records using photomultiplier tubes (PMTs). The total field of view is of 5 degrees, which is large to allow observations of extended sources and surveys. Winston cones were added in front of the PMTs to act as non-imaging light concentrators, conveying light into the photocathodes. Thus, at the same time, the light collection is improved and the albedo from the ground reduced. The efficiency of the wave guide inside the cones depends on their geometry. They were optimized to produce a cut at 30 degrees with respect to their axis of symmetry, which corresponds to the dimensions of the mirror. In order to protect the electronics during the day, it can be hermetically closed, along with the PMTs, with a mobile lid. Although the electronics were entirely modified, the H.E.S.S. II camera follows the same design, but is much larger, with a total of 2048 PMTs. The pixels have the same size but because of the larger focal length, the shower images have a much better resolution (0.067° angular aperture). However, the field of view is reduced to 3.2°. The main improvement of H.E.S.S. II is the reduction of the camera dead-time from about $460\mu s$ to less than $20\mu s$ with a data acquisition rate that went from maximum 1.2 kHz to an average of 3 kHz in stereoscopic mode, the camera being able to function up to 50 kHz. In addition, a level 2 trigger, which is in operation but not yet in the final trigger decision, should limit the night sky background events thus allowing for a lower trigger threshold.

The triggering scheme allows to identify the brief and compact Čerenkov images rejecting backgrounds like the night sky light (NSB). Because, as mentioned, H.E.S.S. needs to reconstruct the air shower in order to determine the parameters of the primary particle, only those triggering at least two telescopes will be recorded. This works through a central trigger station, which sends a confirmation back to the telescope for it to continue to digitize, process, and read out the analog signals, only if simultaneous observations of the same shower took place. If this is not the case and the camera does not receive the signal, it will stop the acquisition and moves on to the next one. Now that CT5 is operational, the possibility of it being the only one triggering the read out has been added, to provide minimal energy threshold.

Concerning the flat-field correction, a system is implemented for each camera, in which a laser located in the dish can emit a homogeneous signal over the entire camera to intercalibrate the response of the different channels. Furthermore, a single photo-electron calibration system is also included in each camera. It consists of a low-intensity source directed at the PMTs when the camera is positioned in its shelter. Five of the latter were built to protect each camera during daylight time. In the case of CT5, the dimensions of the telescope were such that it was necessary to create a system to unload the camera from its focal plane and place it in its shelter. To minimise these handling operations for calibration purposes, an alternative system was set up, consisting of a mobile mylar plate that can be put in front of the PMTs and illuminated by the laser situated in the dish, attenuating its intensity and completely filtering the night sky background. With this system, which is currently being evaluated, it will be possible to do the single photo-electron calibration with the camera located in the focal plane of the telescope.

The system controlling the positioning of the camera in the focal plane uses a CCD camera placed in the dish which monitors the position of 8 luminous sources located at the edge of the focal plane of the camera. This way, the deformation of the structure holding the camera as a function of the direction of observation. In addition, some stars are monitored during observations to verify that each telescope is correctly positioned.

2.1.2 Optical efficiency

The optical efficiency of the H.E.S.S. experiment depends on several parameters. Ideally, it should be of 11.3%, corresponding to the product of the following values:

- $\sim 0.8 - 0.7$: reflectivity of the mirrors
- ~ 0.75: collection efficiency of the Winston cones
- ~ 0.2: quantum efficiency of the PMTs
- ~ 0.9: collection efficiency of the PMTs

However, in fact only a fraction of this value is achieved because the different parameters evolve in time. The reflectivity of the H.E.S.S. I mirrors decreases by an average of 3% per year. Between 2001 and 2010 when the re-aluminisation of the mirrors began, it went from 80% to 65%. The Winston cones located in front of the PMTs also loose their reflectivity due to dirt deposition. Moreover, atmospheric absorption at low altitudes will also influence the optical efficiency. Hence, it is controlled at every period of acquisition by collecting data taken on muon events as selected by the triggering system. In practice, the fraction of the ideal value is what is usually referred to as the optical efficiency of the instrument. The evolution in time of the optical efficiency of each of the telescopes can be seen figure 2.2. For this analysis, the mean value over the used runs was calculated for every source and period of acquisition. They were all found to be between 52% and 54%. The optical efficiency of CT5 (H.E.S.S. II in the figure) drops more rapidly than that of the H.E.S.S. I telescopes (around 7% every year). This is caused by the ageing of the mirror, which is faster than expected. A re-aluminisation is being discussed to solve this problem. The bumps observed come from several realignements of the mirrors.

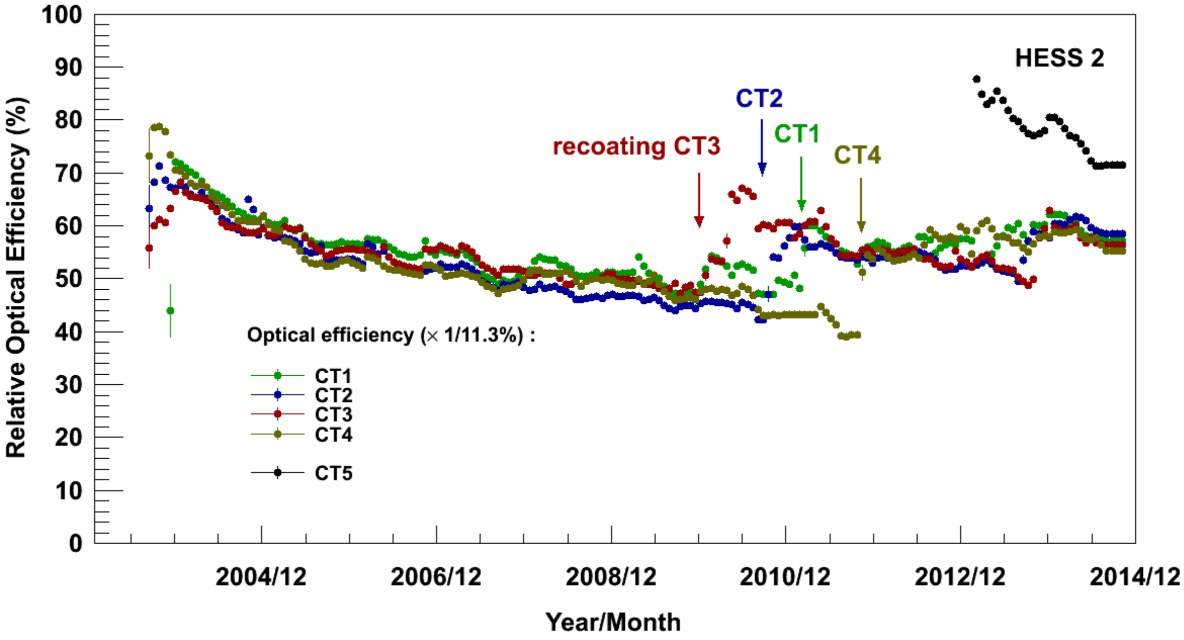

Figure 2.2: H.E.S.S.' optical efficiency as a function of time. From the start of the experiment up to 2010, a global decline of the optical efficiency can be noted, which is to be expected from the wear of the instrument. In 2010, the re-aluminisation of the mirrors improved the optical efficiency. The different peaks in the distributions, the most important one visible in 2006, correspond to cleaning campaigns of the PMTs and cones. In 2012 the curves are more grouped due to the implementation of a new muon reconstruction for the calibration. Concerning the optical efficiency of H.E.S.S. II, it drops faster than that of H.E.S.S. I and the bumps observed come from several realignements of the mirrors.

2.1.3 Simulations

For the H.E.S.S. experiment, simulations are done in two steps. First, the air-shower's development in the atmosphere is simulated via known programs such as CORSIKA or KASKADE, for three different types of particles: gamma, electrons and protons. These take into account the atmospheric profile. Then, the showers pass through the telescope simulations, with a number of parameters which are discretized. For instance, the optical efficiency, the zenith angle, and the azimuthal angle are discrete variables in the simulations. Concerning the zenith angles, the existing values for the simulations are: 0°, 18°, 26°, 32°, 37°, 41°, 46°, 50°, 53°, 57°, 60°, 63°, 66° and each type of particle has its own subset. The simulations have been done only with an azimuthal angle of 0° for protons. For electrons and gamma, the 180° value existed and was added to improve statistics. Originally, this configuration had been generated to study the effects of the geomagnetic field on the development of the air showers. No notable systematic effects had been observed however, due to the fact that the experiment is located on a geomagnetic anomaly. The existing optical efficiencies range between 40% and 100%, with a step of 10%. The events' energy were simulated from 0.05 TeV to 100 TeV. Simulations of gamma-ray sources were achieved by fixing the angle of the incoming particles and thus the angular distance of the source with respect to the center of the camera (off-axis angle). This was done for six different configurations, with off-axis values of 0°, 0.5°, 1°, 1.5°, 2°, 2.5°, 3°. To simulate diffuse emissions, off-axis angle values are taken randomly between 0° and 8° and cumulated.

2.1.4 Proton, gamma and electron acceptance

In order to build a spectrum or calculate a flux, one important step is to estimate the acceptance of the detector for each type of particle. These had to be computed for two reasons: so as to correspond to the cuts in this work, and for the diffuse emissions because they have never been obtained in the first place. To do this, the simulations were used. The acceptance depends upon five parameters :

- True energy: the telescopes were built and optimized to detect photons within a certain energy range around 1 TeV. The ability to detect and reconstruct a particle depends on its initial energy, known as its "true" energy.

- Optical efficiency: the evolution in time of the optical efficiency of the telescopes discussed in the last section affects their acceptance. Because the values of the optical efficiencies in the simulations are discreet, for each event the value of the optical efficiency of the corresponding run was taken and interpolated with the Delaunay triangle method using all available optical efficiencies.

- Zenith angle: at higher zenith angles, the primary particle's shower travels a larger distance in the atmosphere before reaching the telescope, during which the emitted Čerenkov photons will be diluted in a broader light pool and mostly absorbed by the atmosphere. Therefore, only the particles with higher initial energies will produce showers that will generate enough Čerenkov radiation to reach and trigger the telescopes despite their dilution and atmospheric absorption. So the energy dependence of the acceptance implies a zenith dependence as well. The difference in this induced energy threshold between two extreme values of the zenith angle is of about one order of magnitude.

- Distance to the center of the camera or off-axis angle: The trigger efficiency of the telescopes is strongly dependent on the off-axis angle: it is at its maximum and relatively stable in an area around the center of the camera of about 1.5 degrees in radius, and then decreases, because the image is no longer contained in the camera in its entirety. As a consequence, the same occurs with the acceptance.

- Azimuthal angle: showers with different azimuth angles will be affected differently by the magnetic field. Hence, primary particles with the same initial parameters but the azimuth angle may lead to different shower developments and detection at the telescopes' site, changing the acceptance.

Three of these parameters, the optical efficiency, the zenith angle, and the azimuthal angle are discrete variables in the simulations. As of the off-axis angle and the true energy variables, these can be calculated for each simulated event and thus are continuous variables. The obtention of the acceptance for the diffuse emissions as a function of the off-axis angle and the true energy was done as follows.

A circular region with a radius of 2 degrees, corresponding to the off-axis angle, was defined, so that it encompasses the whole camera excluding the edges to avoid badly reconstructed events. This disk was divided into rings of same surface, which represent the off-axis "binning". In this way, each ring is expected to have statistically roughly the same number of generated events, as diffuse emissions are uniformly distributed in the camera. For each ring a spectrum is extracted, using the events N it encloses. This spectrum is then compared to the expected spectrum, which is obtained using the spectral index given in the introduction (4.3.2) for each contribution. N_I represents the number of events initially produced before going through the telescope simulation. The ratio between the integral of the spectrum of the events after going through the telescope and the integral of the computed expected spectrum, N/N_I, is then multiplied by the impact surface S, so as to take into account the impact parameter. Because of the full coverage of the field of view, the result is also multiplied by the solid angle ω, which is given by the angular aperture used in the simulations. The result is the acceptance A given in equation 2.1, per off-axis and energy bin, given in $(\mathrm{m}^2\ \mathrm{TeV}\ \mathrm{sr})^{-1}$. This procedure is applied for each type of particle and for each optical efficiency and zenith and azimuthal angle. The same event selection criteria was applied as for the rest of the analysis.

Concerning point-like gamma, the method is very similar, with the exception being that γ are not expected everywhere in the camera but at a given off-axis angle, fixed by the observation technique. This is why simulations for point-like gamma are also provided per off-axis angle. However, for the acceptance map, the histogram was simply filled with the given off-axis values and then rebinned in order to obtain an histogram with the same format as for the diffuse emissions. Nevertheless, there is no need to multiply by the solid angle when considering a point-like source, so the equation 2.1 is taken with $w = 1$ and the units are $(\mathrm{m}^2\ \mathrm{TeV})^{-1}$. An example of the obtained acceptance plots for point-like gamma is given in figure 2.3. The energy threshold around 100 GeV can be seen along with the mentioned decline of the acceptance with the off-axis angle. In addition, the increase of the acceptance with the energy until a maximum is reached, corresponding to the point in which the shower saturates the camera, can be observed.

$$A(\Delta E_i, \Delta r_i) = \frac{1}{N_I}\int_0^{\eta_{max}} d\Omega \int_{\Delta r_i} dr \int_{\Delta E_i} \frac{dN}{dE} dE = \omega * S * \frac{N}{N_I} \tag{2.1}$$

In this way, a histogram of the acceptance as a function of the off-axis angle and the true energy is computed for each zenith angle, optical efficiency and azimuthal angle for which the simulations exist. To obtain the acceptance for a given event that can come from any zenith and azimuthal angle with a given optical efficiency, interpolations were necessary and performed. Concerning the azimuthal angle, the nearest one, 0 or 180, to the event was chosen. At last, the values of the acceptance obtained for the off-axis angle and energy of an event for all zenith angles and optical efficiencies are used to interpolate its given zenith angle and optical efficiency, using the Delaunay triangles technique.

2.1.5 The Point Spread Function

The Point Spread Function (PSF) represents the response of the instrument to a point-like source and is defined as the probability of reconstructing an event at an angular distance θ from

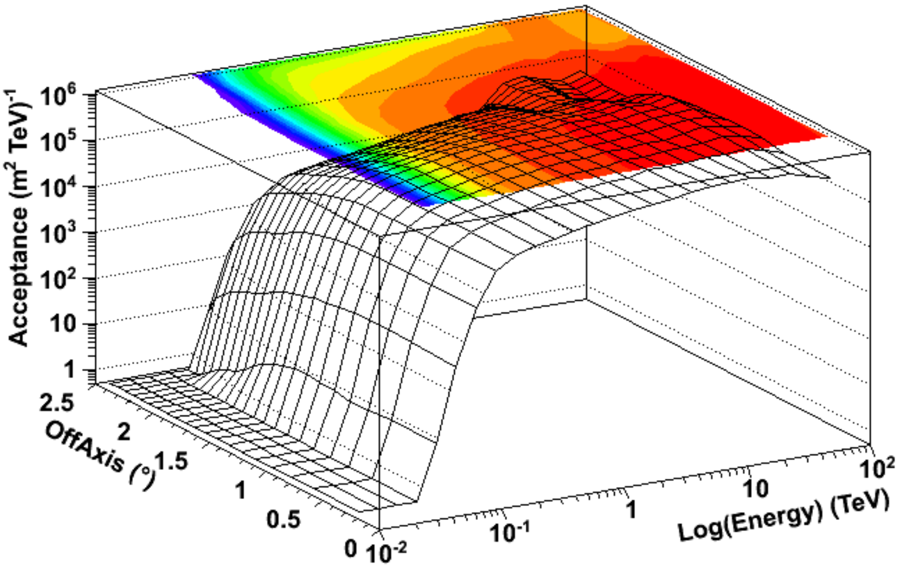

Figure 2.3: Acceptance histogram for point-like gamma as a function of the off-axis angle and the true energy. Several features can be observed. The energy threshold around 100 GeV, the decline of the acceptance when the off-axis angle exceeds 1.5° and its rise with the energy until a maximum is reached, corresponding to the point in which the shower saturates the camera, are clearly visible.

its actual direction. It is normalized to the whole field of view. In practice, it designates a bell-shaped blurred area, which in the case of the H.E.S.S. telescopes is approximately radially symmetric so that it can be considered as a function of $r^2 = x^2 + y^2$ instead of (x,y), defining in this way the angular resolution of the telescopes. The Point Spread Function is directly dependent on the light path, which changes with the type of mirror, so in general it is calculated using the curvature of the dish, its size and its focal length. For IACTs however, the Čerenkov technique makes it a little more complex for the sources are not observed directly but reconstructed from Čherenkov light emitted by secondary charged particle generated in showers from the scattered products of the primary particle's interactions in the atmosphere (see section 1.2). Hence it is first necessary to reconstruct the air-shower to be able to reform the point-like source, and simulations are needed. In fact, the PSF constitutes the biggest difference (~3 orders of magnitude) between IACTs (H.E.S.S.' angular resolution is ~200") and optical telescopes (the Hubble Space Telescope's angular resolution is 0.05").

The important aspects of the PSF of the optics are described next followed by the additional effects on the PSF from the Čerenkov imaging technique. A general overview of the PSF's parameter dependencies is presented then, before explaining in the last section how the PSF is computed.

2.1.5.1 The optical spread

The PSF of the optics, defined as the Point Spread Function of the system in the optical energy range, will influence the image shape and as a consequence the angular resolution of the telescope system. It will depend on the quality of the individual mirror facets, the optical design, the precision of the alignments of the facets and the mechanical stability of the dish and facet supports.

The quality of the individual mirror facets will be characterized by their PSF. In the case of the H.E.S.S. experiment, it was agreed that a mirror facet should concentrate 80% of the reflected light within a circle of 1 mrad diameter around the center of gravity of the image, a specification well below the critical performance as it is well below the pixel size (0.16°). To determine this, it is essential to correctly remove the background and identify the pixels that belong to the light spot. After quality control measurements, it was found that most mirrors passed it by a significant margin, imaging 80% of the light typically within a circle of 0.4 mrad in diameter [18]. The PSF of the telescope is mainly given by the quadratic sum of the these individual PSFs.

In addition, the aberrations resulting from the geometry of the dish influence the PSF of the overall optical system. As seen in section 2.1.1, H.E.S.S.' reflectors follow a Davies-Cotton layout, which limits the off-axis aberrations as compared to parabolic mirror arrangements, while introducing an asynchronism of photon arrivals at the camera. However, this time smearing consitutes a compromise between the performance of the trigger in terms of gamma selection efficiency and background rejection on one side and the image quality on the whole field of view, on the other. For the HESS phase I telescopes, the improvement of the off-axis imaging quality is important given the goal of a uniform response over all of their large FOV of 5°, required for extended sources observations and analysis. For the second phase of construction of the HESS experiment operating a camera of 3.2° FOV and a mirror of about 28 m diameter size, a parabolic dish was preferred, as mentioned in section 2.1.1. For H.E.S.S. I, the choice of $f/d \approx 1.2$ produces optical aberrations at 2° from the center of the camera roughly equal to the pixel size (0.16°), in rms [18]. Concerning the size of the individual facets, although large spherical ones will affect the general optical performance by introducing optical errors, the degradation resulting from the 60 cm H.E.S.S. facets is minimal.

With a total mirror area as large as 108 m^2 for the small telescopes and 614 m^2 for CT5, the shower image has a limited depth of field and the mirrors can be focused either at infinity or at a typical distance S between the air shower and the telescope. Though the former seems a natural choice since it allows the imaging of the photons' direction, which is related to the primary's, the latter provides a more optimal imaging for H.E.S.S, for it reduces the width of the shower image, crucial both for the angular resolution of the instrument and for the gamma/background discrimination (see section 1.1.2). Indeed, the photons from the shower are emitted at a finite distance D from the telescopes, so a mirror focused at infinity will bring additional uncertainties to the reconstruction. For the H.E.S.S. experiment, these uncertainties are of the same order of magnitude as those induced by the shower and camera pixel size and by optical aberrations, which is why an optimal focusing is of importance [19]. To minimize the image's width, the telescopes must be focused at the height of the shower maximum or somewhat higher. This accomplished by placing the camera at a distance $d \approx f/(1-f/S)$ from the mirror, f being the nominal focal length. With a distance S to the shower maximum of around 8 km, this gives $d \approx f + 28$ mm, which is why the entrance of the array of the Winston cones mounts is located about 30 mm behind the camera lid, itself positioned at $d = f = 15$ m. Hence, the 380 mirror facets were aligned so that their individual images of a selected star combined into a single spot on the closed lid of the camera acting as a screen imaged by a CCD camera located in the dish. For more on the alignment of the mirrors, see [20]. Compared to the angular alignment of the mirrors, the influence of their positioning with respect to their nominal location was found to be negligible [18].

Finally, because observations of a source can last over 100 hours, long term stability of the support structure is of importance. Deformations of the dish structure may appear under gravity and wind loads, temperature variations and, concerning the baseframe, by slight unevenness of the azimuthal rail. When moved in elevation, it is expected for a dish of the size of H.E.S.S.' to deform under the influence of gravity, given the weight of its facets. In the design of the H.E.S.S. telescopes, mechanical stiffness and minimal gravity-induced deformations were emphasized while trying to find a compromise between these and the weight and cost of the dish structure. The result is that over the working elevation range (30° to 90°) gravity loads have little impact as compared to the instrinsic PSF of the mirror segments. In turn, the influence of wind loads, temperature and the azimuth angle were found to be uncritical next to the effects of gravity. The dark red color of the mount and dish structure was chosen partly to stabilize the temperature between day and night and avoid deformation of the structure. In addition, the performance, reliability and design of the basic support triangle of the mirror units were tested so that under the load of the mirror and wide ranges of temperature and humidity no significant variations were found on the PSF, which would signal stress on the mirror.

To summarize, the quality of the mirror facets, their layout and precision of alignment as well as the mechanical deformations of the dish and facet supports seem to roughly equally contribute to the optical errors [18, 20]. Nonetheless, as previously mentioned, H.E.S.S.' PSF is well below specifications, even including all stated optical aberrations. Most importantly, its width (defined as the radius in which it concentrates 80% of light) is significantly smaller than the pixel size (0.16°) on the optical axis and comparable to it near the edge of the field of view. This feature is critical to prevent the degradation of the shower images, taking thus full advantage of the camera granularity. Moreover, the angular resolution was found to be stable over all photon arrival directions, an important parameter, as indicated before, for the analysis of extended sources, and particularly for morphological studies.

2.1.5.2 Additional effects due to the Čerenkov imaging

As previously commented, Čerenkov telescopes will have additional angular resolution degradation due to the fact that the sources need to be reconstructed through a series of processes, as opposed to optical telescopes that observe them directly. The shower's development in the atmosphere is subject to various statistical processes. These fluctuations will result in a poorer reconstruction and ultimately limit the achievable angular resolution, even if special emphasis is put on the optimization of the optics of the telescopes, as is the case for the H.E.S.S. experiment (see section 2.1.5.1). Because background rejection depends on particle identification and thus on the shower reconstruction (see section 2.2.3), it will be limited in the same way.

Fluctuations from one shower to another can undermine the angular resolution by not allowing a good reconstruction and particle identification (for background discrimination), which are of prime concern when determining the PSF. For primary gamma-rays with the same energy, the densities of the air showers they produce can vary at observational level, although they should remain approximately constant for a fixed primary energy and zenith angle. These variations have a number of origins, several of which are studied and discussed in [21] and enumerated next:

- the first point of interaction in the atmosphere of the primary particle can vary within a few interaction lengths for hadrons, radiation length for electrons and conversion length for γ creating a randomly distributed height of the shower maximum which in turn changes number of Čerenkov photons at ground level. Fluctuations are greater for hadrons because the interaction length is much larger than the characteristic lengths for the electromagnetic particles.

- fluctuations in the number of Čerenkov photons, attributed to those in the number of electrons and positrons (which come from the production kinematics, see section 1.2) or in their energies during the shower development

- Coulomb scattering of low energy electrons and positrons that could cause a deviation of the emitted Čerenkov photons

- strong correlation between secondary particles in the air-shower, giving rise to non-Poissonian fluctuations

- the Earth magnetic field deflects shower particles depending on their charge, so the shower direction reconstruction can vary according to the way the energy was distributed between electrons and positrons in the first conversion of a gamma-ray

- atmospheric variations can also influence the shower development and absorption of Čerenkov photons which depends on the wave lengths. This creates fluctuations at ground level.

Moreover, detection of all emitted Čerenkov photons is, of course, unrealistic, for the collection area of the instrument is small as compared to the size of the light pool at ground level (known as the effective detection area). The H.E.S.S. system, with about 100 m^2 mirror area per telescope (H.E.S.S. I), an exhibited photon detection efficiency of 10% (in the visible-near ultraviolet) and 120 m spacing between telescopes, detects about 10^{-3} of the Čerenkov photons. Because photon densities in the air shower are already low, for this relative efficiency the poor photon statistics degrade the resolution, which would approach the limiting angular resolution with an efficiency of around 10^{-2}. For the same reason, with a lower optical efficiency and less photons, the reconstruction will be less accurate and the angular resolution will also worsen.

In the case of H.E.S.S., special effort was put into widening as much as possible the field of view (5°) compared to other Čerenkov telescopes, which is usually incompatible with a good angular resolution. This is in part why a Davies-Cotton layout was preferred over a parabolic one.

2.1.5.3 The Point Spread Function parameter dependency

To summarize, the Point Spread Function of the H.E.S.S instrument depends on several parameters, which are listed next. They all amount to the same effect, being the fact that lower intensities in the camera image will lead to a worse reconstruction and hence, angular resolution.

- Detection efficiency: the optical efficiency of the instrument characterizes how well it is able to collect and focus light on the camera pixels. It is to be expected that a worse optical efficiency will lead to a worse reconstruction and larger PSF.

- Energy: At small energies, images will have small sizes, the image orientation will not be well defined so their intersection will be poorly known. Notwithstanding, the number of Čerenkov photons in an air shower is directly proportional to the energy of the primary particle, so at larger energies the image will contain more light, resulting in a better definition. So the reconstruction errors will be smaller for high-energy particles. At the highest energies, however, part of the information is lost because of large images exceeding the size of the camera or their high intensities saturating the electronics. Hence the resolution deteriorates. The PSF simulations are computed for energies integrated following a power-law with a given index, ranging from 2 to 3.2 with 0.2 steps.

- Elevation: Moreover, as seen in the section 2.1.4 about the acceptance, at high zenith angles only very energetic primary particles will produce enough Čerenkov photons to trigger the telescopes after being absorbed and diluted over the increased distance in the atmosphere. Thus, as the zenith angle increases, so does the energy threshold, attaining $\sim$1 TeV for the highest zenith angle. In section 2.1.5.1 it was commented that the gravity-induced deformations of the dish structure, along with small contributions from the facets support units, should lead to a slight broadening of the PSF with elevation. An additional effect comes from the fact that at large zenith angles, the first interaction of the particle with the atmosphere takes place further away from the telescopes, so the shower maximum does the same, because of their correlation. Therefore, images are more compact, with a smaller width and length. Another consequence of this difference in the shower development is that the Čerenkov light pools broadens, so the photon density at ground level decreases. Hence, not only images become smaller, but also dimmer and the error on the image direction and intersection point of their axes become more important. As a consequence, for a fixed energy, the angular resolution will decrease for larger zenith angles. For higher energies however, the shower image start to saturate or exceed the dimensions of the camera, explaining the degradation of the resolution. In addition, showers arriving from the zenith will reach the ground whereas for larger zenith angles they will be entirely contained in the atmosphere and no information will be lost. As a result, for a fixed very high energy value, an improvement of the angular resolution at higher zenith angle is observed.

- Off-axis angle: The PSF's width σ is expected to broaden with increasing distance from the optical axis, for the shower image is no longer contained in the camera. As seen in section 2.1.4, it is for the same reason that the acceptance of the camera decreases towards its edges. This dependence is generally weaker than the zenith-angle one, remaining relatively stable even at large off-axis angles.

- Other dependencies: All other possible effects, like an azimuth or impact-parameter dependence (within 150 m) are found to be negligible. For higher values of the latter, the dependence increases and the energy rises steeply with increasing distance between the shower axis and the telescope, for a fixed image amplitude [22].

In a nutshell, at zenith angles above around 50°, the angular resolution worsens rapidly (PSF becomes wider), while remaining relatively stable below that value. Concerning the energy, for values from around 1 TeV to 15 TeV, the angular resolution is the best, with a small improvement at higher values. However, outside this region it decreases quickly. Moreover, the PSF will broaden for larger off-axis values, specially for high zenith angles and energies. These effects of the dependencies on the energy, off-axis angle (also called offset) and zenith angle can be seen in figure 2.4.

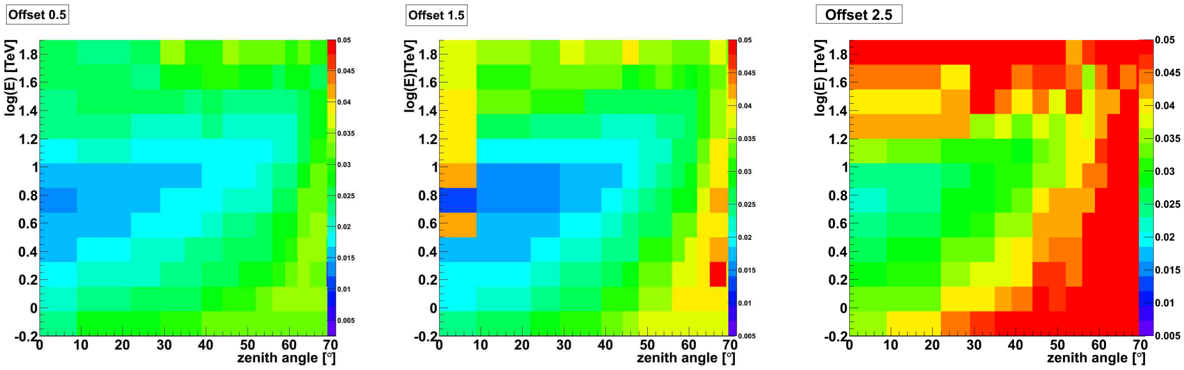

Figure 2.4: Color coded width of the PSF (σ) for all zenith angles and energies, and 3 off-axis angles: 0.5°, 1.5° and 2.5°. It can be seen that at larger off-axis angles, the PSF broadens, only slightly for the first two but significantly for the last one, specially for high zenith angles and energies. At zenith angles above around 50°, the angular resolution worsens rapidly (PSF becomes wider), while remaining relatively stable below that value. Concerning the energy, for values from around 1 TeV to 15 TeV, the angular resolution is the best, with a small improvement around 6 TeV. However, outside this region it decreases quickly. It can be noticed that for showers to be better reconstructed at higher zenith angles, they need higher energies as well, due to the energy threshold. Taken from [23].

2.1.5.4 Obtaining the PSF

To summarize, the final PSF of the instrument has two contributions: the optical system provides a PSF bellow specifications, with a width σ of around 0.01°. However, it is further enlarged by about 0.02° due to the fact that the showers are reconstructed. The final width of the simulated PSF obtained with an average value of each of its parameters is thus of about 0.03°.

The PSF will vary for different observing conditions, such as the zenith and off-axis angles or the optical efficiency (see section 2.1.5.1) and for different parameters involved in the shower reconstruction, like the number of telescopes, the reconstruction algorithm, the gamma-like event selection cuts or the event's energy (see section 2.1.5.2). Besides, some of these parameters are correlated. For example, the observation angle will indirectly influence the energy threshold. Hence, the PSF is usually given for a specific set of runs and cuts, using a particular analysis method. A different PSF could be obtained per bin for each of its parameters. However, for the method developed in this work, because the PSF is convoluted with another function, the general PSF obtained for a source energy spectrum taken as a power-law, was preferred for the implementation. The PSF for the H.E.S.S. data is provided through predefined tables generated by means of a simulation.

For this work, the Model ++ analysis model (2.2.1.2) with standard cuts for the gamma-like event selection were chosen. The zenithal and off-axis angle as well as the optical efficiency are directly taken into account when providing the list of runs (given in section 6.1 for each source) for which the PSF is needed. The source spectrum index must be specified, so the published one for each source was provided (see section 6.1). Because the tables of the chosen analysis method stop at an index of 3.2, for source with a higher index (particularly PKS 2155-304) during the considered period, this limit was taken. As an example, the PSF obtained for PKS 2155-304 during the period known as the "Chandra" flare used in this analysis is shown figure 2.5 from above (left plot) and in 3-D (right plot). Finally, only events reconstructed with at least 2 telescopes were selected.

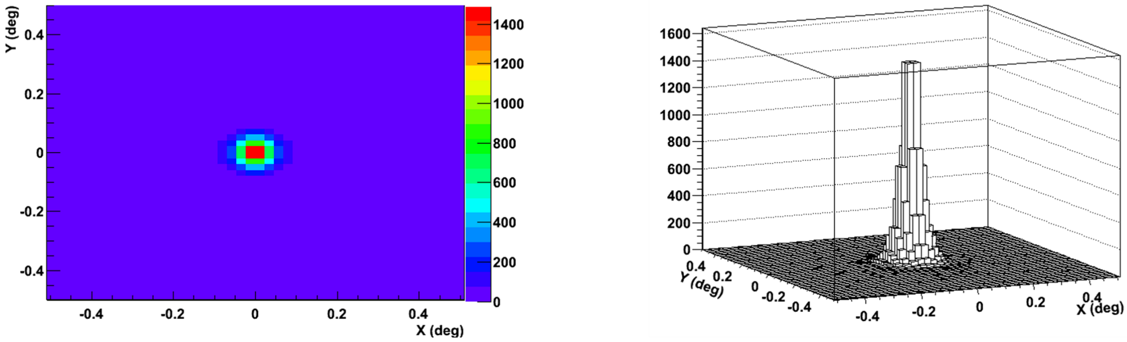

(a) Topview

(b) Sideview

Figure 2.5: The PSF of PKS 2155-304 as seen from above (left plot) and in 3-D (right side).

2.2 Shower reconstruction

Three parameters can be deduced from the air shower reconstruction: the primary particle's direction in space, its type and its energy. Air showers generate elongated images in the cameras, when viewed with a telescope at a distance of around 100 m from the shower axis. The direction of the image will correspond to the orientation of the shower axis, while its intensity will give the energy and the shape of the image will allow to discriminate between gamma-rays and hadronic background showers.

In figure 2.6 are illustrated typical shapes of shower images in the camera. On the left can be seen that of an electromagnetic one (gamma or electron), which is, to a good approximation, elliptical in shape. Muons on the camera leave a characteristic circle or arc of a circle depending on whether it went through the mirror of the telescope or not whereas for hadronic showers the designs are usually more complex, for as mentioned before (section 1.2.1.2), they are composed of many different kind of particles, including muons and secondary hadrons, as well as electromagnetic components. In the represented image of a hadronic shower for instance, a muon crossed the telescope, leaving a distinctive ring superimposed over the rest of the hadronic shower.

Actually, the muon rings are used to verify the calibration of the telescopes. The number of photoelectrons expected for a certain ring radius is computed using a model in which the optical efficiency of the instrument, including the transparency of the atmosphere, the reflectivity of the mirrors, the efficiency of the light guides in the focal plane and the probability of conversion of the Čerenkov photon and of collection of the resulting photoelectron, constitutes a unique fit parameter. This value is then compared to the obtained intensity of the image (ring or arc of circle) which depends, along with its shape, on the impact parameter and inclination of the

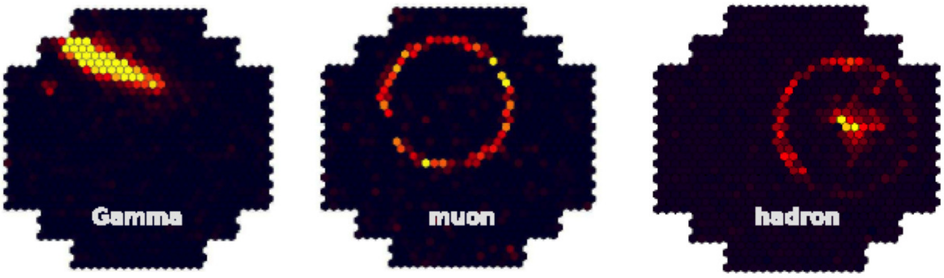

Figure 2.6: Examples of shower images induced by different particles. A primary gamma will generally produce an elliptical shape whereas a hadron's image will more complex, for hadronic showers are usually very irregular. The characteristic ring of a muon going through the camera is also shown.

track in the atmosphere. For single telescopes a large proportion of the triggers are muons, but the requirement of keeping only events triggering at least two telescopes eliminates the majority of them.

In practice, parameterizing the image shapes to sort out the different particles and reconstruct their energy and position is not an easy feat. Several methods have been developed with this aim, some of which are described next. However, characterizing the images is not enough to identify the particles so, the necessity of subtracting the background or excluding the source for standard analyses is explained, followed by a list of the benefits of doing neither like, in the analysis method developed in this work.

2.2.1 Shower reconstruction models

Different methods have been developed to reconstruct the energy and characterize the image of the shower of an incoming particle. The first technique called the "Hillas parametrization" will be presented. Then, a method based on a semi-analytical shower model, which was developed for the CAT experiment[24] but adapted to H.E.S.S. will be described. The combination of these two analysis methods result in the combined analysis, in which new variables can be introduced, as will be seen. Lastly, a third model, based on a 3-D reconstruction of the shower is also briefly introduced.

2.2.1.1 Hillas parameters

From the beginning of ground based gamma-ray astronomy, data analysis techniques have been mostly based on the "Hillas Parametrisation" of the shower images, relying on the fact that the gamma-ray images in the camera focal plane are, to a good approximation, elliptical in shape. The image properties are, in this case, reduced to a few numbers, reflecting the modeling of the image by a two-dimensional ellipse [25]. The most commonly used of these parameters can be seen in figure 2.7.

The angular distance θ between the expected source position and the reconstructed direction of the source is also widely used in standard analysis. The nominal angular distance d between the expected source position and the image's center of gravity as well as the azimuthal angle ϕ of the image main axis and the orientation angle given by the angular distance α between the expected position of the source and the image main axis, characterize the shower's direction and expected source position in the camera. These are needed to obtain the two parameters of the

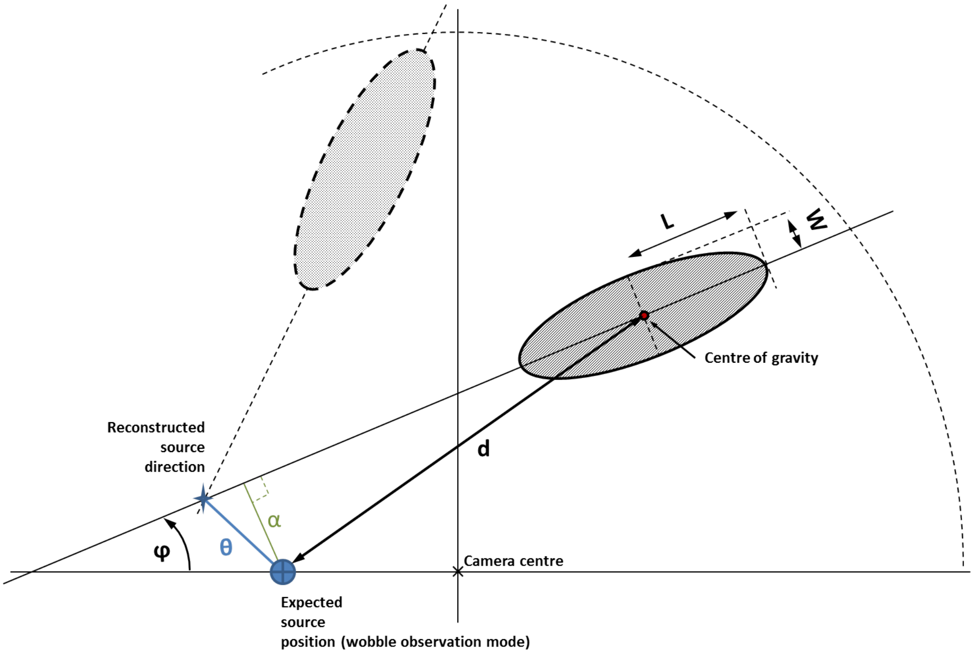

Figure 2.7: Definition of the Hillas parameters on a shower image in the camera. d represents the nominal angular distance between the expected source position and the image's center of gravity, ϕ the azimuthal angle of the image main axis, α the angular distance characterizing the orientation of the shower image and L and w the length and width of the ellipse respectively. θ is the angular distance between the expected source position and the reconstructed one. The filled area shows what is called the "size" of the image.

source position and impact parameter of the shower, known as the core location. Seeing that they are only given by the direction of the elongation of the shower image, to lift the degeneracy several telescopes are needed. This observation of the same shower from different points of view is called stereoscopy and constitutes an essential asset in ground based gamma-ray astronomy.

Actually, the HEGRA collaboration pioneered the reconstructing techniques of the shower geometry that allows to pinpoint the source position and impact parameter of the shower [26]. The source's position is computed as the intersection of the symmetry axis of the images in the cameras when superimposing them, as illustrated in figure 2.8. As for the core location, the same principle is used with the only difference being that it is given by the intersection of the image axes emerging from the telescopes, and not their superposition.

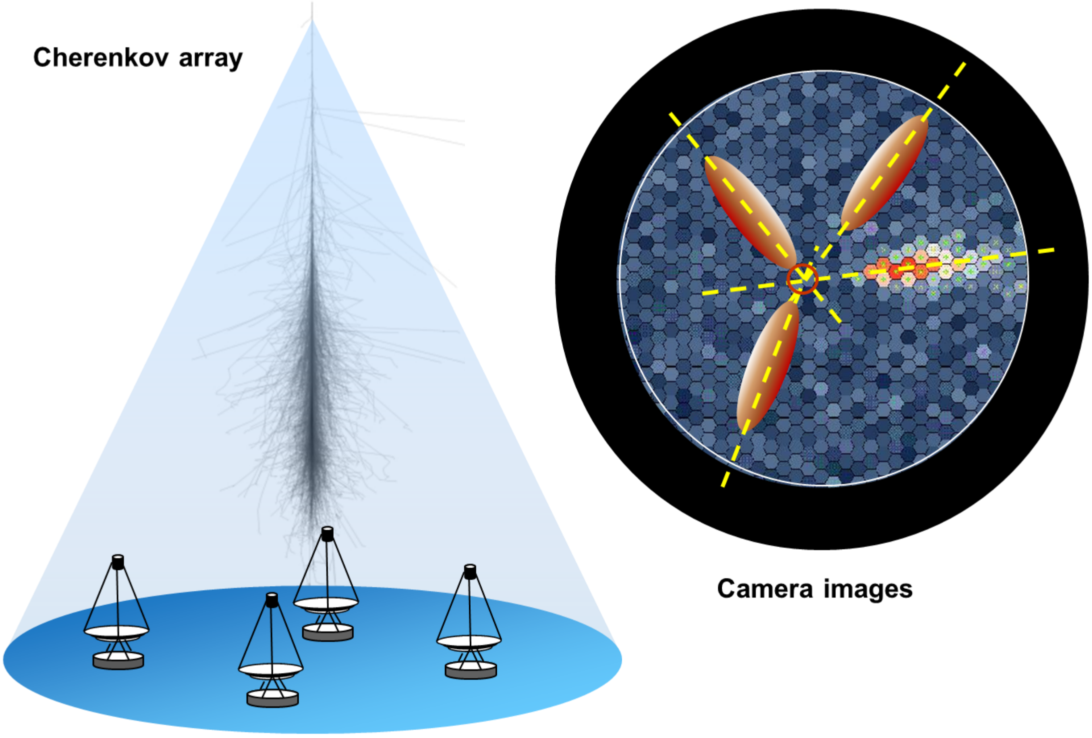

Figure 2.8: Stereoscopic view of an air shower. The position of the source is on the symmetry axis of the image. The multiple view lifts the degeneracy.

On another hand, the total image amplitude or size along with the nominal distance will determine the energy of the primary particle, given by the intensity of the image. The energy and particle type can be determined without the need of stereoscopy, as is done with the model in section 2.2.1.2. Nonetheless, having several telescopes will improve the background rejection, lift the degeneracy in the determination of the energy and yield a better energy resolution. Thus, for each telescope, the event's energy is estimated by comparing it to look up tables. These are constructed with simulations and contain the mean energy of the primary particle in two-dimensional bins of image size and impact parameter. However, the estimation of the energy as a weighted average of each single telescope reconstruction leads to a much better resolution.

In figure 2.7, is also represented the length L and width W of the ellipse obtained for each telescope. To exploit the fact that hadronic showers are on average longer and wider than electromagnetic ones so as to reject them, cuts on combinations of the width and length have long been used. However, a cut on these parameters has a poor acceptance at high energies. Parameters that scale with the energy would be more convenient. Hence, the *Scaled Cuts* technique was developed by the HEGRA collaboration [26], in which the width and length are compared to the expectation value and variance (σ^2) obtained from simulations. These depend on the image total charge q and reconstructed impact distance ρ given by the core location. The *Scaled Width* (SW) and *Scaled Length* (SL) are expressed as follows:

$$SW = \frac{W(q,\rho) - \langle W(q,\rho)\rangle}{\sigma_W(q,\rho)},\ SL = \frac{L(q,\rho) - \langle L(q,\rho)\rangle}{\sigma_L(q,\rho)} \tag{2.2}$$

Furthermore, to take advantage of stereoscopy and account for the multiple telescope images, these parameters are combined in the *Mean Scaled Width* (MSW) and *Mean Scaled Length* (MSL):

$$MSW = \frac{\sum_{tels} SW}{\sqrt{ntels}},\ MSL = \frac{\sum_{tels} SL}{\sqrt{ntels}} \tag{2.3}$$

$ntels$ corresponds to the number of telescopes used in the reconstruction of the event. These two discriminant variables will be extensively used in this work as they are at the base of most of the analysis. From simulations, it was obtained that they are almost uncorrelated for γ, which led to the construction of a variable named Mean Scaled Sum (MSS), used in the Hillas analysis to reject background: $MSS = (MSL + MSW)/\sqrt{2}$.

In addition, in the Hillas model, the height of the maximum of the shower is also reconstructed. Actually, what is directly reconstructed is the height of the center of gravity H of the energy distribution of the shower, in radiation length X_0 units and with respect to the ground. Then, a simple shift relates H to the height of the maximum of the shower in radiation units, t_{max} [27], which takes as reference an arbitrary altitude in the atmosphere. Thus H and t_{max} have the same evolution with the energy and zenith angle. To reconstruct H, the different parameters illustrated in figure 2.9 are needed.

In the presented configuration, telescopes point towards the zenith. θ is the known angle between the shower axis and the vertical line joining the center of gravity to the ground. $\vec{ip}$, the vector between telescope T_1 and the impact location as well as $\vec{h}$, the vector between telescope T_1 and telescope T_2 are known. $\vec{r_1}$ and $\vec{r_2}$ are the vectors from the camera in each telescope to the center of gravity. d_1 and d_2 represent the known angles between the shower axis and $\vec{r_1}$ and $\vec{r_2}$. $\vec{r}$ is the vector between the impact parameter and the center of gravity. The four equations:

$$\begin{cases} \vec{h} = \vec{r_1} - \vec{r_2} \\ \vec{ip} = \vec{r_1} - \vec{r} \end{cases} \tag{2.4}$$

$$\begin{cases} sin(\frac{\pi}{2} - \theta + d_2) = \frac{H}{r_2} \\ sin(\frac{\pi}{2} - \theta + d_1) = \frac{H}{r_1} \end{cases} \tag{2.5}$$

relate the four variables $\vec{r_1}$, $\vec{r_2}$, $\vec{r}$ and H, which can be therefore determined. H could then be used to obtain t_{max}. In practice however, the thus built variable is not precisely t_{max}. Indeed, the

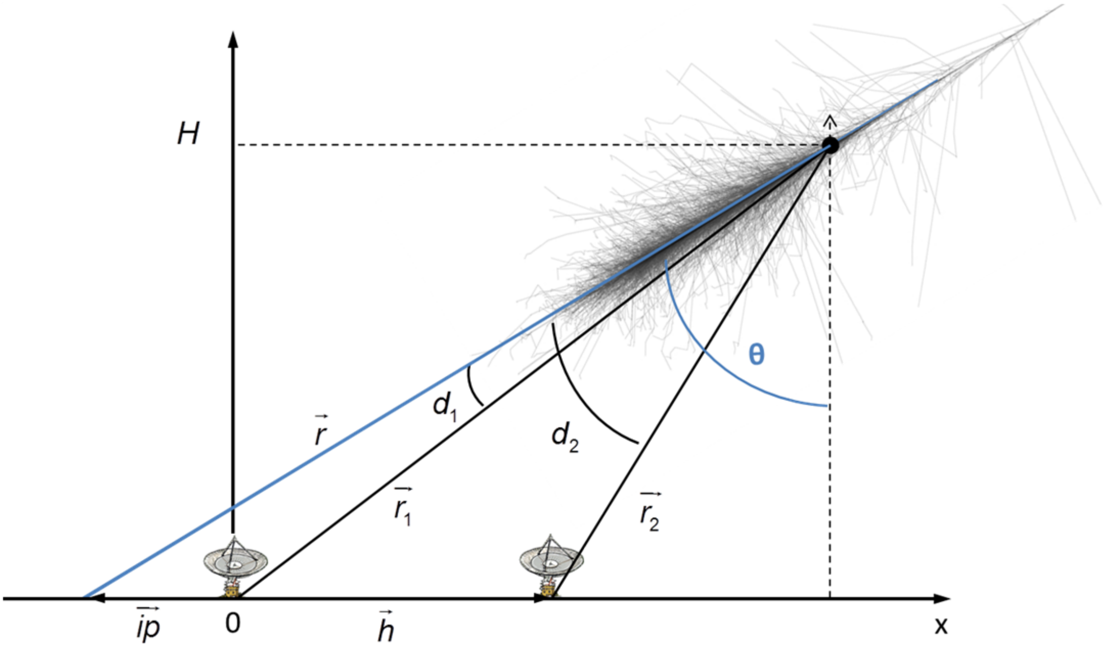

Figure 2.9: Reconstruction of the height H of the center of gravity of the energy distribution of the shower. In this configuration, the telescopes are pointing towards the zenith.

reconstruction is made using the detected Čerenkov emission of the electromagnetic component of the air shower, whereas t_{max} is directly related to the particle multiplicity in the development of the shower. It was noticed that this other variable, called MaxDepth or MDH, also follows the same evolution as t_{max} as a function of energy, but the parameters of the relation might change due to the mentioned difference. MDH, reconstructed with respect to the first point of interaction and expressed in radiation length units, plays a significant role in this work and will be described in section 5.1 and used in the analysis in chapter 5.

2.2.1.2 Analytical model

The Model Analysis developed in the H.E.S.S. collaboration [28] is built on the comparison of the raw (but calibrated) Čerenkov camera pixel images of the shower with a template generated by a semi-analytical shower development model, using a log-likelihood minimization, which is an improvement over the initial method devised by the CAT collaboration [24]. The use of stereoscopy had to be implemented, introducing the first point of interaction in the atmosphere, or primary depth variable (PDH) as a parameter of the model. This variable will be used in this work, as well as another one provided by this analysis method: the *Mean Scaled Goodness* (MSG), constructed next.

The probability density function of observing a signal S in a given pixel, given an expected amplitude μ, a fluctuation of the single photoelectron signal (p.e) $\sigma_s \approx 0.4$ (PMT resolution) is given by [29]:

$$P(S|\mu,\sigma_p,\sigma_s) = \sum_{n=0}^{\inf} \frac{e^{-\mu}\mu^n}{n!\sqrt{2\pi(\sigma_p^2+n\sigma_s^2)}} exp\left(-\frac{(S-n)^2}{2(\sigma_p^2+n\sigma_s^2)}\right) \tag{2.6}$$

By summing over all pixels, the Log likelihood function is defined:

$$lnL = -2 \sum_{pixel} ln[P_i(S_i|\mu, \sigma_p, \sigma_s)] \tag{2.7}$$

The minimization of this function gives the energy, direction and first point of interaction with the atmosphere of the primary particle (impact of the shower). To take into account stereoscopy in the determination of the source position, the *Model Analysis* uses the correlations between the images to find the best fit. Hence, combining the multiple views, not only the shower axis but also the first point of interaction can be unambiguously located in space, provided a good comprehension and precise description of the air shower's evolution.

To separate γ from hadrons, the *goodness-of-fit* variable (G) is introduced by using the average value of the previously mentioned log-likelihood:

$$\langle lnL \rangle = \sum_{pixel} \int_{S_i} P_i(S_i|\mu, \sigma_p, \sigma_s) \cdot lnP_i(S_i|\mu, \sigma_p, \sigma_s) dS_i \tag{2.8}$$

This expectation value can be expressed, to a good approximation, by the analytical formula:

$$\langle lnL \rangle = \sum_{pixel} [1 + ln(2\pi) + ln(\sigma_{p_i}^2 + \mu_i \cdot (1 + \sigma_{s_i}^2))] \tag{2.9}$$

Using the fact that the variance can be similarly expressed and is close to 2, G can be defined as a normal variable, with N_{dof} the number of degrees of freedom:

$$G = \frac{\langle lnL \rangle - lnL}{\sqrt{2 \cdot N_{dof}}} \tag{2.10}$$

By construction, G is centered on 0 and has a width of 1 for gamma rays, whereas it extends to higher values for background events. Using the exact same approach as with the width and length variables of the Hillas parametrization, the G variable is scaled and averaged to give the *Mean Scaled Goodness*.

2.2.1.3 Combined Analysis

The two previous models can be combined to improve background rejection. The *Combined Analysis* uses the MSS variable of the Hillas analysis and MSG of the *Model Analysis*, which comes from a completely different reconstruction technique. These variables are poorly correlated for electromagnetic particles and can be combined into a unique variable: $CombinedCut2 = (MSG + MSS)/\sqrt{2}$, which is also used in this work.

2.2.1.4 3D model

Another existing model for reconstructing showers is the called *3D Model Analysis* [30] and is a kind of 3 dimensional generalization of the Hillas parameters in which the shower is modeled as a 3 dimensional Gaussian presenting a rotational symmetry with respect to its incident direction and emitting an anisotropic light angular distribution. This is then used to predict the collected light in each pixel. A comparison to the actual image allows eight shower parameters to be reconstructed. These permit to select gamma-ray induced showers on the basis of only two criteria with a direct physical meaning: rotational symmetry and small lateral spread. It is the most recent method but has not been further developed for the H.E.S.S. experiment, so it was not used in this work.

2.2.2 Obtaining the true energy from the reconstructed energy

An important aspect for spectra is the control of the bias in energy. Using the simulations, the curves of the reconstructed energy as a function of the true energy were obtained for the four types of particles. As an example, the plot for point-like gamma is shown in figure 2.10. The plots for electrons, protons and diffuse gamma are found in appendix A. These are represented over the whole energy interval for which simulations are available (0.05 - 100 TeV), although the analysis only uses the interval 0.2 - 10 TeV. Energy biases are expected at low and high reconstructed energies. At low energies, near the threshold, the bias is positive, due to the fact that most showers have an energy too small that don't trigger either because the charge per pixel is not sufficient or because there are not enough activated pixels. Only the ones with upper energy fluctuations are kept. At high energies, saturation creates an opposite effect, with a negative bias. The plots obtained for electromagnetic particles have roughly the same shape, with only very slight biases observed. The central part only displays a minimal deviation from linearity at the extremities. Overall, the energy seems to be well reconstructed. Concerning protons, it is difficult to conclude due to the low statistics in the simulations.

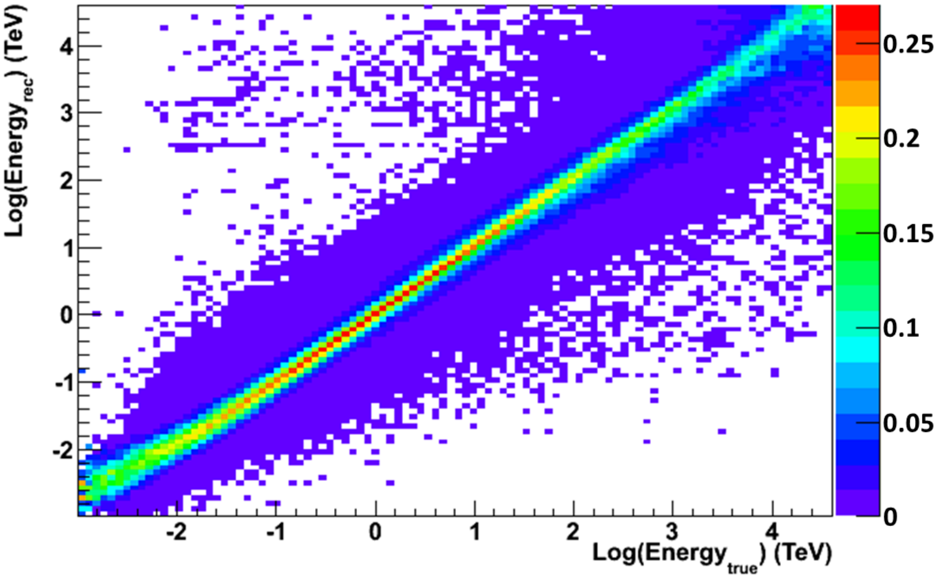

Figure 2.10: Reconstructed energy as a function of the true energy for point-like gamma. Slices in reconstructed energy bins are normalized.

To enter an event in the spectrum, its true energy needs to be estimated. For a given reconstructed energy, the corresponding bin slice is normalized, so that the corresponding true energy distribution can be used as a PDF. Next, a value for the true energy is randomly selected following the PDF distribution, of which three examples at different energies can be seen in figure 2.11, low energy in the left plot, high energy in the right plot and a slice in the linear segment of the graph in the middle plot. This will be the chosen energy for the spectrum reconstruction. Hence, each event provides four different true energy values, one for each type of particle, that will be included in the four spectra. It can be noted that, so as not to be bothered by low statistics (which are already limited for protons), all zenith angles were merged. If this had not been the case, an evolution of the biases as a function of the zenith angle was expected.

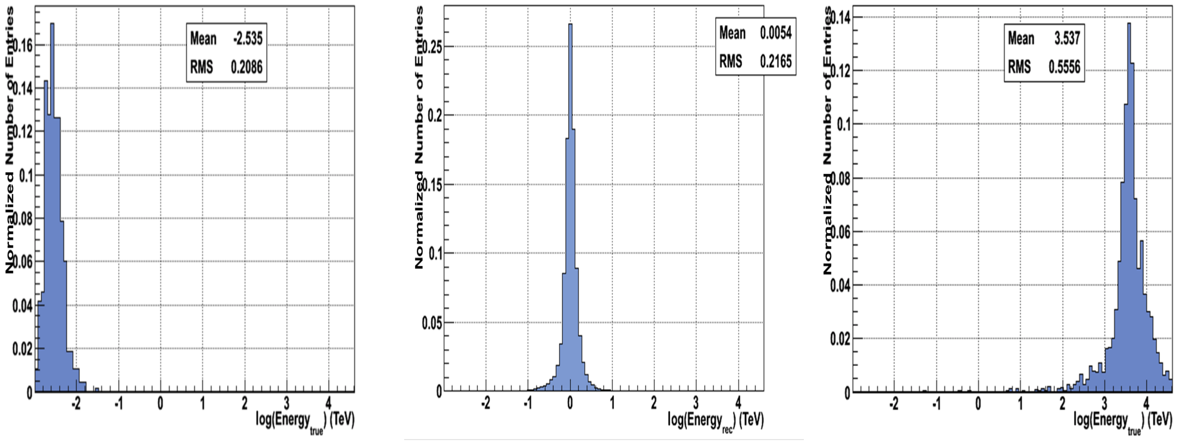

(a) 0.07 TeV

(b) 1 TeV

(c) 38.9 TeV

Figure 2.11: True energy probability density functions for a given reconstructed energy, at 0.07 TeV (left plot), 1 TeV (middle plot) corresponding to the linear section and 38.9 TeV (right plot). The X-axis represents the logarithm of the true energy.

2.2.3 Standard methods for gamma selection

Although it can be reduced by a factor of ~100, not all the background of non gamma-ray induced air-showers can be properly removed using the shape selection criteria. First, primary electrons produce showers very similar to the gamma-ray's. Although the height of the shower maximum differs by about one radiation length as seen in the last chapter, it can also fluctuate by the same value, rendering a rejection using solely this variable completely inefficient. Detecting the Čerenkov radiation of the primary electron is a technique which might become possible with future arrays. In addition, even hadronic showers generate an irreducible background, due to their electromagnetic components (spaliation of hadrons producing π^0 which in turn give $\pi^0 \rightarrow \gamma\gamma$, as seen in section 1.2). Hadrons are the dominant background in the whole energy range, even if the contribution from electrons becomes more important at low energies (<100 GeV). As a consequence, the standard analyses in the H.E.S.S. collaboration use different methods to further purify the gamma.

Besides the cuts applied on the discriminant variables, depending on what is being studied, either the gamma coming from the source or, on the contrary, only the diffuse gamma present in all the field of view, the treatment of the sky map will differ. In the case of diffuse emissions study, as electrons and gamma cannot be identified using the standard methods, the usual approach is first to exclude the source region. Then, if outside the galactic plane, it can be supposed that electrons are predominant and base the study on this emission, as will be seen in chapter 4. In the galactic plane however, the diffuse galactic gamma emission is significant and has a complex morphology. It is superimposed over the uniformly distributed diffuse electrons. These features are exploited for the diffuse gamma study, but with an important drawback being that all active gamma-ray sources must be excluded and the galactic center region is extremely populated, leaving not much room for diffuse emissions studies.

Concerning the active sources analyses, the standard technique is to somehow subtract its background. The classical method of single-telescope instruments was the "*on/off*" observing mode, in which observations of the target source and of an empty field at the same zenith angle would alternate. Since the background should be the same in the two fields of view at equal zenith angle, their subtraction would leave only the γ events. Nonetheless, a major disadvantage of this method was that half of the time was spent off source, decreasing statistics for analyses. There are other models to evaluate the background that can be applied by H.E.S.S. because of its large field of view (5°), of which some are described next. They are all applied with wobble observations mode, which is now the main one for H.E.S.S. and consists on observing the source at different positions in the camera at a certain distance from its center, typically 0.5°. This is particularly useful for background subtraction as will be explained next.

- In the *Ring*-background model [31], a ring around the center of the camera, at the same distance from is as the source is used to estimate the background. In figure 2.12a, the source's or target position is shown in dark blue while the ring in light blue is the one used for background estimation. Because the ring is at the same distance from the center of the camera and the acceptance of the latter is roughly radial, it should be on average constant on the whole area of the ring. The mean background level in the ring is computed and then normalized to that of the defined source region.

- A very similar approach is the one used in the *Multiple-Off* method, for which instead of a ring several regions equal to the source's are selected inside the ring. Both methods yield very similar results, though the advantage of the *Multiple-Off* technique is that it is easier to normalize, with a round number of times de source's area used for the background. This second method is illustrated in figure 2.12c.

The θ^2 distribution obtained on the Crab nebula, corresponding merely to the number of events found in a ring at a distance of θ (degrees) around the position of the source, is also shown in figure 2.12c. The θ^2 variable is built so that the rings' area is constant. The source can be clearly seen at the center, with a decreasing intensity at increasing distance from it, ending in a constant background level over the whole area outside the source's region. For comparison, the crosses indicate the background level obtained with the *Multiple-Off* method which seems to estimate the background fairly well.

- Another type of subtraction method represented in figure 2.12b, is the *Template*-background model, in which the source area is used for background evaluation by simply taking a subset of events that failed to pass the selection criteria for γ. These are considered as indicative of the local background level. However, because the acceptance of the camera for background and gamma-ray events is not the same, their ratio must be determined and is required for the background computation. Although this method has the advantage of determining the background in the same region as the signal, it yields slightly worse results than the other two that were described, due to the fact that even if events pass the gamma-ray selection criteria, as mentioned before, an irreducible background persists and its estimation from that of the rejected background is not straightforward.

In the method developed in this work, particle discrimination is not based on cuts. Hence, not only electrons and gamma can be identified, but no gamma are lost in the selection or subtraction process. These specificities of the method are very important particularly for diffuse emissions studies.

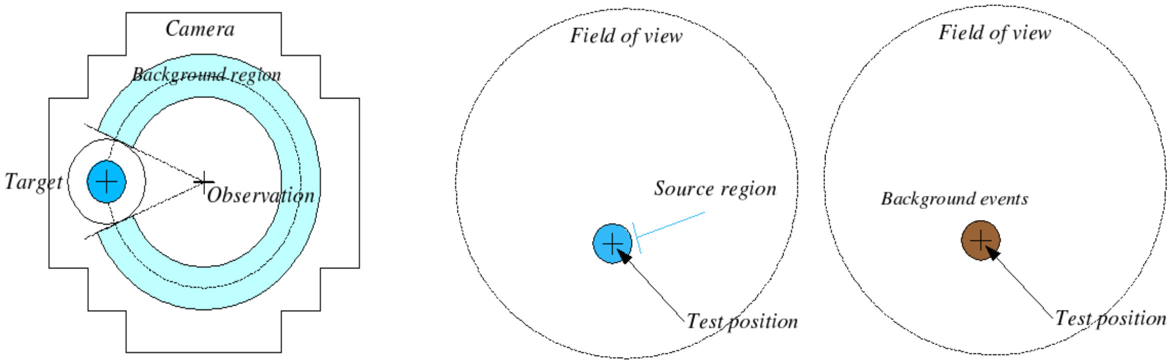

(a) *Ring*-background (b) *Template*

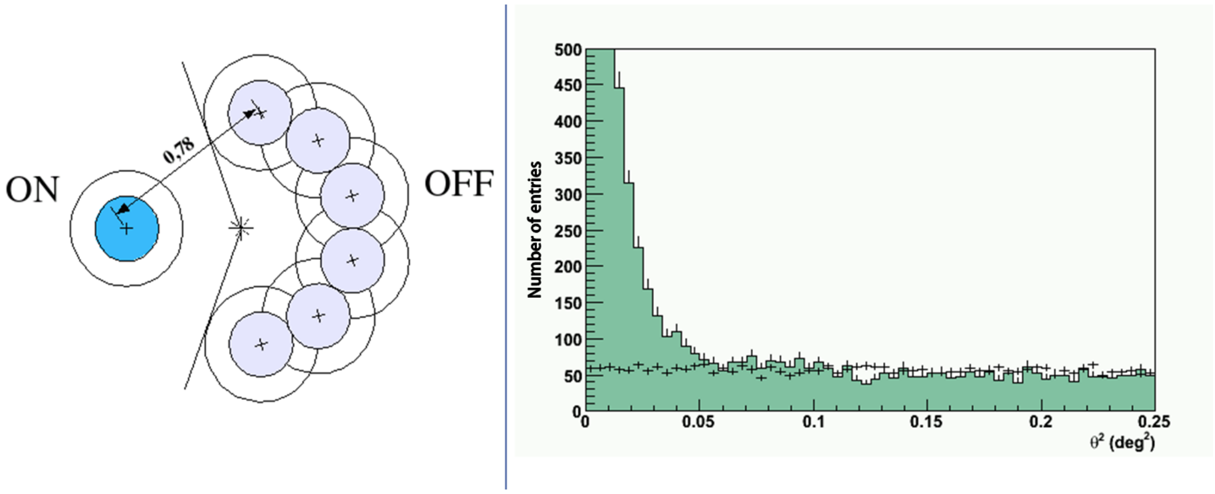

(c) *Multiple-Off*

Figure 2.12: Examples of background subtraction techniques. Top: sky maps illustrating the *Ring*-background (left) and *Template* model (right) subtraction methods. Bottom: the *Multiple-Off* regions subtraction method shown on a sky map (left) along with the corresponding calculated θ^2 for the Crab Nebulae where the estimated background can be seen.

Part II

The gamma-ray emissions

Since the physicist Victor Hess confirmed the existence of cosmic rays in 1912 [32], they have played an important role in particle physics, leading to the discovery of new particles like positrons, pions or kaons. The arrival in 1950 of the first particle accelerators on Earth shifted the main attention of particle physicists from cosmic rays to accelerator physics. Astrophysicists however remained interested in the elucidation of their origin and understanding of their acceleration mechanisms.

From Earth's vicinity, there are two ways of attempting to gain access to this knowledge. On the one hand, the cosmic rays arriving on Earth in the form of diffuse emissions after their propagation in space and countless deviations, can be detected, analyzed and characterized, as described in chapter 4. On the other, the acceleration processes and the astrophysical sources in which they take place can be indirectly investigated. Indeed, the accelerated cosmic rays can interact with the source's environment and produce secondary particles, which are detected on Earth. Of these, gamma-rays are one of the most studied, for they are not deviated by magnetic fields during their propagation, as are the charged particles, and are of interest in a wide variety of subjects. For instance, in some exotic physics models, dark matter candidates could be a source of gamma-rays. This possibility is explored in chapter 4. The diffuse gamma-ray emissions are also presented in this chapter, because that is where dark matter is being looked for, as it is not a confined source in space.

In the next chapter, an overview of the known gamma-ray (and therefore cosmic ray) sources is given, as well as the description of how cosmic rays are accelerated and generate the high energetic photons in these active sources.

Chapter 3

The active gamma-ray sources

Sommaire

More than a 100 years after the discovery of cosmic rays as radiation coming from outside the solar system with very high energies ($> 10^6$eV), their origin and acceleration mechanisms are still under dispute. In this chapter will first be introduced the different acceleration processes believed to be involved in the production of cosmic rays. Then, the emission of gamma-rays of these very energetic charged particles will be described. Finally, an overview is given of the different astrophysical sites, called active gamma-ray sources, that could lead to such scenarios.

3.1 The acceleration of charged cosmic rays

As will be seen in section 4.3.1.1, the flux of hadronic cosmic-rays decreases with the energy, globally following a power-law function. This kind of energy dependence is indicative of non-thermal processes at the acceleration site. This lead Fermi to devise a process that could explain this kind of acceleration [33], called the "2nd order Fermi process". He later suggested a second one, the "1st order Fermi process" which is now commonly referred to as "Fermi acceleration" [34]. These two mechanisms are explained next. Nonetheless, although they can describe well the acceleration of particles, these models are too simplified and do not consider important physical aspects present in astrophysical sources. Hence in a last section, extensions that have been made to these models are briefly mentioned.

3.1.1 2nd order Fermi process

The 2nd order Fermi acceleration is based on the concept that a charged particle will gain energy by moving in the presence of randomly traveling "magnetic mirrors". When the particle hits a "mirror", if the latter was moving towards the particle, it will increase its energy. The opposite holds true: if the mirror is receding, then the particle's energy decreases. In the process suggested by Fermi in 1949, the "magnetic mirrors" are interstellar magnetized clouds, with magnetic inhomogeneities within. The probability for a collision is proportional to $v - V cos\theta$, with v and V the velocities of the particle and the cloud, respectively, and θ the angle between the two. Hence, head-on collisions happen more often in average than head-tail ones. So, after a certain number of collisions, the particles should be globally accelerated. The resulting gain in energy ΔE is found to be proportional to β^2, with $\beta = V/c$. The process is called "2nd order" because of this second order dependence. The process is illustrated in figure 3.1.

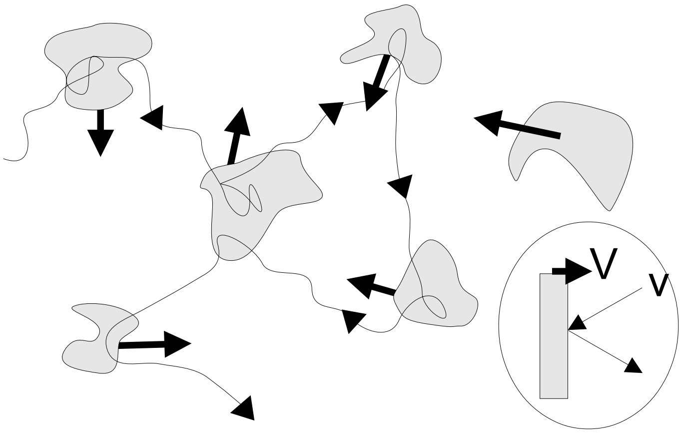

Figure 3.1: The 2nd order Fermi acceleration process: a particle of velocity v collides with a magnetic inhomogeneity that is moving at speed V. The particle gains energy and is diffused to another inhomogeneity. After enough collisions, the particle will be accelerated. Taken from [35]

This mechanism however is not very efficient due to the slow and random motion of the clouds, giving a non-negligible head-tail collision probability which decelerates particles. What is more, this induces β«1, thus the energy gain, proportional to β^2, is also very small giving acceleration times of around 10^8 years typically. However, the average time a particle spends in the galaxy is 10^7 years, which is not enough to explain the fluxes measured on Earth.

3.1.2 1st order Fermi process

The 1st order Fermi process requires the existence of a shock wave in the environment of the charged particle, considering a special geometry in which only frontal collisions can take place. Figure 3.2 illustrates the principle. By traveling back and forth between the upstream and the downstream region of a shock wave, reflected every time by magnetic inhomogeneities as those described for the 2nd order process, the particle gains energy at each passage. These multiple reflections greatly increase the energy and the resulting gain is proportional to β, being thus much more efficient than the 2nd order process.

A major difficulty in this process is that to enter the shock and start accelerating in the first place, a particle needs to have an energy v»V_{shock}, which exceeds the thermal energy by far.

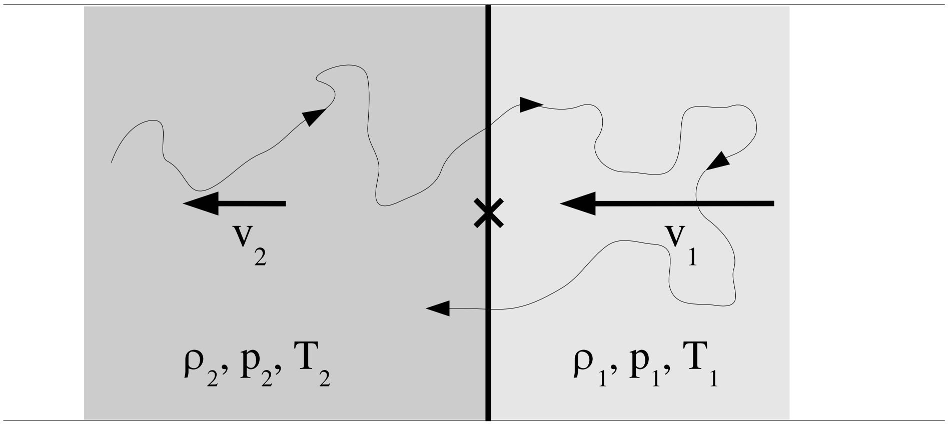

Figure 3.2: A shock wave traveling in a medium will define a sharp change of pressure, delimiting hence two regions with different densities ρ, pressures p and temperatures T and thus create magnetic inhomogeneities. The particle will pass from one side to the other, then be diffused, change direction and pass again through the shock wave, each time gaining energy. Taken from [35]

As a consequence, a previous mechanism of particle acceleration needs to take place and the acceleration occurs in various steps. Several processes have been proposed to explain this first phase of acceleration but, as for the second one, it is far from being well understood.

3.1.3 Diffuse shock acceleration

The success of these two particle acceleration processes devised by Fermi is largely due to the fact that they naturally yield an energy spectrum that, when taking into account propagation effects like the energy-dependent diffusion out of the Galaxy, can be well represented by a power-law function with a spectral index Γ similar to the one observed ($\Gamma \gtrsim 2$). This comes from the fact that at each iteration, the particle has a certain chance of diffusing out of the region in which the acceleration is occurring.

Important limiting factors to these models are the magnetic field and dimension of the astrophysical object in which the acceleration is taking place. Indeed, for a particle to reach such high energies as the ones observed, they need to stay long enough in the acceleration region. The Larmor radius for a relativistic particle with charge Ze in a magnetic field with B its component normal to the particle's velocity is:

$$r_L = \frac{1.08}{Z}\left(\frac{E}{10^{15}\ \mathrm{eV}}\right)\left(\frac{B}{1\ \mu\mathrm{G}}\right)^{-1} \tag{3.1}$$

Because the acceleration is gradual and with many irregular loops, for the particle to stay confined, the accleration region's size L (expressed in pc[1]) should be much greater than $2r_L$. Actually, the characteristic velocity βc of the diffusion centers must also be introduced [36] and this gives the relation:

$$\left(\frac{B}{1\ \mu\mathrm{G}}\right)\left(\frac{L}{1\ \mathrm{pc}}\right) > 2\frac{1}{Z\beta}\left(\frac{E}{10^{15}\ \mathrm{eV}}\right) \tag{3.2}$$

---

[1] A parsec, noted pc, is the distance at which one astronomical unit subtends an angle of one arcsecond. 1 pc $\approx$ 3.26 light years.

yielding a maximum value for the energy:

$$\left(\frac{E}{10^{15}\ \mathrm{eV}}\right) < \frac{Z\beta}{2}\left(\frac{B}{1\ \mu\mathrm{G}}\right)\left(\frac{L}{1\ \mathrm{pc}}\right) \tag{3.3}$$

Other effects can limit the value of the maximum energy to which the particles can be accelerated, like the age of the system or the characteristic times of energy losses induced by radiative processes that the particles will experience (see next section).

The previously mentioned acceleration models however are not complete, for there are several aspects unaccounted for. The diffusive shock acceleration model is based on a 1st order Fermi process, to which is added the presence of magnetic field waves like Alfvén's. This allows a coupling between the particles and the macroscopical phenomenon of the shock wave. However, even this improved Fermi process, along with both of the originals, were introduced with the approximation of the "test particle", meaning that the particles' movement and acceleration don't affect the shock dynamics, which is not the case. In fact, the particles will have a retroactive effect on the shock, creating magnetic instabilities when they are diffused. The structure of the shock wave for instance, can be modified, with the accelerated particles exciting the waves that in turn confine them even more. Also, the magnetic field can be amplified by big amplitude Alfvén waves generated when the charged particles are efficiently accelerated at the shock region [37, 38]. The result will be to lower the diffusion coefficients, allowing the particles to pass through the shock wave more often, rendering a more efficient acceleration. When these non-linear effects are taken into account, the maximum energy achievable can be enhanced.

As a consequence, only certain astrophysical sources can accelerate cosmic rays to the observed energies. These are summarized in figure 3.3 and will be described in section 3.3. It can be noted that to reach proton acceleration above 10^{20}eV, the only remaining site candidates are Active Galactic Nuclei (AGNs) and FRII galaxies, Gamma-Ray Bursts (GRBs), which don't appear in figure 3.3, and neutron stars.

3.2 Charged particles producing gamma-rays

Because charged particles will be deviated during their propagation in the interstellar medium, which is full of magnetic fields, the information on their origin is generally lost. At very high energies cosmic rays are expected to follow almost a straight line. However, experiments that detect these cosmic rays such as the Auger observatory or the Telescope Array (TA) observatory have not been able to determine any anisotropy, due to their very low flux, although recently the Telescope Array claimed to have an indication of it (called a "hotspot") in the Northern Hemisphere [40]. The study of high energy gamma-rays has emerged as a possible way of learning about cosmic ray acceleration sites as they are believed to originate from them and they travel in a straight line from the source because of their neutrality. The processes that allow accelerated charged particles to produce gamma-rays can be divided into two groups: the leptonic and the hadronic, which are explained next and shown in figure 3.4. It is noted that a second messenger exists that can give information on cosmic ray sources: the neutrino. However, they interact very little with matter and are hence hard to detect. Experiments such as IceCube in the South Pole ice and ANTARES (Astronomy with a Neutrino Telescope and Abyss environmental RESearch) and NESTOR (Neutrino Extended Submarine Telescope with Oceanographic Research) in the Mediterranean Sea, explore this field. In the future, the international project KM3NeT (Cubic Kilometre Neutrino Telescope), which includes experiments like ORCA (Oscillation Research with Cosmics in the Abyss) and ARCA (Astrophysics Research with Cosmics in the Abyss) targeting particular energy domains, will complete the list.

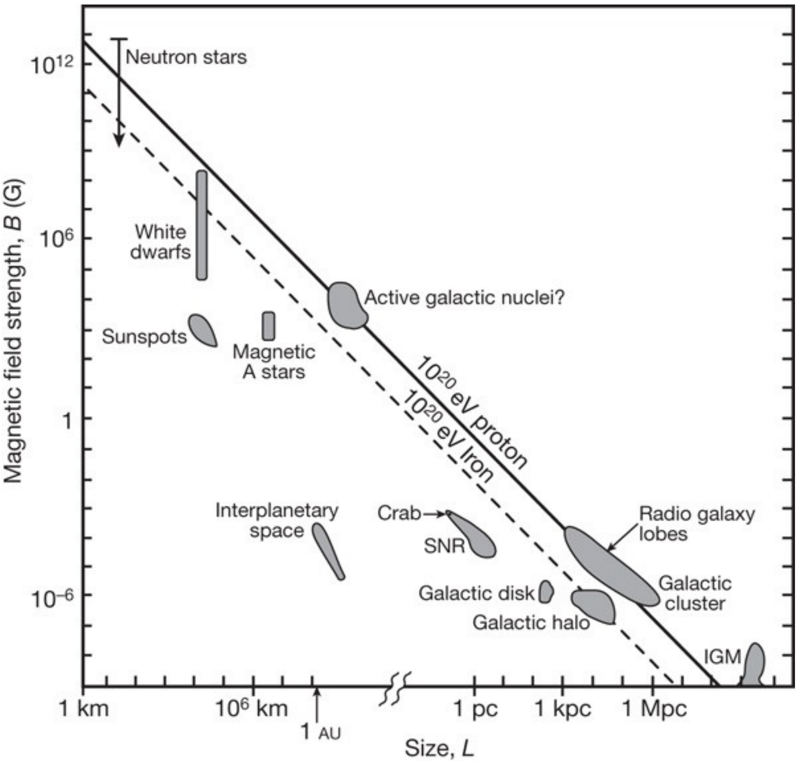

Figure 3.3: Astrophysical source candidates for charged cosmic ray acceleration, as a function of their magnetic field and size. Objects below the diagonal line cannot accelerate protons to 10^{20}eV. IGM stands for InterGalactic Medium. Taken from [39]

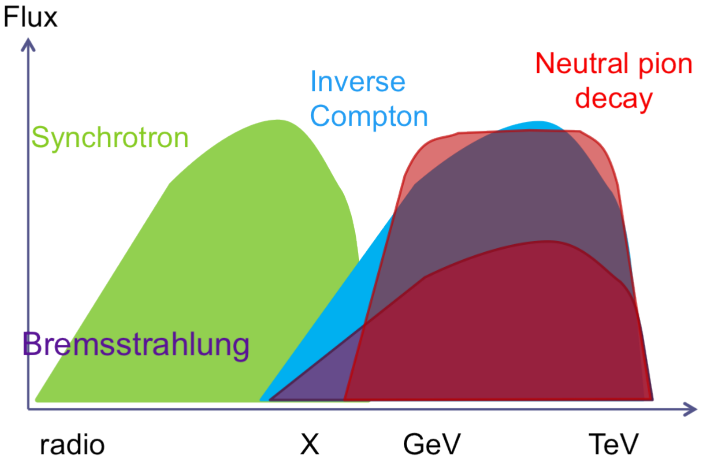

Figure 3.4: The photon production processes in active sources. The leptonic radiative processes include the inverse-Compton emission and the "bremsstrahlung" radiation, both of which produce gamma-rays, and the synchrotron radiation, which is typically in the radio to X-ray domain. The main hadronic scenario for gamma-ray production is through the decay of neutral mesons, predominantly neutral pions.

3.2.1 Leptonic radiative processes

Concerning electrons and positrons, three radiative processes are involved: the inverse-Compton emission, the "bremsstrahlung" radiation and the synchrotron radiation.

Inverse-Compton

In the inverse-Compton scattering, an electron of very high energy transfers part of it to an ambient photon (from the radio, infrared or optical domains). Depending on the kinematic regime, a different portion of the energy is transfered. Two of them can be distinguished. In the Thomson regime, the energy of the photon in the center-of-mass frame is very small with respect to the energy mass of the electron. In this case, the energy of the diffused photon ϵ_f is around $\epsilon_f \sim \gamma^2 \epsilon_i$, ϵ_i being the initial energy of the photon. The efficiency for the transfer depends on the initial directions of the electrons and the photons. What is more, in this regime, if the electrons possesses a spectrum which can be represented by a power-law with spectral index p, it will also be the case for the spectrum of the produced photon and the index will be $\frac{p+1}{2}$. In the relativistic or Klein-Nishina regime, the emitted photons will in majority have an energy $\epsilon_f \sim 4\gamma\epsilon_i$. They will also evolve as a power-law if it is the case of the electrons emitting them, with a spectral index $p+1$. Moreover, the rate of energy losses of the electrons will be governed by the energy density of the target photon fields.

Bremsstrahlung

The "bremsstrahlung" radiation is produced by the deceleration of a charged particle that is deflected by another charged particle, typically an electron by an atomic nucleus. The energy loss will then be proportional to the energy of the incoming particle. This gamma-ray production process will be dominant for electrons under 10 GeV. As seen in section 1.2, it also plays an important role in the development of air showers.

Synchrotron

Finally, the synchrotron emission is generated by the acceleration of relativistic charged particles through magnetic fields. Because of the ever-present magnetic fields of the interstellar medium, electrons generally produce this radiation, which is usually seen from radio to X-ray energies. If the primary electrons follow a power-law of spectral index p, the photons' spectrum will also be represented by a power-law, of index $\frac{p+1}{2}$. This process will be dominant, along with Inverse-Compton scattering, for electrons with energies above 10 GeV.

3.2.2 Hadronic processes for gamma-ray emissions

Cosmic ray protons or heavier nucleons can also participate in these mechanisms but not significantly. They will mainly contribute via the decay of neutral mesons (π^0,K^0,..), the predominant one being $\pi^0 \rightarrow \gamma\gamma$. Indeed, in hadronic processes, an accelerated proton or nuclei will collide with an atom of the interstellar medium, thus generating instable particles as π^0. As a consequence, a local matter density, giving more proton targets, will favor this type of process, which is one of the few giving information about the hadronic component of cosmic rays. Another kind of messenger is the neutrino resulting from the decay of charged mesons ($\pi^\pm$,$K^\pm$,..) also produced during the propagation of accelerated hadrons.

3.3 Gamma-ray sources

As seen, charged particle acceleration sites can produce γ and hence the study of gamma-ray sources will yield important information on cosmic rays. These sources are called "active", as opposed to the passive ones which are not associated with cosmic ray acceleration sites but rather provide material with which cosmic rays traveling in the medium can interact, generating gamma-rays. These "passive" source create diffuse emissions, as will be seen in chapter 4.

The difficulty is being able to identify which gamma emitting process is at work to know which was the primary accelerated charged particle: an electron or a protons. If the physics of basic radiation models are well constrained, the properties of the whole particle distribution can be characterized from its emission at very high energies. This would be crucial for recognizing the acceleration mechanisms at work. Hence a good understanding of the source as a whole, with all the astrophysical processes involved in its emission is of great importance.

Next are presented the most studied different types of gamma-ray sources. However, to analyze the active gamma sources, one needs to take into account the propagation of the gamma-rays all the way to Earth, which is briefly treated in the last section.

3.3.1 Charged particle accelerators

Gamma-ray sources are generally divided into two families: the galactic and the extragalactic ones. The focus is mainly on the extragalactic sources called AGNs, for these will be studied in the subsequent work.

3.3.1.1 The extragalactic sources

Two types of extragalactic sources are presented next: the mentioned AGNs and GRBs. Both are among the remaining candidates for accelerating charged cosmic rays, particularly protons, up to 10^{20} eV.

The active Galactic Nuclei

The observation in the 90's of AGNs at the high-energy end of the spectrum was an important discovery achieved by Imaging Atmospheric Cherenkov Telescopes. AGNs are extragalactic sources currently believed to host a supermassive central black hole (SMBH) surrounded by a rotating accretion disk. In about 10% of the cases, the release of gravitational energy powers the formation of prominent jets along the rotation axis of the black hole. If these energetic particle beams are aligned to within a few degrees with the line of sight to the Earth, the AGN is called a "Blazar", and a relativistic boosting effect is observe, which leads to its TeV emission. Another type of AGN producing TeV radiation have been recently detected: the radio galaxies M 87 and Cen A. Blazars are characterized by a high flux variability, most noticeable during flares, on time scales from years down to minutes and appear at all wavelengths. However, the blazars' minute time scale variability at TeV energies has never been so well resolved before in any AGN at longer wavelengths.

Concerning AGN physics, there is a missing link between accretion physics, supermassive black hole magnetospheres and jet formation, three areas that must somehow be associated by revisiting the central engines and the accompanying relativistic jets. In order to explain how particles can be accelerated to very high energies so quickly, in the relatively small region in which such a process can occur, most current theories of particle acceleration have been challenged. Plasma physics are believed to play an important role in the acceleration of particles to relativistic speeds. This can be achieved through many processes taking place in collisionless plasmas with non uniform velocity fields, where the high energy particles density might increase until it affects the flow itself and the acceleration mechanism. First and second order Fermi acceleration processes (shocks and turbulence) are expected in AGNs. Magnetic reconnection and direct electric fields could possibly also be found in the rotating SMBH vicinity and contribute to the acceleration processes. Different acceleration scenarii and magnetic field topologies will predict particular spectral indices for the accelerated particles. Special interest has been shown on relativistic reconnection, since events in the jets or SMBH environment might provide a good match to the AGNs non-thermal emission properties, like fast very high energy variability. Also, they are thought to be efficient particle accelerators.

The spectral energy distribution of TeV AGNs is double peaked. It presents a first bump in X-rays and a second one in gamma-rays. The low energy emission in AGNs is believed to be dominated by the synchrotron radiation from a relativistic electron population. The second peak however can be attributed to several processes, which can be of leptonic or hadronic origin. The leptonic mechanisms include the Synchrotron Self-Compton (SSC), in which the electrons interact by the Inverse Compton (IC) process with the synchrotron photons they produced at lower energies, scattering them at higher energies, and the External Compton (EC), in which the seed soft photon field for IC is provided by radiation emitted elsewhere. The former is associated to most AGN types while the latter seems to better match data from a particular kind of AGNs known as Flat-Spectrum Radio Quasars (FSRQ). Concerning the hadronic component, the predominant process is the π^0 decay into $\gamma\gamma$.

More thorough studies of the spectral shape and variability of these particle populations will help to make progress in the understanding of the jet formation and composition, the processes behind the accelerated particles, and the microphysics of the radiation mechanisms. Likewise, light might be shed on other fundamental issues such as the cosmological galaxy evolution and structure formation through a better Extragalactic Background Light (EBL) determination, the microstructure of space-time at the smallest scales when testing the behavior of highly energetic photons, or even plasma physics. Indeed, AGNs constitute the perfect laboratories for the study of relativistic plasma under extreme conditions inaccessible to experiments.

On the other hand, distant AGNs' energy spectra depend on many parameters, among which is the cosmological expansion and star formation history of the universe. Hence, they can be of significant interest for observational cosmology. Furthermore, the analysis of the spectral features of AGNs has lead to an indirect measurement of the EBL, the diffuse and nearly isotropic background of infrared-optical-ultraviolet radiation from outside our Galaxy, cumulated mainly from star formation and AGNs. A detailed study of the EBL as a function of energy and redshift could, in turn, yield insight into the cosmic history of star and galaxy formation in the Universe, as the EBL holds fundamental information about these processes. Because of the extremely high redshifts at which they can be observed, GRB spectra would constitute an important addition for the EBL analysis.

Gamma-Ray Bursts

GRBs are the most luminous and violent explosions in the Universe. They were discovered in 1967 but their research has made rapid progress this last two decades, boosted by results in the gamma energy domain from satellite instruments, the most recent being the Large Area Telescope (LAT) and Gamma-ray Burst Monitor (GBM) onboard the Fermi Gamma-ray Space Telescope. Not much about them is known or understood, hence being one of the most enigmatic phenomena in the Universe. Their central engine's identity or nature has not been confirmed yet, although at least some long GRBs (>2 s) have been associated with the explosion of massive stars resulting in a supernova from core collapse. GRBs are characterized by a prompt MeV-band emission accompanied by afterglows that span the radio to X-ray, decaying gradually overs hours to days or more. The latest observations of Fermi, have revealed intense radiation in the GeV band from a respectable number of GRBs. In general, this emission lasts longer than the one in the MeV band and may release a considerable fraction of its energy. Even though the GeV emission can be interpreted in many ways and the afterglow has been tentatively explained in some cases, its origin remains elusive. Robust estimates of the total energy radiated in the GeV band can help put constraints on the central engine.

As for AGNs, the low-energy emission of GRBs is also believed to be predominantly from synchrotron radiation from a relativistic electron population, and at high energies the radiation process is still overly debated. In GRBs this concerns the radio to X-ray afterglow emission. Unfortunately again, both leptonic and hadronic models fit most of the spectral data. Furthermore, the spectra of GRBs also show high variability, particularly during the beginning of their emission called "prompt" emission. For GRBs, the variability can be seen in the MeV and GeV energy bands and happens in short timescales (∼0.01-1000 s). Moreover, GRBs are also of interest for cosmology, for they occur at such large distances that they open a window to the era of cosmic reionization and the earliest star formation. One recently detected GRB (z∼8.2) represents the most ancient known astrophysical source.

3.3.1.2 Galactic sources

A big advantage of galactic sources with respect to extragalactic ones is that, thanks to their proximity, their morphology can be resolved and studied in detail, along with their possible spectral variations in different regions of the source. The ability of detecting such structures at TeV energies could be vital for identifying the process involved in the production of gamma-rays. Indeed, Inverse Compton scattering should show narrow structures, similar to those seen in X-rays, which are governed by the rapid cooling of the radiating electrons. On the other hand, hadronic processes are expected to generate smoother structures.

Next will be presented the most studied types of galactic sources: pulsars and pulsar wind nebulae, as well as supernova remnants. Other kinds of sources studied with H.E.S.S. include binary systems and globular clusters, as well as the galactic center, which will be described in section 6.1 and the diffuse emission, which are the subject of next chapter.

The supernova remnants

A supernova is a highly energetic stellar explosion that has two possible trigger processes. One is the sudden reignition of nuclear fusion in a degenerate star, like a white dwarf. This can happen if, for example, the star accretes enough material from a companion in a binary system. The core temperature raises until it reaches a level in which carbon fusion can start, triggering runaway nuclear fusion which disrupts the star. A supernova explosion will also occur when a massive star releases gravitational potential energy by suddenly collapsing.

The explosion expels most of the star's outer layers at velocities up to about 10% of the speed of light, creating a shock wave that travels through the surrounding interstellar medium. The shell of gas and dust, consisting of the remains of the material in the outer layers of the star after the explosion, form a structure known as a supernova remnant. It will be bounded by the expanding shock wave and the interstellar medium it clears and shocks along the way. For a long time supernova remnants were suspected to be the source of very high energy cosmic rays. Recently, the Fermi collaboration found evidence of galactic cosmic ray production in supernova remnants [41]. However, for now, there has been no conclusive experimental evidence supporting this for cosmic rays above the previously mentioned "knee" ($\sim 10^{15}$eV) in the energy spectrum.

The Crab Nebula is, at X-ray and gamma-ray energies, the strongest persistent source in the northern sky, with a flux that has been measured above 10 TeV. Hence it is a reference source for the calibration of the H.E.S.S. experiment. In winter 2002/2003, it was observed with the first two telescopes with the goal of verifying the performance of the instrument. At the center of the nebula is the Crab pulsar, a neutron star which emits a pulsed signal from radio to gamma-rays.

Pulsars and pulsar wind nebula

Another class of objects which has attracted much attention are the pulsars, along with their associated pulsar wind nebula. A pulsar is a highly magnetized, rotating neutron star, resulting from a supernova explosion, which emits a beam of photons, thus signaling its presence only when the direction of the light is in the line of sight of the observer. Because of the rotation of the star, the emission appears as pulses, which are short (from roughly milliseconds to seconds) and regular. Although most of these sources emit in the radio or the X-ray domain, they are widely studied in gamma-rays as well.

In contrast to shock acceleration (SNR), in pulsars, charged particles leading to this very high energy emission are accelerated to relativistic speeds by the strong electric fields located in some specific regions of the pulsar depending on the model (polar cap, outer gap, ... [[42]]). This fields appear in order to reestablish the local neutrality, which is lost due to the significant leakage of charged particles following the open magnetic field lines created by the rapid rotation of the pulsar. These charged particles, called the pulsar's wind, will stream into the interstellar medium and generate a standing shock wave before slowing down to non relativistic speed. Beyond this radius, the synchrotron emission will become stronger.

Pulsar wind nebulas are nebulas which are powered by a pulsar's wind. Although in young supernova they are often found inside the shells of supernova remnants, they have also been seen around old pulsar whose supernova remnant no longer exists. In pulsar wind nebula, shock acceleration takes place in a second phase in the wind termination shock, after a first acceleration by the pulsar. The crab nebula is considered a pulsar wind nebula.

3.3.2 Absorption

The observation of active sources on Earth can reveal much about the acceleration mechanism of charged cosmic rays through the identification of the gamma emission process. An important aspect that has to be taken into account though, is the fact that the spectrum measured on Earth might be affected by the propagation of gamma in the Galaxy. As mentioned before, because gamma-rays are neutral, they are not deviated by magnetic fields and travel in a straight way from the source. However, there is an absorption process of gamma that leads to the attenuation of the observed flux on Earth.

Indeed, gamma-rays of energy E_1 can interact with photons at lower energies (E_2) with a cross section which depends on the energy of both particles:

$$\sigma = \pi r_e^2 \frac{m_e^2 c^4}{w^2} [2ln(\frac{2w}{m_e c^2}) - 1] \tag{3.4}$$

with r_e and m_e the radius and mass of the electron, respectively, and $w = \sqrt{E_1 E_2}$.

The result of the collision will be a conversion into an electron-positron pair, whenever the available energy is more than the mass energy of the pair. Hence, because of the existence of the

Cosmic Microwave Background, no sources above 200 TeV will be detected further than 1 Mpc, distance at which all the photons at these energies will have disappeared via pair production. Figure 3.5 gives the gamma horizon as the photon's maximum energy that will be detected on Earth as a function of the distance of the source, measured in redshift. At 1 TeV, the gamma-rays will be more likely to interact and be affected by infrared photons. This knowledge is crucial particularly when studying extragalactic gamma-ray sources, for at high energies the absorption due to the cosmic infrared background will drastically reduce the flux.

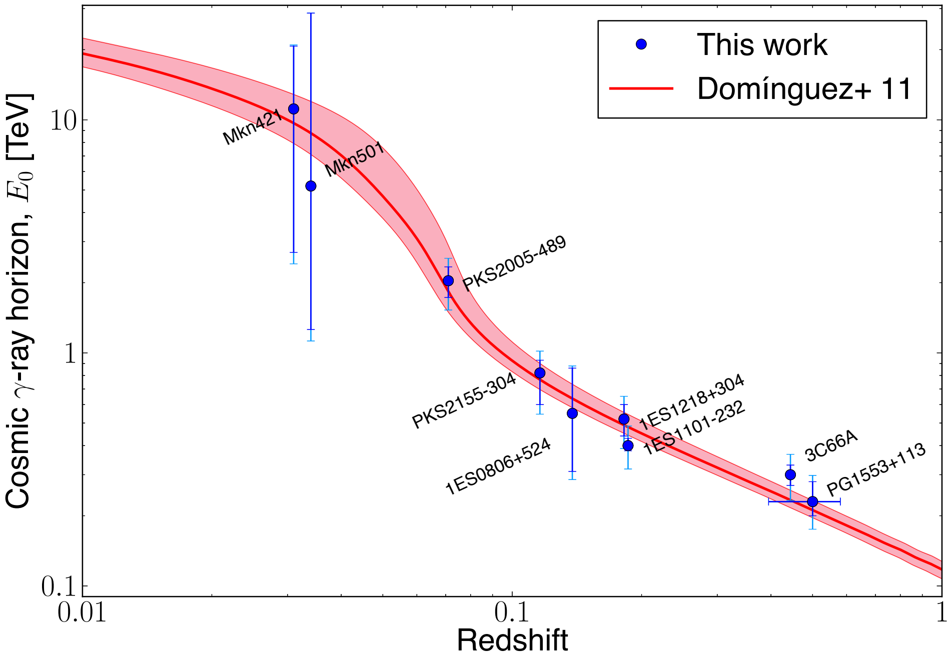

Figure 3.5: The gamma horizon in energy as a function of redshift, for different AGNs. The results are compared to those from a previous publication by the same group. Taken from [43]

Chapter 4

The diffuse emissions

Sommaire

After discussing the possible sources of cosmic rays in the previous chapter, their propagation and resulting flux on Earth will be treated next. In the case of gamma, these are not only influenced by the processes induced by the matter or particles the cosmic rays encounter after their emission while they travel through space, as for hadrons and electrons. Gamma-rays can be produced in passive sources, which are targets to accelerated charged cosmic rays. In a first section, the propagation of cosmic rays will be described, as well as the production of diffuse gamma resulting in the observed diffuse emissions in the vicinity of Earth. Furthermore, the possibility of detecting gamma-rays coming from exotic sources such as dark matter is also discussed. At last, the observation of these emissions and their associated results are presented, along with the possibility of using them for dark matter research.

4.1 Composition of the diffuse emissions

Once they are emitted, charged cosmic rays will propagate through space and suffer a number of processes that might reduce their flux or completely eliminate them by the time they reach Earth. One particularity is that, as charged particles, they will be deflected by the magnetic fields of the Galaxy and loose all information on their direction. Hence, unlike for gamma-rays, no sources of hadrons or electrons are seen from Earth and their detected fluxes are isotropic, at least at TeV energies (unexplained anisotropies are observed at higher energies, see [44, 45]). Gamma, however, are also observed in "dark" regions of the sky, far from active sources. This is due to the fact that there exist other types of sources for gamma that will emit them in a diffuse way. The characteristics of these three types of diffuse emissions: hadrons, electrons and gamma, are described next.

4.1.1 Hadrons

In 1966, soon after the discovery of the Cosmic Microwave Background, the oldest light of our Universe dating from the epoch of recombination, Greisen, Zatsepin and Kuzmin predicted a cutoff in the spectrum of cosmic rays at around 10^{19}eV [46, 47]. For protons, this is due to their interaction with gamma from the CMB and the fact that it exceeds the threshold of pion production through the resonance Δ^+:

$$p+\gamma \rightarrow \Delta^+ \rightarrow N+\pi \tag{4.1}$$

where N can be either a proton and a neutron, associated with either a neutral pion π^0 or a charged one π^+, respectively. This cutoff is referred to as the GZK cutoff or effect and was first observed by the HiRes (High Resolution Fly's Eye) experiment in 2006 [48], after the Akeno Giant Air Shower Array (AGASA) presented evidence for detection of events above the cutoff and a lack of correlations between these and nearby astrophysical sources [49]. The cutoff was later corroborated by the Auger observatory [50], which combined the techniques of AGASA and HiRes, a ground array and an air fluorescence detector respectively, on the same site. In 2010, HiRes clearly confirmed its previous results using more statistics [51].

Concerning nuclei, at around the same energies, the dominant process will be their disintegration on CMB or infrared background (another cosmic photon background):

$$X^A+\gamma \rightarrow X^{(A-1)}+N \tag{4.2}$$

with X a nucleus with A nucleon and again N either a proton or a neutron. Depending on the mass of the nucleus, this process will happen at different energies. For iron it is comparable to the GZK cutoff value.

Although there is some level of consensus on the fact that cosmic rays up to around 10^{15}eV have a galactic origin because of their confinement in the galaxies due to the many magnetic fields, and above $\sim 10^{19}$eV an extragalactic one, the intermediate energy region is still under much debate.

4.1.2 Electrons

In contrast with hadronic cosmic rays, electrons loose their energy much faster by synchrotron radiation and inverse Compton scattering. These rapid energy losses, which are energy-dependent, will provoke a much steeper spectrum than that of hadronic cosmic rays. What is more, the lifetime of a very high-energy electron can be expressed as:

$$t \approx 5 \times 10^5\ (\mathrm{E}/1\ \mathrm{TeV})^{-1}((\mathrm{B}/5\ \mu\mathrm{G})^2{+}1.6(w/1\ \mathrm{eV\ cm}^{-3}))^{-1}\ \text{years}$$

with w the energy density in low frequency photons (hv « 0.1 eV) in the interstellar medium and B the mean interstellar magnetic field [52]. This very short lifetime implies that the source of electrons detected at TeV energies on Earth must be local (distance<1 kpc, see [53, 54]) if supposing a standard diffusion-dominated model of Galactic cosmic-ray transport.

4.1.3 Gamma-rays

The gamma-ray diffuse emission is generally divided into two components: the galactic and the extragalactic one. These are not well understood and are of significant interest for astrophysics, particle physics and cosmology. They will be introduced next, followed by a brief mention of other possible sources for this diffuse emissions.

4.1.3.1 The galactic diffuse emission

The galactic contribution of the diffuse emission is mainly due to the propagation and interaction of protons and electrons with the gas from the interstellar medium and of electrons with the radiation field of the galaxy. In the case of protons, their interaction creates neutral pions and kaons that in turn decay into gamma. Electrons, for their part, produce gamma through bremsstrahlung radiation as well as inverse Compton, when interacting with the gas and the radiation field, respectively. Interstellar matter spreads mainly along the galactic plane. Consequently, a gamma-ray isotropic diffuse emission is expected around this region, constituting the galactic component.

In addition, giant molecular clouds represent an interesting class of passive sources of gamma rays. Cosmic rays from external sources interact with the relatively dense material of clouds, generating localized sources of gamma rays. The flux of these can be further enhanced if cosmic rays are trapped in the magnetic fields of the clouds. These kind of sources, which are targets for accelerated cosmic rays, are known as passive sources, as opposed to the active ones that are assumed to directly produce the photons, as seen in chapter 3. These clouds are more concentrated in the galactic plane and have an inhomogeneous distribution. Hence, the galactic diffuse emission is highly anisotropic.

The study of the galactic component, because of its origin, could reveal much about the sources, acceleration mechanisms and propagation of cosmic rays, together with the matter distribution. Additionally, it is a background for the active sources so it can disturb their position determination and spectrum reconstruction. Furthermore, it can also be a foreground of a much fainter extragalactic component.

4.1.3.2 The extragalactic diffuse emission

The gamma contributing to the extragalactic component, however, come essentially from the propagation of cosmic rays originating from very distant sources such as blazars, starburst galaxies and clusters of galaxies. At such scales the universe is supposed to be more homogeneous, hence this extragalactic emission is considered uniform. Besides, it should suffer the same absorption processes described in 3.3.2. Moreover, because the cosmic rays from which they come were energetic enough to escape the magnetic field of their host galaxy, this emission is also expected at higher energies. However, it is not easily separated from the galactic element.

If well determined, this extragalactic constituent could be used in cosmological and blazar studies. Moreover, its origin is still unknown and it has not yet been identified for very high energies. It should not be considerable at GeV energies.

4.1.3.3 Other possible sources

Besides these two components, other sources, concealed in the diffuse emission, could complete the picture, such as non-resolved astrophysical sources, misidentified electrons and hadrons or more exotic signals like evaporating black holes [55], topological defects during the formation of the Universe, as cosmic strings [56] or magnetic monopoles [57], or dark matter producing gamma rays. The latter is the subject of the next section.

4.2 Dark matter as a source of gamma-rays

Thanks to the satellite WMAP (Wilkinson Microwave Anisotropy Probe), it is now admitted that baryonic matter only constitutes about 17% of all matter [58] (the Planck satellite finds a slightly smaller but compatible value [59]), the rest being called "Dark Matter". Next is given a quick overview of the discovery of "Dark Matter" as well as potential candidates to explain it. In at least one of the most promising theories, these "Dark Matter particles" would be able to produce gamma-rays, as mentioned at the end of this section.

4.2.1 Dark matter observations

In 1934, after studying the motion of galaxies in the Coma cluster, Swiss astrophysicist Fritz Zwicky concluded that there was about 400 times more estimated mass than was visually observable. Most scientists at that time thought it was due to errors in his calculations. Still, this "missing mass problem" was later corroborated by more observations of large scale structures with unexplained gravitational effects.

It is possible to assess the mass of galaxies, clusters of galaxies, and even the entire universe through dynamical and general relativistic means. Among others, measurements such as the galactic rotation curve that illustrates the velocity of rotation of the stars or gas in the galaxy versus the distance from the galactic center, or the gravitational lensing, which is based on the effect on light from background galaxies, depend on the mass of the considered objects. At the same time, a direct detection of the visible "luminous" matter these objects contain (stars, gas and dust of the interstellar and intergalactic medium) can also provide a fair guess of their mass. These two approaches, however, lead to very different results.

If only the seen mass is present in the galaxy, for instance, stars far from the center couldn't possibly move at such high speeds without breaking lose of the gravitational pull. Hence, it appears that more than 80% of the mass of the universe is missing. To account for these discrepancies, a hypothesized "dark matter" was postulated by Zwicky. It can only be evidenced by its gravitational effects, for it does not interact with electromagnetic radiation, being, by definition, utterly transparent. As it represents almost 25% of the mass-energy of our universe, it is one of the cornerstones of the Lambda-CDM model (where CDM stands for Cold Dark Matter), often referred to as the standard model of big bang cosmology.

4.2.2 Dark Matter candidates

As important as dark matter is believed to be in the cosmos, direct evidence of its existence and a concrete understanding of its nature have remained elusive. In the Lambda-CDM model, it is described as being cold (i.e. its velocity was non-relativistic at the epoch of radiation-matter equality), dissipationless (cannot cool by radiating photons) and collisionless (i.e., the dark matter particles interact with each other and other particles only through gravity).

For a long time it was believed that neutrinos could be it. This neutral elementary particle, usually traveling close to the speed of light, can pass through ordinary matter almost unaffected. Besides, even with a very small mass, its sheer numbers (billions going through the Earth every second) could explain the missing matter mystery. However, the constraints obtained for the neutrino mass were below what was needed. As of today, the standard model (SM) of particle physics which is the most accepted theory of the electromagnetic, weak, and strong nuclear interactions, does not include any viable dark matter particle possessing all of the required properties. Other non-baryonic potential dark matter particles include axions, sterile neutrinos and magnetic monopoles, as well as particles appearing in universal extra-dimensional (UED) extensions of the SM like the Kaluza Klein theory [60].

More suitable candidates are to be found among high energy physics models, in the form of non-baryonic matter, as opposed to ordinary matter (made of protons and neutrons). Some of these, like the supersymmetric extension of the Standard Model (abbreviated as SUSY) predict the existence of massive particles that interact feebly, called WIMP's (Weakly Interactive Massive Particles).

In the SUSY scenario, an additional symmetry between bosons and fermions is introduced. Each particle and field is then related to a superpartner called "sparticle", differing only by half a unit of spin, with the same internal quantum numbers and opposed R-parity (+1 for Standard Model particles, -1 for supersymmetric ones). By definition, a dark matter particle is either exactly stable or quasi-stable over a time-scale that is much longer than the age of the universe. With SUSY, a particle that fits is the neutralino, a mixture of four superpartners that can produce four states, the lightest of which is typically stable if the R-parity is conserved. If not, it may decay into baryonic particles. The neutralino constitutes one of the most promising candidates for dark matter so far.

4.2.3 An exotic process of gamma-ray production

In the SUSY scenario, neutralinos (noted χ) are able to annihilate and give γ via several processes:

- $\chi\chi \to \gamma\gamma$ direct production of photons by neutralino annihilation.
- $\chi\chi \to q\bar{q} \to X\gamma$ processes happen when the χ annihilation results in quarks, which will fragment and hadronize. The thus created neutral pions and kaons in turn will decay into gamma, giving a continous γ spectrum until the energy of the neutralino.
- neutralinos can also annihilate generating Z, W and higgs bosons ($\chi\chi \to \gamma Z$, for instance), which in turn decay into quarks, producing gamma-rays as mentioned above. However, the bosons created in these processes will take mass energy, resulting in a γ spectrum with a spectral line shifted away from the mass of the χ.

If the R-parity is not conserved, decay into electrons and positrons could be possible [61] and explain anomalies such as the ones mentioned in section 4.3.3.

4.3 Detecting the diffuse emissions

The hadron, electron and gamma diffuse emissions have been detected and studied in Earth's vicinity. Next are given an overview of the observations of these emissions and associated general results, as well as the specific flux and index obtained when fitting the spectra of these emissions with a power-law and extrapolating at energies around 1 TeV (the H.E.S.S. energy domain). The last section discusses studies of anomalies in the spectra of these emissions that have been performed in the framework of a search for dark matter.

4.3.1 Observations

Hereafter is presented a collection of some general results on the observations of these emissions at H.E.S.S. energies.

4.3.1.1 Hadrons

Up to energies of $\sim 10^{14}$eV, hadronic cosmic rays can be directly detected with balloons or satellites. At higher energies however, their fluxes decrease and the fiducial volume of the detectors are too small to measure the total energy so that it is necessary to come back to Earth for indirect detection, as happens with gamma-rays (see chapter 1). Still, for heavy nuclei the fluxes are so low, that significant collection areas are required, as the Auger experiment's, which is of 3000 km^2. The spectrum of cosmic rays measured in Earth's vicinity covers 30 orders of magnitude in flux and 12 in energy, as can be seen figure 4.1. Globally, it can be described as power-law, a function of the form $E^{-\Gamma}$. Nonetheless, some distinctive features can be seen, like changes in the slope at around 10^{15}eV (called the "knee") and at about 10^{15}eV (named the "ankle"). The first is hypothesized to be due to the transition form a galactic to an extragalactic emission, whereas the last is thought to be the passage from protons to heaviest ions detection. Different experiments are able to identify the various nuclei in the diffuse emission of hadrons. The composition follows approximatively that of the elements present in our Solar System, with about 89% of protons, 10% of Helium and 1% of heavier nuclei. The results are summarized in figure 4.2.

4.3.1.2 Electrons

Concerning electrons, until 2008, all measurements had been done using balloons or satellites. Nonetheless, as for hadrons and gamma, the decrease of the flux at high energies made direct measurements difficult. Thanks to its good background rejection capabilities, the H.E.S.S. experiment was the first ground experiment to achieve such measurement [52]. The results for the cumulated electron-positron spectrum obtained with different instruments are condensed in figure 4.3. Above 7 GeV, the spectrum can be described with two power-laws: one up to 900 GeV, at which point the spectrum suffers a break, and the index of the second one becomes much steeper. The flux of electrons at 10 GeV is 1% of that of protons.

4.3.1.3 Gamma

At present, the observation of gamma diffuse emissions is the best way to investigate the acceleration and propagation of cosmic rays, as well as the matter distribution. This can be achieved not only thanks to the gamma ray cartography, but also by analyzing its spectrum.

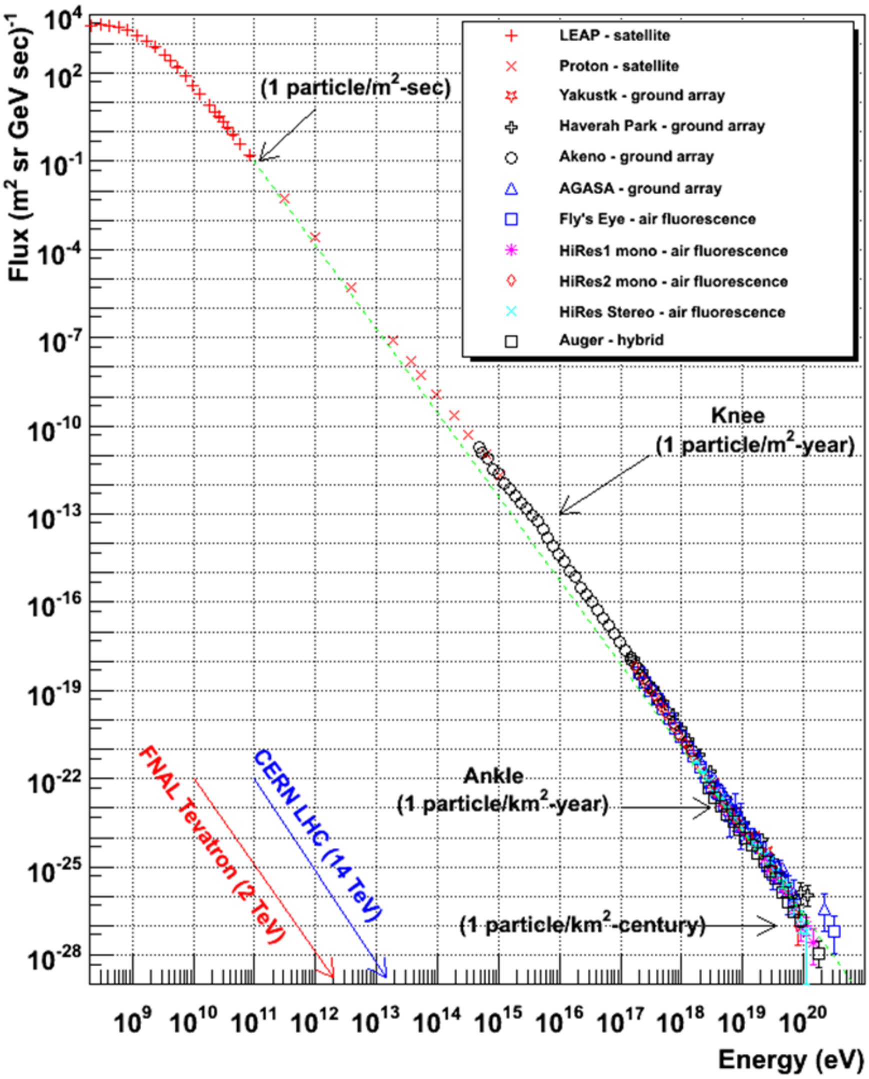

Figure 4.1: Cosmic rays spectrum as seen by different experiments. Although the general evolution of the spectrum follows a power-law, two breaks in the slope can be seen at 10^{15}eV and 10^{18}eV, corresponding to the "knee" and the "ankle". Credit: http://www.physics.utah.edu/ whanlon/spectrum1.png

The galactic as much as the extragalactic diffuse gamma emissions have been extensively observed with the gamma-ray experiments introduced in 1. Specific results for the galactic and extragalactic emissions are given in section 4.3.2.

Concerning the galactic emission, in 2006, H.E.S.S. discovered an extended region of very high energy ($>10^{11}$eV) gamma ray emission [63] correlated spatially with a complex of giant molecular overlapping clouds in the central 200 parsecs of the Milky Way, which provide an efficient target for the nucleonic cosmic rays permeating them. The mapping of this extended emission was made possible by the wide field of view (5°) and the improved angular resolution

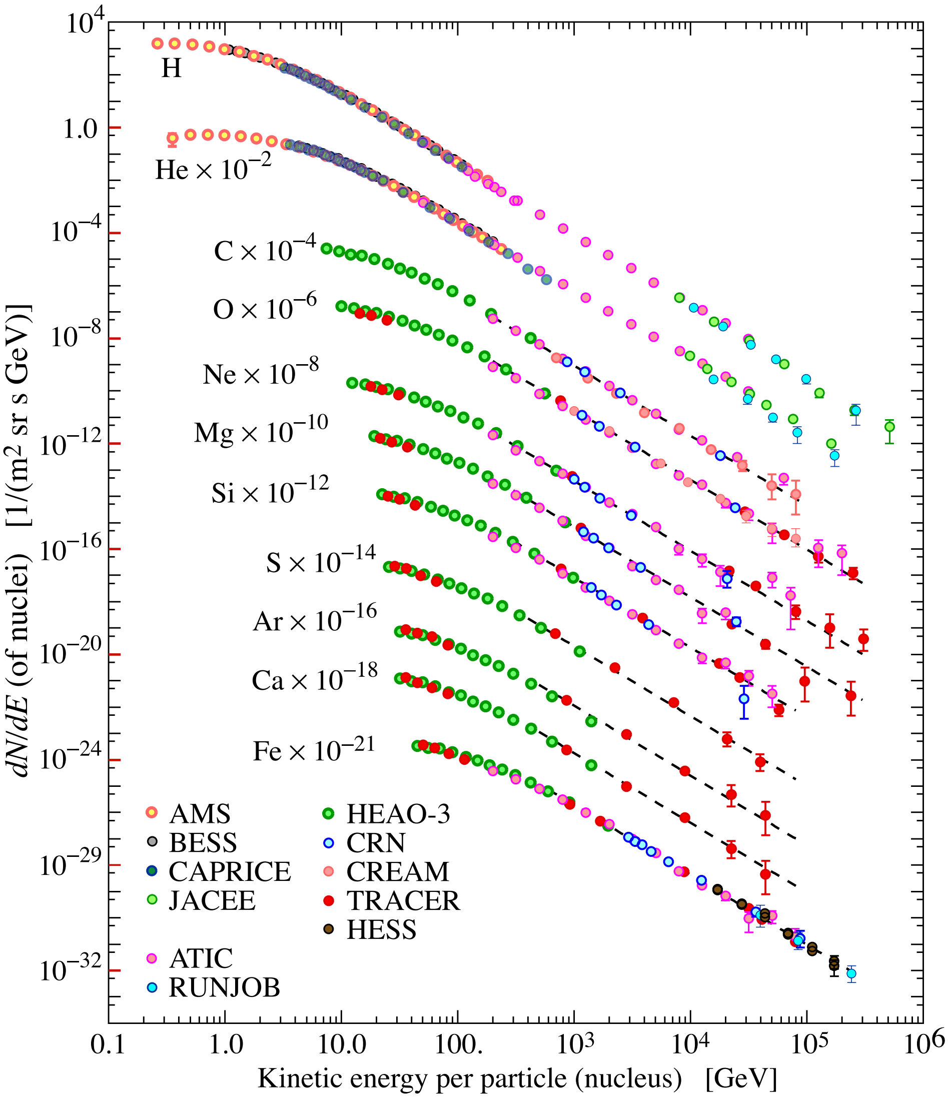

Figure 4.2: Cosmic rays composition as seen by different experiments. Hadronic cosmic rays include 89% of protons, 10% of Helium and 1% of heavier nuclei (right plot). Plot taken from [15].

(better than 0.1°) of H.E.S.S., taken together. Several active gamma-ray sources were identified. Hence, a lot of processes are involved in the gamma ray production in this area, including the various emitting sources and the propagation and interaction of the galactic and extragalactic radiations with the medium and magnetic fields. It will be further detailed in section 6.1.3.

Moreover, as mentioned, diffuse emissions present significant potential in the search for dark matter. Hence, in this framework, sites which are thought to have higher densities of dark matter, can be privileged. This is the case of the galactic center, where all dark matter distribution and galaxy profile models predict a high concentration of it. Hence the galactic diffuse emission has a huge potential in dark matter searches. In addition, other sources such as dwarf spheroidal galaxies or globular clusters, believed to contain higher amounts of dark matter, can be observed. Upper limits on the annihilation cross section were deduced from observations of these sources

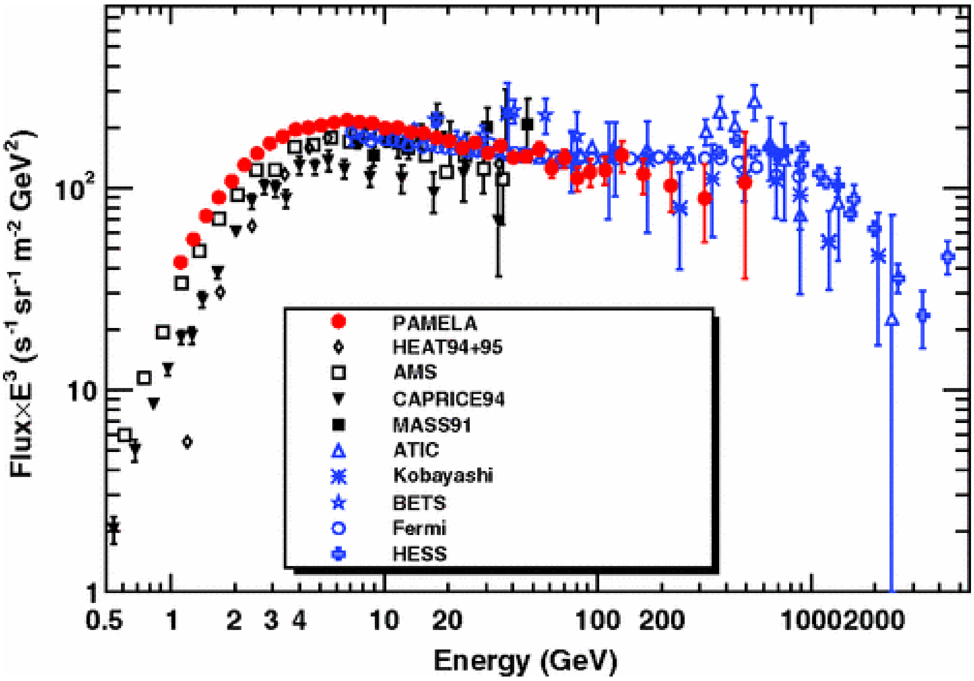

Figure 4.3: Total spectrum of electrons and positrons measured on Earth's vicinity. A break can be found at 900 GeV. Before and after, the spectrum can be well represented by a powe-rlaw. The second one presents a steeper slope. [62]

with IACT (for instance, see [64] for the former, [65] for the latter, or [66], where the source could be one or the other).

4.3.2 Previous results at H.E.S.S. energies on diffuse emissions

By extrapolating the data published by experiments operating at lower energies to the energy region of the H.E.S.S. experiment, one can estimate roughly the relative contribution expected in the H.E.S.S. data. The extrapolation is based on the following results:

- The Fermi collaboration [67] has published results for the extragalactic diffuse gamma ray component from the first year of data taking period. They propose a simple power-law to describe the differential flux above 100 MeV:

  $$\frac{d\Phi}{dE} = \Phi_0 \left(\frac{E}{E_0}\right)^{-\Gamma}$$

  With the parameter Γ estimated to be 2.41 ± 0.05. This is the value used later in the analysis. Adapting the integrated flux value from their paper, the differential flux at 1 TeV is:

  $$\Phi_0(1\ \mathrm{TeV}) = (3.33 \pm 0.56) \cdot 10^{-7} (\mathrm{TeV} \cdot \mathrm{m}^2 \cdot \mathrm{s} \cdot \mathrm{sr})^{-1}$$

Another parameterization, fitting a wider range in energy and covering also the EGRET published data, was proposed in [68]. The flux was parameterized by a broken power-law for the gamma ray extragalactic contribution:

$$\frac{dJ}{dE} = \frac{C}{\left(\left(\frac{E}{E_b}\right)^{\Gamma_3} + \left(\frac{E}{E_b}\right)^{\Gamma_4}\right)}$$

By fitting data, the parameter Γ_3 was found to be close to unity whereas Γ_4 was the one determined previously.

- Concerning the galactic component, the Fermi collaboration [67] also estimated a contribution, which is of the form:

  $$\frac{d\Phi}{dE} = k \cdot E^{-\Gamma}$$

  This equation is predicted with a power-law index of the order of 2.34 and with a flux amplitude at 100 GeV of:

  $$E^2 \frac{d\Phi}{dE}(E = 10^5 \text{ MeV}) \approx 2 \cdot 10^{-4} \text{MeV} \cdot \text{cm}^{-2} \cdot \text{s}^{-1} \cdot \text{sr}^{-1}$$

- The H.E.S.S. collaboration [69] provided a law (smoothly broken power-law) of the following form for the diffuse electron contribution:

  $$\Phi(E > 600GeV) = k \cdot \left(\frac{E}{E_B}\right)^{-\Gamma_1} \cdot \left(1 + \left(\frac{E}{E_B}\right)^{\frac{1}{\alpha}}\right)^{-(\Gamma_2 - \Gamma_1)\alpha}$$

  At higher energies however (up to ∼3 TeV), a simple power-law may describe the data [52] with a flux of $(1.17 \pm 0.02) \cdot 10^{-4}$ $\text{TeV}^{-1}\text{m}^{-2}\text{s}^{-1}\text{sr}^{-1}$ at 1 TeV and a spectral index of 3.9±0.1.

- For the hadron component, a compilation of experimental results [70] has been published and finds a contribution of the form:

  $$E^{2.5} \cdot \frac{d\Phi}{dE} = k \cdot E^{-\Gamma}$$

  This equation is adjusted with a power-law index of the order of 0.3 and yields a flux at 1 TeV of the order of $1 \cdot 10^{-1} (\text{TeV} \cdot \text{m}^2 \cdot \text{s} \cdot \text{sr})^{-1}$.

The values of the parameters used can be found in the referenced papers. The compilation of these results and their extrapolation to the energy range of the H.E.S.S. experiment (from 100 GeV up to 10 TeV) is presented in figure 4.4.

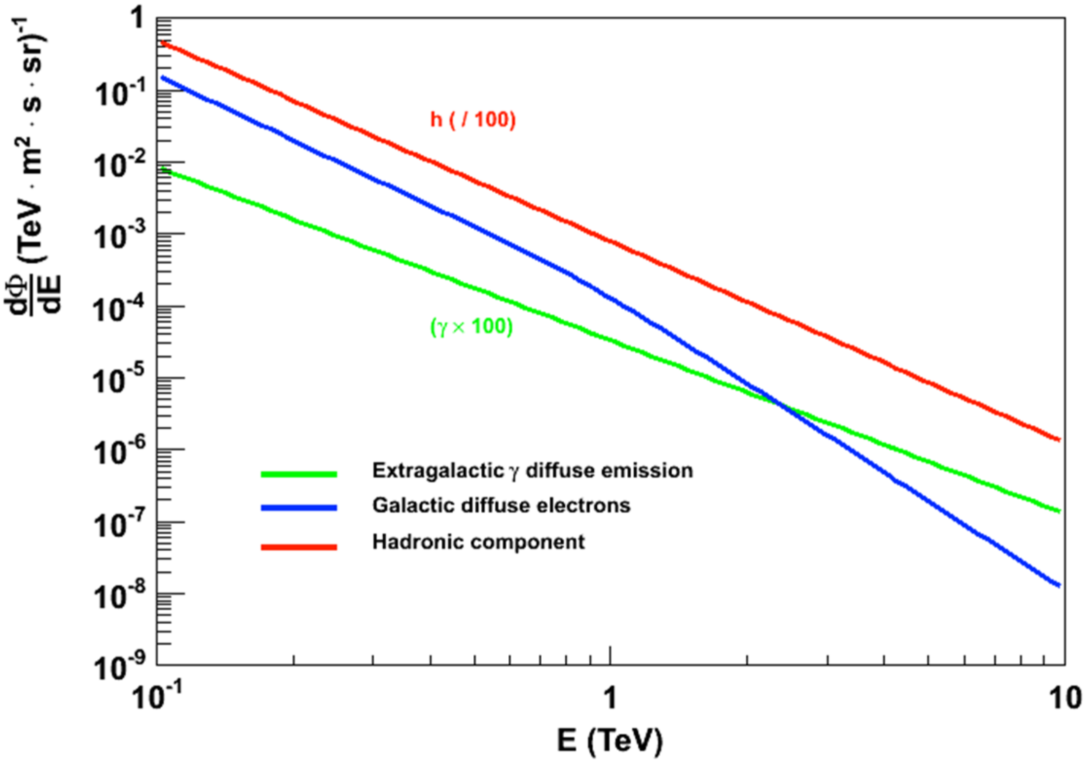

Figure 4.4: Extrapolation of the diffuse components to the energy domain of the H.E.S.S. experiment. Red, green and blue curves represent the hadron, gamma and electron spectrum respectively. Hadron and gamma fluxes have been scaled.

Integrating these curves from a hundred GeV to a few tens of TeV one can predict a ratio of about 10 to 3 for electrons compared to hadrons and a second ratio of another three orders of magnitude to reach the diffuse gamma ray flux:

$$\epsilon_p = 99.71\%$$
$$\epsilon_e = (0.287 \pm 0.015)\%$$
$$\epsilon_\gamma = 2.180 \cdot 10^{-4}$$

Taking this into consideration, it is unrealistic to base a method on the removal of the background from the data to reveal the diffuse gamma ray component. Thus, a method able to separate these different components without data reduction, as the one developed, is more appropriate for this study.

4.3.3 Spectral anomalies

As mentioned previously, in addition to their intrinsic interest described above, the spectrum of the diffuse gamma and electrons emission can also be used to look for dark matter. A recent rise of interest in the Dark Matter problem has been triggered by observations of anomalies [61, 71, 72] in several high energy (>1 GeV) experiments. These were reported as excesses in obtained spectra at different high energy ranges depending on the experiment. The Advanced Thin Ionization Calorimeter (ATIC) and the Polar Patrol Balloon and Balloon borne Electron Telescope with Scintillating fibers (PPB-BETS) show a bump in the total e^+e^- flux between 100 GeV and 1 TeV, seen in figure 4.5). Athough later observations by H.E.S.S. could not be conclusive on this feature, Fermi data invalidated it, as visualized in the same figure.

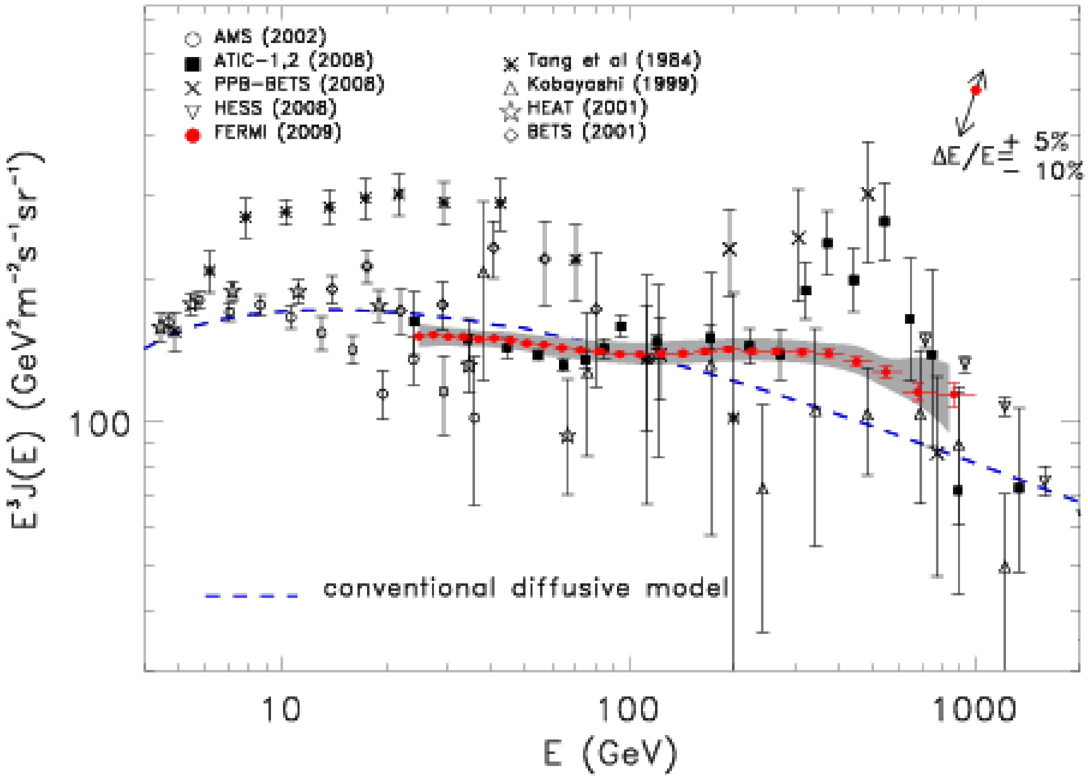

Figure 4.5: Electron total flux as seen by ATIC, PPB-BETS, H.E.S.S. and Fermi between ∼10 and ∼10^3 GeV. The first two experiments observed an anomaly invalidated later by the Fermi data. [73]

Moreover, the Payload for Antimatter Matter Exploration and Light-nuclei Astrophysics (PAMELA), Fermi and AMS-02 collaborations saw a prominent upturn in the positron fraction above 100 GeV, shown figure 4.6, in contrast to what is expected (see figure 4.7) from high-energy cosmic rays interacting with the interstellar medium. This excess can be explained either by the presence of nearby pulsars or with dark matter annihilation models.

Recently, an independent paper was published claiming a possible dark matter annihilation line at around 130 GeV at a precise location in the galactic center, using the Fermi data [76]. The search was performed by selecting regions in the sky with optimal signal-to-background ratio,

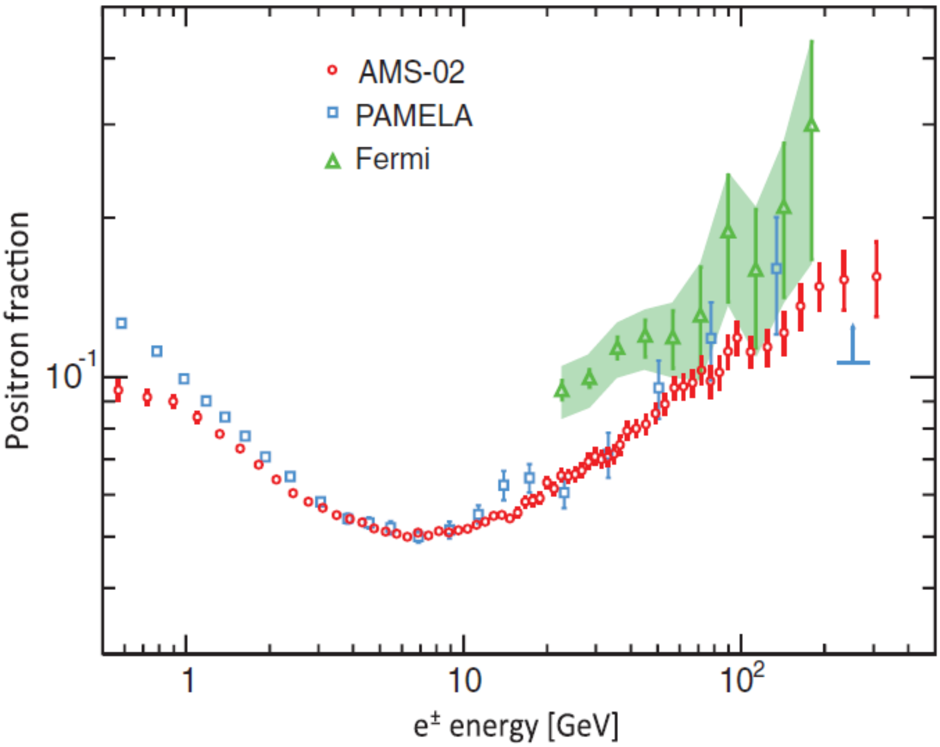

Figure 4.6: Positron fraction $e^+/(e^+ + e^-)$ as measured by PAMELA, Fermi and AMS02. Taken from [74]

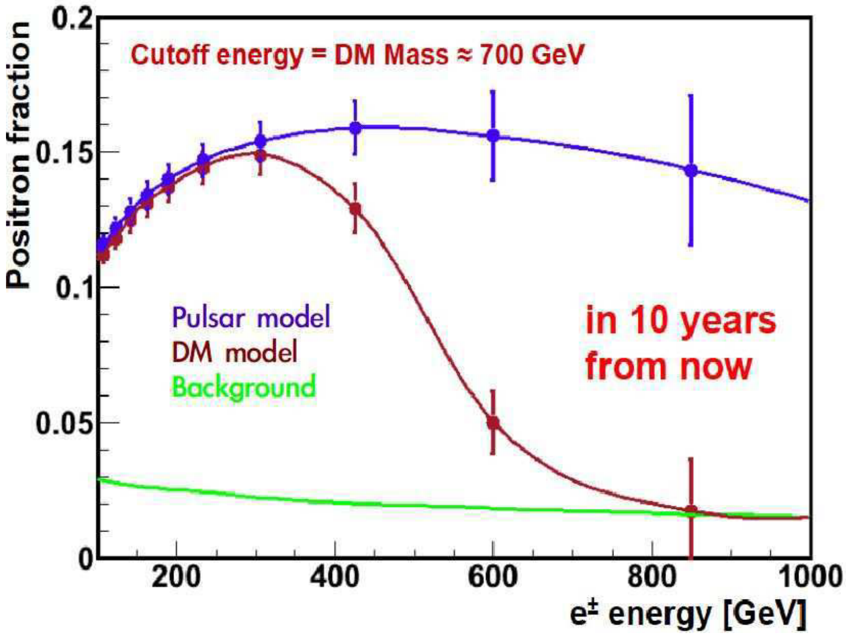

Figure 4.7: Expected positron fraction $e^+/(e^+ + e^-)$ depending on the source: dark matter of mass ≈ 700 GeV in brown, pulsars in purple or cosmic-rays interacting with interstellar matter (background) in green. Taken from [75]

depending on the assumed density profile of dark matter. However, when taking into account the look-elsewhere effect, the significance of the observed signature drops from 4.6σ to 3.2σ. Up to now, analyses of this region with other experiments and even by the Fermi collaboration have yielded no similar results.

The possibility that the anomalies are due to annihilating or decaying dark matter led to much excitement in the particle physics community, although standard astrophysical sources such as pulsars or nearby supernova remnants provide a viable explanation as well. Furthermore, the mentioned increases in positron and electron fluxes are in some cases not consistent from one experiment to another. This can lead to contradictions in the proposed models, which is one of the reasons why analyzing and trying to interpret the anomalies has been difficult. What is more, the way the dark matter particles decay or annihilate may depend not only on the particle model but also on a wide variety of parameters like the dark matter distribution in the considered object.

Moreover, a lot of processes can be involved in the gamma ray and electrons production, depending on the targeted area, including the various emitting sources and the propagation and interaction of the galactic and extragalactic radiations with the medium and magnetic fields. An understanding of these mechanisms are needed to lead to predictions, for example on the spectral shape. Then, a comparison with obtained data might reveal anomalies or discrepancies due to the presence of dark matter. In the collaborations, the predictions of different models are compared to the studied data, in hope of finding a signature that may correspond to a dark matter particle.

Part III

Data Analysis

Although H.E.S.S. can detect diffuse hadrons, electrons and gamma as well as gamma coming from active astrophysical sources, in practice it is difficult to tag a particular event as one type of particle or another (see section 2.2.3). In the framework of this thesis, a method was developed to extract the concentrations of each of the constituents of the diffuse emissions, excluding the region of the active source present in the field of view (FOV). Their contribution to the global spectrum was calculated as well. The idea is to assign to each event three probabilities associated to the three diffuse types of particle and estimated using probability density functions (PDFs). In this way, a separate energy spectrum can be reconstructed for each population, using all the events weighted by the different probabilities. By fitting these spectra with multi-parameter functions using an unbinned likelihood method, each population can be separately characterized. The analysis is broken down as follows. The first chapter concentrates on the treatment of the discriminant variables' PDFs and the particle disentanglement while the second chapter deals exclusively with the active source modelization and its use for validating the diffuse emissions proportions obtained in the previous chapter. Finally, in the last chapter, their spectra are presented.

In section 5.1, the five discriminant variables used in this work are studied. In the first two subsections, their discriminative power is improved and the correspondence between data and simulations tested, leading to an event selection described in the last subsection. In the next section of the chapter, can be found the definition of the probability density functions, constructed from the discriminant variables, that are used to extract the concentration of each type of diffuse emission. A particle separation test is made with the elaboration of a toy Monte Carlo. In the following subsection are the corresponding results when applied in the field of view of PKS 2155-304. A short discussion giving an upper limit for the flux of diffuse gamma closes the chapter. In the fields of view observed by H.E.S.S., active astrophysical sources are always present. In the framework of the method developed to disentangle the different types of particles based on discriminant variables, the active source PKS 2155-304 was used as a benchmark. Indeed, the data discrimination was tested using the astrophysical source to compare the number of point-like photons found by the standard analyses and by the developed method. However, because this method cannot be used with any type of cut, it cannot be adjusted to the data selection of the standard analyses and the number of point-like gamma could not be directly compared. Thus another way of modeling the source is needed. In this work, the source morphology was used for this purpose. Because the original source distribution will always be convoluted with the detector's response, the modelization depends on the instrument. After a quick overview of the different studied point-like sources, in section 6.2, the Point Spread Function of the instrument is discussed as a way to modelize point-like sources. However, it is seen that for a good representation of the source, the PSF needs further handling and a technique to fit the source using a PSF convoluted by a Gaussian is described and discussed in section 6.2.1. In the last section, a comparison of the intensity of PKS 2155-304 obtained with different methods can be found. In chapter 7, two methods for reconstructing the diffuse emissions spectra are presented. In section 7.1.1), the X_{eff} estimator, which makes use of both the discriminant variables' PDFs and the estimated concentrations, is introduced and the way it is used to compute the probabilities for each type of diffuse emission is explained. The corresponding spectra for electrons and protons are given. The second section describes the implementation of the *sPlot* tool. This known unfolding technique yields at the same time the diffuse emissions proportions and the events' weight in the spectrum of each population directly by fitting the data. The method is first tested with a Toy Monte Carlo and then applied on PKS 2155-304 data. The preliminary results thus obtained are shown in the last subsection.

Chapter 5

Disentangling the diffuse emissions

Sommaire

A number of shower parameters were introduced in chapter 2. Some of them, known as the "discriminant variables", will be used in this work to discriminate particles. In the first section of this chapter, these are treated so as to improve their discriminative power and their correspondence to the data. A discussion on the resulting data selection closes the section. In the next one, probability density functions are built with the use of these discriminant variables. Then, their discriminative power is tested and applied on the data using the field of view of PKS 2155-304. The region of this AGN was selected because of its location well outside the galactic plane and hence with a dominant extragalactic component for the diffuse gamma ray emission present in the background of the source. The proportion of each type of particle thus obtained is used to calculate an upper limit on the flux of the diffuse gamma emission, considered to be mainly of extragalactic origin, as presented in the last section.

5.1 The discriminant variables

The method developed in this work to disentangle the different types of particles is based on five discriminant variables. The mean scaled length (MSL), width (MSW) and goodness (MSG) are related to the characteristics of the shape of the shower development. Two variables with more power to distinguish photons from electrons were added: the reconstructed positions of the maximum of the shower expansion (MDH) and the estimated first interaction point of the particle in the atmosphere (PDH). This section focuses on the treatment of the simulations to, on the one hand, enhance the discriminative power of the variables as much as possible (section 5.1.1) and, on the other, make them match real events as best as possible with the use of a dedicated data sample (section 5.1.2). Both aspects are essential for a good differentiation of the particles when applied on the data. The probability density functions for the discriminant variables used in this work were obtained by fitting their histograms. For simulations, this was done for each type of particle and choosing an optical efficiency of 50%, as it was the simulation's value nearest to the one computed for observational data (see section 2.1.2). The fitted histograms of the discriminant variables can be seen in appendix B and the functions used for the fits are listed in appendix B.

5.1.1 Improving the discriminant variables

To begin, the correlation of the discriminant variables with different parameters needs to be studied because their correction could lead to a better particle discrimination by narrowing their distribution. For instance, the reconstructed maximum of the shower expansion and the point of first interaction with the atmosphere were found to depend on the zenith angle. In the case of the maximum of the shower expansion it furthermore evolves as a logarithmic function of the energy. The next two subsections deal with these corrections. However, only the plots for the simulations are shown, for the data requires previous special handling explained in section 5.1.2 before applying these corrections. Furthermore, although not needed in the method, the simulated point-like gamma PDFs were studied in the same way as the diffuse emissions' PDFs for they were extensively used to test and correct the latter.

5.1.1.1 Zenith dependency correction

A correlation of PDH and MDH with the zenith angle is expected for all the studied particles: simulated point-like source gamma, diffuse gamma, diffuse electrons and diffuse protons. This comes from the fact that MDH (X_{max} in figure 5.1) is measured as a vertical distance in radiation length units between a reference point high in the atmosphere and the maximum of the shower development, as seen in figure 5.1. Hence, if taken as a function of the cosine of the zenith angle, the evolution is linear: ($PDF = a_{zen} \cdot \cos(z) + b_{zen}$) and easy to correct ($PDF_{corr} = PDF + a_{zen} \cdot (1 - \cos(z))$), with PDF=MDH or PDH. Figures 5.2 and 5.3 show the effect of the correction on MDH and PDH respectively for simulated point-like photons. Each type of particle and each discriminant variable calls for a specific set of parameters for the correction. Moreover, these also depend on the chosen optical efficiency. However, only the a_{zen} parameter is needed for the correction. The obtained values are summarized in table 5.1.

After the correction, the variables PDH and MDH no longer depend on the zenith angle. Figures 5.4 and 5.5 illustrate the effect of the correction on the mean and RMS of MDH, respectively, for simulated diffuse gamma, for each optical efficiency. These graphs for all other particles can be found in appendix C. Before the correction, the mean value of MDH varies for each zenith angle (in black). After correction (in green), these are all superimposed. As

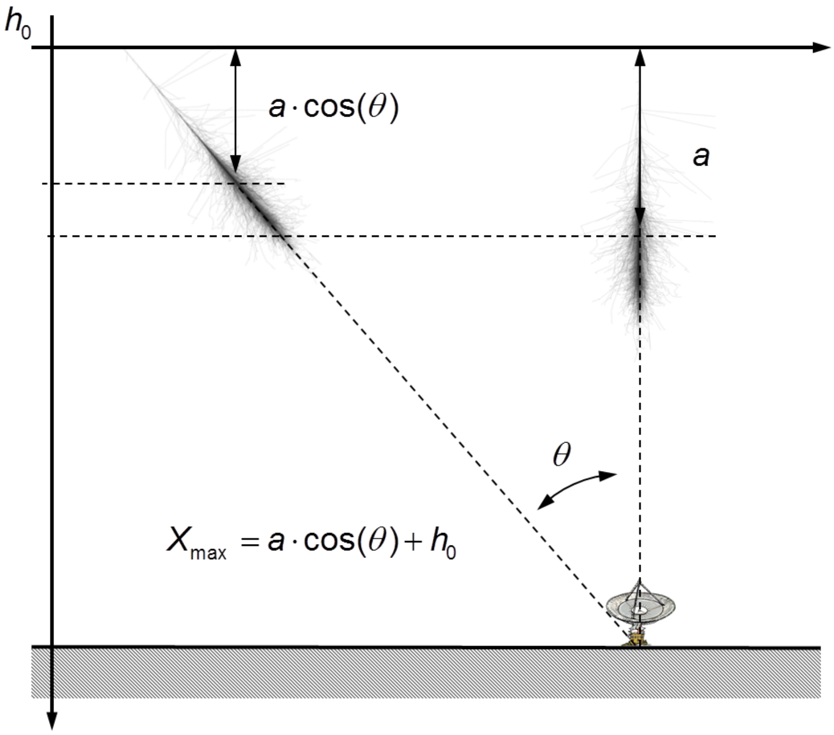

Figure 5.1: Zenithal angle dependency of MDH.

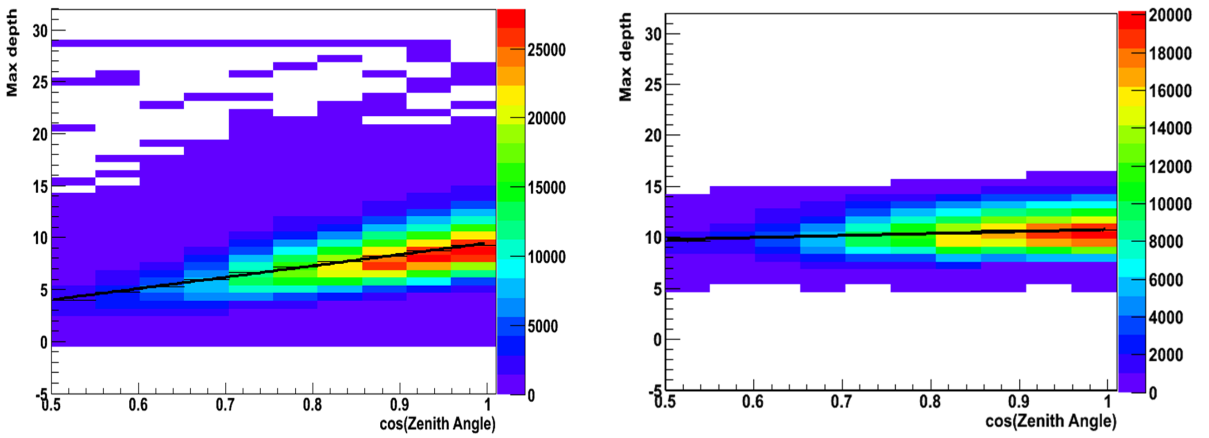

(a) Before correction

(b) After correction

Figure 5.2: MDH as function of the zenith angle, before (left) and after (right) corrections for simulated point-like photons. The black line corresponds to the fit of the profile of the histogram.

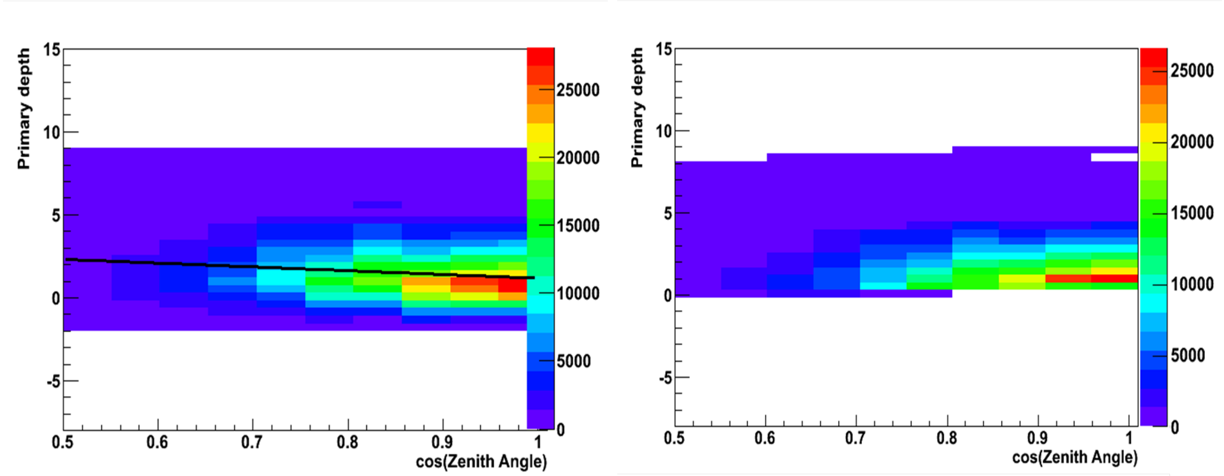

(a) Before correction

(b) After correction

Figure 5.3: PDH as function of the zenith angle, before (left) and after (right) corrections for simulated point-like photons. The black line corresponds to the fit of the profile of the histogram.

expected, this correction does not modify the distributions' widths per zenith angle. However, the global PDF distribution including all zenith angles is expected to be narrower, and after the correction, the distributions per zenithal angle seem to be superimposable, with their mean values coinciding, which was not the case before. It can be noticed that the RMS is seen to decrease when the zenith angle increases, which is explained by the fact that the energy threshold rises, so only primary particles with higher energies trigger. These, as explained in section 2.1.5.3, have a better resolution. As a consequence, the total RMS of this discriminant variable will be dominated by the energy threshold chosen for the analysis.

Concerning the optical efficiency, a dependence of the mean value and RMS of MDH is expected and can be observed. Indeed, for lower values of the optical efficiency, the energy threshold will be higher. The explanation of this is the same as for the zenith angle dependency, with the difference being that instead of photons being diluted and absorbed in the atmosphere, they arrive at the telescope but are not detected because of the lower efficiency of the optical system. Hence, only primary particles with higher energies will trigger the camera, and the energy, and thus angular, resolution will be improved (lower RMS values) for low optical efficiencies. The mean value of MDH will be affected by the induced energy evolution for it is directly dependent on this parameter (see section 1.2.2). However, the mean value of MDH scales with the logarithm of the energy E, so the effect is much less pronounced than for the RMS, which varies as $1/\sqrt{E}$.

The zenith angle correction was also applied on the data, but because of the special treatment needed to obtain the PDFs from the data, the approach for data is described later (see section 5.1.2).

5.1.1.2 Energy dependency correction

As mentioned in section 1.2, the maximum of the shower expansion evolves with the energy of the incoming particle. If plotted against the logarithm of the energy, the dependency is linear:

$$MDH = a_e \cdot (ln(y) + b_e) \tag{5.1}$$

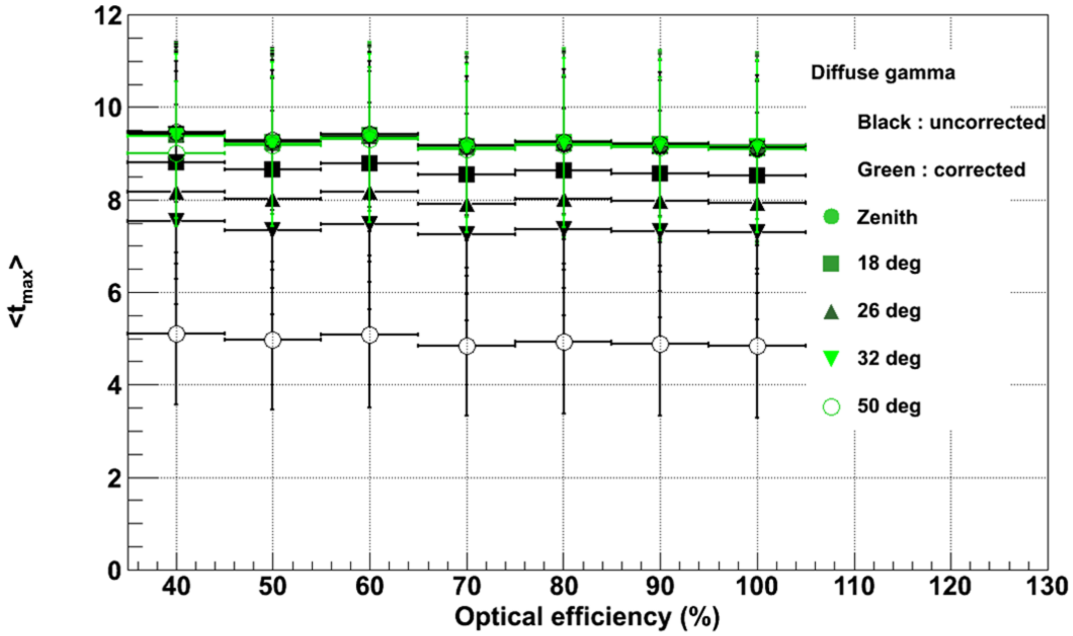

Figure 5.4: Effect of zenith correction on the mean value of MDH ($< t_{max} >$ in the figure) for simulated diffuse gamma and all optical efficiencies. Before correction (in black), the mean value of MDH is different for each zenith angle. After correction (in green) they are superimposed.

and the correction is:

$$MDH_{corr} = MDH - a_e \cdot ln(y) \tag{5.2}$$

with $y = E/E_c$ (E_c being the critical energy), so that only parameter a_e is needed. To obtain it, a 2D model is constructed using the function taken to represent the t_{max} distribution corrected from the zenith angle for each type of particle (see appendix B). The amplitude of the Gaussian will evolve as a function of the fitted energy spectrum and the relation 5.2 for the energy dependence. Its width will remain free in the fit. Each particle calls for its own fit and parameter a_e value. Furthermore, the fit was done for each zenith angle for which simulations existed as well as for all cumulated zenith angles. Parameter a_e will also depend on the chosen optical efficiency. Figure 5.6 summarizes the value of parameter a_e obtained for each zenith angle and optical efficiency for simulated point-like gamma. It can be observed that at low zenith angles the correction is very dependent on the optical efficiency. When the latter decreases, the energy threshold becomes higher and the a_e parameter increases. Thus the evolution of t_{max} as a function of the energy doesn't seem to follow the law 5.1. At high zenith angles, low energies are excluded and no variation is found with the optical efficiency, so the divergence from the formula 5.1 seems to appear for these. The plots for the other particles can be found in appendix C. In the case of gamma and electrons, each event was corrected with the value of parameter a_e found for the nearest zenith angle and optical efficiency of the simulations. Concerning protons, because of low statistics, to lower the error on the correction, the one for all cumulated zenith angle was used for all events regardless of their corresponding zenith angle.

In table 5.1 are shown the values of parameter a_e resulting from the fits of the distributions including all cumulated zenith angles, for all four types of particles. In figure 5.7 are the distri-

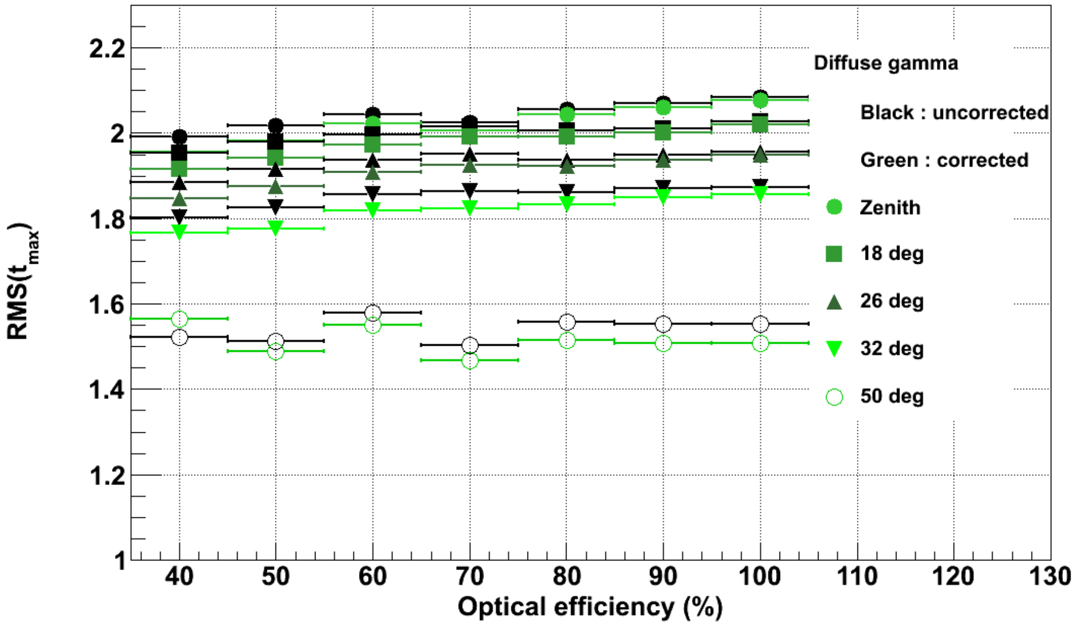

Figure 5.5: Effect of zenith correction on the rms of MDH ($RMS(t_{max})$ in the figure) for simulated diffuse gamma and all optical efficiencies. The correction does not seem to influence the width of the distribution. However, the evolution of the latter with the zenith angle will limit the effect of the correction. The narrower distributions, represented by a smaller rms for high zenith angles are explained by the fact that the energy threshold increases, so only showers with higher energies will trigger. These are known to have a better reconstruction and hence angular resolution.

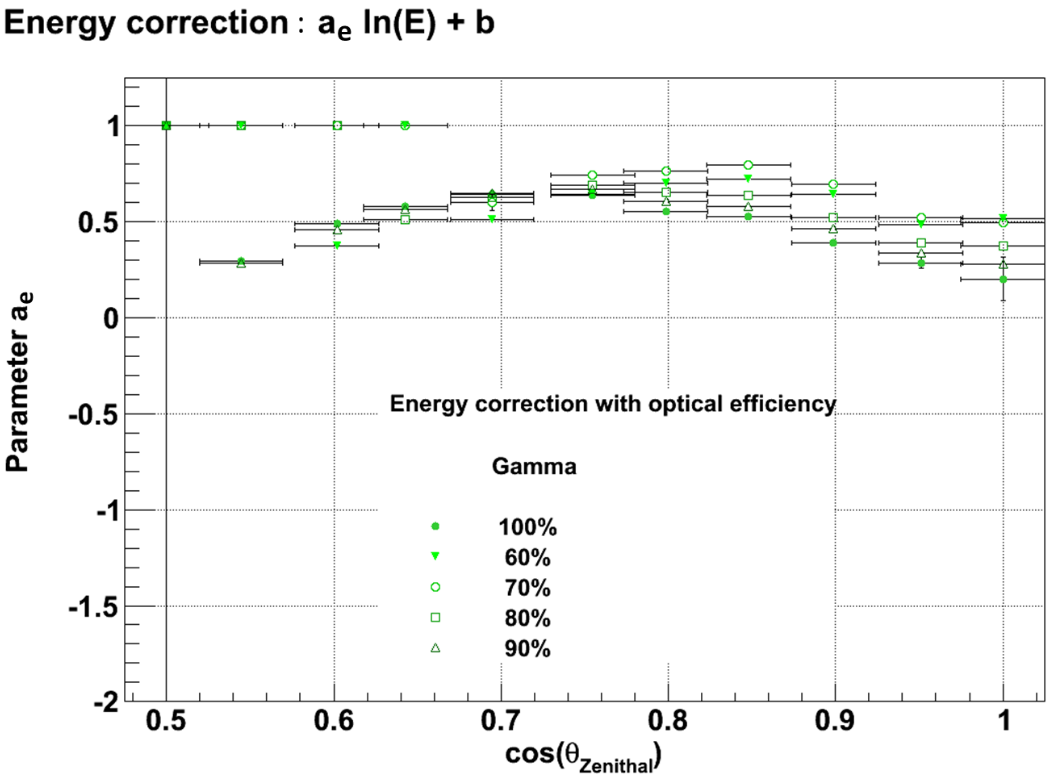

Figure 5.6: Parameter a_e for each optical efficiency and zenith angle for simulated point-like gamma. The values at 1 correspond to fits that did not converge. At high zenith angles, the optical efficiency doesn't influence the determination of the fit and t_{max} appears to follow the expected evolution as a function of the energy. However, when the zenith angle decreases, lower energies are included depending on the optical efficiency (which also influences the energy threshold) and a variation of the a_e parameter is seen. Thus, it seems that low energies introduce a divergence from the law 5.1.

butions of MDH as a function of the energy for simulated point-like photons, diffuse photons, electrons and protons. As an example, those with a zenith angle of 0° for point-like gamma and electrons are shown while for diffuse gamma and protons it is those with all cumulated zenith angles. The left plots correspond to the simulated data distributions before the energy correction. One can see that the distributions are narrower around an inclined slope, which reflects the logarithmic dependency. The model fitted on the simulations (middle plot), is also seen on figure 5.7, giving a value for parameter a_e. After its subtraction from the initial distribution, the residues are shown on the right plot. It can be seen that the region of the signal is well reproduced by the model. in its region there is no residue left, as can be seen in the right plot. After using parameter a_e to correct MDH, this discriminant variable becomes roughly independent of the energy.

	Diffuse γ	γ	Electrons	Protons
Zenith dependency parameter a_{zen}				
MDH	11.55±0.02	10.93±0.02	10.30±0.03	10.10±0.29
PDH	-1.15±0.02	-2.28±0.02	-1.68±0.02	-4.38±0.22
Energy dependency parameter a_e				
MDH	0.318 ± 0.004	0.391 ± 0.004	0.297 ± 0.003	-0.558 ± 0.038

Table 5.1: Zenith and energy dependency parameters values, a_{zen} and a_e respectively. obtained when fitting the distribution of MDH as a function of the energy, after applying the zenith angle correction of section 5.1.1.1. For point-like and diffuse gamma, as well as electrons, the shown value is at the zenith. For protons, it is the one obtained when taking all available statistics, cumulating the zenith angles. The latter is used for all proton events.

Figure 5.8 illustrates the successive effect of the zenith angle and the energy dependencies corrections on the distributions of the MDH variable for simulated diffuse photons and point-like photons (green), electrons (blue) and protons (red). These distributions become narrower after each correction, increasing the discriminant power of this variable. As for the zenith angle correction, the energy dependency needs also to be applied on the data, as explained in the next section.

The studies on the zenithal angle and energy corrections have been performed with the other variables without any significant effect observed. MSL and MSW are intrinsic properties of the shower and do not depend on its position in the sky, so no evolution with the zenith angle was expected. Neither was it predicted for MSG and PDH, which are obtained by fitting the shower with a model that already takes it into account, although a slight correlation was found and corrected in section 5.1.1.1. The MDH reconstruction on the other hand, is done with the Hillas method, which does not consider the distance traveled in the atmosphere depending on the line of sight. This creates the zenith angle dependencies. Concerning the energy correction, MSL, MSW and MSG, as seen in section 2.2.1.1, were built so as to be independent of the charge and thus, of the energy. Their study confirmed this. The first point of interaction in the atmosphere, PDH, depends on the conversion length for photons and radiation length for electrons (see section 1.2.2), which are more or less constant at the high energies considered (see section 1.2). So PDH should not vary with the energy, which was indeed observed. In the case of protons however, the cross-section characterizing the interaction length is still dependent on the energy in the H.E.S.S. energy domain. The fact that no evolution was noticed might be explained by the low statistics of the proton simulations.

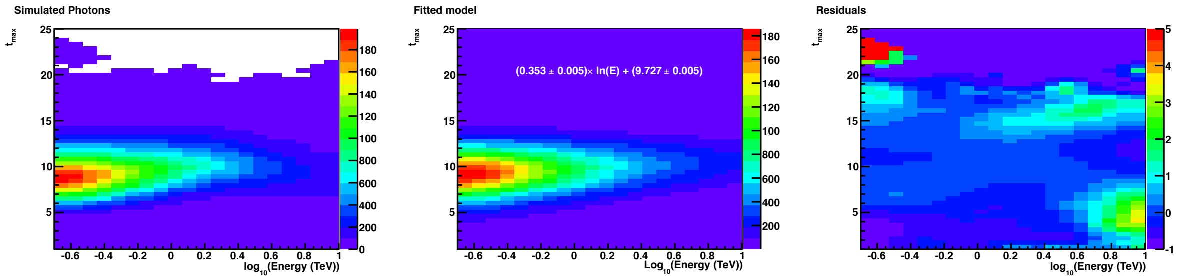

(a) Point-like gamma

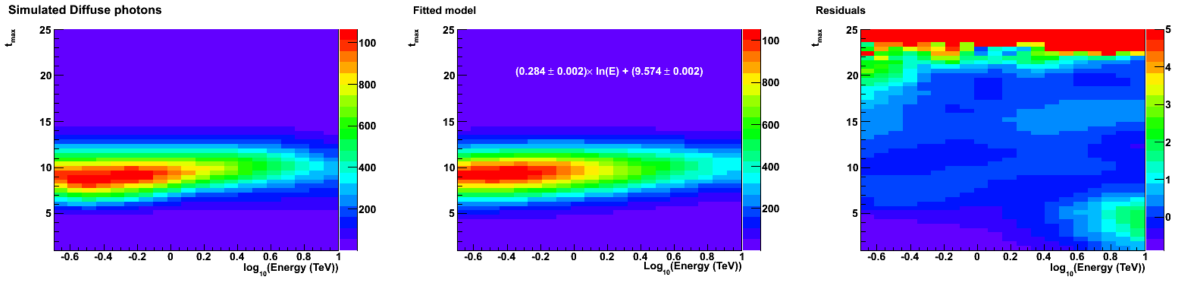

(b) Diffuse gamma

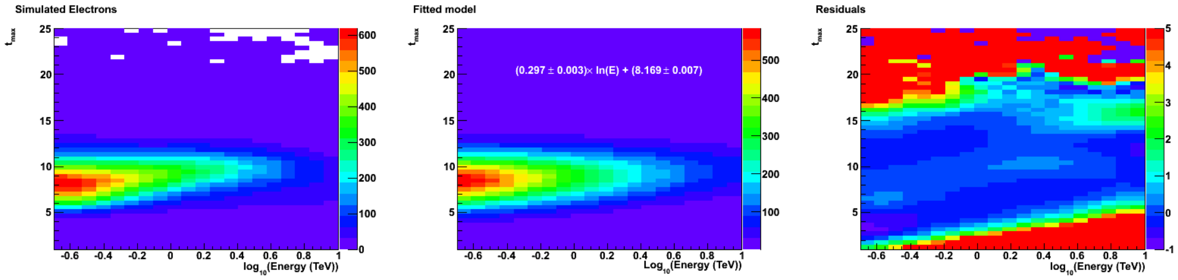

(c) Electrons

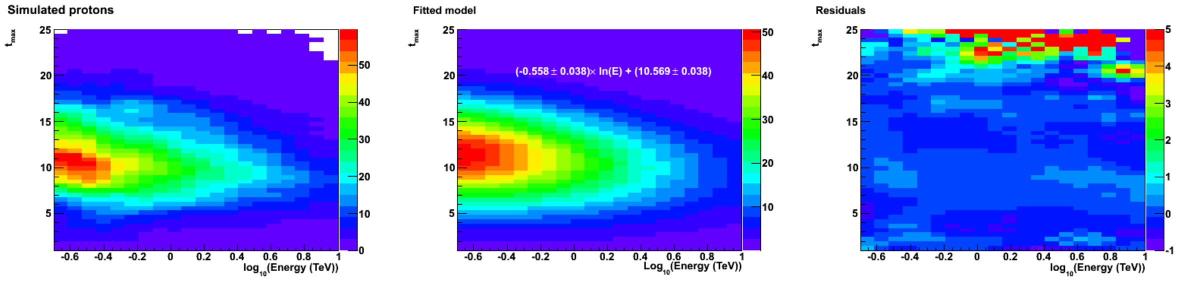

(d) Protons

Figure 5.7: Distributions of MDH as a function of the energy for simulated point-like photons, diffuse photons, electrons and protons. For point-like gamma and electrons, the distributions correspond to a zenith angle of 0°, whereas for diffuse gamma and protons, the shown plots were obtained for data including all zenith angles. On the left plots are distributions before the energy correction. The distributions are narrower around an inclined slope, which reflects the logarithmic dependency. The plot in the middle represent the model fitted on the simulations, which gives the value for parameter a_e. On the right plot is the residue after subtraction of the fitted model from the initial distribution. It can be seen that the model represent well the initial distributions, for in the area where there is data the residue is negligible.

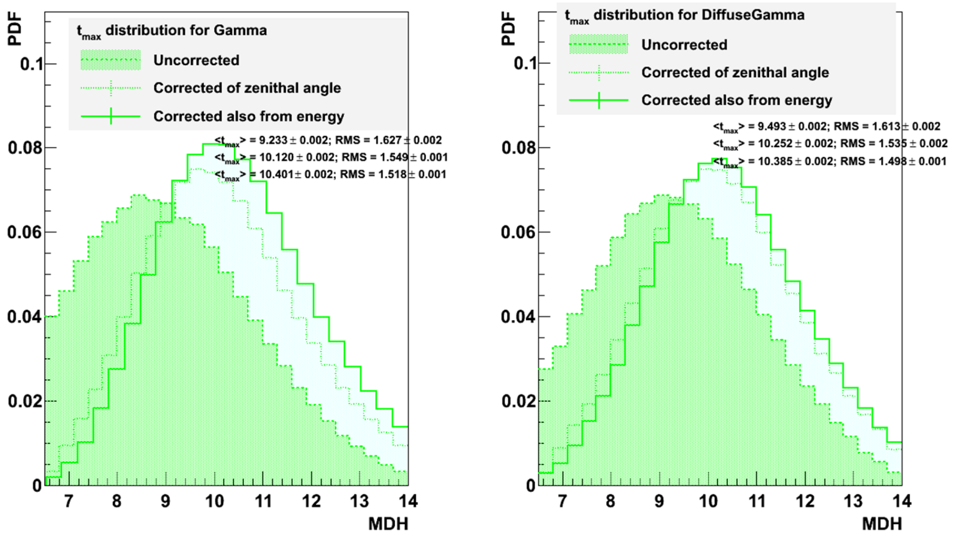

(a) Point-like gamma (b) Diffuse gamma

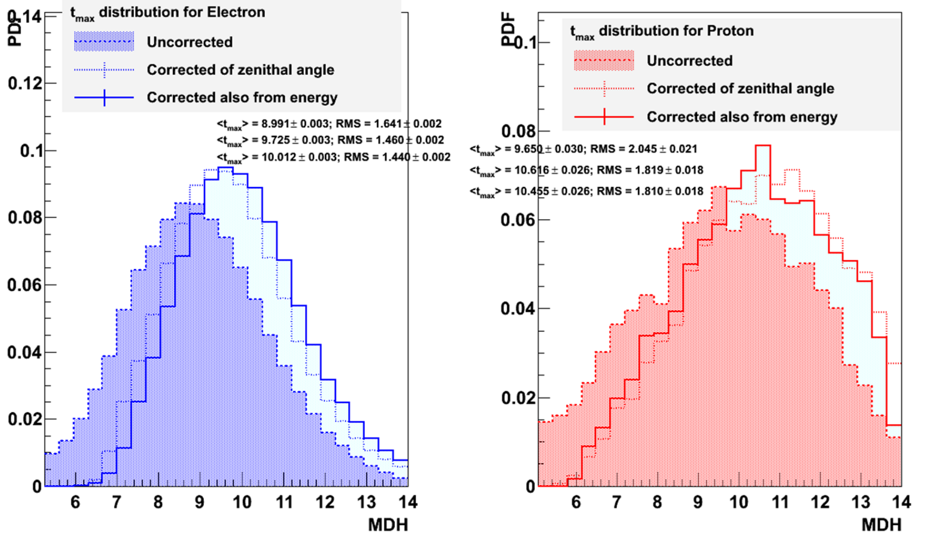

(c) Electrons (d) Protons

Figure 5.8: Effect of the zenith correction and of the subsequent energy correction on the MDH distribution, for simulated point-like photons, diffuse photons, electrons and protons (from left to right and top to bottom). these distributions were obtained when cumulating all zenith angles and energies. The displayed values for $< t_{max} >$ and RMS show the evolution of the mean value of the distribution and its width in RMS before and after each successive correction (from top to bottom). It can be observed that the distributions become narrower and thus more discriminative, which is th purpose of the corrections.

5.1.2 Matching data and simulations

Even if the simulations have been well corrected and their discriminative power improved, their potential for particle separation in the data depends on how well they represent it. This is dealt with in the next section, taking the data from the "Chandra flare" as a reference to compare the simulations to. Nonetheless, the discriminant variable's reconstruction in the data may change with the aging of the experimental system, so that it may not correspond to the data from the "Chandra flare" to which the simulations were matched. This aspect was investigated in the subsequent section.

5.1.2.1 Controlling the simulations with data samples

The problem arises as to which simulated particle's PDF distributions must be taken to represent the data. To overcome this, different regions can be defined in the sky map and cuts can be applied to obtain samples for each type of particle. To do this, the 14 runs from the "Chandra flare" were selected as explained in section 5.1.4. The sky map was divided into two regions: a source region inside 0.3 degrees and a background region outside 0.4 degrees. The named "CombinedCut2" variable defined as $CombinedCut2 = (MSG + \frac{MSL+MSW}{\sqrt{2}})/\sqrt{2}$ (see section 2.2.1.2) was used to purify the samples in each region.

In the source region (inside a 0.3 degree radius) during this flaring period there is a very important concentration of point-like gamma, found to be approximatively 68% with only around 32% of background events when integrating the convoluted PSF function and background level found in chapter 6. Hence, the distributions extracted from this data set show very clearly the PDF of point-like gamma, with a narrow peak, superimposed over the protons which create the widen asymmetric tail of the distribution in figure 5.9. An upper cut on the $CombinedCut2$ variable has the effect of purifying the data. For instance, an upper cut of 1 on this variable reduces the background events to 4%, so the distributions can be compared to those of simulated point-like γ with the same cuts.

In the outer region, protons are expected to be predominant, with 99.8% of hadrons (see section 4.3.2). However, in section 5.2.3 an estimation of the concentration of protons in this area is computed and found to be $(98.42 \pm 0.03)\%$. This small difference is due to the event selection of the stereoscopic trigger applied on data events, which enhances the electromagnetic contributions. During normal observations the central triggering lowers by a factor of about 3-4 the trigger rate of the experiment and this concerns mostly the hadron events. The PDFs extracted from this data set that excludes the source should be comparable to that of simulated protons. A lower cut of 3 applied on the $CombinedCut2$ variable eliminates gamma and electrons, further enriching the sample in protons. For electrons, it could be possible to increase their concentration by applying an upper cut on the $CombinedCut2$ variable in this region of the skymap. The proportion of electrons would then be significant (around 40% for an upper cut value of 1) and would offer the possibility to study the behavior of the discriminant variables of this population. In this work however, only the discriminant variables for point-like source gamma and diffuse protons were obtained from the data.

Before comparing the point-like gamma and proton PDFs with thus obtained "signal" and "background" PDFs, respectively, the latter had to be corrected in the same way the simulations were (see section 5.1.1). The zenith corrections (parameter a_{zen}) for the data in the two previously defined regions (right part of the plot) and the simulations (left part of the plot) can be found in figure 5.10. Two upper cuts on the $CombinedCut2$ variable (1 and 3) were tested on all particle simulations (in the case of protons, the name "protons<1" was used when upper cuts were applied) and the signal region. In the case of the background and simulated

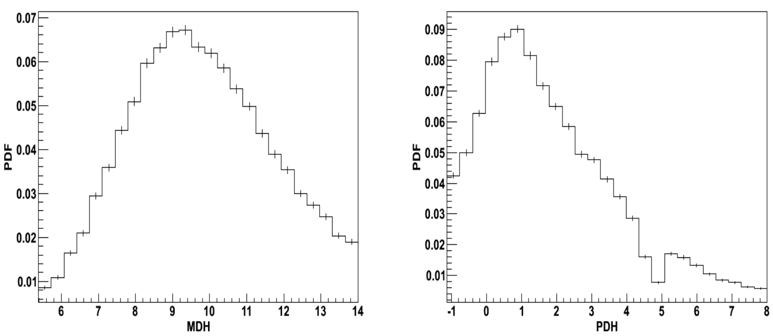

(a) MDH (b) PDH

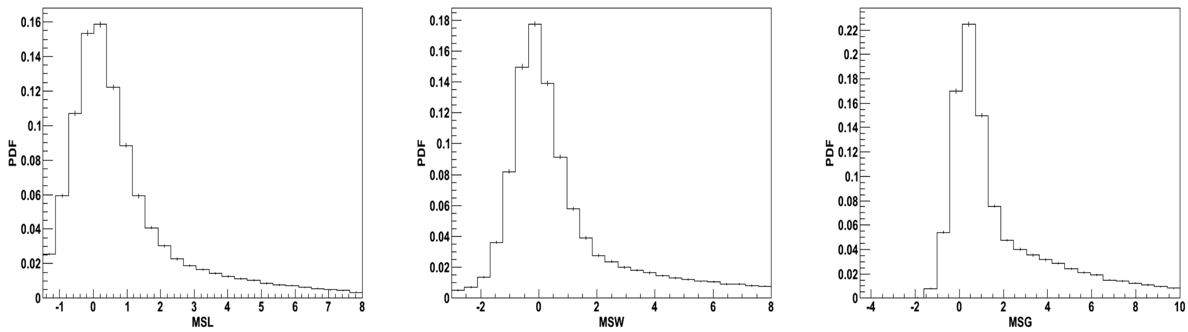

(c) MSL (d) MSW (e) MSG

Figure 5.9: Distributions extracted from the data set inside a 0.3 degree radius, without any cuts. The PDF of point-like gamma can be seen, with a narrow peak, superimposed over the protons which create the widen asymmetric tail of the distribution.

protons, a lower cut of 3 was applied. The values for the corrections obtained without any cut on *CombinedCut*2 (*CombinedCut*2=0 in the plot) were added.

The following observations can be made:

- When upper cuts are applied, a correspondence between the corrections for simulated point-like gamma and data inside the source region is clearly visible. This means that when the distributions are constructed from data believed to be constituted mainly of point-like gamma (because of the selected region and cut), they behave in the same way as point-like gamma simulations.

- Concerning again upper cuts, the looser the cut, the more background is included in the signal region and the correction gets closer to that of protons and background. The opposite is also true. With tighter cuts, the simulated protons' correction ("Protons<1") tend to resemble more the gamma's.

- As mentioned before, a lower cut of 3 on the *CombinedCut*2 variable will have the effect of enriching in protons. Hence, if applied in the outer region, data and simulated protons ("protons" in the figure) should be even more comparable. However, in the plots a small

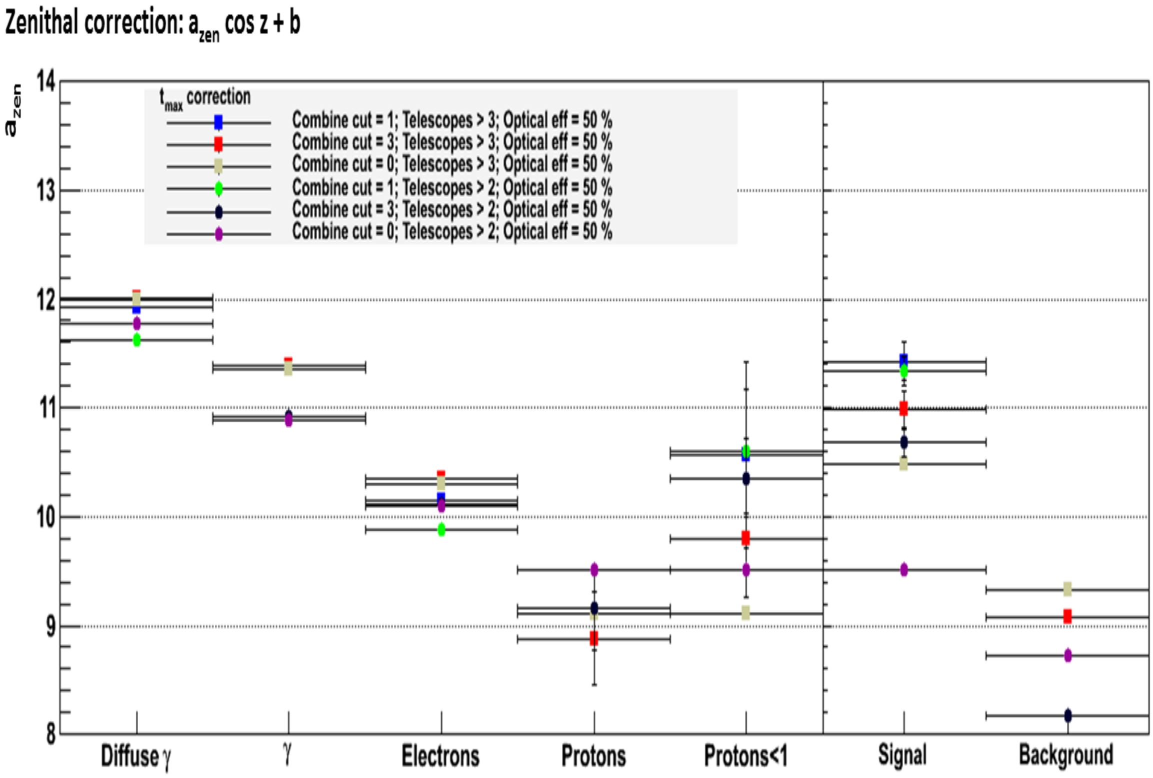

Figure 5.10: Zenith angle corrections for simulations (left) and data (right) with different cuts on the *CombinedCut*2 variable, written as *CombinedCut*2=1 and *CombinedCut*2=3. These are upper cuts in the case of diffuse gamma, gamma and electron simulations, and were also applied on proton simulations, grouped under "protons<1" and the signal region. Concerning proton simulations and the background region, *CombinedCut*2=3 corresponds to a lower cut. The value of the correction with no cut on *CombinedCut*2 (*CombinedCut*2=0) was also added. Simulations were taken for a 50% optical efficiency, which is the nearest to the computed efficiency in the data. Two telescope cuts were used for comparison. On the data inside the signal region, the looser the cut, the more background is included and the correction gets closer to that of protons and background. A hard cut will make the data dominated by point-like gamma, and the corrections between these simulations and the data in the signal region become comparable. Even the simulated protons' correction becomes closer to that of gamma.

> offset can be noticed, which could be explained by the presence of ions in the data which amount to about 14% (dominated by heliums). Because the nuclear cross section evolves as the mass of the nucleus, the mean value of MDH in the background region will decrease. This effect is also expected for the mean value of PDH.

After applying the zenith angle and energy corrections, it was noticed for each discriminant variable that the maximums of the two distributions, the one obtained from data in a specific region and the other from simulations, did not match, which is essential to be able to disentangle the particles in the data using the simulations. This was the case with or witout a cut on the $CombinedCut2$ variable. Hence, a shift had to be applied to adjust the distributions of the simulations. To estimate this, the maximum of the distributions had to be precisely determined.

As the zenith angle and energy corrections have an influence on the width of the distributions and thus in the obtaining of the maximum of the distribution, the values for the corrections to be used had to be carefully chosen. Because of the offset seen, with or without a cut on $CombinedCut2$, between the zenith correction of simulated protons and that of the purest sample of protons obtained in the background region, it was decided to use on each type of data its own result. Besides, in the distribution corrected in this way were narrower. The same was done for the energy correction. In the signal region however, the cut on the $CombinedCut2$ variable can greatly influence the zenith angle correction, which can be really different from the correction of point-like gamma. Nonetheless, as commented previously, when the data sample in the signal region is enriched with gamma, it gives the same result for the zenith correction as the simulated gamma. This observation led to testing the correction value obtained with the point-like gamma simulations on the data from the signal region, with no $CombinedCut2$ cut. The result was only the narrowing of the main peak of the distributions, which is supposed to correspond to the gamma. The effect was further enhanced after applying the energy correction of the simulated point-like gamma, hence allowing a direct comparison with the maximum of the simulated distribution.

To calculate the maximums, the integral of each histogram over a sliding window of three bins was maximized before taking the barycentre of the thus selected bins. In the case of MDH and PDH, because of the more uneven form of the PDF, the maximum of the fitted functions (appendices B and B) were taken. The gaps that were found for the five discriminant variables are summarized in table 5.2, corresponding to data minus simulations. These values were henceforth added to the simulations in order to make them match the data position. These differences in the mean values of the distributions can be explained as a consequence of the small initial shift in the first point of interaction (PDH) between data and simulations. This discrepancy can be caused by any imperfection in the modelization of the atmosphere, as PDH depends on the atmoshperic profile. If the interaction with the atmosphere starts a bit earlier, which seems to be the case of the data as compared to the simulations, because of the lower density the air shower will go deeper, its development will be slower and there will be less multiple scattering. Therefore, the maximum of the shower development will be further away from the first point of interaction in the case of the data. Because the variable MDH is reconstructed with respect to this first point of interaction, it will have higher values for data, as seen in the table. Furtermore, because MSL corresponds to the longitudinal profile of the air shower, it will increase for this longer air shower. Again, the larger MSL mean value for the data is seen in table 5.2. Finally, MSW depends directly on the multiple scatterings. A lower number of them will reduce the image's width, as is the case of the data' MSW as compared to simulations. The only variable for which the shift cannot be explained in this way is MSG, for it doesn't represent any physical quantity in the shower morphology, serving just as an indication of the quality of the adjustment providing the value of PDH, as described in section 2.2.1.2.

	MSL	MSW	MSG	MDH	PDH
Point-like gamma	0.19	-0.21	-0.89	0.28	-0.03
Protons	-0.01	-0.43	-0.76	0.17	-0.01

Table 5.2: Shift values (data - simulations) between point-like gamma and protons simulations and corresponding data for the five discriminant variables.

As the electron and diffuse gamma PDFs were also used in the comparison with the data explained in the next paragraph, these had to be corrected as well. After applying the zenith angle and energy corrections of the simulations, their shift had to be estimated. However, as no clean sample of them could be obtained from data, the shift for point-like gamma was used. This is justified by the fact that the electromagnetic showers' development only depends on the medium's properties, precisely its density ρ and atomic number Z (through the critical energy E_C and radiation length X_0 for electrons and cross section σ for conversion processes in the case of gamma, as seen in section 1.2). Hence all electromagnetic showers suffer the same effects and can be corrected with the same value. It can be noted that, the gap between gamma and electrons mentioned in section 1.2 is preserved after the shift.

After the described analysis of the behavior of the mean of discriminant variables and their consequent correction for a better match between data and simulations, their form can also be studied. In order to test the validity of the functions obtained from simulations, the ratios between them and those extracted from purified data samples were computed. In the region outside the source (radius higher than 0.4°), the simulated protons' PDF was easily tested because the lower cut of 3 on the CombineCut2 variable effectively eliminates all other particles. The superposition of the data with the histograms of the simulated PDF in this region is shown for the five discriminant variables in figure 5.11. Their ratio is in the bottom plots. Concerning the region inside a radius of 0.3° the same was done with an upper cut of 3 on the CombineCut2 variable. Moreover, in this region, the PDF of the different contributions, protons, electrons and point-like gamma were added in different proportions, estimated by taking the concentrations found in section 5.2.3 for each particle and evaluating the percentage of each which remains after applying the CombineCut2 cut. The PDFs can be seen in figure 5.12. Discrepancies between simulations and data can be observed, particularly in the distribution tails, where the ratio move away from unity. As a consequence, specific intervals will have to be selected for each discriminant variable. This data selection is treated in the discussion section 5.1.4.

5.1.2.2 Time dependency study

Because the study of the diffuse emissions requires the analysis of data taken over a large period of time, the issue of a possible evolution of the system and observing conditions affecting the distribution of the discriminant variables in the data over time was addressed. This time dependence should have been partially resolved with the zenith angle correction, which is one of the parameters that varies over time.

For the discussion hereafter the PDFs are obtained by excluding a region of 0.2° around the source's position in the data. Because this area corresponds mainly to extragalactic background, it is expected to remain stable over time and the same could be presumed for the PDFs. Any variations would be more likely related to the instrument and observing parameters. All 764

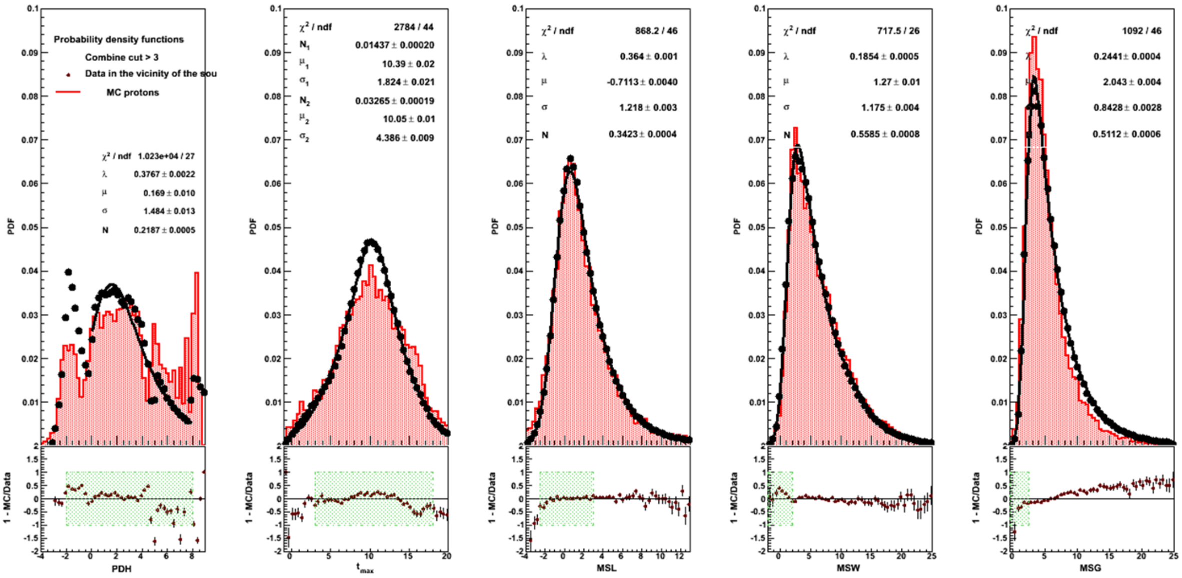

Figure 5.11: Histograms of the PDFs extracted from data outside the source in black dots and those computed with the simulations in red. The ratio between both is represented under each plot. The functions in black are the fit of the data but were not used for the analysis. A lower cut of 3 in the CombineCut2 variable was applied to further purify the sample in protons. The green boxes correspond to the interval in which the plots for the signal are represented in figure 5.12. Neither the intervals of these plots nor the ones for the signal regions represent the data selection. The latter is explained in section 5.1.4 and tries to take into account as best as possible the intervals in which the ratios of these histograms and those in the signal region are close to 1.

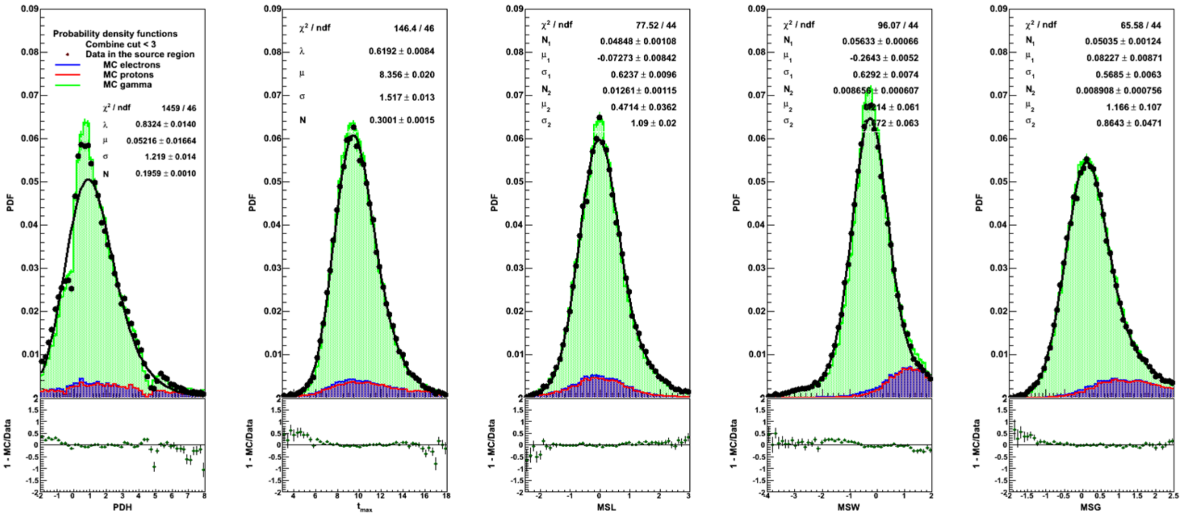

Figure 5.12: Histograms of the PDFs extracted from data inside a radius of 0.3° around the source in black dots and those computed with the simulations in green. The ratio between both PDFs is represented under each plot. In red are the protons and blue, these added to electrons. The functions in black are the fit of the data but were not used for the analysis. An upper cut of 3 in the CombineCut2 variable was applied to purify the sample in gamma and electrons. The intervals do not correspond to the data selection. See comment in figure 5.11 and section 5.1.4 for more on it.

runs of PKS 2155-304 cumulated over 10 years of observations were tested for time-dependency. Runs were removed when needed as explained next.

As seen in figures 5.13 and 5.14, the mean of the PDF distributions obtained per run (points in red) deviate for some runs from the mean of the distribution obtained for the reference period of the "Chandra flare" (green line). However, shifting the mean for each run to match the one of the "Chandra flare" was found to be counterproductive. This is due to the fact that the mean and the RMS are correlated, and a deviated mean can also represent a wider distribution, if it is asymmetrical. In figures 5.15 and 5.16, the top plots represent the discriminant variables distributions' mean value against RMS per run. The events are found to be concentrated around an average value for the mean and the RMS, for each discriminant variable. However, depending on the variable, some runs are found far from the concentrated regions, corresponding to distributions with mean and RMS values which are far from average.

Although all the runs used for these plots passed the run quality criteria, there was clearly a problem with the variables reconstruction and these very wide or narrow distributions typically can hinder the particle discrimination in the data. To get rid of them, the data points in the plot of the mean against the RMS for MDH were fitted with a 2D Gaussian function. All runs deviating more than 3σ from the maximum of the fit were excluded, as shown in figures 5.15 and 5.16, bottom plots, which corresponded to about 16% of the total. This run exclusion appears to eliminate abnormal distributions of other variables as well, as can be noticed from the impoverishment of the population outside of the main bulk, and is seen to effectively remove the runs for which the mean value deviated significantly from the "Chandra flare"'s. This run selection was applied whenever the complete statistics of PKS 2155-304 needed to be used, as

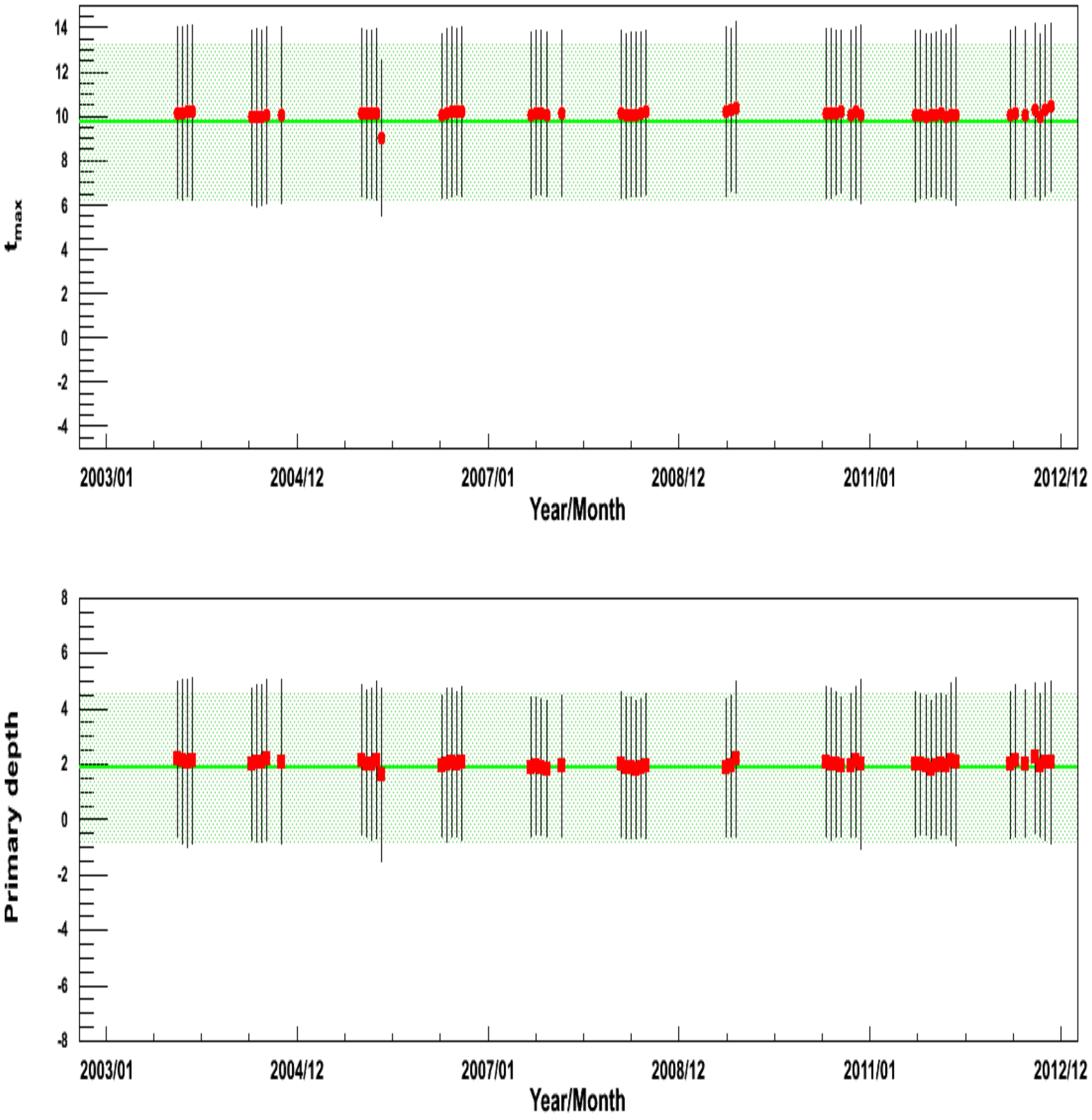

Figure 5.13: The evolution of the mean of the PDF distributions of the discriminant variables PDH and MDH obtained from the data in a radius of 0.2° around the center of the source PKS 2155-304 (in red squares), as a function of the run numbers. The distributions and means are computed per run. These mean values sometimes show a deviation from the mean of the distribution computed for all 14 runs of the "Chandra flare", represented by a green line. The green shaded area correspond to the width of this distribution.

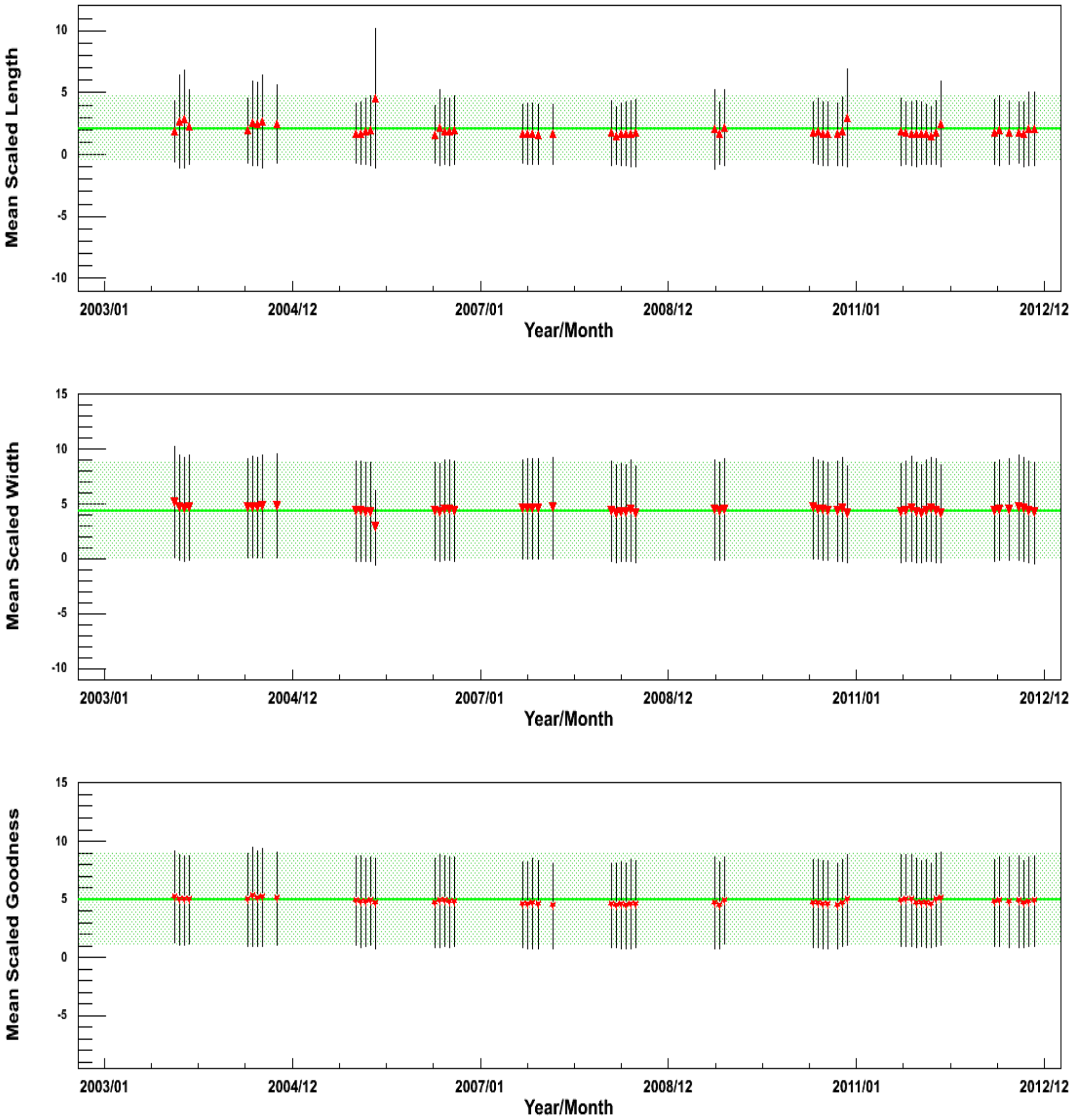

Figure 5.14: Time dependency of the discriminant variables MSL, MSW and MSG. See figure 5.13 for comments.

was the case for part of the analysis which is described in the rest of the chapter. No run of the "Chandra" flare was excluded, although two of them are at the limit of the fit.

Another possibility would have been to see how the runs with problems were distributed in time. If an annual modulation was observed for instance, it could indicate an influence of the observation conditions, like the weather affecting the conductivity of the atmosphere. Another option would be to see if these runs are concentrated at the beginning of the night, when the camera is not yet warm, affecting the data acquisition. Finally, the multiplicity (number of telescopes used for reconstruction) could also have been investigated. Hence, further studies are needed. In the meantime, the problematic runs' exclusion in the analysis does not penalize it, because PKS 2155-304 has been extensively observed and the are more than enough statistics for this source.

5.1.3 Correlations

A last aspect that was studied using the simulations was the correlation between the different discriminant variables. For instance, a correlation is known to exist between PDH and MSL, MSW and MDH. Indeed, the first point of interaction in the atmosphere will influence the shower development and thus the position of the shower maximum MDH, as commented in section 1.2.2, the MSW and MSL of the shower image in the camera, as mentioned in section 5.1.2.1. This can be seen in tables 5.3, where the correlation factors for diffuse gamma and protons, using 2 telescopes for reconstruction, are presented. Seeing the discussed effect on the MSW variable of a slight difference in PDH (section 1.2.2), a stronger correlation between these was intially expected. However, because the shifts were calculated using both simulations and data, other effects besides the correlation between these two variables could be involved, depending on how well the simulations reproduce the data. Moreover, as mentioned in section 2.2.1.3, a strong correlation appears between MSL and MSW for protons, as well as MSG, because these parameters are hard to determine in hadronic showers images, as they were specifically designed for gamma, and in fact allow the discrimination between electromagnetic and hadronic showers. Finally, a slightly higher correlation between MSL and MDH and PDH for electromagnetic particles is noticed, which is not visible for protons.

	Photons				
	MSL	MSW	MSG	MDH	PDH
MSL	1	0.06	0.09	0.20	0.30
MSW		1	0.04	0.14	0.07
MSG			1	-0.04	0.03
MDH				1	0.34
PDH				1	

	Protons				
	MSL	MSW	MSG	MDH	PDH
MSL	1	0.37	0.38	-0.11	0.18
MSW		1	0.50	0.03	0.08
MSG			1	-0.02	0.15
MDH				1	0.42
PDH					1

Table 5.3: Correlation factors for diffuse gamma and protons.

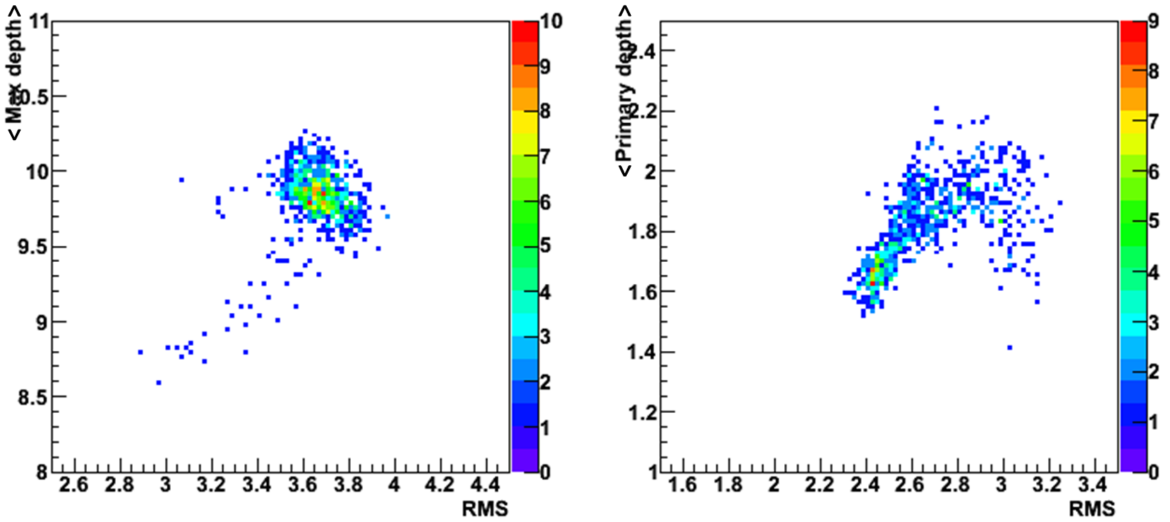

(a) MDH and PDH

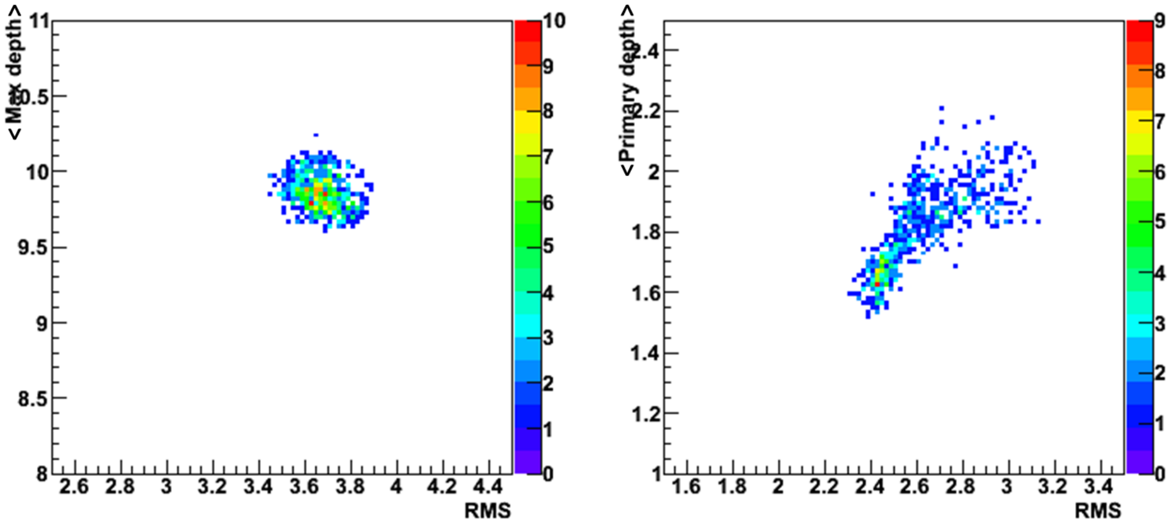

(b) MDH and PDH after a run selection

Figure 5.15: The mean values of the distributions of MDH and PDH obtained per run are plotted against their RMS. Most points are found within a region around an average mean and rms. The points extending far from the main grouping correspond to distributions with different widths and means, which could affect the particle discrimination. Thus a cut was applied on the runs with non-standard discriminant variables distributions, as defined by a 3σ radius from the center of the accumulation of runs in the Mean vs RMS plot for MDH when fitted by a 2D Gaussian function. The influence on the other variables can be observed as an impoverishment of the distribution tails.

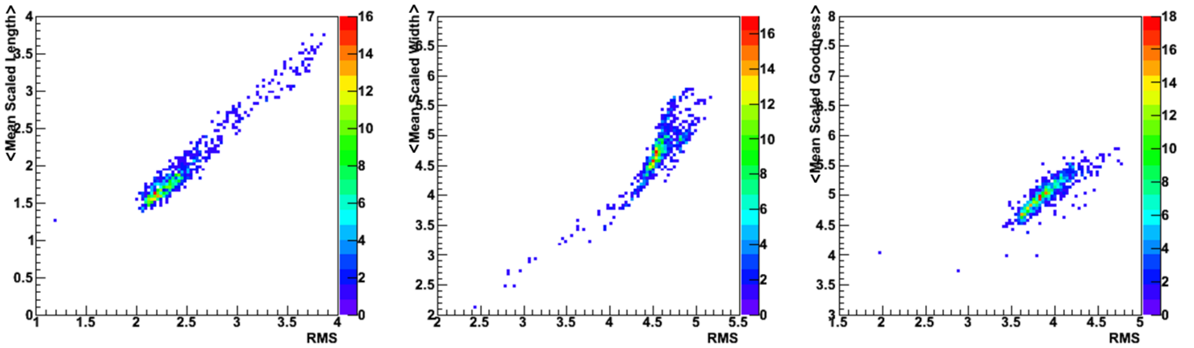

(a) MSL, MSW and MSG

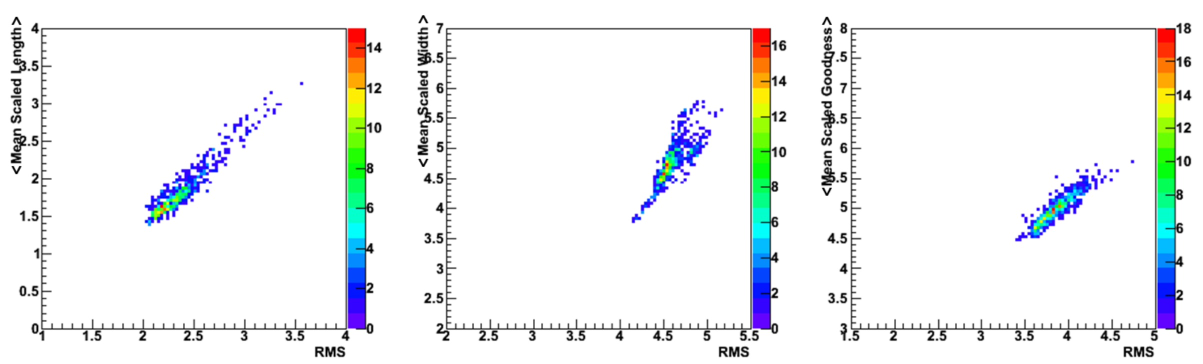

(b) MSL, MSW and MSG after a run selection

Figure 5.16: See figure 5.15 for comments.

The correlation plots for the discriminant variables of simulated point-like photons, reconstructed with 2 and 3 telescopes, can be seen in figures 5.17 and 5.18 respectively. The strong correlation between PDH and MDH is clearly visible in the bottom right plot. It can be noted that the intervals displayed do not correspond to the data selection and that X and Y axis don't have the same scale. The effect of a bad reconstruction appears in the upper left plot, which disappears when taking 3 telescopes in coincidence for the reconstruction. The plots for the other particles are in appendix D.

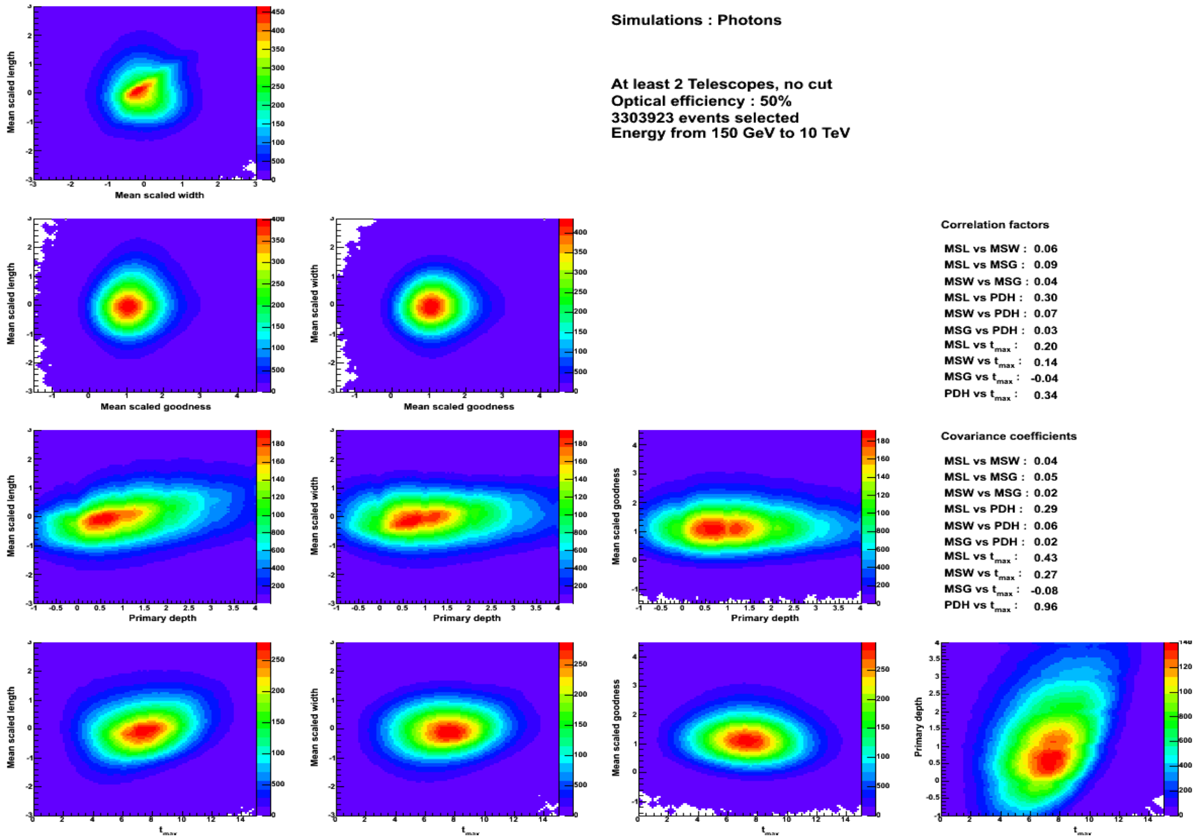

Simulations : Photons

At least 2 Telescopes, no cut
Optical efficiency : 50%
3303923 events selected
Energy from 150 GeV to 10 TeV

Correlation factors

MSL vs MSW : 0.06
MSL vs MSG : 0.09
MSW vs MSG : 0.04
MSL vs PDH : 0.30
MSW vs PDH : 0.07
MSG vs PDH : 0.03
MSL vs t_{max} : 0.20
MSW vs t_{max} : 0.14
MSG vs t_{max} : -0.04
PDH vs t_{max} : 0.34

Covariance coefficients

MSL vs MSW : 0.04
MSL vs MSG : 0.05
MSW vs MSG : 0.02
MSL vs PDH : 0.29
MSW vs PDH : 0.06
MSG vs PDH : 0.02
MSL vs t_{max} : 0.43
MSW vs t_{max} : 0.27
MSG vs t_{max} : -0.08
PDH vs t_{max} : 0.96

Figure 5.17: Correlation plots between the discriminant variables for point-like gamma. From left to right: MSL, MSW, MSG and PDH on the Y axis. From top to bottom: MSW, MSG, PDH and MDH on the X axis. The strong correlation between MDH and PDH can be observed in the bottom right plot. The eliminated values of PDH can also be seen. Moreover, in the correlation plot of MSL against MSW, the effect of a bad reconstruction can be noticed as a small correlation. This disappears when including 3 telescopes for the reconstruction, as in figure 5.18.

The observed correlation between MDH and PDH reduces their discriminant power. Another possibility, which was not explored in this work, would have been to use a linear combination of these variables as discriminant variable.

5.1.4 Discussion

To have the best match between simulations and data and exclude the regions in which discrepancies are observed, corresponding to the distribution tails as mentioned in section 5.1.2.1, the intervals in which the discriminant variables were used were adjusted. In the case of MDH

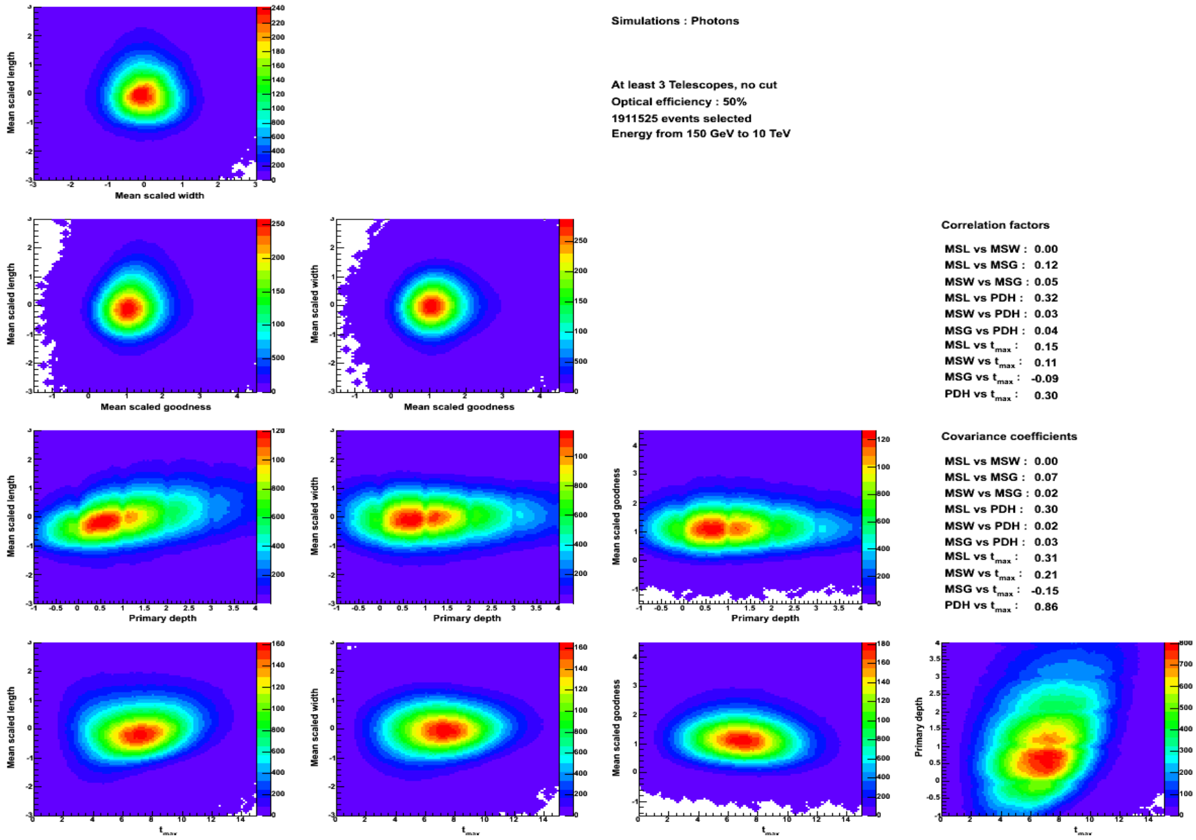

Figure 5.18: Correlations between the different discriminant variables for point-like gamma, using 3 telescopes for reconstruction. See figure 5.17 for comments.

and PDH, because the zenith angle and energy corrections are different for each type of particle, the intervals have to be adapted for each particle. However, this represents and issue when applying the selection on observational data. Indeed, as the type of particle is not known, it is not clear the correction for which particle has to be used. Two choices arise: either the correction and selection for all types of particles are applied to each event, or the correction for one type of particle is selected and applied for observational and simulated data alike, no matter the particle in the case of simulations. So as not to eliminate too much statistics, the data selection for all events was performed with the diffuse gamma zenith and energy corrections. The chosen cuts are shown in table 5.4. Another issue were the peaks that can be seen at integer values for PDH. These correspond to fits that did not converge well in the reconstruction, and should therefore not be taken into account. Thus, the most significant ones in the diffuse gamma interval used for data selection, at 5 and 8, were discarded.

Moreover, the PDF' shape could change depending on the energy domain. This was tested on two energy intervals: 150 GeV - 10 TeV and 300 GeV - 3 TeV. In figure 5.19 can be seen the PDFs for the five discriminant variables of diffuse gamma and protons, for both energy domains. Their ratio can be seen in the bottom plots. The interval selection also takes into account the compatibility between the PDFs obtained in different energy intervals. This way, the PDFs can be used in any interval between the two mentioned ones. The chosen energy domain for the analysis was 0.2 - 10 TeV. The figures for the other two types of particles are in appendix E.

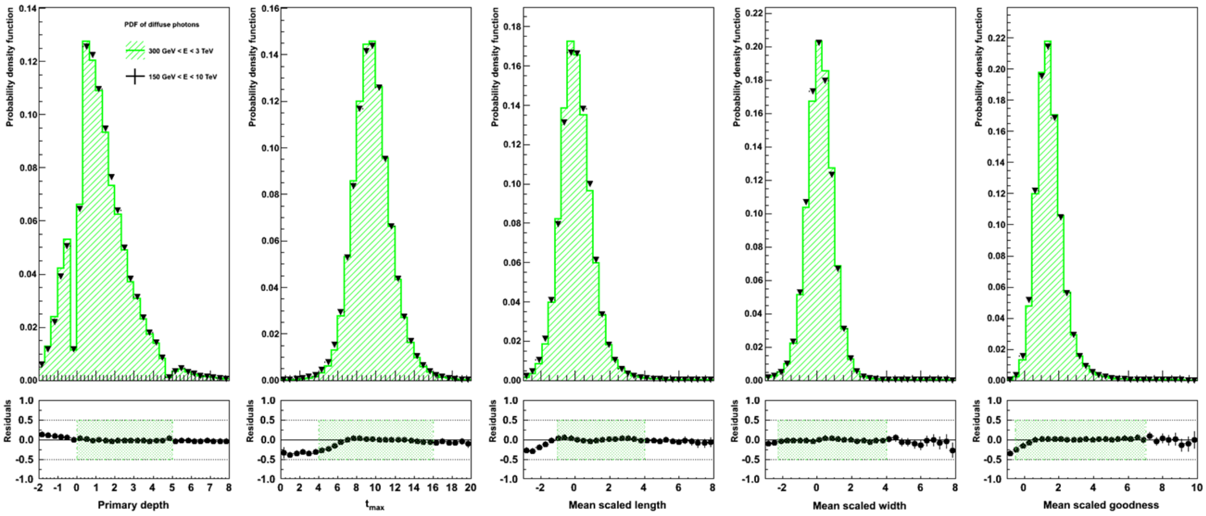

(a) PDFs for diffuse gamma in different energy domains

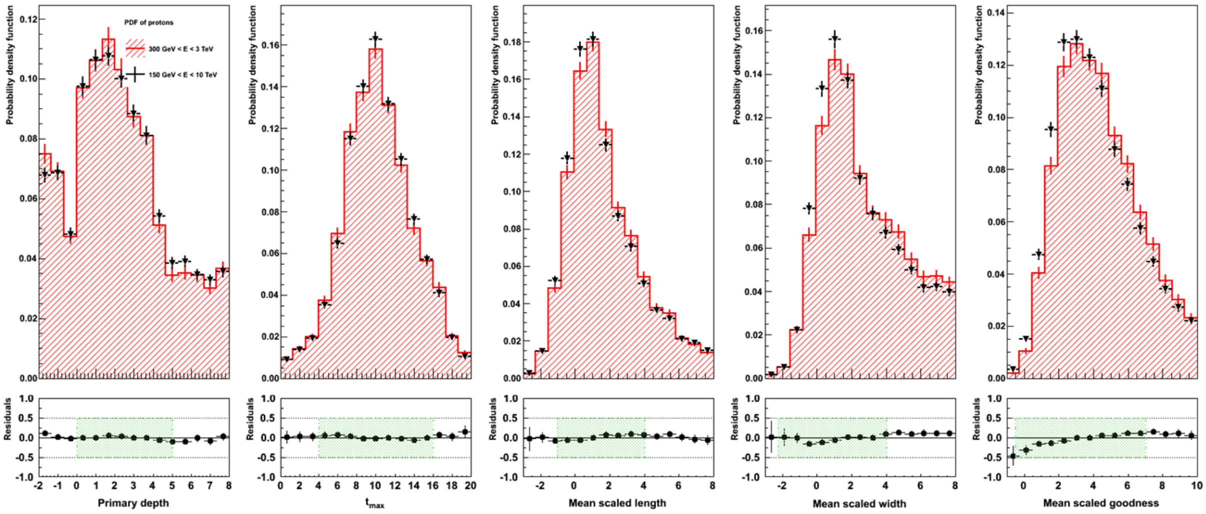

(b) PDFs for protons in different energy domains

Figure 5.19: PDFs obtained in two different energy domains: 150 GeV - 10 TeV and 300 GeV - 3 TeV for all types of particles. The bottom plots represent the ratios between the PDFs obtained for the two energy domains. The interval selection for each variable takes into account the compatibility of the PDFs obtained for different energy domains. In this way, they can be used in any energy interval included between the two mentioned intervals.

	Minimum	Maximum
MDH	6.5	14.0
PDH	0.5	10.0
MSL	-1.5	8.0
MSW	-3.0	8.0
MSG	-2.0	10.0
Energy (TeV)	0.2	10.0

Table 5.4: Intervals used for the data selection. For MDH and PDH the zenith (and energy concerning MDH) corrections applied for the cut are the ones obtained for the diffuse gamma.

Finally, a minimum of 2 telescopes in coincidence were asked for the reconstruction and events with an off-axis angle of more than 2°, very close to the camera borders, were eliminated, to ensure a better reconstruction of the events.

The intervals in which the PDFs were used in the analysis, specifically for fits and data/simulation comparisons, had to be adjusted for MDH and PDH. Indeed, as explained, these two discriminant variables need corrections and those of the diffuse gamma were used for the data selection. For both PDH and MDH, the diffuse gamma's corresponds to the biggest correction. Hence, if any other particle is first cut with this correction but then its own correction is applied for the analysis, the lower limit must be adapted in the analysis, in this case lowered, in order to keep all events that passed the selection criteria. So point-like gamma, electrons and protons have different lower limits, for MDH and PDH. For a lower limit PDF_{min}, the adapted one will be $PDF_{min} + a_{zen}^{i=e,p,\gamma} - a_{zen}^{diffuse\gamma}$. The values are given in table 5.5. Concerning the energy correction for MDH, the effect of applying the diffuse gamma correction for the selection and then the own particle's correction was tested on simulations. The result was that, if keeping the limits computed for the zenith angle correction, no events were lost for electrons, while only 0.1% of point-like gamma and 1% of protons were lost. Hence, the limits were not further adapted for the energy correction of each type of particle. Because MSL, MSW and MSG have no corrections, the same intervals used for the cuts were kept. This is also the case of the upper limit of MDH and PDH, that was not concerned by the adjustment.

	Minimum				Maximum
	Diffuse γ	γ	Electrons	Protons	All particles
MDH	6.5	5.88	5.25	5.05	14.0
PDH	0.5	-0.63	-0.03	-2.73	10.0
MSL	-1.5				8.0
MSW	-3.0				8.0
MSG	-2.0				10.0

Table 5.5: Intervals used for the analysis for each type of particle. Because of the correction applied on MDH and PDH for the data selection, the minimum had to be adjusted for each type of particle.

5.2 Disentangling the components of the background signal

Once the corrections have been applied to the studied variables and simulations have been made to match the data, the next step is to use them to construct PDFs in a way that allows particle discrimination. Their discriminative power is then validated with a Toy Monte Carlo. Finally, a concentration of each contribution to the diffuse background signal can be put forward.

5.2.1 Building the probability density functions

The construction of the probability density functions that will allow particle discrimination is based on the five discriminant variables described and studied in section 5.1. The three mean scaled length, width and goodness related to the characteristics of the shape of the shower development are efficient enough to distinguish the hadron shower component from electromagnetic showers. But these variables do not separate the electrons from diffuse gamma particles. This situation can be seen on the figures 5.20, where are drawn the normalized probability density functions of these discriminant variables obtained for simulated protons in red, electrons in blue and diffuse photons in green. Hereafter in this section, when talking about gamma distributions, diffuse gamma will be implied. The point-like gamma's PDFs are so similar to the diffuse ones that the same conclusions can be drawn for diffuse and point-like gamma. However, this also entails that no differentiation between the two types of gamma can be made with PDFs.

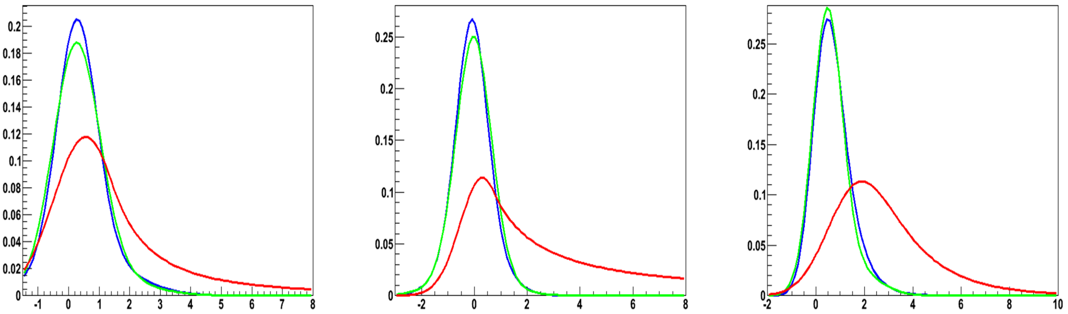

(a) MSL (b) MSW (c) MSG

Figure 5.20: Above plots represent the PDF functions adjusted on simulated data for mean scaled length (left), mean scaled width (middle) and mean scaled goodness (right) discriminant variables. Protons are in red, electrons in blue are superimposed on the photons in green which can be difficultly distinguished. The functions used for the fit are given in appendix B.

Electrons and diffuse gamma are difficult to distinguish as their distributions are more or less superimposed in these histograms.

The reconstructed positions of the maximum of the shower expansion (MDH) and the estimated first interaction point (PDH) of the particle in the atmosphere provide additional information to improve the hadron discrimination and to start to disentangle gamma and electron contributions. As mentioned in sections 1.2 and 5.1, for electrons and gamma, the values of MDH (t_{max}) differ in average by at most one radiation length and those of PDH by around ∼22%. This can be seen in figure 5.21, which represents the fitted distributions of the normalized probability density function of these two variables for simulated samples of protons (red), electrons (bleu) and diffuse photons (green).

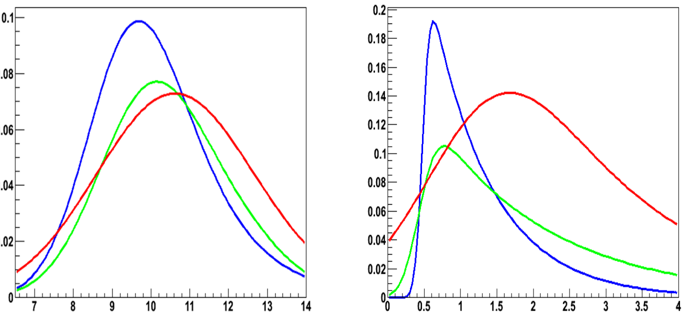

(a) MDH

(b) PDH

Figure 5.21: Plots represent the PDF functions adjusted on simulated data for the depth of the maximum of the shower expansion (left) and primary interaction position (right) discriminant variables. Protons are in red, electrons in blue and photons in green. The functions used for the fit are given in appendix B. As the three types of particles have different intervals for these two variables (see section 5.1.4), the smallest intervals were chosen for the representation.

The values of PDH and MDH for simulated diffuse gamma and electrons were found to be of the same order of magnitude as the ones presented in section 1.2.2. The reconstructed values of 9.683 ± 0.008 and 10.002 ± 0.005 for the t_{max} parameters (corresponding to the MDH observable) in case of electrons and gamma respectively are in relatively good agreement with the expected order of magnitude, discussed in section 1.2.2.

If these five variables were to be combined in a unique estimator, then the three first ones would dominate and impoverish the discrimination between electrons and gamma. An alternative to this is to separate the initial sample into two subsamples of more or less comparable statistics and elaborate two PDFs. Several functions and discriminant variables combinations were tested for these PDFs. Presented next is the one that seemed to improve the discrimination efficiency for the purpose of this work (other possible combinations have been studied in the past).

The first function that was defined, including the three variables discriminating the shapes of the showers in the camera, allows distinguishing the hadron from the electromagnetic component. This function is a simple product of the probability functions of these three variables:

$$\begin{aligned} f_{i=h,EM} &= f_i(MSL) \cdot f_i(MSW) \cdot f_i(MSG) \\ f(D) &= \eta_h f_h + (1-\eta_h) f_{EM} \\ 1 &= \eta_h + \eta_{EM} \end{aligned}$$

with η_{EM} being the sum of the gamma and electron concentrations.

A second probability density function is constructed with the two variables describing the reconstruction of the shape of the showers in the atmosphere. It will be used to separate hadrons but also the two electromagnetic contributions. It is also elaborated from a simple product of the probability function of these two discriminant variables:

$$
\begin{aligned}
f'_{i=e,\gamma,h} &= f_i(MDH) \cdot f_i(PDH) \\
f'(D) &= \eta_h f'_h + \eta_e f'_e + (1 - \eta_h - \eta_e) f'_\gamma \\
1 &= \eta_h + \eta_e + \eta_\gamma
\end{aligned}
$$

Then, a combined simultaneous adjustment of these two PDFs can be performed on the two selected subsamples, using an unbinned extended likelihood method. This is done by minimizing the following expression:

$$
-NLL = \sum_{i=1,N_A} -log(f_A(D^i_A)) + \sum_{i=1,N_B} -log(f'_B(D^i_B)) + \sum_{k=A,B} (N^{exp}_k - N_k log(N^{exp}_k))
$$

where $N_k = N_A$ or N_B and the N^{exp}_k are free parameters in the fit. They are random variables that follow a Poisson distribution, with $< N^{exp}_k >= N_k$. The other three free parameters of the fit are the fractions of the three components (η_i). Are assumed the normalization condition between them, $1 = \eta_e + \eta_\gamma + \eta_h$ and the constraint between the fraction of electrons and gamma and the fraction of the electromagnetic component $\eta_{EM} = \eta_e + \eta_\gamma$.

5.2.2 Testing the particle discrimination: Estimation of populations from toy Monte Carlo

After building the PDFs that would allow us to discern the different particles, it is necesarry to test their discriminative power. This was done on a set of simulated data. Looking at the relation between the three fractions ($\eta_e + \eta_\gamma + \eta_p = 1$), the uncertainty on each fraction will be dominated by the one of the largest component present in the data sample. So, assuming Gaussian errors, to be sensitive to a population of less than a thousandth of the largest sample, as expected for the diffuse gamma contribution according to what was seen in section 4.3.2, it is necessary to involve more than a million events. Applying the method to simulated data generated by toy Monte Carlo, the initial configuration injected in the sample was recovered. Initially set to $(\eta_\gamma; \eta_e; \eta_p) = (0.2; 20.0; 79.8)\%$, the final values using a sample of 5 000 000 simulated events for these three fractions are the following:

$$
\begin{aligned}
\eta_\gamma &= (0.174 \pm 0.060)\% \\
\eta_e &= (17.97 \pm 0.061)\% \\
\eta_p &= (79.831 \pm 0.044)\%
\end{aligned}
$$

The fitted parameters have been found to be close to the initial values. The correlation matrix and the covariance coefficients between the three fractions are shown in figure 5.22, from left to right respectively. As expected, a clear anti-correlation between η_e and η_γ (middle histogram) is visible but a looser correlation with the proton fraction is also seen. This is mainly due to the large sample of this last component and the more difficult discrimination between electrons and gamma.

The convergence of the fitting procedure was tested by verifying the evolution of the maximum of likelihood value brought arbitrarily to zero for the three fractions around the best estimated value, on the one hand (in blue, figure 5.23), and on the other by checking the profile

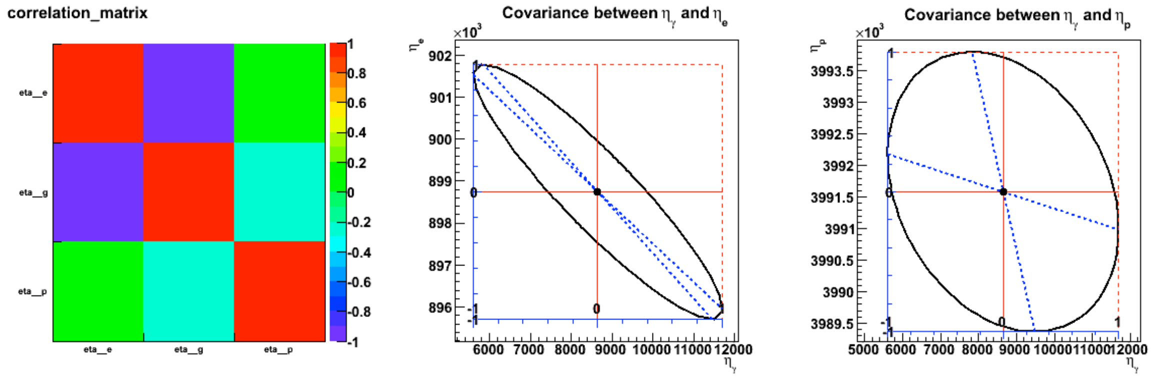

Figure 5.22: Representation of the correlation between the three free parameters of the fit (left plot). Covariance ellipses between electron and gamma fractions (center) and gamma and hadrons (right).

likelihood corresponding to the evolution of this estimator if we scan one parameter and let the other ones free to vary around the best estimation (in red, figure 5.23). From this last distribution, the correlation between the fraction of electrons and gamma can be seen but the hadron sample estimation seems to converge the same way no matter what is done to the other two fractions. This confirms the loose correlation of the hadrons with respect to the other components, as seen in figures 5.22.

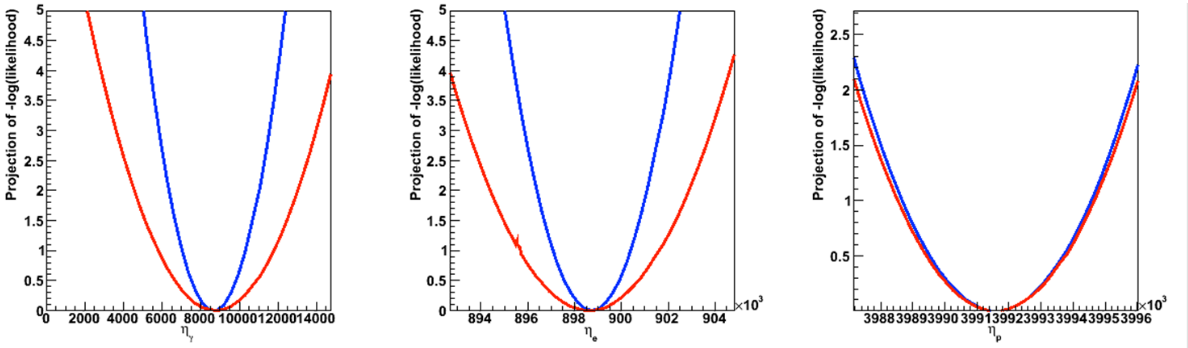

Figure 5.23: Evolution of the maximum likelihood value for the three fractions around the best-estimated value (in blue) and the profile likelihood (in red) if one parameter (fraction) is scanned and the others are free to vary around the best estimate value.

5.2.3 Estimating the populations in the region of PKS 2155-304

Due to the lack of statistics during the "Chandra flare", the number of diffuse gamma is expected to be too small to contribute to the η adjustments. To extract a diffuse gamma component from the data, it is necessary to analyze a bigger sample of background events, as mentioned in section 5.2.2. For this study, a signal region of PKS 2155-304 of the size of 0.4° around the nominal position of the source was excluded. Using all the statistics accumulated during the ten years of data taking of the HESS experiment, with a total of about 54 millions events recorded, 19 million passed the mentioned event and run selection criteria. Fitting these statistics, the following concentrations were found:

$$\begin{aligned}
&\eta_\gamma < 6.8 \cdot 10^{-4} \qquad 95\% CL \\
&\eta_e = (1.58 \pm 0.01)\% \\
&\eta_p = (98.42 \pm 0.03)\%
\end{aligned}$$

It is observed that the obtained concentration of protons in the diffuse emissions is lower than the one expected (see section 4.3.2). This is explained by the fact that the experiment is optimized for gamma detection, so many proton events are eliminated due to the trigger's background rejection.

5.3 Estimating the flux of the diffuse gamma emissions

Once the concentrations of each type of particle have been acquired and given their acceptance, it is possible to put forward a preliminary result on the flux of these diffuse emissions. The published diffuse emission results presented in section 4.3.2 were needed to do so, as explained next.

To calculate the flux, the concentrations of each type of particle found in section 5.2.3 for 19 million events that passed the event selection criteria were taken. Concerning the gamma, two hypotheses had to be stated: that at these energies and at such a high galactic latitude, the extragalactic component dominates over the galactic one and all others, and that this emission is stable over the FERMI-HESS energy range. Hence, the index 2.41 ± 0.05 given by the FERMI collaboration for the extragalactic diffuse gamma-ray contribution at lower energies than HESS was used to simulate a power-law, taking the amount of events for gamma given by the concentrations and correcting with the acceptance function calculated in section 2.1.4 and the time of observation. In the case of gamma, only a maximum concentration was obtained. As a result, an upper limit for the gamma flux of $(1.09 \pm 0.05) \cdot 10^{-6}$ $\text{TeV}^{-1}\text{m}^{-2}\text{s}^{-1}\text{sr}^{-1}$ at 1 TeV was found, which is compatible with the extrapolated value of $\Phi_0(1\ \text{TeV}) = (3.33 \pm 0.56) \cdot 10^{-7} (\text{TeV} \cdot \text{m}^2 \cdot \text{s} \cdot \text{sr})^{-1}$ given in section 4.3.2.

5.4 Conclusions

To separate the different diffuse emissions (gamma, electrons and hadrons), probability density functions were built. The method was tested and applied on the field of view of AGN PKS 2155-304. To obtain the concentrations of the diffuse emissions, the data is separated into two subsamples and a likelihood method is used to fit the different components. This was first tested with a toy Monte Carlo, before applying it on all the data taken during the more than 10 years of observation of the H.E.S.S. experiment of this AGN. Because of the very weak emission of the diffuse gamma, only an upper limit of $6.8 \cdot 10^{-4}$ on its concentration was obtained with the analysed sample, yielding an estimated upper limit on the flux of $(1.09 \pm 0.05) \cdot 10^{-6}$ $\text{TeV}^{-1}\text{m}^{-2}\text{s}^{-1}\text{sr}^{-1}$ at 1 TeV, using the spectral index provided in previous publications in a lower energy range. For electrons and protons, the obtained proportions ($1.58 \pm 0.01\%$ and $98.42 \pm 0.03\%$, respectively) are of the expected order of magnitude for a population enriched in the electromagnetic component due to trigger background rejection.

Chapter 6

Source modelization

Sommaire

In this chapter, a method is developed to reconstruct the morphology of an astrophysical source using the global response of the optical system. Although the focus of this chapter is on the Active Galactic Nucleus (AGN) PKS 2155-304 that serves as benchmark for this method, four other AGNs and the Galactic Center supermassive black hole Sagittarius A* were added for a more thorough study of the employed point-like source modelization. These different sources are introduced in the first part of the chapter, before proceeding with their morphology characterisation. The latter is used to estimate the intensity of PKS 2155-304 with different set of cuts, so as to compare the method developed to disentangle particles based on dicriminant variables (see chapter 5) to the standard ones. The chapter closes with compatible results.

6.1 Active sources

Active sources can be classified into different categories depending on their morphology as seen by the detector. In the case of H.E.S.S., the precision of the reconstruction determines its angular resolution, also known as the Point-Spread Function (PSF). By definition, the PSF will represent a point-like source and, from there, any larger sources will be considered extended.

6.1.1 Point-like sources

A source will be considered point-like when its spatial event distribution matches the PSF. With the H.E.S.S. experiment, extragalactic sources appear point-like. This is also the case of some galactic sources, like the very much studied Crab Nebulae mentioned in section 3.3.1.2.

Next will be detailed the point-like sources used in this work. All but Sagittarius A* are AGNs (see section 3.3.1.1), alone in their respective fields of view. Their position can be seen in the sky map, figure 6.1. The region of the black hole at the center of our galaxy (grey spot on figure 6.1), Sagittarius A*, was added because of its interest as a strongly emitting point-like source in a highly complex region often used for the study of the gamma diffuse galactic component, which is not significantly present in the field of view of AGNs. All these sources have been well studied before and their spectra at TeV energies have been characterized in articles published by the H.E.S.S. collaboration.

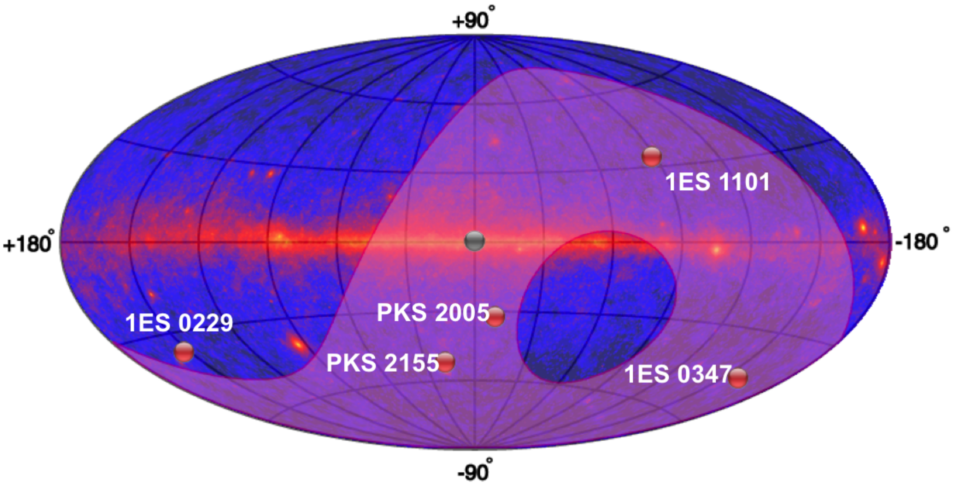

Figure 6.1: The positions of the five studied AGN. The black hole at the center of the galaxy, Sagittarius A*, was also included in the analysis and is marked in grey. The purple area represents the region of the sky which can be observed with H.E.S.S. Credit: http://tevcat.uchicago.edu.

PKS 2155-304

At a redshift of $z = 0.116$, the Active Galactic Nucleus PKS2155-304 is one of the most distant well-established sources of TeV gamma rays in the southern hemisphere and the brightest source seen by the H.E.S.S. telescopes. For Blazars such as PKS 2155-304, as explained in section 3.3.1.1 the relativistic jet emerging from the vicinity of the black hole is directed to the observer and is responsible for the production of high-energy gamma rays. As for all AGNs, the exact nature of the jet and the detailed mechanisms of gamma-ray production are strongly debated. PKS 2155-304 belongs to a special class of AGNs, the BL Lacertae, characterized by rapid and large-amplitude flux variability across all wavelengths of the electromagnetic spectrum. This variability is extremely interesting for a number of topics concerning cosmic ray acceleration and exotic physics as was explained in section 3.3.1.

This AGN was discovered by the Mark 6 telescope (Durham telescopes) in 1999, while the CANGAROO collaboration published limits on data taken in 1997 [77] and 1999 [78]. This shows the high variability of the source, when comparing the sensitivity of these two instruments. In 2002-2003 it was detected by the first H.E.S.S. telescope (a study of these first observations can be found in [79]) and catalogued as HESS J2158-30. It has been observed by H.E.S.S. every year since, resulting in many diverse publications. PKS 2155-304 is well known for its flaring activity, with two famous flares in 2006, the "big flare" in July 28th and the "Chandra flare" (naming comes from the simultaneous observation campaign of the flare with the Chandra satellite) in July 29th and 30th. These were studied extensively, resulting in six publications [80, 81, 82, 83, 84, 85]. Two of them dealt with exotic physics, searching for Lorentz invariance Violation [81, 84] and two were part of multiwavelength campaigns [82, 85]. The H.E.S.S. collaboration also participated in another two simultaneous observations of PKS 2155-304 in a lower state [86, 87]. Axions, very light particles that appear in some theories of exotic physics, were studied with PKS 2155-304 data in a dedicated article [88].

The region of the AGN PKS 2155-304 was selected to be a benchmark for this method for, besides the great statistics, it met the following criteria: it is well below the galactic plane ($\delta_{J2000} = -30°13'$), at such high redshifts the source is considered point-like, and there is a relatively poor population in the surrounding region. It has been well studied before. For the spectral study, the 14 runs taken during the "Chandra flare"[1] were chosen. Previous results on the study of this period include one from the H.E.S.S. collaboration [85] which provides a value of $\Gamma = 3.61 \pm 0.04$ for the source index, when adapting from the results given night by night in the paper. Concerning the source flux, the adaptation from the same paper gives a value of $\Phi_0(1\ \text{TeV}) = (4.28 \pm 0.11) \cdot 10^{-11}\ \text{TeV}^{-1}\text{cm}^{-2}\text{s}^{-1}$ at 1 TeV.

PKS 2005-489

As PKS 2155-304, PKS 2005-489 is a high frequency peaked BL Lac object in the Southern Hemisphere ($\delta_{J2000} = -48°50'$) and one of the brightest at all wavelengths, which is why it has been part of multiwavelengths obervations campaigns, in a high state [89] as well as during a four year monitoring [90]. It was initially discovered as a strong radio source in the Parkes 2.7 GHz survey in 1975 and first detected by the H.E.S.S. telescopes in 2005 [91], which registered it as HESS J2009-488. It has a redshift of $z = 0.071$. The selected period for its study is from the year 2004 to 2007 for a total of 158 hours (352 runs of 28 mins each), yielding for the H.E.S.S. experiment [90] a spectral index of $\Gamma = 3.2 \pm 0.16_{\text{stat}} \pm 0.2_{\text{syst}}$ and a flux of $\Phi_0(1\ \text{TeV}) = (0.75 \pm 0.21) \cdot 10^{-12}\ \text{TeV}^{-1}\text{cm}^{-2}\text{s}^{-1}$ (adapted from the value given in the paper).

1ES 1101-232

The BL Lac object 1ES 1101-232, or HESS J1103-234 for the H.E.S.S. experiment, located in an elliptical host galaxy at a redshift of $z = 0.186$ and $\delta_{J2000} = -23°30'$, was initially discovered by the Ariel-5 X-ray satellite. The chosen observations of the source were the ones conducted by the H.E.S.S. collaboration in April and June 2004 and in March 2005 (43 hours after quality selection of the runs) led to a paper [92] in which the source's obtained spectral index is $\Gamma = 2.94 \pm 0.20$ and flux at 1 TeV $\Phi_0(1\ \text{TeV}) = (5.63 \pm 0.89) \cdot 10^{-13}\ \text{TeV}^{-1}\text{cm}^{-2}\text{s}^{-1}$.

1ES 0347-121

1ES 0347-121 with a redshift of $z = 0.188$ is one of the most distant objects for which the very high energy spectrum is measured. Classified as a BL Lac object, it resides at $\delta_{J2000} = -11°59'$ in a host elliptical galaxy and is thought to harbor a supermassive black hole. This AGN was first seen in X-ray Einstein IPC (Imaging Proportional Counter) Slew Survey in 1992. In the H.E.S.S. catalog, it appears as HESS J0349-119. For its analysis, the H.E.S.S. observations taken between August and December 2006 were chosen, with a total of 25.4 hours of good quality runs. This data gave a spectral index of $\Gamma = 3.10 \pm 0.23_{\text{stat}} \pm 0.10_{\text{syst}}$ and flux at 1

---

[1] Run numbers from 33787 to 33801 exception of number 33794 which does not exist.

TeV of $\Phi_0(1\ \text{TeV}) = (4.52 \pm 0.85_{\text{stat}} \pm 0.90_{\text{syst}}) \cdot 10^{-13}\ \text{TeV}^{-1}\text{cm}^{-2}\text{s}^{-1}$ published by the H.E.S.S. collaboration in [93].

1ES 0229+200

Another high-frequency peaked BL Lac first discovered by the Einstein IPC Slew Survey in 1992 is 1ES 0229+200. It is hosted by an elliptical galaxy at a redshift of $z = 0.1396$ and $\delta_{J2000} = 20°16'$. In the H.E.S.S. catalog, it is listed as HESS J0232+202. This AGN is studied with 98 runs taken in 2005 and 2006 for a total live time of 41.8 hours. Previous results by the H.E.S.S. collaboration on the same period yield a flux of $\Phi_0(1\ \text{TeV}) = (6.23 \pm 2.25) \cdot 10^{-13}\ \text{TeV}^{-1}\text{cm}^{-2}\text{s}^{-1}$ (adapted from the published value given in integrated flux) and a spectral index of $\Gamma = 2.50 \pm 0.19_{\text{stat}} \pm 0.10_{\text{syst}}$ [94].

Sagittarius A*

Sagittarius A* is the name of the black hole at the center of the Milky Way. For the H.E.S.S. telescopes, this highly emitting γ-ray source is point-like and filed as HESS J1745-290. The presence of various γ emitting sources in its field of view makes it a complex region for analysis, which is why it constitutes a separate section (see section 6.1.3).

6.1.2 Extended sources

By definition, any source larger than the PSF will be considered extended, typically, supernova remnants and pulsar wind nebulae as seen by the H.E.S.S. experiment, as well as diffuse emissions. Unlike point-like sources, no common model exists, so extended sources have to be treated on a case by case basis. For this, a hypothesis on the gamma-ray emission mechanism has to be made. A possibility for some sources would be to use the counterpart in other wavelengths, if noticing, for instance, a similarity in the morphology of X-rays and that of γ-rays (figure 6.2 gives an example of this). Then, the supposition put forward that the gamma-rays are produced by electrons, for, if it is the case, this population would be responsible for gamma as well as X-ray emissions and a correlation would exist between the two distributions. In theses cases, an analysis of the measured X-ray flux coupled with predictions from a theoretical propagation model to the TeV domain, may provide a pattern for the gamma-ray emission. As seen in section 3.2 in chapter 3, if gamma-rays are produced in hadronic processes, a correlation with observations at other wavelengths could also exist and be used, provided that some conditions on the medium density and magnetic field are met. This could happen if taking a supernova remnant's shock wave as the emission site, for instance. However, modeling extended sources is much more complex and time-consuming than point-like sources. This is the reason why only the latter were used to develop the method in this work.

6.1.3 The galactic center region

As commented previously, several sources were identified by the H.E.S.S. experiment in the galactic center region [63], ranging from diffuse emission extending in the direction of the Galactic plane of cosmic rays interacting with the dense (10^3cm^{-3}) gas or exotic processes like dark matter annihilation (studied with H.E.S.S. data in [97] and [98]) to several identified active sources' emissions. The former seems to spatially coincide with the interstellar material in giant molecular clouds in these parts, as traced by their CO emission. Of the latter can be mentioned a very highly emitting point-like source at the center of the galaxy HESS J1745-290, which

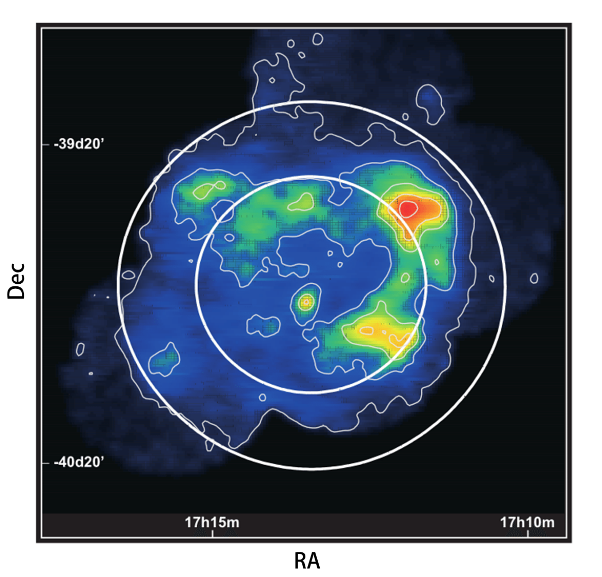

Figure 6.2: The supernova remnant RXJ1713.7-3946 is an extended source with a noticeable correlation between its emission in gamma-rays (H.E.S.S. map in full color scale) and X-rays (thin gray contours, corresponding to ASCA data in the 1-3 keV range [95]). The comparable angular resolution for both sets of telescopes makes the comparison easier. The superimposed thick white contours indicate the 94% and 98% levels of the detection efficiency weighted H.E.S.S. exposure, given by the product of relative detection efficiency and the observation time. Credit [96].

seems to coincide with the position of the supermassive black hole Sagittarius A* as seen in other wavelengths, the supernove remnant Sagittarius A East which is thought to be partly superimposed on the galactic center source and the composite supernova remnant G 0.9+0.1. The first and the last are clearly visible on the upper plot of figure 6.3. After their subtraction, the mentioned diffuse emission is revealed (lower plot in figure 6.3), which could include different components. Unidentified and unresolved sources could be producing this radition. Nonetheless, as discussed, it seems to coincide with molecular clouds present in the region, so it could also be generated by nearby active sources hidden by the clouds and interacting with these. A combination of both explanations is possible too. Until now, this type of diffuse emission is unique, at H.E.S.S. energies, to the galactic center and is superimposed over the galactic and extragalactic isotropic ones. The diffuse emissions are the focus of chapter 4. Since then, an extended scan of the central section of the galaxy was performed by the H.E.S.S. telescopes, including the area within ±30 deg in longitude and ±3 deg in latitude [99]. Thanks to another two observation campaigns, this region was extended to cover the region $l = 250 - 65$ deg and $|b| < 5°$. A source catalog and diffuse emission analysis papers for this region are in preparation.

After its discovery as a strong compact radio source in 1974, Sagittarius A* has served as a unique laboratory for the study of astrophysics of galactic nuclei in general. The H.E.S.S. telescopes first reported the observations of a high energy γ-ray emitting point-like source in 2004 [103]. The source was named HESS J1745-290 and its spectrum and variability as well as positioning have been widely investigated ([104] and [105] respectively). The obtained spectral index when fitting with a power-law is of $\Gamma = 2.29 \pm 0.02_{\text{stat}} \pm 0.10_{\text{syst}}$ and the flux at 1 TeV of $\Phi(1 \text{ TeV}) = (2.40 \pm 0.05_{\text{stat}} \pm 0.40_{\text{syst}}) \cdot 10^{-12} \text{ TeV}^{-1}\text{cm}^{-2}\text{s}^{-1}$ [104], using selected runs from

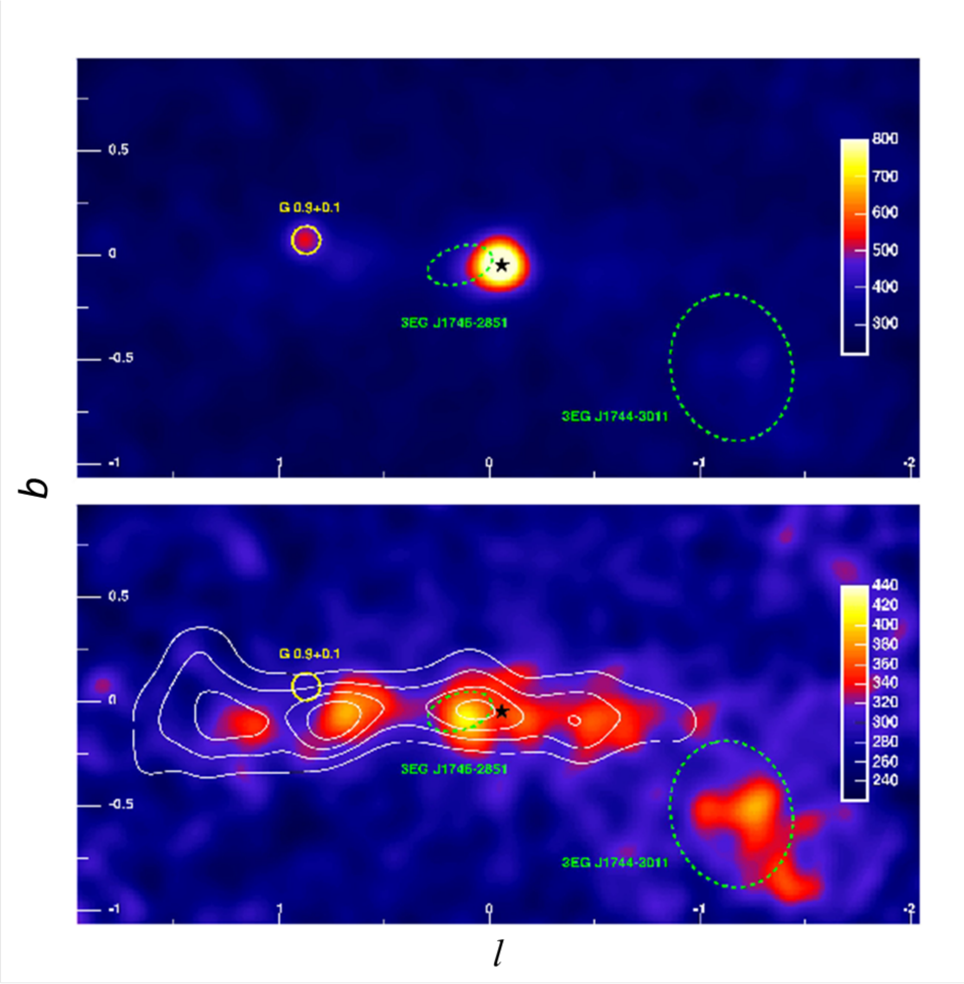

Figure 6.3: Top: Initial sky map with all events. Two highly emitting γ-ray sources can be seen. Bottom: the same map after subtraction of the two mentioned dominant sources. Two significant features appear: an extended emission spatially coincident with the unidentified EGRET source 3EGJ1744-3011, investigated in [100] and extended emission along the galactic plane, characterized in [63] and thoroughly discussed in chapter 4. The yellow circle shows the position and size of the composite supernova remnant G 0.9+0.1 whereas the green dashed ellipses represent the 95% confidence region for the positions of two unidentified EGRET source, found in [101]. The white contour lines are evenly spaced and correspond to the density of molecular gas, as traced by the velocity integrated CS line emission [102]. They were smoothed to match H.E.S.S.' angular resolution. Credit [63].

2004, 2005 and 2006. These runs focus on the field of view of Sagittarius A*, with the standard observation window of 5°. The same ones were chosen for the analysis in this work so as to be able to compare the results. The source was also studied with simultaneous observations with the Chandra satellite during an X-ray flare [106].

6.2 Modelizing point-like sources

By definition, it should be possible to use the PSF as a model of any point-like source. To test this, an attempt at subtracting the benchmark source PKS 2155-304 during the "Chandra" flare was made using the PSF obtained in section 2.1.5.4. The sky map of the field of view was built using all events passing the Model++ event selection cuts (see section 2.2.1.2). The PSF histogram is supposed to be normalized to this number of events. In figure 6.4 is shown the field of view of PKS 2155-304 before and after subtraction of the PSF at the position of the source. It is clear that the PSF is too narrow compared to the source and does not represent it satisfactorily. The next section is dedicated to improving the modelization of a point-like source using the PSF.

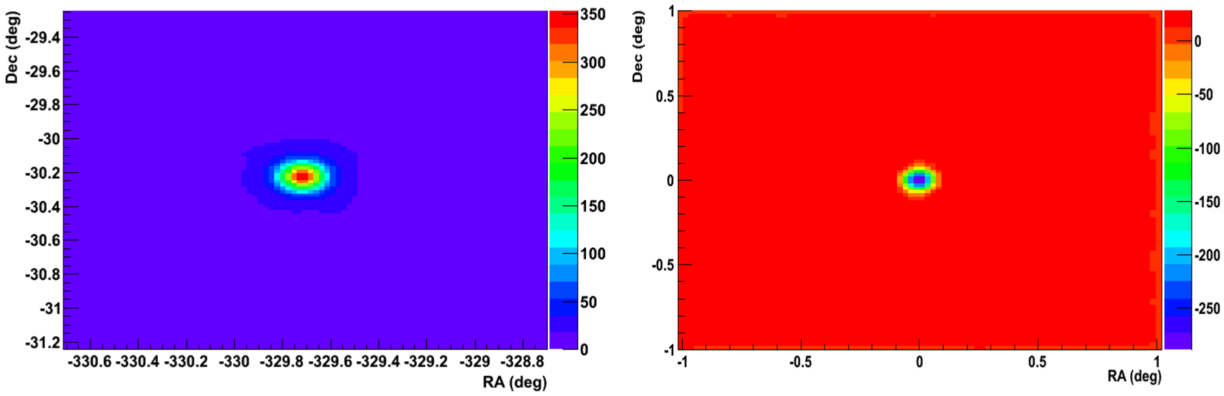

(a) PKS2155-304 before subtraction of the PSF

(b) PKS2155-304 after subtraction of the PSF

Figure 6.4: The FOV of PKS 2155 before (left) and after (right) subtraction of the PSF. The AGN can be seen in the left plot, while on the right one a clear depression appears, signifying that the PSF is two narrow compared to the source.

6.2.1 Fitting a point-like source with a convoluted PSF

The obtention of the PSF with simulations remains a theoretical response of the detector to a point-like source, and it seems to be underestimated. It was assumed that the main problem came from the way the different systematics on the parameters of the experimental device are taken into account in the simulations. These can include, as previously discussed, the alignment of the mirrors, the positioning of the cones in the focal plan, the distortion of the structure of the telescope, among other possibilities. The error was presumed to be statistical and Gaussian in nature. Thus, the PSF was convoluted with a 2D asymmetric Gaussian function:

$$f(x,y) = A \exp\left(-\left(\frac{(x-x_0)^2}{2\sigma_{gx}^2} + \frac{(y-y_0)^2}{2\sigma_{gy}^2}\right)\right),$$

which means that each bin of the PSF histogram was scattered over the adjoining ones following a gaussian distribution. This function is expected to give a more realistic model of a point-like source.

The width of the gaussian function with which the PSF will be convoluted needs to be determined. In order to do this, a fit of the convoluted function was performed on the source, in a region of 0.3° around the source's position for weak sources and with a radius of 0.8° for bright sources like PKS 2155-304. The source position was calculated by maximizing the integral over a 5x5 bins area and taking the weighted average. This function was added to a constant to take into account the background, assuming a steady contribution on the edge of the signal region. The width of the gaussian on the x and y axis (σ_{gx} and σ_{gy} respectively), the background level b and the normalization N remained free in the fit. The source position, given by right ascension X and declination Y, is a free parameter in the fit.

However, the event selection and acceptance correction can change the normalization of the PSF and background level. Thus, on one hand, the sky map of the field of view of the different sources was reconstructed with the events passing the selection criteria established for the analysis, explained in section 5.1.4. On the other hand, the acceptance of the instrument must also be considered when building the sky map. The effect of the acceptance correction was studied on the field of view of PKS2155-304 and is presented in section 6.2.3.

6.2.2 Fit results

The values of the six parameters of the fitting function, mentioned in the previous section, are summarized next, when applied on the field of view of PKS 2155-304 during the "Chandra" flare (14 runs):

$$\begin{aligned}
X &= -329.7055 \pm 0.0004 \text{ deg}\\
Y &= -30.2215 \pm 0.0004 \text{ deg}\\
b &= 14.42 \pm 0.05 \text{ events}\\
\sigma_{gx} &= (3.24 \pm 0.06) \times 10^{-2} \text{ deg}\\
\sigma_{gy} &= (2.19 \pm 0.07) \times 10^{-2} \text{ deg}
\end{aligned}$$

The deviation of the position of the maximum given by the fit from the one initially calculated as explained before, which was $X_i = (-329.7070 \pm 0.0183)^\circ$ and $Y_i = (-30.2176 \pm 0.0158)^\circ$, is extremely small. This fit of the source position was tested with an initial deviation of up to 0.05° in X and Y from the computed maximum, resulting in the same compatibility. The difference with the position of the source given by the H.E.S.S. collaboration, $X_{HESS} = -329.7167^\circ$ and $Y_{HESS} = -30.2256^\circ$, is not significant (within the same bin, the size of a 1 bin being 0.02°). The value of the background level will be discussed in the next section 6.2.3. Finally, the results lead to a convoluted PSF which is wider than the original PSF. The same procedure was applied on the other five studied active sources. The values of σ_{gx} and σ_{gy} are summarized in table 6.1.

An asymmetry can be seen in the source fit, which is not surprising knowing that the simulated PSF is symmetrical while observing conditions and the detector's response shouldn't necessarily produce this. The gaussian function seems to only slightly correct the original PSF, with its width significantly smaller than that of the original PSF ($\sigma \approx 0.03$). The exception to this is PKS 2155-304, for which the two widths are similar, which leads to a computed R68 of the convoluted PSF of $R_{68}(PSF_{conv}) = 0.078 \pm 0.001$ against $R_{68}(PSF) = 0.061 \pm 0.001$ for the original PSF, significantly widening the source. Moreover, it seems to have a characteristic

Active source	$\sigma_{gx}(\times 10^{-2})^{\circ}$	$\sigma_{gy}(\times 10^{-2})^{\circ}$
PKS 2155-304	3.24 ± 0.06	2.19 ± 0.07
PKS 2005-489	0.177 ± 0.007	0.323 ± 0.008
1ES 1101-232	0.332 ± 0.079	0.301 ± 0.064
1ES 0347-121	0.204 ± 0.002	1.367 ± 0.046
Sagittarius A*	0.301 ± 0.001	2.837 ± 0.267

Table 6.1: Values for the width (σ_{gx} and σ_{gy} on the x and y axis, respectively) of the gaussian function for the convolution of the PSF obtained for the studied active sources.

behavior on the X axis, with a wider spread, whereas for all other sources the opposite is observed. This is probably due to the fact the tables used to calculate the PSF were only obtained up to a spectral index of 3.2, providing and adapted PSF for all sources but PKS 2155-304. With a softer spectrum, PKS 2155-304 has more low energy events, which is known to provide a worse angular resolution. Because an initial PSF with a harder spectral index than the one of the source was used (3.2 against about 3.7), an additional widening was to be expected. Nonetheless, the subsequent subtraction to its sky map is noticeably better, as illustrated figure 6.5, although a residue at the center of the source is noticed, as well as small depressions at the edge of the source. The fit could be further improved for this strongly emitting source by using a more sophisticated model. Nonetheless, weaker sources seem to be better fitted, as seen in figure 6.6 taking 1ES 1101-232 as an example.

The choice of the region for the fit is its only predefined parameter and can influence, in particular, the determination of the background level. The way to select it depends mainly on the knowledge and use of the acceptance of the detector over the whole field of view and is studied next.

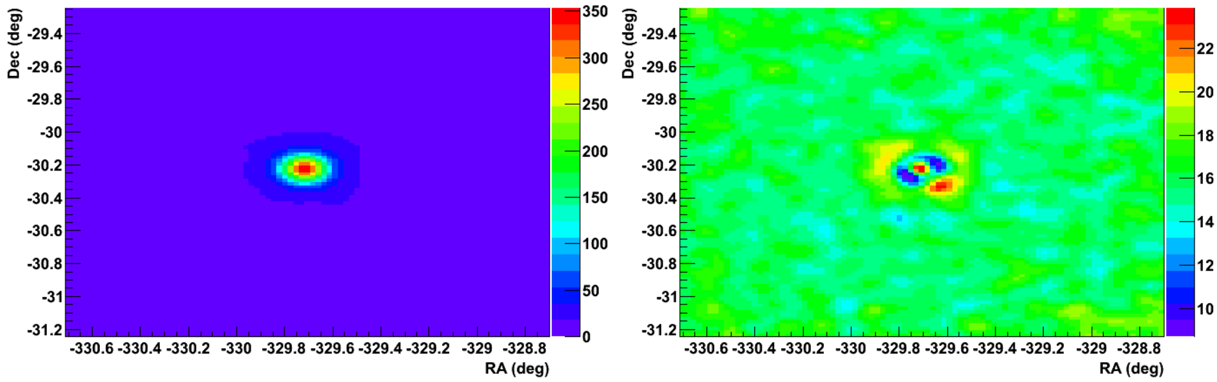

(a) Before subtraction

(b) After subtraction

Figure 6.5: FOV of PKS2155-304 before (left) and after (right) subtraction of the convoluted PSF at the position of the source. The AGN can be seen in the left plot. On the right plot is the FOV after the subtraction. A residue of about 17% at the center of the source is noticed, as well as small depressions (3%) at the edge of the source.

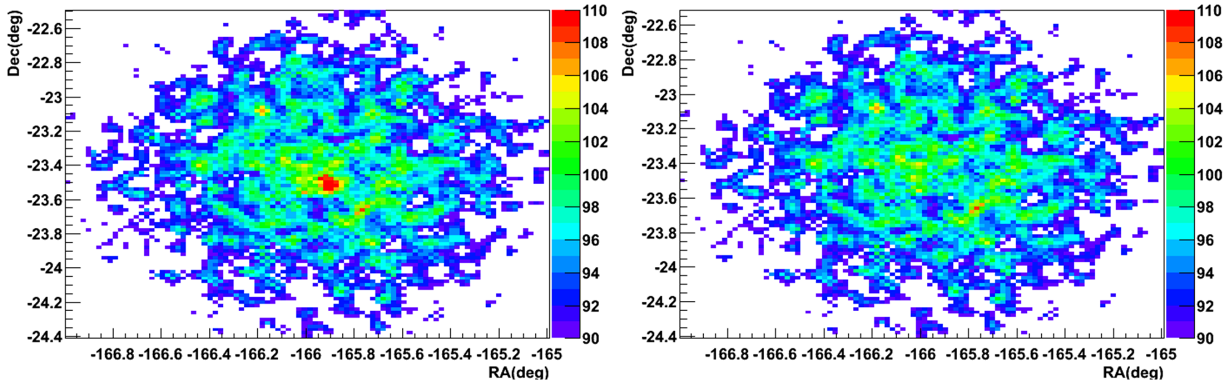

(a) Before subtraction (b) After subtraction

Figure 6.6: FOV of 1ES 1101-232 before (left) and after (right) subtraction of the convoluted PSF at the position of the source. The AGN can be seen in the left plot whereas on the right plot it has neatly been subtracted, leaving only background.

6.2.3 Effects of the acceptance correction of the field of view

As mentioned, the instrument's acceptance needs to be considered for the sky map reconstruction. Although in the case of the spectra, each event will be corrected individually with the acceptance function corresponding to its parameter values (see section 2.1.4) for the spectrum of each type of particle, in the case of the whole sky map, the acceptance provided in the form of sky map by the H.E.S.S. collaboration software was taken. Figure 6.7 presents the acceptance map for the 14 runs taken during the "Chandra flare" of PKS 2155-304. The period (selected runs) is required for the calculation of this map, as it corresponds to the acceptance integrated over the time of observation and all the energy events (or source spectral index). Moreover, it takes into account the acceptance of the instrument for both gamma-like and background events. Because the trigger of the camera and hence the acceptance degrades with increasing distance to the center of the camera, the number of events decreases closer to the edges. This can be observed figure 6.8 on the left hand side plot, which shows a side view of the region of PKS 2155-304. The purpose of the correction by the acceptance map is to take into account the inhomogeneities of the camera response over the whole field of view. Thus, a visible effect of the correction is to flatten the background by increasing the weight of the events closer to the edges (right hand plot in figure 6.8) while considering that at the center of the camera no correction is needed, which is why the map used for the correction corresponds to a relative acceptance, with a value of 1 at the center.

To evaluate the effect on the background level determination by the PSF fit of this acceptance correction, the region of fit around the source was investigated. For this, both the uncorrected and acceptance corrected sky maps of PKS 215-304 were used. For nine concentric circular regions around the position of the maximum of the source starting at a radius of 0.2°, the background level was fitted. Figure 6.9 summarizes these results, with those of a second source (1ES 1101-232) added to verify the behavior of the fit on an uncorrected sky map. For the second source, the values were rescaled.

The reason for testing uncorrected sky maps is that besides PKS 2155-304, sky maps were not corrected from the acceptance. This is due to the fact that the acceptance correction does not have the same effect on strongly emitting sources and weaker sources. Because the background is

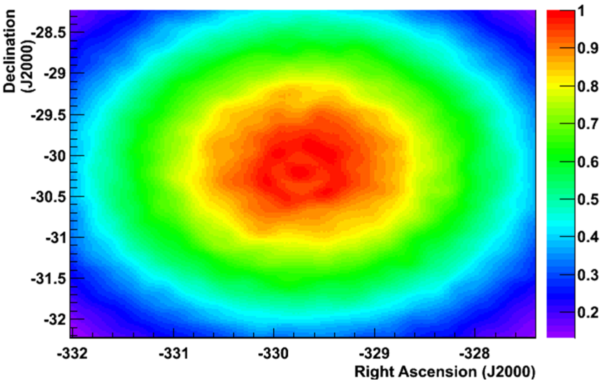

Figure 6.7: Sky map representing the acceptance of the instrument in the field of view of PKS 2155-304.

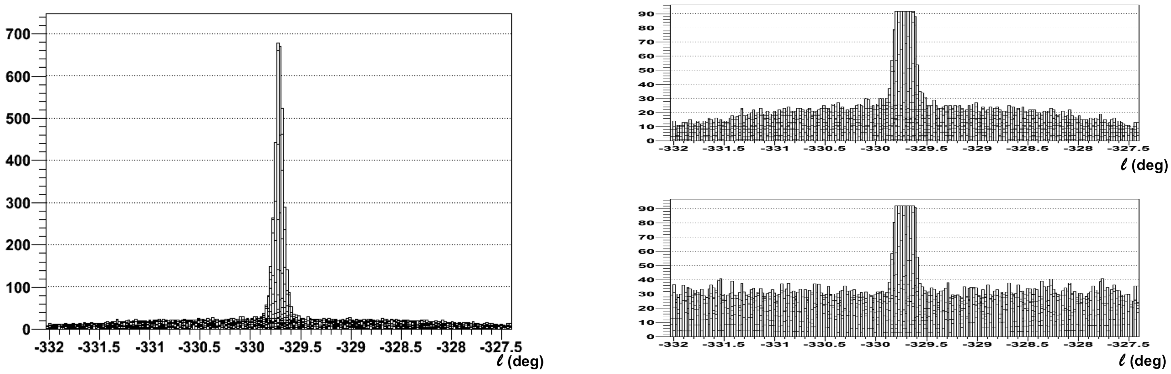

(a) PKS2155-304 before correcting from the acceptance. (b) Zoomed side view of the field of view of PKS2155-304 before (top) and after (bottom) correcting from the acceptance.

Figure 6.8: On the left side can be seen the side view of the FOV of PKS2155-304 before correcting with the acceptance sky map. On the right, a zoom is made on this view (upper plot). The same window is shown after correcting with the acceptance sky map (lower plot). Whereas on the uncorrected plot the background level can be seen to drop with increasing distance from the center of the camera, the correction's effect is to flatten it: the background level becomes stable over the whole field of view, and compatible with one.

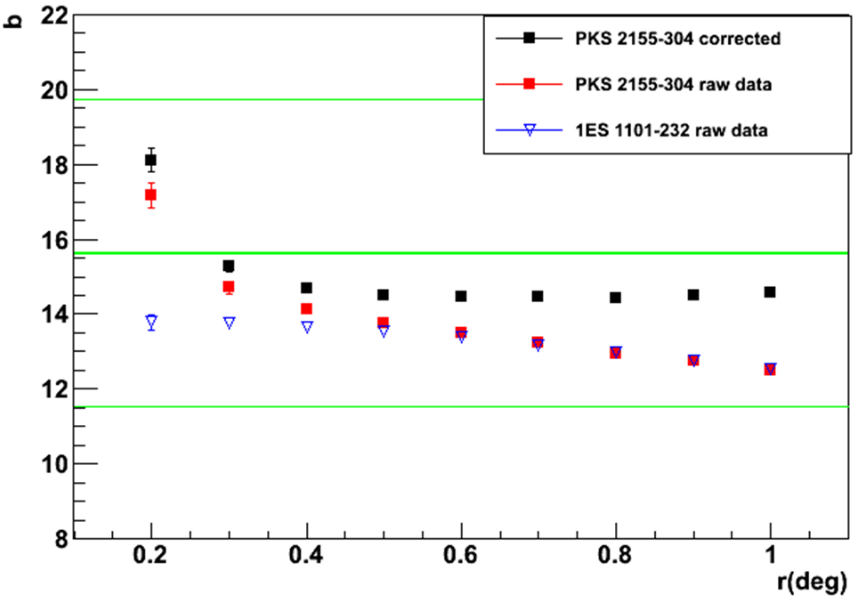

Figure 6.9: Background values resulting from the fit of PKS 2155-304 (squares) and 1ES 1101-232 (triangles) in their respective fields of view. The fit is performed on a circular region around the maximum of the source for nine different radii, from 0.2° to 1° with steps of 0.1°. In the case of PKS 2155-304, the fit was tested on data both with (black) and without (red) acceptance correction. Its effect is to flatten the obtained background values above a radius of 0.5° whereas the uncorrected ones decrease along with the detector's acceptance. The effect of the strong luminosity of PKS 2155-304 during its flare can be seen when taking small regions for the fit, as the source influences the background determination and the effect of the stable acceptance in the camera cannot be seen. However, for weak sources, this feature appears clearly. A systematic bias can be observed with respect to the computed average value of the background outside the source (green line), which is later discussed.

not subtracted, in the case of the latter, the rising of the background around the source hinders the convergence of the convoluted PSF fit, which is why it was decided that it would not to be applied for weak sources. The systematics associated with it can be evaluated on the strong source PKS 2155-304.

On figure 6.9, it is noted that without the acceptance correction (red squares), the background in the field of view of PKS 2155-304 decreases between 0.4° and 1° around the position of the source, following the evolution of the acceptance of the detector. The effect of the acceptance correction on the PKS 2155-304 data (figure 6.8) is to flatten the background. This can also be noticed on figure 6.9, where the black squares represent the level of the background obtained when fitting PKS 2155-304 with a corrected field of view. However, these remain constant only after a radius of 0.4° for the region of the fit. For PKS 2155-304's flare, if the radius of the region taken for the fit is under 0.4° the source starts to influence the results with an increasing overestimation when approaching the source's position, with (black squares) or without (red squares) the acceptance correction. This is due to the very strong emission of PKS 2155-304 during this period, that makes the source's contribution dominant over the background. The fact that a spectral index slightly lower than the measured value was used to produce the initial

PSF, as mentioned in the previous section, might also play a role. Indeed, the correction with the gaussian function is more important, and the resulting convoluted PSF less representative of the true signal. Hence, for this source, the correction with the acceptance map is noticeable mainly on the part of the plot which depends solely on the acceptance, corresponding to fitting regions of more than 0.4° radius.

However, for weak sources like 1ES 1101-232 (blue triangles in figure 6.9), even with a small region around the source for the determination of the background (radius of 0.2°), no influence of the source on the fit is seen. The resulting background level depends only on the acceptance. Indeed, the stable acceptance in the central region of the camera can be observed between 0.2° and 0.4°. After that, the decline of the detector's acceptance is reproduced in the same way as in the field of view of PKS 2155-304.

So as to verify that the background was being correctly estimated, taking the corrected FOV of PKS 2155-304, the value given by the fits was compared to the average number of events per bin in a circular region of radius 1°, when excluding a source region with a radius of 0.2°. The distribution of the number of events per bin in the selected region, seen figure 6.10, yields a mean value of $\mu = 15.62 \pm 0.07$ (thick green line) with a standard deviation $\sigma = 4.104 \pm 0.047$ (marked with thin green lines), using a gaussian fit. Another excluded source region of radius 0.4° was also tested, resulting in a compatible mean and standard deviation.

This background level value can be compared to the one given by the fitting method (black squares in figure 6.9), when fit regions are large enough so that the source does not influence the background determination (radii above 0.4°). Taking for example the fit shown in section 6.2.2, which uses a region of radius 0.8°, a background value of 14.42 ± 0.05 events per bin was obtained. It can be pointed out that with or without correction, there is a systematic bias of the fitted value of the background as compared to the computed one.

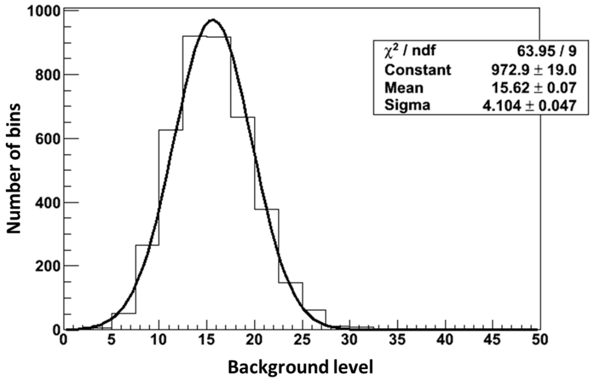

Figure 6.10: The distribution of the background level is fitted with a gaussian function. Its mean value is $\mu = 15.62$, with a standard deviation $\sigma = 4.1$.

As a conclusion, for an acceptance corrected field of view, any region for the fit should give the same results. In the case of PKS 2155-304, the correction was applied on the sky maps. Considering the very high luminosity of the chosen period of PKS 2155-304, however, so as to avoid the effect of the source, only regions above 0.5° must be used. A radius of 0.8° was chosen for the fit region because it gave the lowest error on the background determination and was near the average of the radii yielding a constant value for the background level.

For uncorrected weak sources, which is the case of the rest of the studied sources in their respective selected periods of observation, any region between a 0.2° and a 0.4° radius, where the acceptance in the camera is constant, can be taken. Hence a radius of 0.3° was selected for the circular region around the source's maximum to be fitted and no acceptance correction of the sky map was done.

6.3 Estimation of the intensity of the "Chandra" flare signal

Finally, the number of events coming from the source in the signal region was computed and compared to the number of gamma in the ON region provided by H.E.S.S. standard analysis methods. The Model ++ analysis method (see section 2.2.1.2) and data selection criteria were used. At least two telescopes in coincidence were required for the event reconstruction. The number of gamma were estimated in regions of 0.1, 0.2 and 0.3 degrees around the source, corresponding to θ^2's under 0.01 deg^2, 0.04 deg^2 and 0.09 deg^2, respectively. These are the results, assuming gaussian uncertainties, when fitting PKS 2155-304 during the "Chandra flare":

$$\begin{aligned} 0.1^\circ : N_\gamma &= 18384 \pm 136 \\ 0.2^\circ : N_\gamma &= 22174 \pm 149 \\ 0.3^\circ : N_\gamma &= 22553 \pm 150 \end{aligned}$$

When computing the number of gamma events in the source region with Model ++ analysis reconstruction algorithms and the ring background subtraction method, the following results, assuming gaussian uncertainties, are obtained:

$$\begin{aligned} \theta^2 < 0.01\ \mathrm{deg}^2 : N_\gamma &= 18329 \pm 135 \\ \theta^2 < 0.04\ \mathrm{deg}^2 : N_\gamma &= 22073 \pm 149 \\ \theta^2 < 0.09\ \mathrm{deg}^2 : N_\gamma &= 22631 \pm 150 \end{aligned}$$

The *Multiple-Off* background subtraction method provides the following values:

$$\begin{aligned} \theta^2 < 0.01\ \mathrm{deg}^2 : N_\gamma &= 18329 \pm 135 \\ \theta^2 < 0.04\ \mathrm{deg}^2 : N_\gamma &= 22077 \pm 149 \\ \theta^2 < 0.09\ \mathrm{deg}^2 : N_\gamma &= 22640 \pm 150 \end{aligned}$$

Moreover, the number of point-like photons can also be computed with the particle separation method based on discriminant variables that was explained in the previous chapter and that uses the cuts detailed in section 5.1.4. The method yields the following values:

$$\begin{aligned} 0.2^\circ : N_\gamma &= 24600 \pm^{+468}_{-463} \\ 0.3^\circ : N_\gamma &= 24614 \pm^{+529}_{-532} \end{aligned}$$

The advantage of the convoluted PSF fitting method, is that it can be applied with any selection criteria. When using the same as the method developed in this work, the results are, using gaussian uncertainties:

$$0.2^\circ : N_\gamma = 24135 \pm 155$$
$$0.3^\circ : N_\gamma = 24681 \pm 157$$

The number of gamma found when fitting the source with the convoluted PSF is compatible with the one given by standard background subtraction methods and with the method based on discriminant variables, developed in this work, when using the respective data selection criteria. Moreover, it seems to stabilize when enlarging the area (if we continue, for a radius of 0.4°, $N_\gamma = 22626 \pm 150$), which is to be expected because the farther from the source, the smaller the distribution tails. This also corroborates the fact that the background estimation is biased when taking a region with a radius smaller than 0.4°, as was shown in figure 6.9. These results seem to confirm the possibility of using the discriminant variable method to disentangle particles.

6.4 Conclusions

A method to characterize the active point-like sources present in the field of view was developed in this chapter. The idea was to improve the original PSF by convoluting it with an asymmetric gaussian function, for a better representation of the source's morphology. The parameters of the gaussian function are obtained when fitting the studied source. The method provided an estimation of the number of photons in the source, compatible with the ones given by the standard methods when using the same selection criteria. This independent evaluation is of importance, for it is a good way of testing the validity of the method introduced in the last chapter, in which particle disentanglement is achieved using PDFs built from dedicated discriminant variables. For this, only a specific set of cuts could be applied, rendering impossible direct comparison of the results for the number of photons in the source with the ones from standard analyses. However, by applying the same cuts used to develop the method based on probability density functions, in the PSF fitting method, both yielded compatible results. As the PSF fitting method's value had already been compared to the one given by the standard analyses, this is a manner of validating the discriminative capacity of the method using probability density functions.

Chapter 7

Diffuse emissions spectral reconstruction

Sommaire

Two different ways of building the spectra for each type of diffuse emissions are presented. The first one was developed to make use of the previously obtained proportions. The X_{eff} estimator, built from the discriminant variables and the estimated concentrations, is introduced in the next section. This variable is used to calculate the probabilities to be assigned to each event of belonging to one population or another, thus weighing it individually in the energy spectrum reconstruction for each type of particle. The spectra for electrons and protons are then computed and fitted, yielding a spectral index and flux for each kind of emission. The second section of this chapter explains the implementation of another technique, *sPlot*, to "unfold" the contributions to a spectrum. *sPlot* is tested on Toy Monte Carlo before being applied on the data from the region of PKS 2155-304, to conclude the chapter.

7.1 The X_{eff} method

The method described in this section uses the PDFs and concentrations obtained in chapter 5 to discriminate between the diffuse components so as to build probabilities for each type of particle. After being processed, each event will contribute differently to the spectrum for electrons and protons, depending on the value of its discriminant variables.

7.1.1 Calculating probabilities: the X_{eff} estimator

The computation of the probabilities to be used as weights for the events in the spectra are discussed next. Having the fraction values of the various components of the diffuse emission signals, an X_{eff} estimator can be built for each of them, by using the simulations. This estimator, used to discriminate between the three different particles, is of the form:

$$X_{eff}^{i=g,e,p} = \frac{\eta_i F_i}{\eta_e F_e + \eta_p F_p + (1 - \eta_e - \eta_p) F_g}$$

where F_i is the function that results from the multiplication of all five discriminant variables distribution values ($F_i = f(MSL) * f(MSW) * f(MSG) * f(MDH) * f(PDH)$) and η_g, η_e and η_p are the obtained fractions for γ, electrons and protons respectively, with $\eta_g + \eta_e + \eta_p = 1$. It can be computed for any type of particle and for this work the estimator X_{eff}^e, with the distributions of simulated electrons chosen for the numerator calculation. The principle of the method is to build $X_{eff}^e(\gamma)$, $X_{eff}^e(e)$ and $X_{eff}^e(p)$, which represent X_{eff}^e applied to γ, electrons and protons. For each simulated event, the electron discriminant variables distributions give the probability corresponding to the value of the discriminant variable of the event. The probabilities found for the five discriminant variables are multiplied to obtain f_e. Multiplied by η_e, it gives the numerator. By doing the same for the denominator, a X_{eff}^e distribution for each of the simulated particles can be obtained.

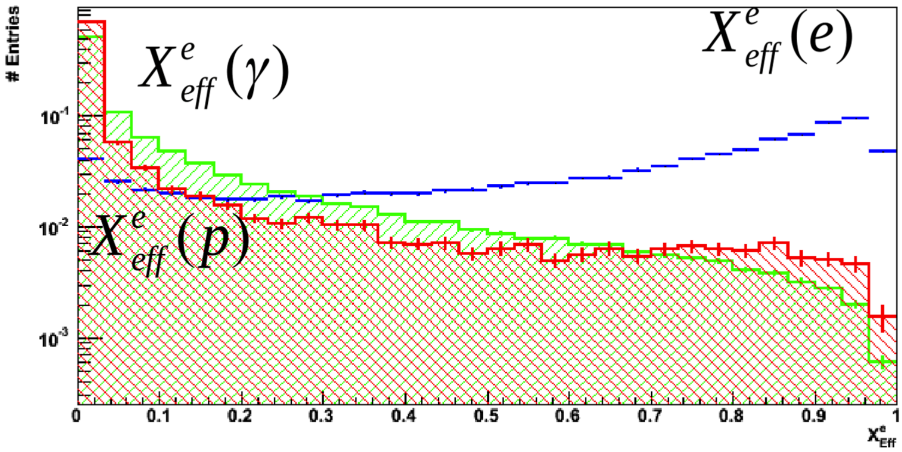

Figure 7.1: X_{eff}^e distributions for simulated gamma (green), electrons (blue) and protons (red).

However, even though it may seem so by looking at the expression, these estimators may not be directly used as probabilities for weighting the events. This is due to the fact that their sum does not equal one, for when X_{eff}^e =0 there are still electrons in the data sample, and on the other hand when X_{eff}^e =1, a bit of the other particles are still present, as can be seen in figure 7.1. This is why it was necessary to construct a probability with these estimators:

$$P_{i=g,e,p} = \frac{f(X_{eff}^e(i))}{f(X_{eff}^e(\gamma)) + f(X_{eff}^e(e)) + f(X_{eff}^e(p))}$$

The distributions are in figure 7.2, with a sum (black points), as expected, equal to one. These probabilities can now be directly used, together with the acceptance function calculated in section 2.1.4, to weight the contribution of each event to each of the two spectra: electrons and protons.

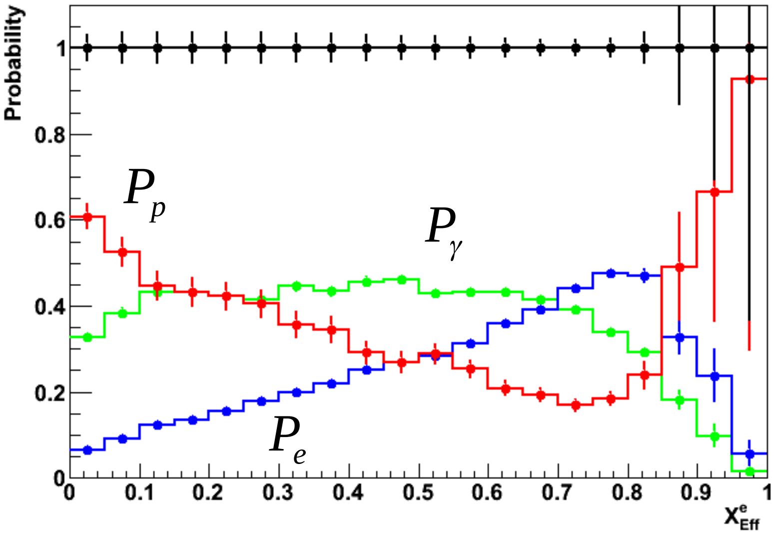

Figure 7.2: Distributions of the probabilities obtained using the X^e_{eff} estimator for simulated protons (red), electrons (blue) and gamma (green). Their total sum is shown in black.

7.1.2 Results

Because only an upper limit on the diffuse gamma flux was obtained, the spectrum could not be computed. The fitted spectra for the diffuse electrons and for the protons can be seen figure 7.3. They were obtained by dividing each weighted event by the corresponding acceptance and taking into account the observation time. For the fit, it was supposed that all components followed a spectral power-law:

$$\frac{dN}{dE} = \Phi_0 \left(\frac{E}{1\ \text{TeV}} \right)^{-\Gamma} \tag{7.1}$$

where Φ_0 is the flux at 1 TeV and Γ the spectral index. Most previous studies of the emissions support this hypothesis (see chapter 4.3.2). Each fit is non-binned and weighted. The adjustment is done between 1 and 10 TeV to avoid the data with very low values of the acceptance, which was the case below the 1 TeV threshold. The diffuse electrons resulting flux at 1 TeV and spectral index are $(4.995 \pm 0.138_{\text{stat}}) \cdot 10^{-5}$ TeV^{-1}m^{-2}s^{-1}sr^{-1} and $\Gamma = 2.18 \pm 0.03_{\text{stat}}$ respectively. Concerning the protons, a flux at 1 TeV of $(1.151 \pm 0.011_{\text{stat}}) \cdot 10^{-2}$ TeV^{-1}m^{-2}s^{-1}sr^{-1} was obtained, as well as a spectral index of $\Gamma = 2.77 \pm 0.01_{\text{stat}}$. When compared to the values extrapolated in section 4.3.2 at 1 TeV of $(1.17 \pm 0.02) \cdot 10^{-4}$ TeV^{-1}m^{-2}s^{-1}sr^{-1} for electrons and around $10^{-1}(\text{TeV} \cdot \text{m}^2 \cdot \text{s} \cdot \text{sr})^{-1}$ for protons, it can be seen that both fluxes are lower than the extrapolated values. Moreover, the electrons' spectral index is much harder than the one given in section 4.3.2 ($\Gamma = 2.18$ against a $\Gamma = 3.9 \pm 0.1$) at lower energies (<3 TeV). However, the proton's spectral index is compatible with the extrapolated value ($\Gamma = 2.77 \pm 0.01$ against ~ 2.8, as seen in section 4.3.2), when taking into account the systematic errors discussed in the next section.

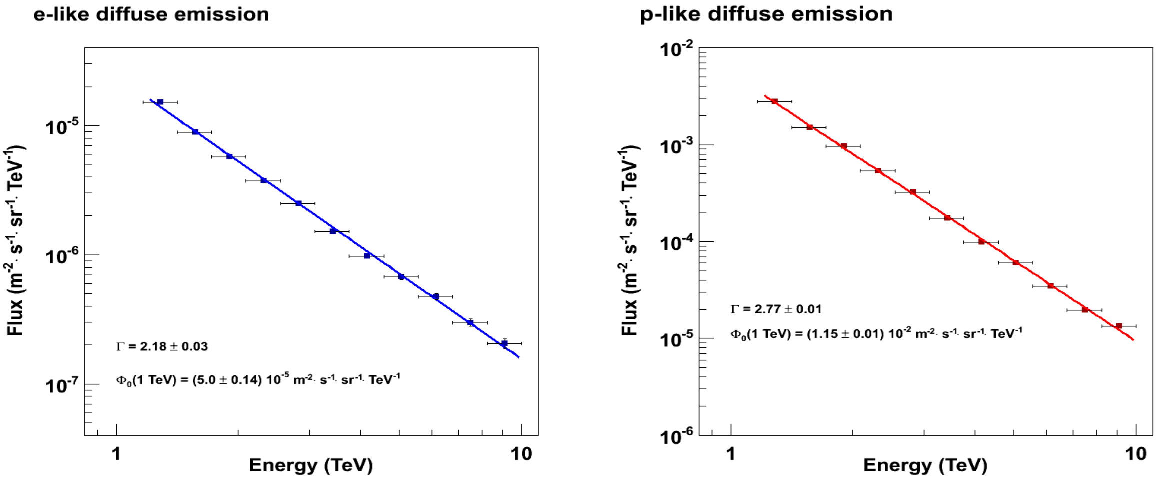

(a) Electrons spectrum

(b) Protons spectrum

Figure 7.3: The spectra of the diffuse electrons and protons. The obtained values for the electrons' flux at 1 TeV is $(4.995 \pm 0.138_{\rm stat}) \cdot 10^{-5}$ $\rm TeV^{-1}m^{-2}s^{-1}sr^{-1}$ while its corresponding spectral index is $\Gamma = 2.18 \pm 0.03_{\rm stat}$. For protons, the flux at 1 TeV and spectral index are, respectively, $(1.151 \pm 0.011_{\rm stat}) \cdot 10^{-2}$ $\rm TeV^{-1}m^{-2}s^{-1}sr^{-1}$ and $\Gamma = 2.77 \pm 0.01_{\rm stat}$.

7.1.3 Systematics

For the diffuse emissions, the following systematic errors were considered:

- Energy interval for fit: two intervals were considered for fitting the spectra: 1.-10. TeV and 1.-8. TeV, giving a difference in range of 20%.

- Proportions estimation: the concentrations of the diffuse emissions estimated in section 5.2.3 play a key role in the determination of the probabilities for the diffuse emissions spectra. The concentration of protons was made to vary within its estimation error of 0.03%. As the electron's is directly correlated, there was no need to test it in the same manner. The effect on the electron's spectrum was asymmetric, as can be seen in table 7.1 .

- PDFs parameters: for all types of particles, the different variables PDFs' Chi square was checked. For the worst fits, the parameters with the biggest relative errors were selected and tested within their error bars. For all particles, PDH was clearly the PDF with the worst fit. For diffuse and point-like gamma as well as for protons, the selected parameter for the systematic study was the mean μ, which was made to vary of about 8.16%, 6.05% and 0.83% respectively. For electrons, the chosen parameter was the width σ, using a variation of 3.40%. In addition, for protons two other variables' parameters were added: the mean μ of MSL and the parameter characterizing the exponential decline λ of the

MDH fit. These were made to vary of about 3.92% and 45.9% respectively. For MDH, the errors are asymmetric, as can be noticed in table 7.1 .

	Flux error in %	Spectral index error in %
Protons diffuse emission		
Energy interval for fit (±20%)	0.212	0.36
Proportions estimation (±0.03%)	0.087	<0.36
PDFs parameters, all particles	0.087	<0.36
Electrons diffuse emission		
Energy interval for fit (±20%)	0.657	0.83
Proportions estimation (±0.03%)	$\pm^{0.981}_{0.260}$	$\pm^{0.46}_{1.38}$
PDFs parameters, all particles	<0.020	<0.46
MDH parameters for protons	$\pm^{0.541}_{0.180}$	$\pm^{0.92}_{0.46}$

Table 7.1: Flux and spectral index systematic relative errors. The upper limits correspond to the precision of the result.

The flux results for the diffuse emissions are summarized in table 7.2.

	Flux ($\mathrm{TeV^{-1}m^{-2}s^{-1}sr^{-1}}$)	Spectral index
Electrons	$5.00 \pm 0.14_{\mathrm{stat}} \pm^{0.11\mathrm{syst}}_{0.05\mathrm{syst}} \cdot 10^{-5}$	$2.18 \pm 0.03_{\mathrm{stat}} \pm^{0.05\mathrm{syst}}_{0.06\mathrm{syst}}$
Protons	$1.15 \pm 0.01_{\mathrm{stat}} \pm 0.44_{\mathrm{syst}} \cdot 10^{-2}$	$2.77 \pm 0.01_{\mathrm{stat}} \pm 0.01_{\mathrm{syst}}$

Table 7.2: Flux and spectral index of electrons and protons with statistical and systematic uncertainties.

7.2 Disentangling the diffuse emissions with the *sPlot* method

Several tools exist that allow to disentangle the contributions of different sources to the distribution of a given variable. In this chapter, one of them, called *sPlot*, is described and tested, first on simulated events and then on data from PKS 2155-304.

7.2.1 The *sPlot* technique

The *sPlot* technique is based on the assumption that the variables characterizing the data can be split into two sets: one for which the distributions of all the contributions are known, called the "discriminating" variables and one for which they are not, named the "control" variables. For *sPlot* to work, these two sets of variables must be uncorrelated. The *sPlot* method uses the knowledge on the discriminating variables and a maximum Likelihood analysis to reconstruct the distributions of the control variables, independently for each source contributing to the data sample. For further details, see [107].

In the framework of this work, the *sPlot* technique can be used to unfold the different diffuse emission's contributions to the spectrum. As in section 5.2.1, the events were divided into two subsamples of similar statistics associated with two different PDFs, one for hadronic vs electromagnetic differentiation using MSL, MSW and MSG and one allowing the separation between electrons and photons, with PDH and MDH. These PDFs obtained from simulations acted as the discriminating variable. The selected control variable was the true energy, as the aim is to reconstruct the spectrum for each type of particle, which corresponds to the individual distributions of the events with respect to the true energy for each contribution to the data sample. The method first calculates the weights to be applied on each event for its contribution to each spectrum. These are called "sWeights" and are expected to take into account correlations between the spectra for each contribution, hence decorrelating them. In this step, the concentrations of each type of particle are obtained as they are free parameters in the fit. Next, the sWeights are used on the data, together with the acceptance functions calculated in section 2.1.4 and the observation time, to produce the different spectra and fit them, yielding the spectral indices and fluxes for each source. The *sPlot* technique was first tested on simulated events and then applied on the "Chandra flare" data taken from a region excluding a 0.4° radius circular area around the source.

7.2.2 Validating the *sPlot* method with a Toy Monte Carlo

A total of 1 000 000 events was simulated. The initial concentrations of the different diffuse emissions were the following:

$$\begin{aligned}\epsilon_\gamma &= 0.2\%\\ \epsilon_e &= 2.0\%\\ \epsilon_p &= 97.8\%\end{aligned}$$

The number of events obtained with *sPlot* are in good agreement:

$$\begin{aligned}\eta_\gamma &= 1966.8 \pm 34.1\\ \eta_e &= 20054.9 \pm 101.6\\ \eta_p &= 977979.0 \pm 700\end{aligned}$$

Figures 7.4, 7.5 and 7.6 show the distributions for all discriminant variables resulting when applying the obtained sWeights on the data (black points). The PDFs used to construct the discriminating variable in the *sPlot* model are superimposed in green, blue and red, respectively for gamma, electrons and protons.

In figure 7.7 can be seen the spectra given by *sPlot* for each type of particle (same color code), as well as their sum (black line) superimposed over the black data points. The obtained spectral indices, $\Gamma_\gamma = 2.006 \pm 0.023$, $\Gamma_e = 3.985 \pm 0.016$ and $\Gamma_p = 3.001 \pm 0.001$ are in remarkable good agreement with the simulated ones: $\Gamma_\gamma = 2$, $\Gamma_e = 4$ and $\Gamma_p = 3$.

The convergence of the fits for the six free parameters (3 concentrations and 3 spectral indices) can be seen in figure 7.8. In figure 7.9, it is observed that these are, as desired and expected, uncorrelated.

7.2.3 Applying *sPlot* on PKS 2155-304 data

The power-law fit of the spectra obtained when applying *sPlot* on the data from the "Chandra" flare excluding a source region of radius 0.4°, yielded spectral indices of $\Gamma_e = 2.46 \pm 0.08$ and

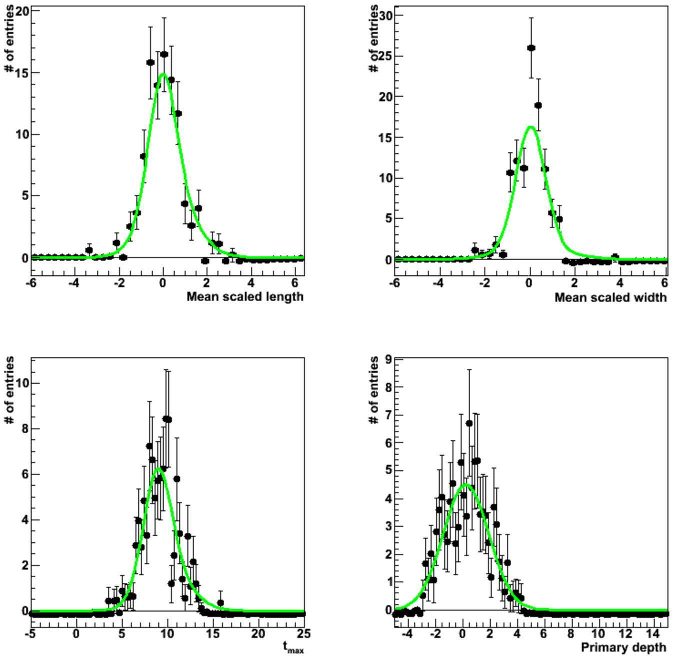

Figure 7.4: Gamma PDFs (in green) for each discriminant variable, obtained when applying the *sPlot* technique on simulated data (in black).

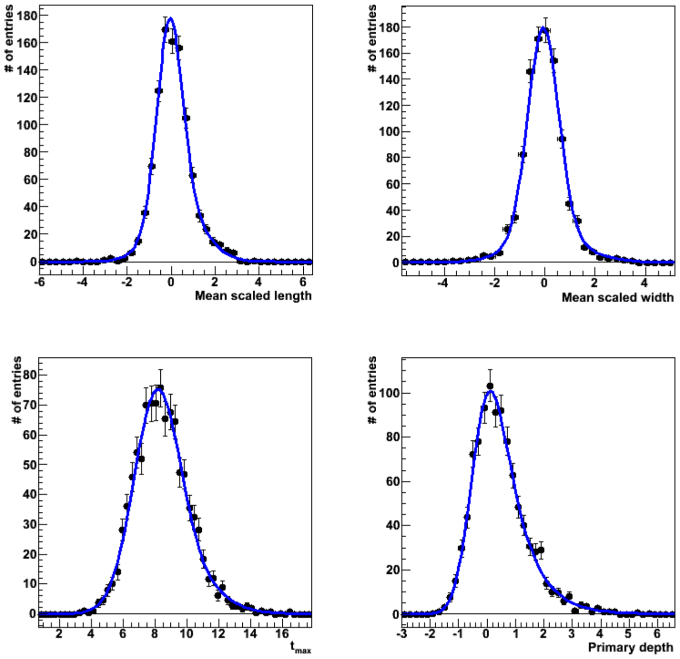

Figure 7.5: Electron PDFs (in blue) for each discriminant variable, obtained when applying the *sPlot* technique on simulated data (in black).

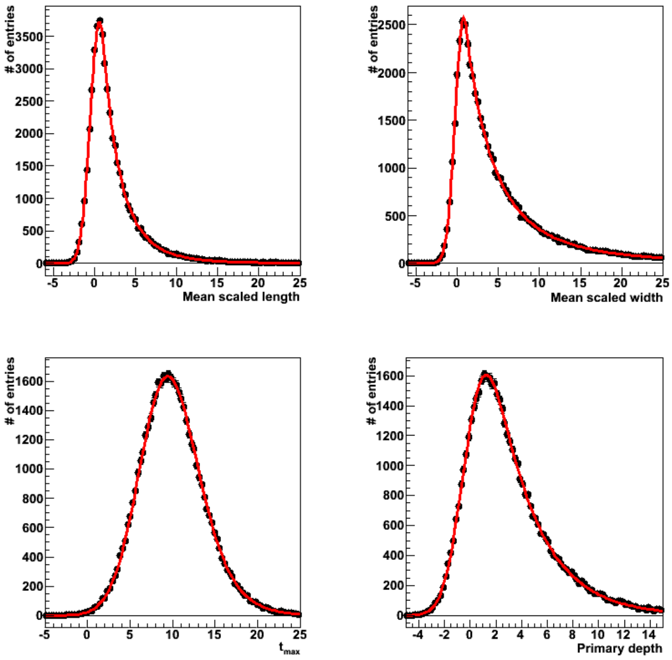

Figure 7.6: Proton PDFs (in red) for each discriminant variable, obtained when applying the *sPlot* technique on simulated data (in black).

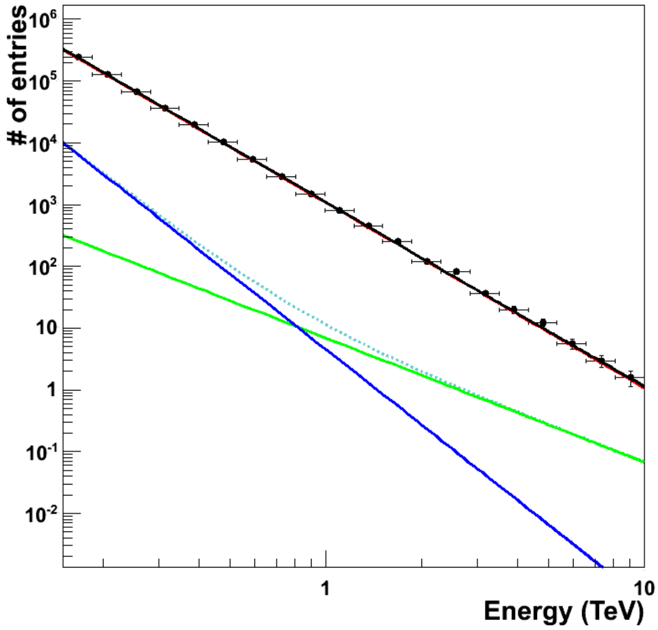

Figure 7.7: Spectrum for the diffuse emissions obtained when applying the *sPlot* technique on simulated data (black points). The contribution of each diffuse emission (green for gamma, blue for electrons and red for protons) to the spectrum are shown, as well as their total sum (black line). The sum of the two electromagnetic contributions is represented by a dashed turquoise line.

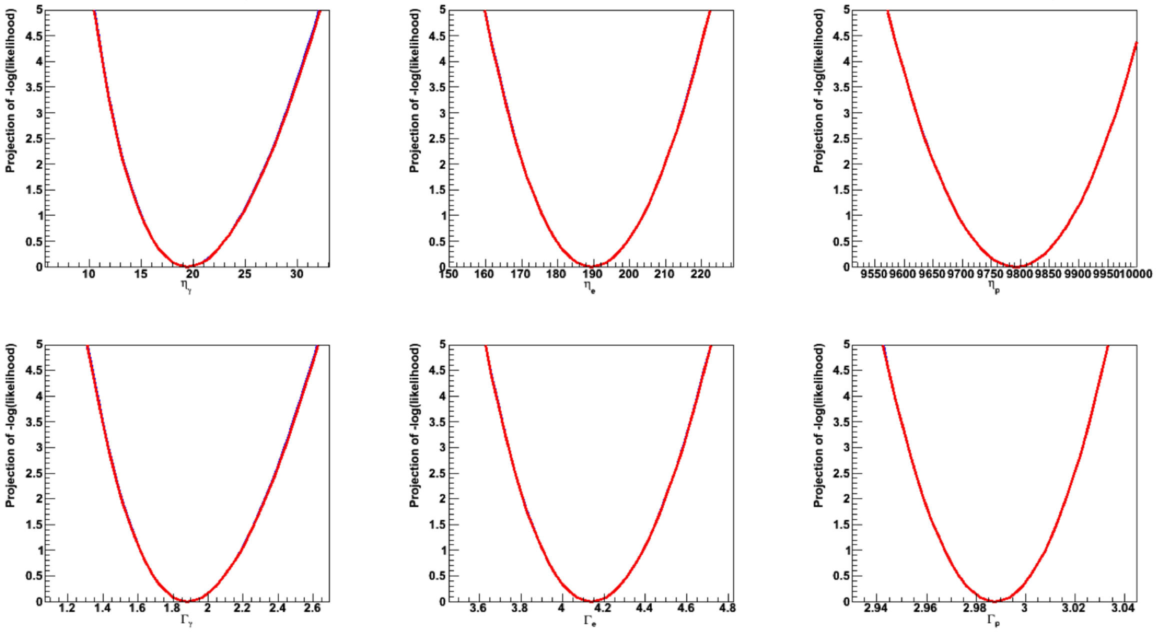

Figure 7.8: Likelihood profiles for the three concentrations and three spectral indices obtained with *sPlot* showing the convergence of the fits.

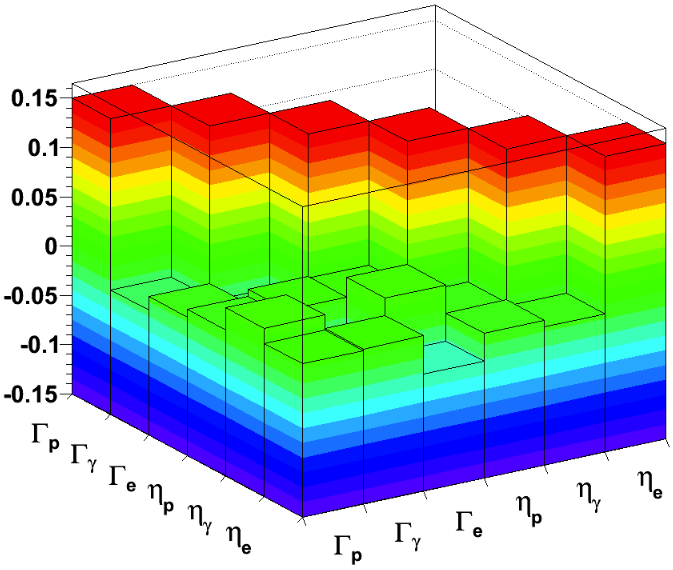

Figure 7.9: Correlation matrix between the three concentrations and three spectral indices obtained with *sPlot* illustrating their lack of correlation.

$\Gamma_p = 2.87 \pm 0.01$ for electrons and protons respectively, and a flux ratio of $\Phi_0^e(1\ \mathrm{TeV})/\Phi_0^p(1\ \mathrm{TeV}) = (2.78 \pm 0.06) \cdot 10^{-3}$. As in chapter 5, no diffuse gamma emission was detected.

The method was also tested on the source region inside a radius of 0.3°, giving a flux of $\Phi_0(1\ \mathrm{TeV}) = (1.73 \pm 0.04) \cdot 10^{-11}\ \mathrm{TeV}^{-1}\mathrm{cm}^{-2}\mathrm{s}^{-1}$ and spectral index of $\Gamma = 3.33 \pm 0.03$ when fitting the reconstructed spectrum with a power-law. Because different event selection criteria during a flare might change significantly the flux, the one obtained cannot be directly compared to the value presented in section 6.1.1. They are however, of the same order of magnitude. The spectral index is in the range provided in the publication [85]. These results seem promising.

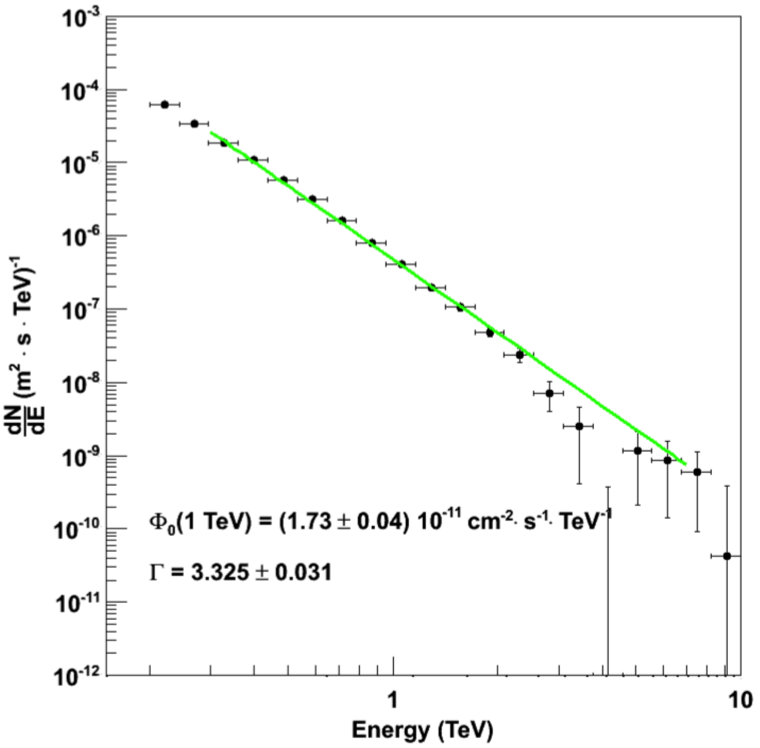

Figure 7.10: Spectrum of AGN PKS 2155-304 obtained with *sPlot*. When fitted with a power-law, it yields a flux of $\Phi_0(1\ \mathrm{TeV}) = (1.73 \pm 0.04) \cdot 10^{-11}\ \mathrm{TeV}^{-1}\mathrm{cm}^{-2}\mathrm{s}^{-1}$ and spectral index of $\Gamma = 3.33 \pm 0.03$.

7.3 Conclusions

In this chapter, two techniques were used to disentangle the different components of the background. The first one produced the spectra using directly the obtained concentrations of chapter 5. The second is a known unfolding tool, which was first tested on a Toy Monte Carlo and then applied on PKS 2155-304 data. For electrons and protons, the obtained values for their spectra's indices were respectively $\Gamma_e = 2.18 \pm 0.03_{\mathrm{stat}} \pm^{0.05\mathrm{syst}}_{0.06\mathrm{syst}}$ and $\Gamma_p = 2.77 \pm 0.01_{\mathrm{stat}} \pm 0.01_{\mathrm{syst}}$ for the first method, and $\Gamma_e = 2.46 \pm 0.08_{\mathrm{stat}}$ and $\Gamma_p = 2.87 \pm 0.01_{\mathrm{stat}}$ for the second. These values, although not compatible, differ by 10 % for electrons and less than 4% for protons. In both cases, no gamma were found outside the source. Concerning the fluxes, a ratio of

$\Phi_0^e(1\ \text{TeV})/\Phi_0^p(1\ \text{TeV}) = (4.339 \pm^{1.916}_{1.864}) \cdot 10^{-3}$ was obtained for the first technique, to be compared with $\Phi_0^e(1\ \text{TeV})/\Phi_0^p(1\ \text{TeV}) = (2.78 \pm 0.06) \cdot 10^{-3}$ for the second. They are of the same order of magnitude as the one computed from the published values: $\Phi_0^e(1\ \text{TeV})/\Phi_0^p(1\ \text{TeV}) = (1.17 \pm 0.02) \cdot 10^{-3}$. Regarding the obtained spectral indices, the proton one is compatible with previous results given in chapter 4 whereas for electrons no comparison is possible since there is no publication for the electron spectrum above 3 TeV up to now.

Conclusion

In this work a method was developed to extract the contribution of each of the VHE diffuse emissions by using probability density functions to distinguish between the different components. To do this, the bulk of the work focused on creating specialized samples to be able to compare the simulations, with the goal of handling them so that they best represent the data. An active source, the AGN PKS 2155-304, was used as benchmark to accomplish this.

An essential work required for the development of this method, is the study of the discriminant variables that are used to build the probability density functions that allow particle disentanglement. The discriminative power was tested and several attempts at improving it were performed. The focus was on two aspects: on one hand the dependencies on different parameters were studied and on the other the accurate representation of the data with the simulations was tested, by controlling the intervals in which the variables can be used as well as the observation periods. This lead to a particular data selection that was used in all subsequent analysis.

The use of the morphology of the source to estimate its intensity has the advantage of being applicable with any given selection criteria, which is not the case of the method that used discriminant variables to disentangle particles. Hence, it was possible to test the validity of the particle discrimination by comparing the number of photons in the source with this method and the one using the source's modelization. In turn, the latter can be compared to the results given by the standard analyses when applying the same data selection. As in both cases the results were compatible, the particle discrimination method based on probability density functions was tested and provided expected results.

Concerning the diffuse emissions, a first aspect of the work involved the estimation of their proportions in the background of PKS 2155-304. As only an upper limit on the concentration for the diffuse gamma emission of $6.8 \cdot 10^{-4}$ was found in the data, no spectrum was computed. However, using the acceptance calculated in this work, an upper limit on the flux of $(1.09 \pm 0.05) \cdot 10^{-6}$ $\text{TeV}^{-1}\text{m}^{-2}\text{s}^{-1}\text{sr}^{-1}$ at 1 TeV could be put forward. A spectral index of 2.41 ± 0.05 was taken for this, which is the one given by the FERMI collaboration for the extragalactic diffuse component, believed to be dominant at the location of PKS 2155-304. A steady behavior of the gamma spectrum at higher energies was thus assumed. This result is compatible with $\Phi_0(1\ \text{TeV}) = (3.33 \pm 0.56) \cdot 10^{-7} (\text{TeV} \cdot \text{m}^2 \cdot \text{s} \cdot \text{sr})^{-1}$, value extrapolated from the one given by the FERMI collaboration. For electrons and protons, the spectra were reconstructed using two methods. The first one required the concentrations obtained previously. For electrons, the resulting flux at 1 TeV of $(4.995 \pm 0.138_{\text{stat}} \pm^{0.11\text{syst}}_{0.05\text{syst}}) \cdot 10^{-5}$ $\text{TeV}^{-1}\text{m}^{-2}\text{s}^{-1}\text{sr}^{-1}$ is half what the H.E.S.S. collaboration has put forward ($(1.17 \pm 0.02) \cdot 10^{-4}$ $\text{TeV}^{-1}\text{m}^{-2}\text{s}^{-1}\text{sr}^{-1}$) and the spectral index much harder ($2.18 \pm 0.03_{\text{stat}} \pm^{0.05\text{syst}}_{0.06\text{syst}}$ against $\sim$3.9). However, the published results were given for a spectrum reconstruction up to 3 TeV, as opposed to the 10 TeV upper limit in this work, thus a direct comparison is not sensible. The values for protons, $\Phi_0(1\ \text{TeV}) = (1.151 \pm 0.011_{\text{stat}} \pm 0.44_{\text{syst}}) \cdot 10^{-2}$ $\text{TeV}^{-1}\text{m}^{-2}\text{s}^{-1}\text{sr}^{-1}$ for the flux and $\Gamma = 2.77 \pm 0.01_{\text{stat}} \pm 0.01_{\text{syst}}$ for the spectral index are close to the results compiled from previous experiments in the same energy domain. A second technique for building the spectra was implemented: the *sPlot* tool. It yielded a spectral index for electrons of $2.46 \pm 0.08_{\mathrm{stat}}$ and for protons of $2.87 \pm 0.01_{\mathrm{stat}}$, results which don't differ much from the ones obtained with the other method. The flux ratio of these two populations when using *sPlot* was found to be $\Phi_0^e(1\ \mathrm{TeV})/\Phi_0^p(1\ \mathrm{TeV}) = (2.78 \pm 0.06) \cdot 10^{-3}$, to be compared with the value $\Phi_0^e(1\ \mathrm{TeV})/\Phi_0^p(1\ \mathrm{TeV}) = (4.34 \pm^{1.92}_{1.87}) \cdot 10^{-3}$ when using the developed X_{eff} method and with the published value $\Phi_0^e(1\ \mathrm{TeV})/\Phi_0^p(1\ \mathrm{TeV}) = (1.17 \pm 0.02) \cdot 10^{-3}$. They are all of the same order of magnitude.

The next step would be to apply the method on the region of the galactic center, where several sources of gamma-rays are known to exist. In this area, a strong galactic diffuse emission is expected, which could be studied by constraining the extragalactic emission, found when applying the method on fields of view of different AGNs. However, it would still need further improvement to provide more reliable results. Moreover, further work on the discriminant variables is required to improve their discriminative power and compatibility with data as well as test other possible variables or combinations. The discriminant variables can be studied with different cuts that remove the hadronic components, for a better understanding, as this technique is well known. Also, the other nuclei that are known to be present in the diffuse emissions should be considered, particularly helium, which represents an important fraction (about 14%). In addition, other methods, for instance those based on Boosted-Decision Trees (BDT), can be tested. These different types of methods are interesting alternatives to standard analyses, which loose much statistics in event and area selections, and could be more easily developed and applied in future experiments like CTA, if the tools are properly adapted since the beginning.

Appendices

Appendix A

Reconstructed energy as a function of true energy

The energy bias explained in section 2.2.2 had to be computed for every type of particle. Here are presented those for diffuse gamma, electrons and protons. The lack of statistics for protons at low and high energies do not affect the analysis which only uses the reduced interval 0.2 - 10 TeV, in which the relation between reconstructed and true energy is linear and statistics are highest.

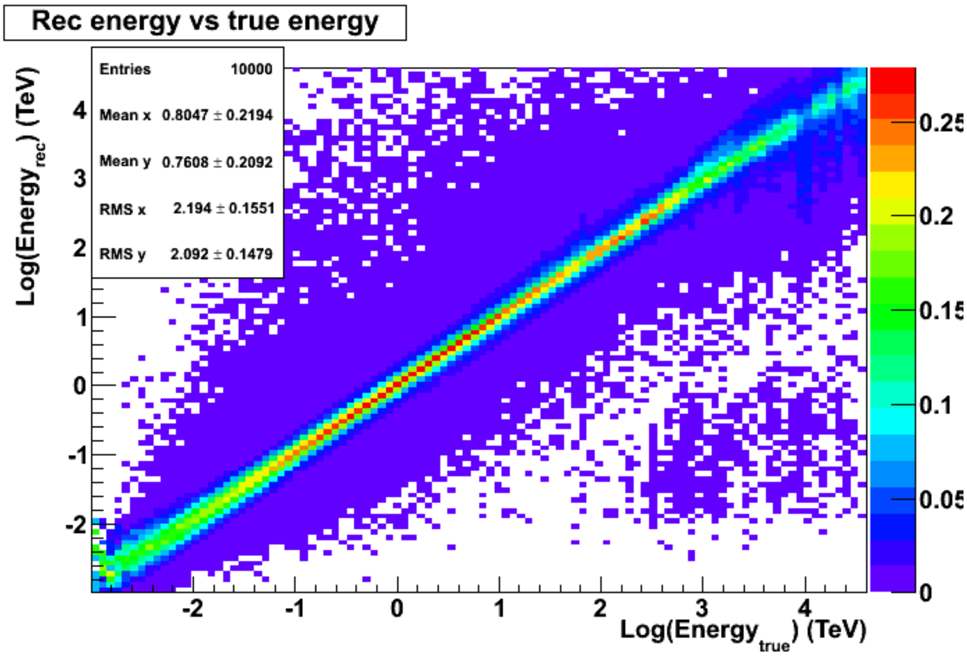

Figure A.1: Reconstructed energy as a function of the true energy for diffuse gamma. Slices in reconstructed energy bins are normalized.

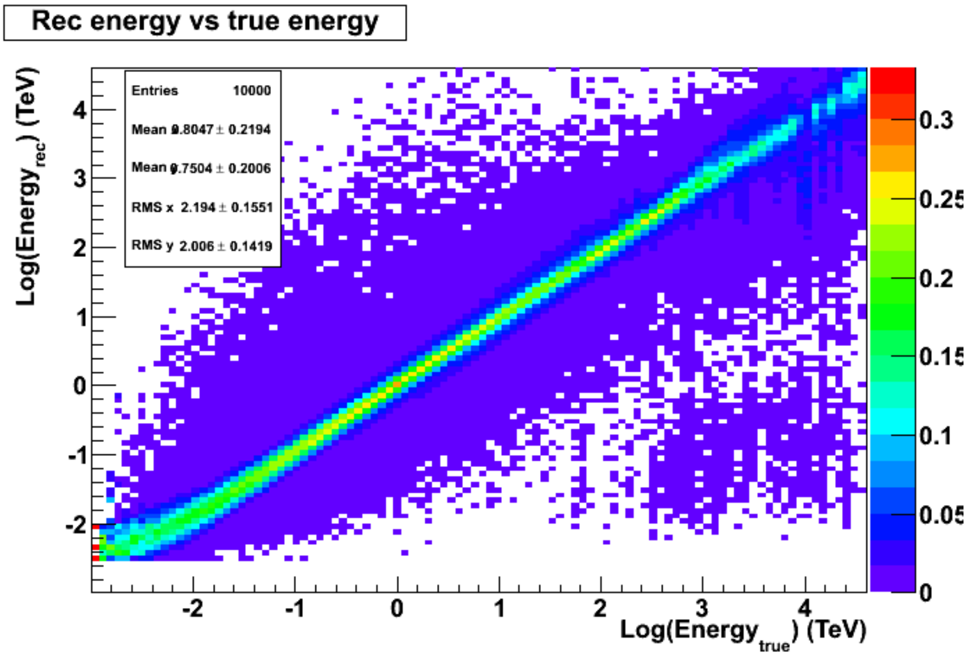

Figure A.2: Reconstructed energy as a function of the true energy for electrons. Slices in reconstructed energy bins are normalized.

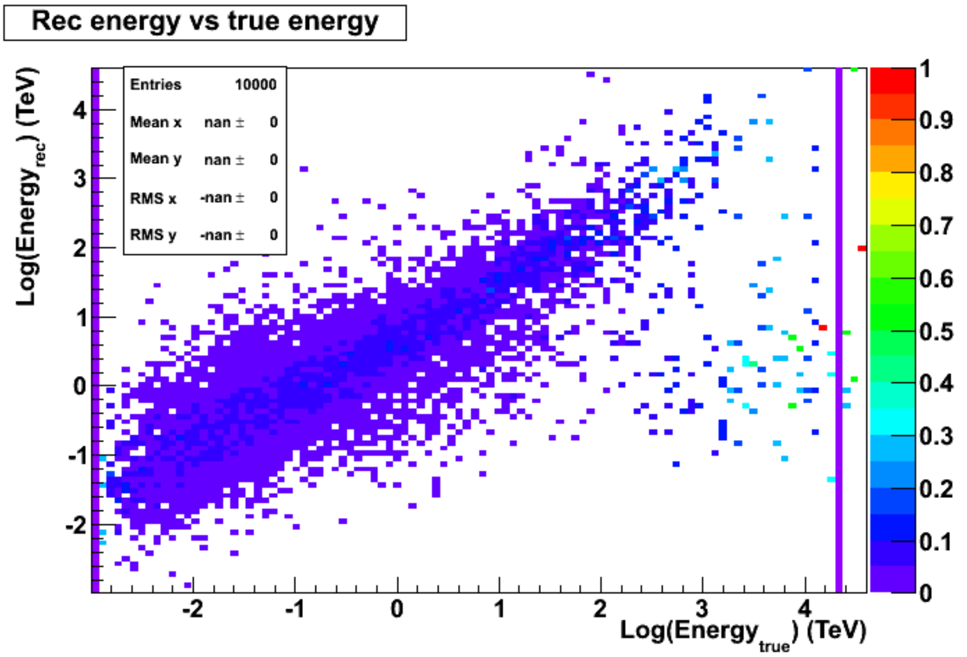

Figure A.3: Reconstructed energy as a function of the true energy for protons. Slices in reconstructed energy bins are normalized.

Appendix B

Distributions of the discriminant variables

In figure B.1 are shown all the discriminant variables distributions (from top to bottom: MSL, MSW, MSG, MDH and PDH) for simulated point-like and diffuse photons (green points), electrons (blue points) and protons (red points), from left to right. These are represented in the form of fitted histograms using the functions summarized in table B.1. These functions are introduced and studied in section 5.1 before being used for the analysis in section 5.2.1. Moreover, the maximum of these fitted functions of MSL, MSW and MSG for point-like gamma and protons were used to match data and simulations, as explained in section 5.1.2.1.

	MSL	MSW	MSG	MDH	PDH
Gamma	Double Gauss	Double Gauss	Double Gauss	Expo-Norm	Expo-Norm
Diffuse gamma	Double Gauss	Double Gauss	Double Gauss	Double Gauss	Expo-Norm
Electrons	Double Gauss	Double Gauss	Expo-Norm	Expo-Norm	Expo-Norm
Protons	Crystal Ball	Crystal Ball	Expo-Norm	Expo-Norm	Expo-Norm

Table B.1: Functions used to fit the five discriminant variables' PDFs for the four simulated types of particles.

The functions are described next:

- Double Gauss probability density function (named "Double Gauss"):

$$f(x; N_1, \bar{x}_1, \sigma_1, N_2, \bar{x}_2, \sigma_2) = N_1 \exp(-\frac{(x-\bar{x}_1)^2}{2\sigma_1^2}) + N_2 \exp(-\frac{(x-\bar{x}_2)^2}{2\sigma_2^2})$$

- The probability density function of the exponentially modified normal distribution (named "Expo-Norm"):

$$f(x; \mu, \sigma, \lambda) = \frac{\lambda}{2} \exp(\frac{\lambda}{2}(2\mu + \lambda\sigma^2 - 2x) \cdot \mathrm{erfc}(\frac{\mu + \lambda\sigma^2 - x}{\sqrt{2}\sigma})$$

  erfc is the complementary error function : $\mathrm{erfc}(x) = 1 - \mathrm{erf}(x) = \frac{2}{\sqrt{\pi}} \int_x^\infty e^{-t^2} \mathrm{d}t$

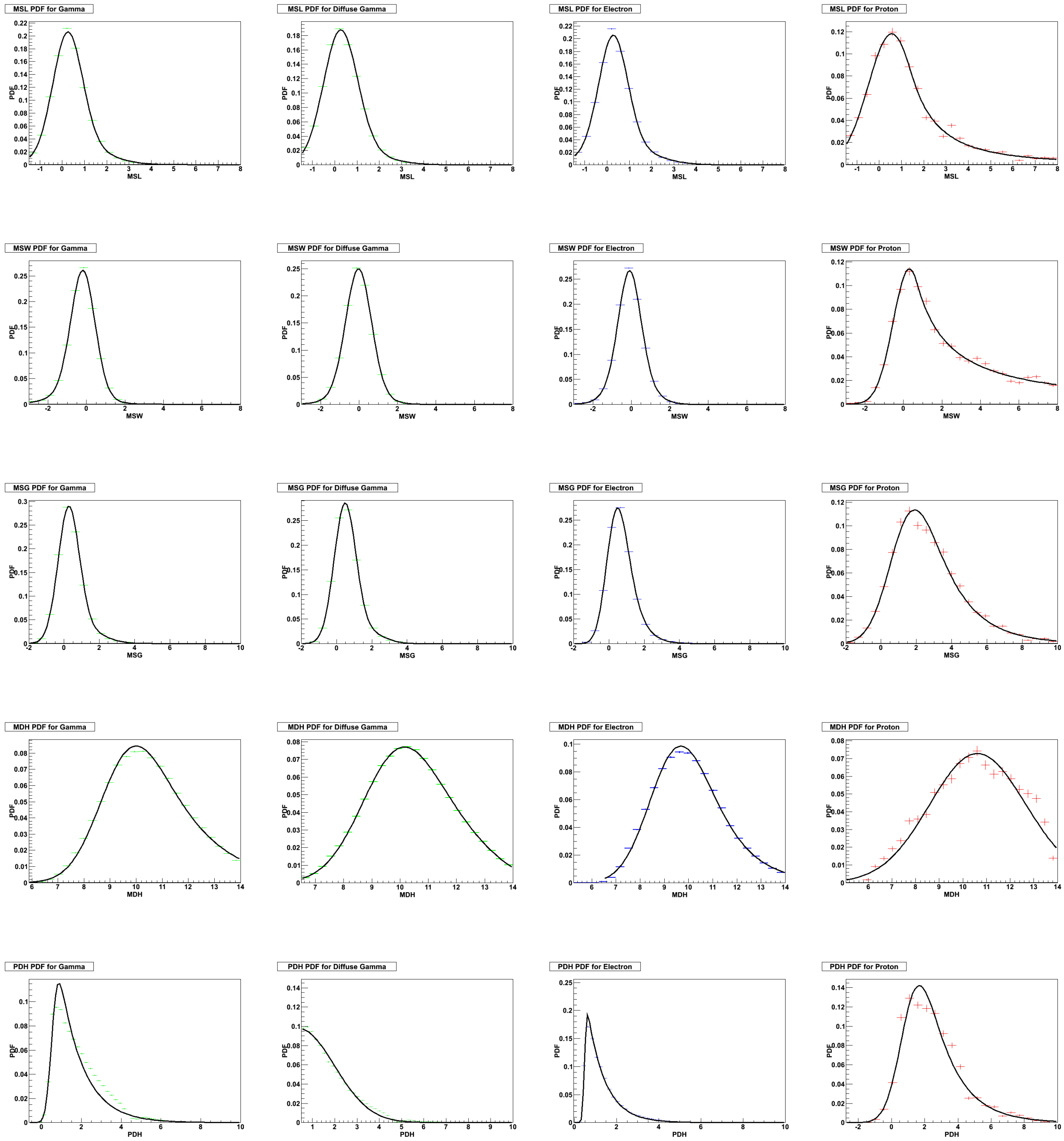

Figure B.1: PDFs of MSL, MSW, MSG, MDH and PDH from top to bottom for point-like gamma, diffuse gamma, electrons and protons from left to right.

- Crystal ball probability density function :

$$f(x;\alpha,n,\bar{x},\sigma) = N\cdot\begin{cases}\exp(-\frac{(x-\bar{x})^2}{2\sigma^2}); & \frac{x-\bar{x}}{\sigma} > -\alpha\\ A\cdot(B-\frac{x-\bar{x}}{\sigma})^{-n}; & \frac{x-\bar{x}}{\sigma} \leq -\alpha\end{cases}$$

where

$$A = \left(\frac{n}{|\alpha|}\right)^n \cdot \exp(-\frac{|\alpha|^2}{2})$$

$$B = \frac{n}{|\alpha|} - |\alpha|$$

$$N = \frac{1}{\sigma(C+D)}$$

is the normalization factor.

$$C = \frac{n}{|\alpha|}\frac{1}{n-1}\cdot\exp(-\frac{|\alpha|^2}{2})$$

$$D = \sqrt{\frac{\pi}{2}}(1+\mathrm{erf}(-\frac{|\alpha|}{\sqrt{2}})$$

erf is the error function evaluated at $-\frac{|\alpha|}{\sqrt{2}}$:

$$\mathrm{erf}(x) = \frac{2}{\sqrt{\pi}}\int_0^\infty e^{-t^2}\mathrm{d}t$$

Appendix C

Effect of zenith and energy corrections

In section 5.1.1 were presented the mean of the MDH distributions as well as their root mean square (rms) as a function of the optical efficiency, for different zenith angles before and after the angular correction. However, only the plots for simulated diffuse gamma were shown. Hereafter are those for point-like gamma, electrons and protons. It can be seen that the point-like gamma simulations are the most complete, with almost every zenith angle represented. Protons are those with less simulated data available.

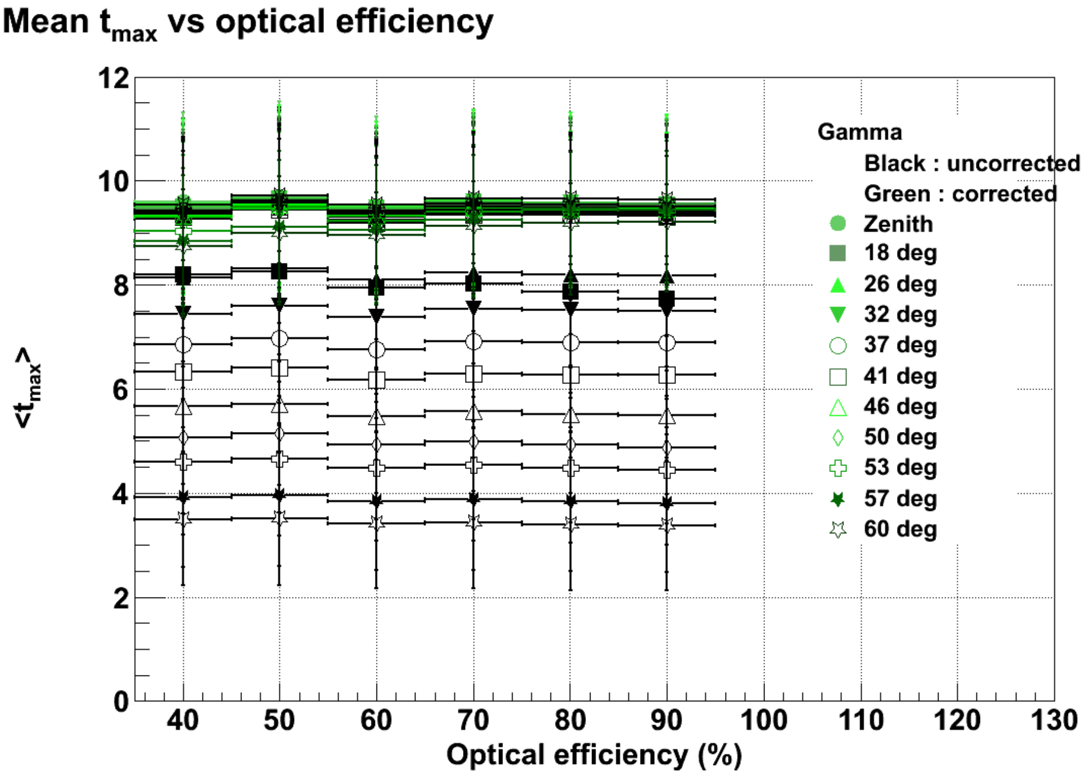

Figure C.1: Effect of zenith correction on the mean value of MDH for simulated point-like gamma and all optical efficiencies. Before correction (in black), the mean value of MDH is different for each zenith angle. After correction (in green) they are superimposed.

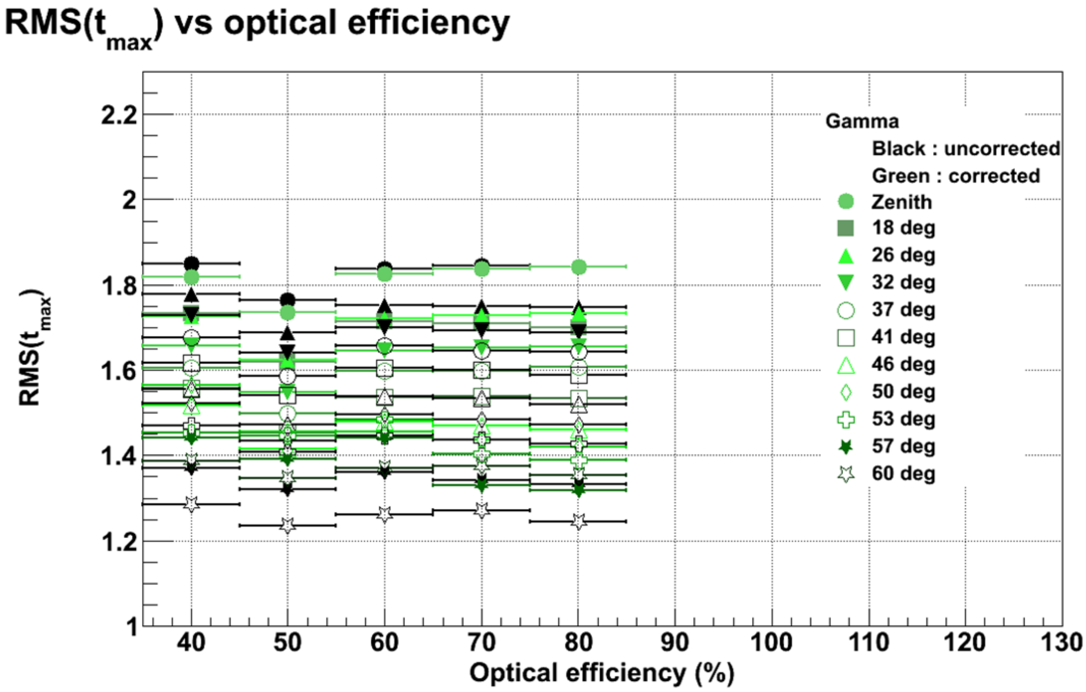

Figure C.2: Effect of zenith correction on the rms of MDH for simulated point-like gamma and all optical efficiencies. The correction does not seem to influence the width of the distribution. However, the evolution of the latter with the zenith angle will limit the effect of the correction. The narrower distributions, represented by a smaller rms for high zenith angles are explained by the fact that the energy threshold increases, so only showers with higher energies will trigger. These are known to have a better reconstruction and hence angular resolution.

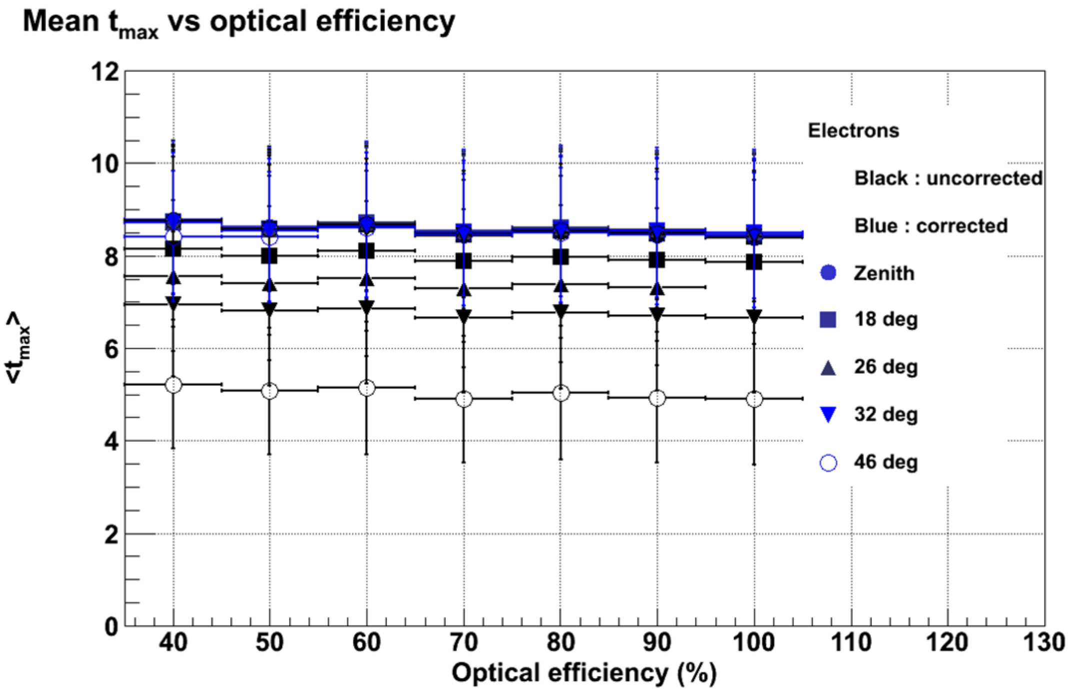

Figure C.3: Effect of zenith correction on the rms of MDH for simulated electrons and all optical efficiencies. See figure C.1 for comments.

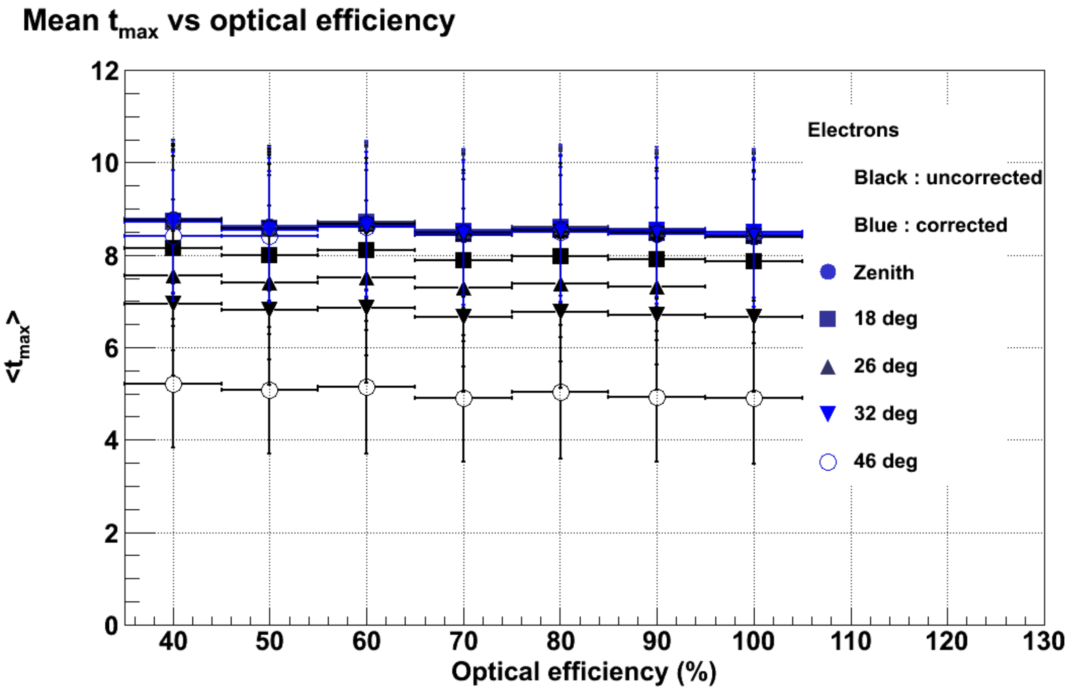

Figure C.4: Effect of zenith correction on the rms of MDH for simulated electrons and all optical efficiencies. See figure C.2 for comments.

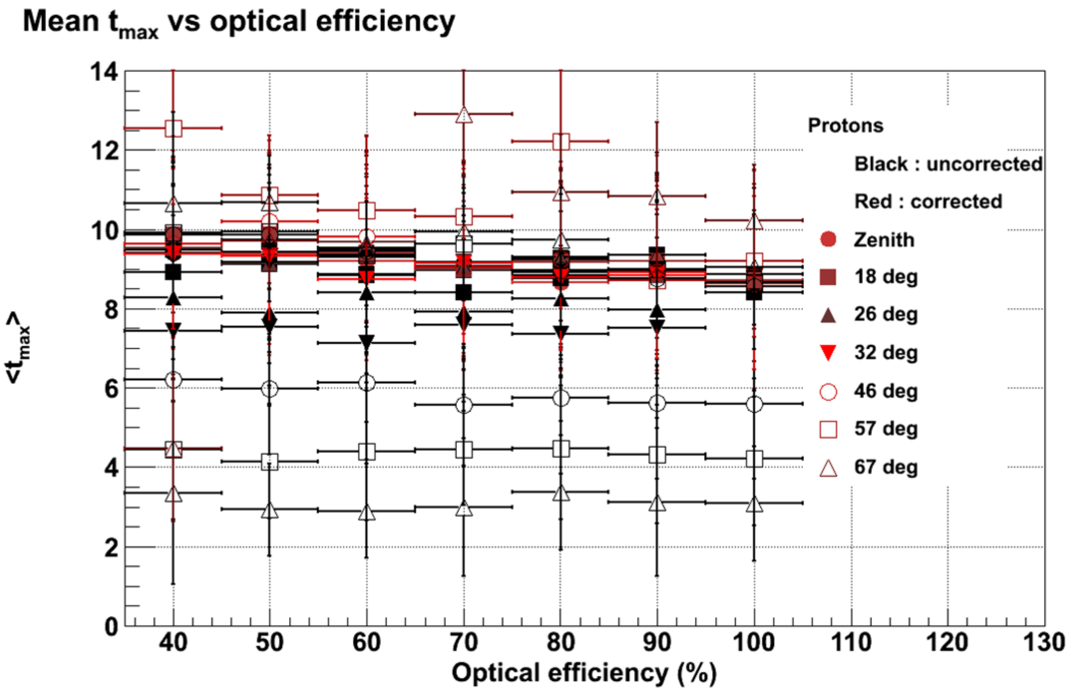

Figure C.5: Effect of zenith correction on the rms of MDH for simulated protons and all optical efficiencies. See figure C.1 for comments.

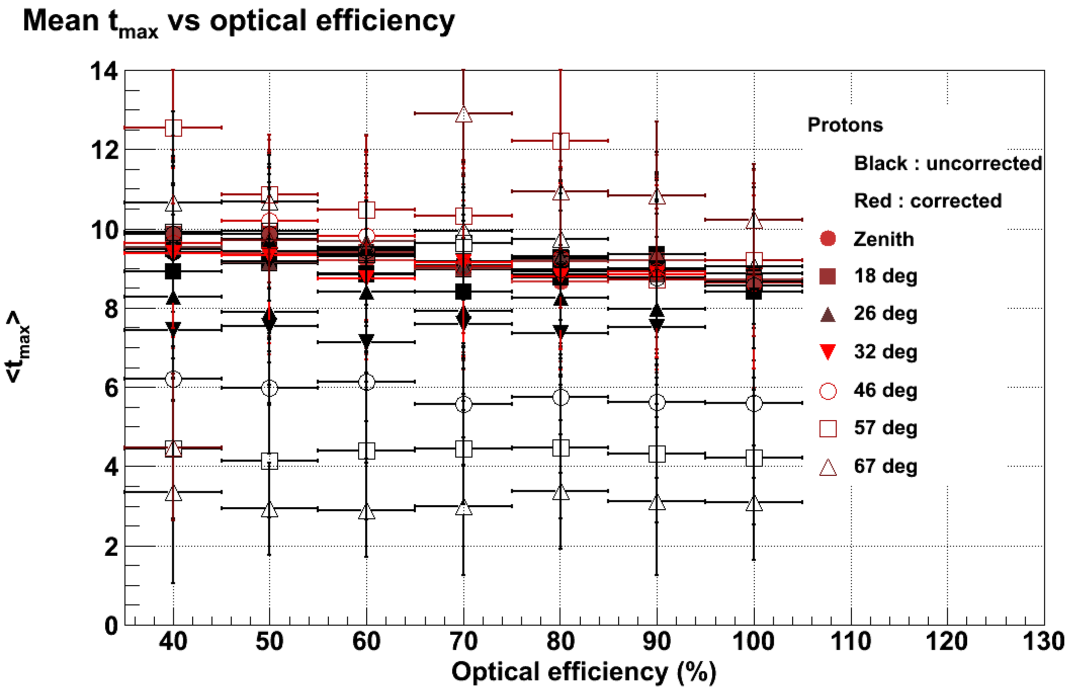

Figure C.6: Effect of zenith correction on the rms of MDH for simulated protons and all optical efficiencies. See figure C.2 for comments.

In addition, concerning the energy correction applied to the MDH PDF, the parameter a_e obtained from the linear fit of the distribution as a function of energy was presented for point-like gamma. Next are shown those for diffuse gamma, electrons and protons.

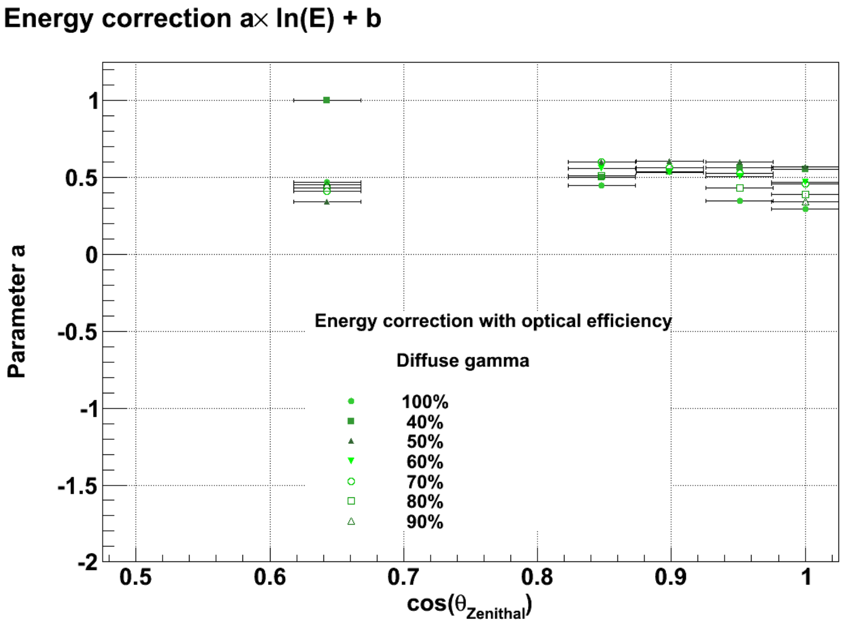

Figure C.7: Parameter a_e for each optical efficiency and zenith angle for simulated diffuse gamma. The values at 1 correspond to fits that did not converge. The evolution as a function of the zenith angle and optical efficiency are mainly due to effects of energy threshold. Indeed, as commented in section 2.1.5.3, for higher values of the zenith angle and lower values of the optical efficiency, the energy threshold increases, thus excluding low energy showers and thus influencing the distribution of MDH as a function of the energy.

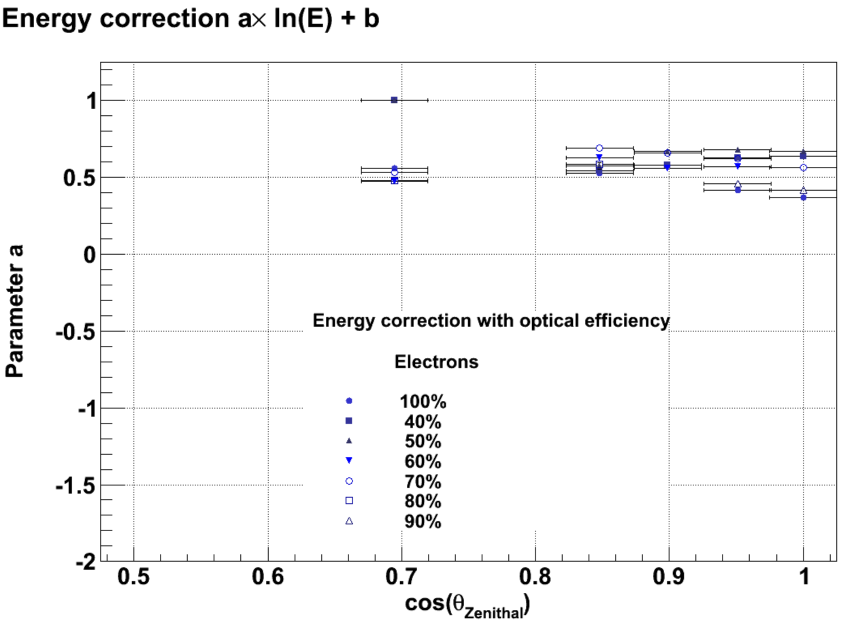

Figure C.8: Parameter a_e for each optical efficiency and zenith angle for simulated electrons. See figure C.7 for comments.

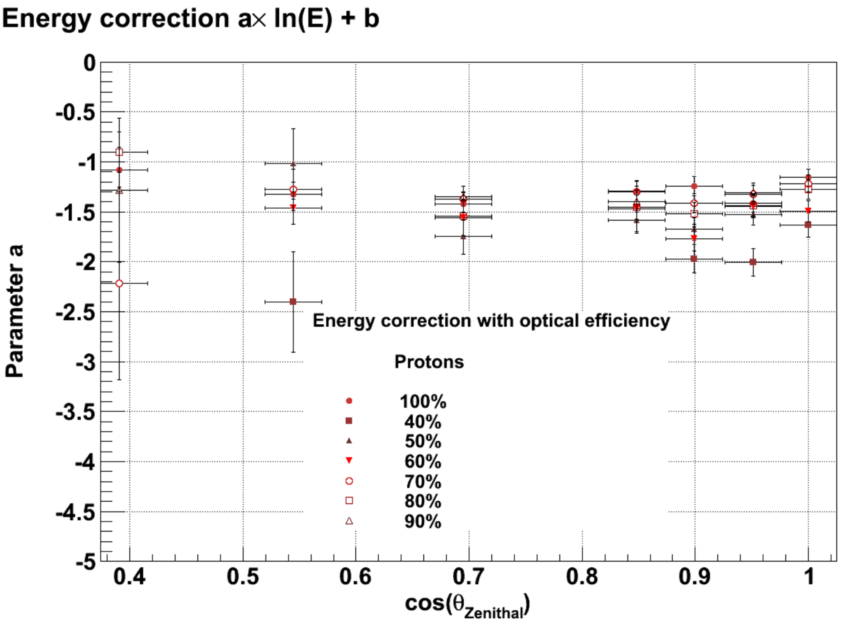

Figure C.9: Parameter a_e for each optical efficiency and zenith angle for simulated protons. See figure C.7 for comments.

Appendix D

Correlations between the discriminant variables

Correlation plots for diffuse gamma (figure D.1), electrons (D.2) and protons (D.3), with 2 telescopes used for reconstruction. The lower statistics of protons can be easily noted. Comments can be found in section 5.1.3

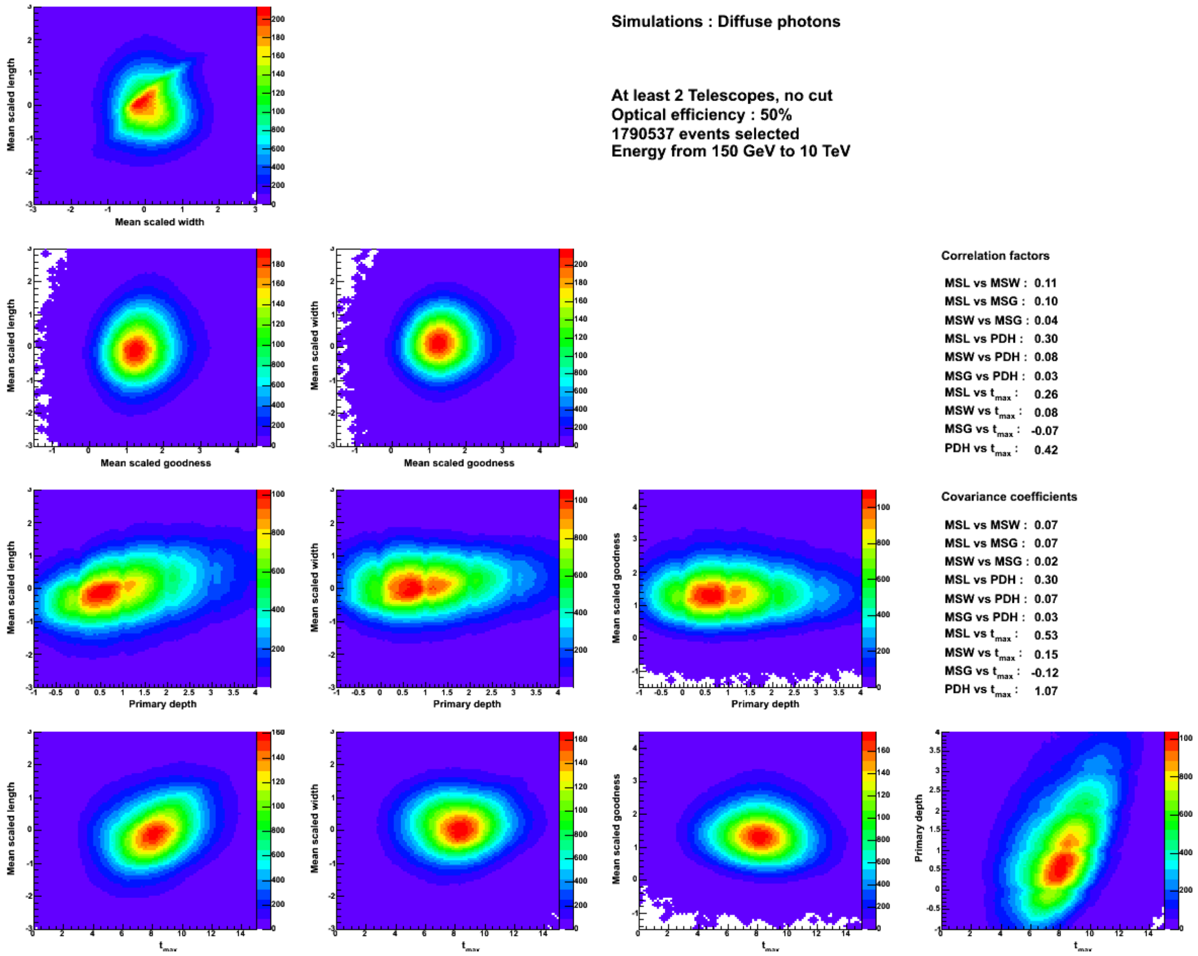

Simulations : Diffuse photons

At least 2 Telescopes, no cut
Optical efficiency : 50%
1790537 events selected
Energy from 150 GeV to 10 TeV

Correlation factors

MSL vs MSW : 0.11
MSL vs MSG : 0.10
MSW vs MSG : 0.04
MSL vs PDH : 0.30
MSW vs PDH : 0.08
MSG vs PDH : 0.03
MSL vs t_{max} : 0.26
MSW vs t_{max} : 0.08
MSG vs t_{max} : -0.07
PDH vs t_{max} : 0.42

Covariance coefficients

MSL vs MSW : 0.07
MSL vs MSG : 0.07
MSW vs MSG : 0.02
MSL vs PDH : 0.30
MSW vs PDH : 0.07
MSG vs PDH : 0.03
MSL vs t_{max} : 0.53
MSW vs t_{max} : 0.15
MSG vs t_{max} : -0.12
PDH vs t_{max} : 1.07

Figure D.1: Correlation plots for diffuse gamma reconstructed with 2 telescopes.

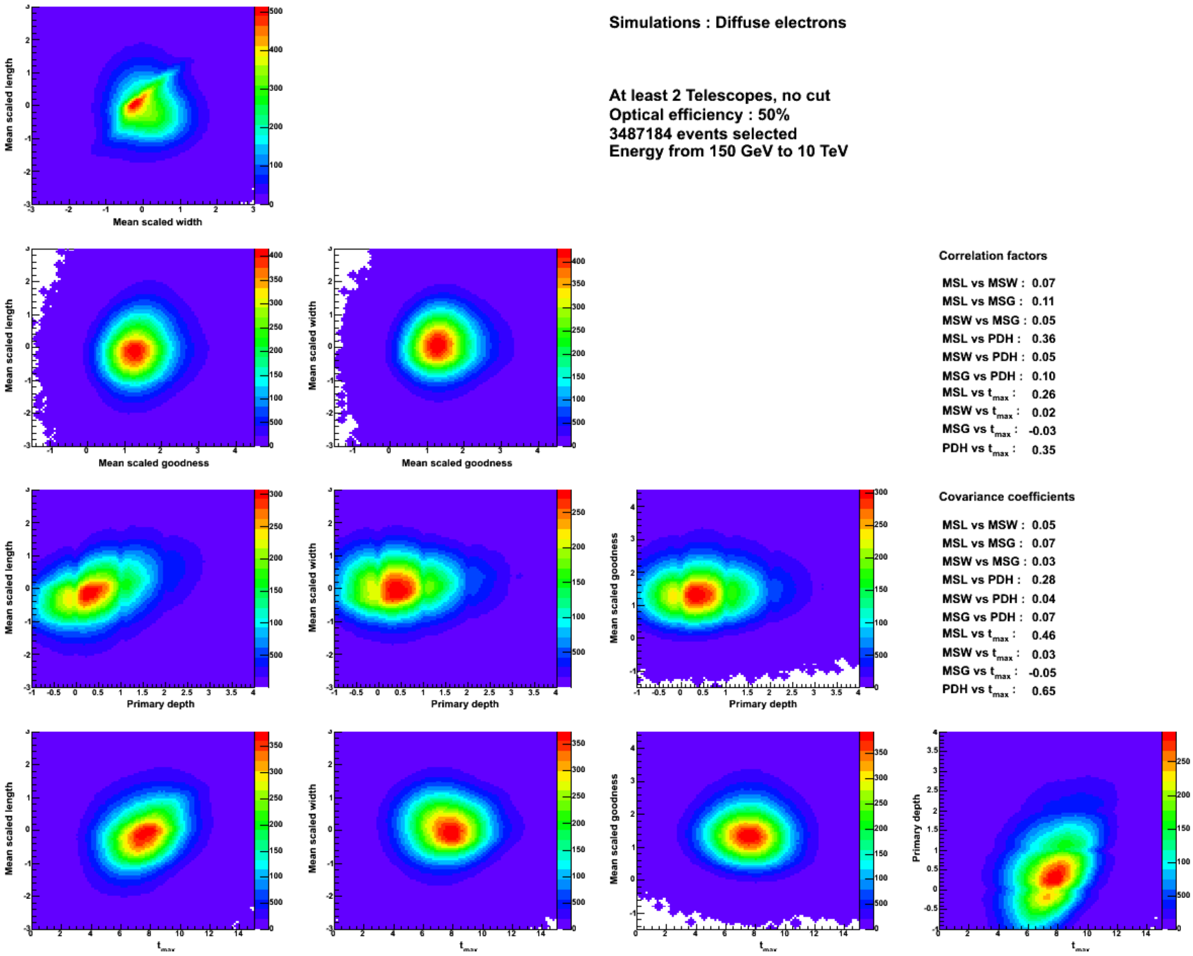

Simulations : Diffuse electrons

At least 2 Telescopes, no cut
Optical efficiency : 50%
3487184 events selected
Energy from 150 GeV to 10 TeV

Correlation factors

MSL vs MSW : 0.07
MSL vs MSG : 0.11
MSW vs MSG : 0.05
MSL vs PDH : 0.36
MSW vs PDH : 0.05
MSG vs PDH : 0.10
MSL vs t_{max} : 0.26
MSW vs t_{max} : 0.02
MSG vs t_{max} : -0.03
PDH vs t_{max} : 0.35

Covariance coefficients

MSL vs MSW : 0.05
MSL vs MSG : 0.07
MSW vs MSG : 0.03
MSL vs PDH : 0.28
MSW vs PDH : 0.04
MSG vs PDH : 0.07
MSL vs t_{max} : 0.46
MSW vs t_{max} : 0.03
MSG vs t_{max} : -0.05
PDH vs t_{max} : 0.65

Figure D.2: Correlation plots for electrons reconstructed with 2 telescopes.

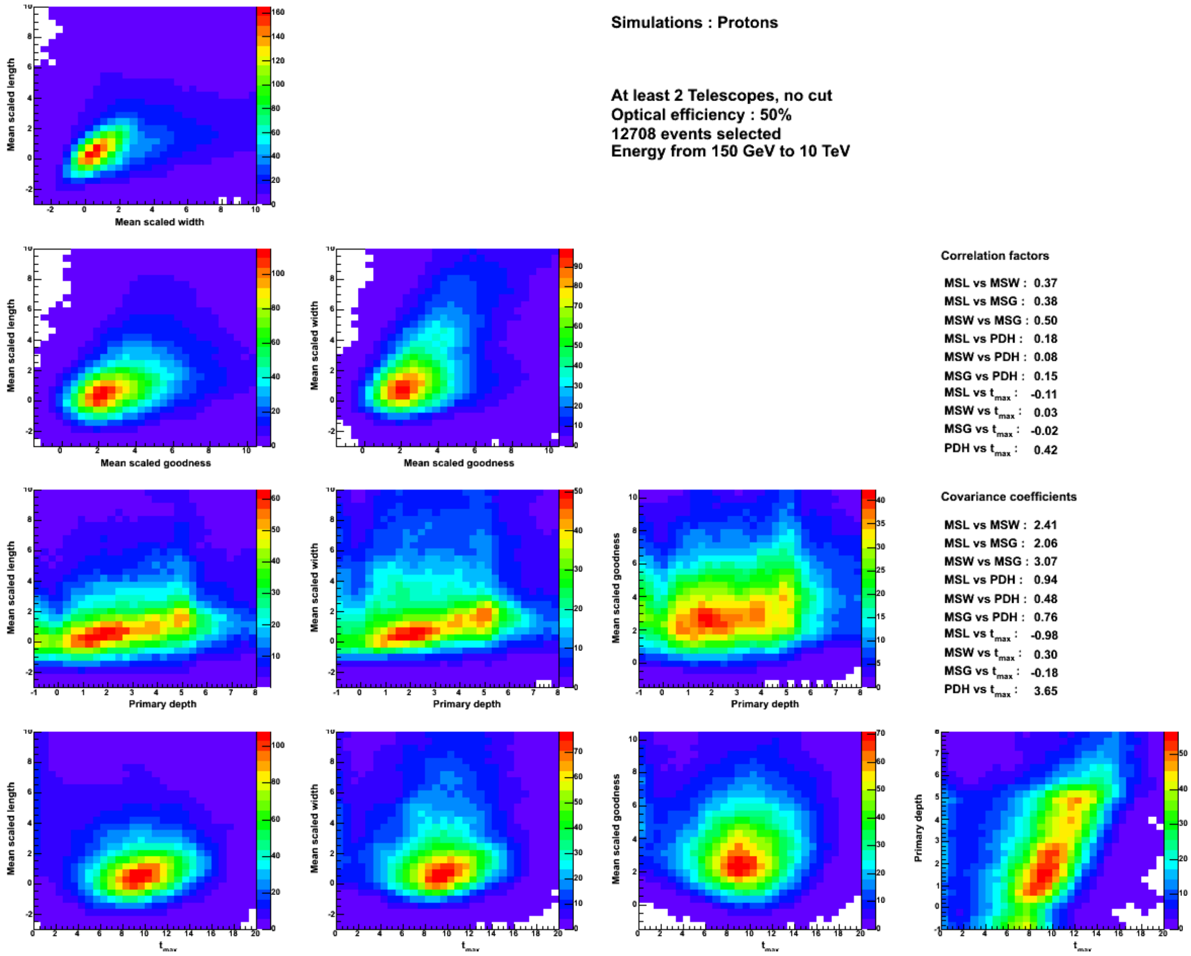

Simulations : Protons

At least 2 Telescopes, no cut
Optical efficiency : 50%
12708 events selected
Energy from 150 GeV to 10 TeV

Correlation factors

MSL vs MSW : 0.37
MSL vs MSG : 0.38
MSW vs MSG : 0.50
MSL vs PDH : 0.18
MSW vs PDH : 0.08
MSG vs PDH : 0.15
MSL vs t_{max} : -0.11
MSW vs t_{max} : 0.03
MSG vs t_{max} : -0.02
PDH vs t_{max} : 0.42

Covariance coefficients

MSL vs MSW : 2.41
MSL vs MSG : 2.06
MSW vs MSG : 3.07
MSL vs PDH : 0.94
MSW vs PDH : 0.48
MSG vs PDH : 0.76
MSL vs t_{max} : -0.98
MSW vs t_{max} : 0.30
MSG vs t_{max} : -0.18
PDH vs t_{max} : 3.65

Figure D.3: Correlation plots for protons reconstructed with 2 telescopes.

Appendix E

Effect of the energy domain on the PDFs

To select the intervals in which the discriminant variables could be used, the influence of the energy domain on their shape was tested. In section 5.1.4 were presented the ratio between the histograms obtained in two energy domains: 150 GeV - 10 TeV and 300 GeV - 3 TeV for the five discriminant variables in the case of simulated diffuse gamma and protons. Here are shown those for point-like gamma and diffuse electrons.

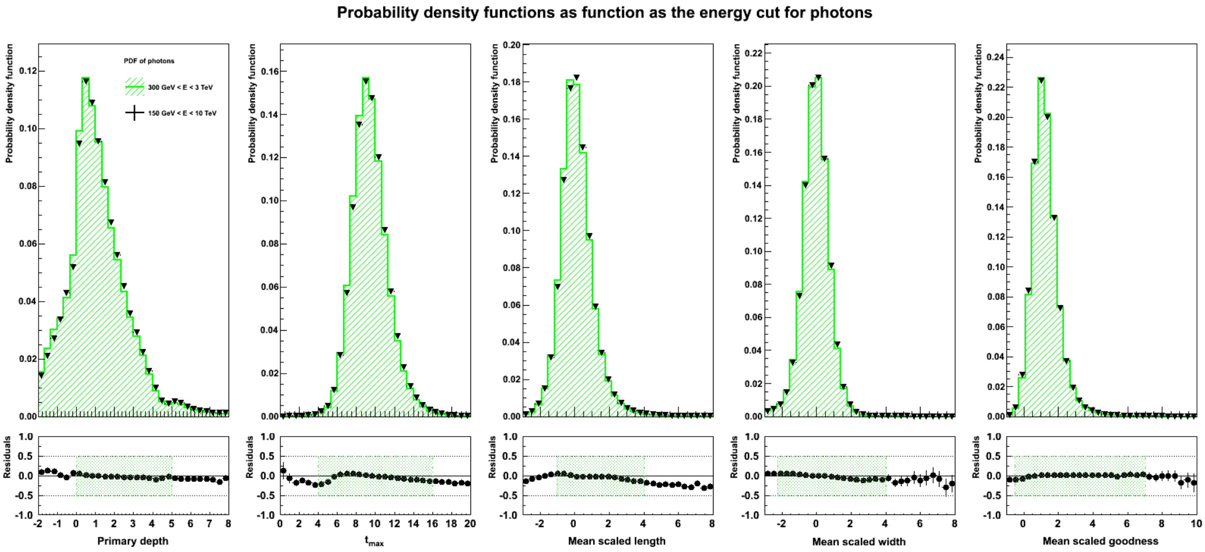

Figure E.1: PDFs for point-like gamma in different energy domains.

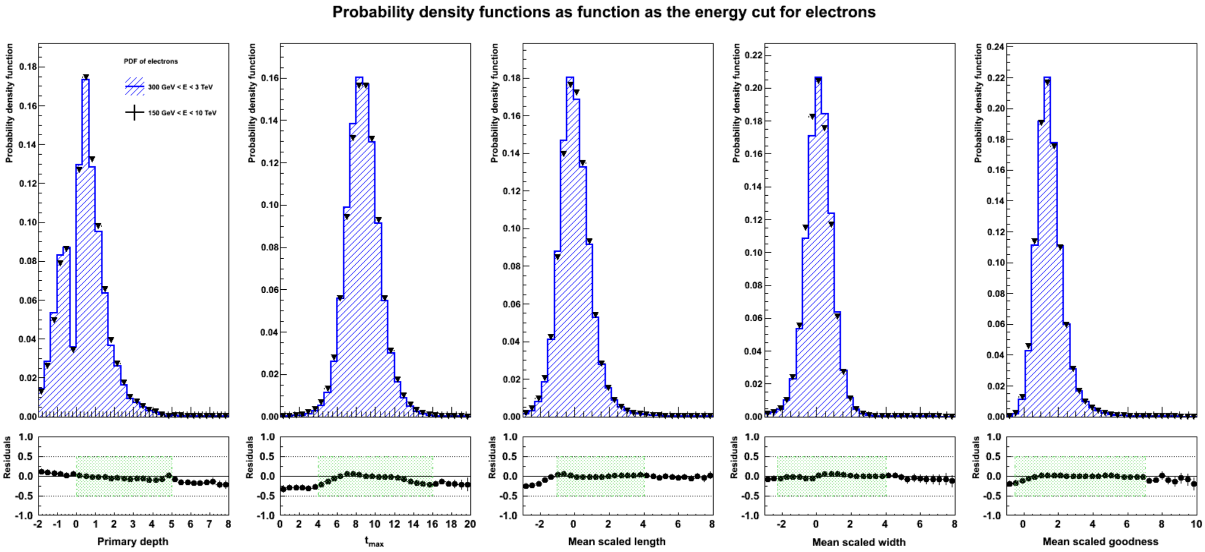

Figure E.2: PDFs for electrons in different energy domains.

Bibliography

[1] C. E. Fichtel, R. C. Hartman, D. A. Kniffen, et al., *High-energy gamma-ray results from the second small astronomy satellite*, ApJ **198** (1975) 163–182.

[2] e. a. Swanenburg, B.N., *Second COS-b catalog of high-energy gamma-ray sources*, Astrophysical Journal **243** (1981) L69–L73.

[3] R. C. Hartman, D. L. Bertsch, S. D. Bloom, et al., *The Third EGRET Catalog of High-Energy Gamma-Ray Sources*, The Astrophysical Journal Supplement Series **123** no. 1, (1999) 79.

[4] W. S. Paciesas, C. A. Meegan, A. von Kienlin, et al., *The Fermi GBM Gamma-Ray Burst Catalog: The First Two Years*, ApJS **199** (2012) 18, `arXiv:1201.3099 [astro-ph.HE]`.

[5] P. L. Nolan, A. A. Abdo, M. Ackermann, et al., *Fermi Large Area Telescope Second Source Catalog*, ApJS **199** (2012) 31, `arXiv:1108.1435 [astro-ph.HE]`.

[6] R. Atkins, W. Benbow, D. Berley, et al., *Observation of TeV Gamma Rays from the Crab Nebula with Milagro Using a New Background Rejection Technique*, The Astrophysical Journal **595** no. 2, (2003) 803.

[7] A. A. Abdo, B. Allen, D. Berley, et al., *TeV Gamma-Ray Sources from a Survey of the Galactic Plane with Milagro*, The Astrophysical Journal Letters **664** no. 2, (2007) L91.

[8] T. C. Weekes, M. F. Cawley, D. J. Fegan, et al., *Observation of TeV gamma rays from the Crab nebula using the atmospheric Cerenkov imaging technique*, ApJ **342** (1989) 379–395.

[9] F. Aharonian, A. Akhperjanian, M. Beilicke, et al., *The Crab Nebula and Pulsar between 500 GeV and 80 TeV: Observations with the HEGRA Stereoscopic Air Cerenkov Telescopes*, The Astrophysical Journal **614** no. 2, (2004) 897.

[10] M. de Naurois and CELESTE Collaboration, *Status and Current Sensitivity of the CELESTE Experiment*, in *American Institute of Physics Conference Series*, F. A. Aharonian and H. J. Völk, eds., p. , 540. Apr., 2001. `astro-ph/0010265`.

[11] J. Cortina, F. Goebel, T. Schweizer, and for the MAGIC Collaboration, *Technical Performance of the MAGIC Telescopes*, ArXiv e-prints (2009), `arXiv:0907.1211 [astro-ph.IM]`.

[12] J. Holder, R. W. Atkins, H. M. Badran, et al., *The first VERITAS telescope*, Astroparticle Physics **25** (2006) 391–401, `astro-ph/0604119`.

[13] M. Actis, G. Agnetta, F. Aharonian, et al., *Design concepts for the Cherenkov Telescope Array CTA: an advanced facility for ground-based high-energy gamma-ray astronomy*, Experimental Astronomy **32** no. 3, (2011) 193–316.

[14] M. De Naurois, *L'expérience CELESTE: Reconversion d'une centrale solaire pour l'astronomie gamma. Première observation de la Nébuleuse du Crabe et du Blazar Markarian 421 entre 30 et 300 GeV.* Theses, Université Pierre et Marie Curie - Paris VI, May, 2000. `https://tel.archives-ouvertes.fr/tel-00004261`. Michel BAUBILLIER: Président Hélène SOL: Rapporteur François LE DIBERDER: Rapporteur David SMITH Patrick FLEURY Marie Claude COUSINOU René ONG.

[15] J. B. et al. (Particle Data Group), *Cosmic Rays*, Phys. Rev. D **86** no. 010001, (2012).

[16] E. Longo and I. Sestili, *Monte Carlo calculation of photon-initiated electromagnetic showers in lead glass*, Nuclear Instruments and Methods **128** no. 2, (1975) 283 – 307.

[17] J. Hinton, *The status of the HESS project*, New Astronomy Reviews **48** no. 5–6, (2004) 331 – 337. 2nd {VERITAS} Symposium on the Astrophysics of Extragalactic Sources.

[18] K. Bernlöhr, O. Carrol, R. Cornils, et al., *The optical system of the H.E.S.S. imaging atmospheric Cherenkov telescopes. Part I: layout and components of the system*, Astroparticle Physics **20** no. 2, (2003) 111 – 128.

[19] W. Hofmann, *How to focus a Cherenkov telescope*, Journal of Physics G: Nuclear and Particle Physics **27** no. 4, (2001) 933.

[20] R. Cornils, S. Gillessen, I. Jung, et al., *The optical system of the H.E.S.S. imaging atmospheric Cherenkov telescopes. Part II: mirror alignment and point spread function*, Astroparticle Physics **20** no. 2, (2003) 129 – 143.

[21] V. Chitnis and P. Bhat, *Čerenkov photon density fluctuations in extensive air showers*, Astroparticle Physics **9** no. 1, (1998) 45 – 63.

[22] D. Berge, *A detailed study of the gamma-ray supernova remnant RX J1713.7-3946 with H.E.S.S.* PhD thesis, Ruperto-Carola University of Heidelberg, 2006.

[23] K. Stycz, *An unbinned Fit of H.E.S.S. Sources using the Log-Likelihood Method.* PhD thesis, Erlangen Centre for Astroparticle Physics, 2010.

[24] F. Piron, A. Djannati-Ataï, M. Punch, et al., *Temporal and spectral gamma-ray properties of Mkn 421 above 250 GeV from CAT observations between 1996 and 2000*, A&A **374** no. 3, (2001) 895–906.

[25] A. M. Hillas, *Cerenkov light images of EAS produced by primary gamma*, International Cosmic Ray Conference **3** (1985) 445–448.

[26] A. Daum, G. Hermann, M. Heß, et al., *First results on the performance of the {HEGRA} {IACT} array*, Astroparticle Physics **8** no. 1–2, (1997) 1 – 11.

[27] B. Rossi, *High-Energy Particles.* New York: Prentice-Hall, 1952.

[28] HESS Collaboration Collaboration, M. de Naurois, J. Guy, A. Djannati-Atai, and J. Tavernet, *Application of an analysis method based on a semianalytical shower model to the first HESS telescope*,.

[29] M. de Naurois, *Analysis methods for Atmospheric Cherenkov Telescopes*, pp. , 149–162. Palaiseau, France, 2005.

[30] H. C. M. Lemoine-Goumard, *3D-reconstruction of gamma-ray showers with a stereoscopic system*, pp. , 173–182. Palaiseau, France, 2005.

[31] S. F. f. t. H. C. J. Hinton, D. Berge, *Background Modeling in Ground-Based Cherenkov Astronomy*, pp. , 183–190. Palaiseau, France, 2005.

[32] V. Hess, *Observation of Penetrating Radiation in Seven Balloon Flights*, Phys.Zeitschr. **13** no. 1084, (1912).

[33] E. Fermi, *On the Origin of the Cosmic Radiation*, Phys. Rev. **75** (1949) 1169–1174.

[34] E. Fermi, *Galactic Magnetic Fields and the Origin of Cosmic Radiation.*, ApJ **119** (1954) 1.

[35] M. De Naurois, *Very High Energy astronomy from H.E.S.S. to CTA. Opening of a new astronomical window on the non-thermal Universe.* Habilitation à diriger des recherches, Université Pierre et Marie Curie - Paris VI, Mar., 2012. `https://tel.archives-ouvertes.fr/tel-00687872`.

[36] A. Hillas, *The Origin of Ultra-High-Energy Cosmic Rays*, Annual Review of Astronomy and Astrophysics **22** (1984) 425–444.

[37] S. Lucek and A. Bell, *Non-Linear Amplification of a Magnetic Field Driven by Cosmic Ray Streaming*, Astrophysics and Space Science **272** no. 1-3, (2000) 255–262.

[38] A. R. Bell, *Turbulent amplification of magnetic field and diffusive shock acceleration of cosmic rays*, Monthly Notices of the Royal Astronomical Society **353** no. 2, (2004) 550–558.

[39] P. M. Bauleo and J. R. Martino, *The dawn of the particle astronomy era in ultra-high-energy cosmic rays*, Nature **458** no. 7240, (2009) 847–851.

[40] R. U. Abbasi, M. Abe, T. Abu-Zayyad, et al., *Indications of Intermediate-scale Anisotropy of Cosmic Rays with Energy Greater Than 57 EeV in the Northern Sky Measured with the Surface Detector of the Telescope Array Experiment*, The Astrophysical Journal Letters **790** no. 2, (2014) L21.

[41] M. Ackermann, M. Ajello, A. Allafort, et al., *Detection of the Characteristic Pion-Decay Signature in Supernova Remnants*, Science **339** no. 6121, (2013) 807–811, `http://www.sciencemag.org/content/339/6121/807.full.pdf`.

[42] J. Arons, *Pulsar Emission: Where to Go*, pp. , 373–420. Springer Berlin Heidelberg, 2009. `http://dx.doi.org/10.1007/978-3-540-76965-1_15`.

[43] A. Domínguez, J. D. Finke, F. Prada, et al., *Detection of the Cosmic γ-Ray Horizon from Multiwavelength Observations of Blazars*, ApJ **770** (2013) 77, `arXiv:1305.2162 [astro-ph.CO]`.

[44] A. A. Abdo, B. T. Allen, T. Aune, et al., *The Large-Scale Cosmic-Ray Anisotropy as Observed with Milagro*, The Astrophysical Journal **698** no. 2, (2009) 2121.

[45] R. Abbasi, Y. Abdou, T. Abu-Zayyad, et al., *Measurement of the Anisotropy of Cosmic-ray Arrival Directions with IceCube*, The Astrophysical Journal Letters **718** no. 2, (2010) L194.

[46] K. Greisen, *End to the Cosmic-Ray Spectrum?*, Phys. Rev. Lett. **16** (1966) 748–750.

[47] G. Zatsepin and V. Kuzmin, *Upper limit of the spectrum of cosmic rays*, JETP Lett. **4** (1966) 78–80.

[48] G. B. Thomson, f. t. High Resolution Fly's Eye, and Collaboration, *Observation of the GZK Cutoff by the HiRes Experiment*, ArXiv Astrophysics e-prints (2006), `astro-ph/0609403`.

[49] M. Takeda, N. Hayashida, K. Honda, et al., *Extension of the Cosmic-Ray Energy Spectrum beyond the Predicted Greisen-Zatsepin-Kuz'min Cutoff*, Phys. Rev. Lett. **81** (1998) 1163–1166.

[50] The Pierre Auger Collaboration Collaboration, J. Abraham, P. Abreu, M. Aglietta, et al., *Observation of the Suppression of the Flux of Cosmic Rays above* 4×10^{19} eV, Phys. Rev. Lett. **101** (2008) 061101.

[51] P. Sokolsky and HiRes Collaboration, *Final Results from the High Resolution Fly's Eye (HiRes) Experiment*, Nuclear Physics B Proceedings Supplements **212** (2011) 74–78, `arXiv:1010.2690 [astro-ph.HE]`.

[52] H.E.S.S. Collaboration Collaboration, F. Aharonian, A. G. Akhperjanian, U. Barres de Almeida, et al., *Energy Spectrum of Cosmic-Ray Electrons at TeV Energies*, Phys. Rev. Lett. **101** (2008) 261104.

[53] F. Aharonian, A. Atoyan, and H. Volk, *High energy electrons and positrons in cosmic rays as an indicator of the existence of a nearby cosmic tevatron*, Astron.Astrophys. **294** (1995) L41–L44.

[54] T. Kobayashi, Y. Komori, K. Yoshida, and J. Nishimura, *The Most Likely Sources of High-Energy Cosmic-Ray Electrons in Supernova Remnants*, The Astrophysical Journal **601** no. 1, (2004) 340.

[55] S. Hawking, *Particle creation by black holes*, Communications in Mathematical Physics **43** no. 3, (1975) 199–220.

[56] M. B. Hindmarsh and T. W. B. Kibble, *Cosmic strings*, Reports on Progress in Physics **58** no. 5, (1995) 477.

[57] C. T. Hill, *Monopolonium*, Nuclear Physics B **224** no. 3, (1983) 469 – 490.

[58] D. N. Spergel, L. Verde, H. V. Peiris, et al., *First-Year Wilkinson Microwave Anisotropy Probe (WMAP) Observations: Determination of Cosmological Parameters*, The Astrophysical Journal Supplement Series **148** no. 1, (2003) 175.

[59] Planck Collaboration, P. A. R. Ade et al., *Planck 2013 results. XVI. Cosmological parameters*, Astron. Astrophys. **571** (2014) A16, `arXiv:1303.5076 [astro-ph.CO]`.

[60] G. Servant and T. M. Tait, *Is the lightest Kaluza–Klein particle a viable dark matter candidate?*, Nuclear Physics B **650** no. 1–2, (2003) 391 – 419.

[61] C.-H. Chen, C.-Q. Geng, and D. Zhuridov, *Resolving Fermi, PAMELA and ATIC anomalies in split supersymmetry without R-parity*, The European Physical Journal C **67** no. 3-4, (2010) 479–487.

[62] O. Adriani, G. C. Barbarino, G. A. Bazilevskaya, et al., *Cosmic-Ray Electron Flux Measured by the PAMELA Experiment between 1 and 625 GeV*, Phys. Rev. Lett. **106** (2011) 201101.

[63] F. Aharonian, A. G. Akhperjanian, A. R. Bazer-Bachi, et al., *Discovery of very-high-energy gamma-rays from the Galactic Centre ridge*, Nature **439** no. 7077, (2006) 695–698.

[64] M. Vivier and for the VERITAS collaboration, *Indirect searches for dark matter annihilations toward dwarf spheroidal galaxies with VERITAS*, ArXiv e-prints (2011), `arXiv:1110.6615 [astro-ph.HE]`.

[65] A. Abramowski, F. Acero, F. Aharonian, et al., *H.E.S.S. Observations of the Globular Clusters NGC 6388 and M15 and Search for a Dark Matter Signal*, The Astrophysical Journal **735** no. 1, (2011) 12.

[66] J. Aleksi, S. Ansoldi, L. Antonelli, et al., *Optimized dark matter searches in deep observations of Segue 1 with MAGIC*, JCAP **1402** (2014) 008, `arXiv:1312.1535 [hep-ph]`.

[67] Fermi LAT Collaboration Collaboration, A. A. Abdo, M. Ackermann, M. Ajello, et al., *Spectrum of the Isotropic Diffuse Gamma-Ray Emission Derived from First-Year Fermi Large Area Telescope Data*, Phys. Rev. Lett. **104** (2010) 101101.

[68] U. Oberlack, *Extragalactic diffuse gamma-ray emission at high energies*, Physics **3** (2010) 21.

[69] Aharonian, F., Akhperjanian, A. G., Anton, G., et al., *Probing the ATIC peak in the cosmic-ray electron spectrum with H.E.S.S.*, A&A **508** no. 2, (2009) 561–564.

[70] A. Kochanov, T. Sinegovskaya, and S. Sinegovsky, *High-energy cosmic-ray fluxes in the Earth atmosphere: Calculations vs experiments*, Astroparticle Physics **30** no. 5, (2008) 219 – 233.

[71] M. Kuhlen and D. Malyshev, *ATIC, PAMELA, HESS, and Fermi data and nearby dark matter subhalos*, Phys. Rev. D **79** (2009) 123517.

[72] V. Barger, Y. Gao, W.-Y. Keung, D. Marfatia, and G. Shaughnessy, *Dark matter and pulsar signals for Fermi LAT, PAMELA, ATIC, {HESS} and {WMAP} data*, Physics Letters B **678** no. 3, (2009) 283 – 292.

[73] A. A. Abdo, M. Ackermann, M. Ajello, et al., *Measurement of the Cosmic Ray* $e^+ + e^-$ *Spectrum from 20 GeV to 1 TeV with the Fermi Large Area Telescope*, Phys. Rev. Lett. **102** (2009) 181101.

[74] AMS Collaboration Collaboration, M. Aguilar, G. Alberti, B. Alpat, et al., *First Result from the Alpha Magnetic Spectrometer on the International Space Station: Precision Measurement of the Positron Fraction in Primary Cosmic Rays of 0.5–350 GeV*, Phys. Rev. Lett. **110** (2013) 141102.

[75] V. Poireau, *Rapports d'embranchement et résonances dans les désintégrations des mésons B en particules charmées dans BaBar et flux cosmique de positons dans AMS*. Habilitation à diriger des recherches, Université de Savoie, Nov., 2013. `https://tel.archives-ouvertes.fr/tel-00909741`.

[76] C. Weniger, *A tentative gamma-ray line from Dark Matter annihilation at the Fermi Large Area Telescope*, Journal of Cosmology and Astroparticle Physics **2012** no. 08, (2012) 007.

[77] K. Nishijima, *Very High Energy Gamma-ray Observations of AGN with CANGAROO*, PASA - Publications of the Astronomical Society of Australia **19** (2002) 26–28.

[78] ICRC, ed., vol. 2626. Hamburg, 2001.

[79] F. Aharonian, A. G. Akhperjanian, K.-M. Aye, et al., *H.E.S.S. observations of PKS 2155-304*, A&A **430** no. 3, (2005) 865–875.

[80] F. Aharonian, A. G. Akhperjanian, A. R. Bazer-Bachi, et al., *An Exceptional Very High Energy Gamma-Ray Flare of PKS 2155–304*, The Astrophysical Journal Letters **664** no. 2, (2007) L71.

[81] H.E.S.S. Collaboration Collaboration, F. Aharonian, A. G. Akhperjanian, U. Barres de Almeida, et al., *Limits on an Energy Dependence of the Speed of Light from a Flare of the Active Galaxy PKS 2155-304*, Phys. Rev. Lett. **101** (2008) 170402.

[82] F. Aharonian, A. G. Akhperjanian, G. Anton, et al., *Simultaneous multiwavelength observations of the second exceptional γ-ray flare of PKS 2155-304 in July 2006*, A&A **502** (2009) 749–770, `arXiv:0906.2002 [astro-ph.CO]`.

[83] H.E.S.S. Collaboration, A. Abramowski, F. Acero, et al., *VHE γ-ray emission of PKS 2155-304: spectral and temporal variability*, A&A **520** (2010) A83, `arXiv:1005.3702 [astro-ph.HE]`.

[84] H.E.S.S. Collaboration, A. Abramowski, F. Acero, et al., *Search for Lorentz Invariance breaking with a likelihood fit of the PKS 2155-304 flare data taken on MJD 53944*, Astroparticle Physics **34** (2011) 738–747, `arXiv:1101.3650 [astro-ph.HE]`.

[85] H.E.S.S. Collaboration, Abramowski, A., Acero, F., et al., *A multiwavelength view of the flaring state of PKS 2155-304 in 2006*, A&A **539** (2012) A149.

[86] H.E.S.S. Collaboration Collaboration, F. Aharonian et al., *Multi-wavelength observations of PKS 2155-304 with H.E.S.S*, Astron.Astrophys. (2005), `arXiv:astro-ph/0506593 [astro-ph]`.

[87] F. Aharonian, A. G. Akhperjanian, G. Anton, et al., *Simultaneous Observations of PKS 2155–304 with HESS, Fermi, RXTE, and Atom: Spectral Energy Distributions and Variability in a Low State*, The Astrophysical Journal Letters **696** no. 2, (2009) L150.

[88] H.E.S.S. Collaboration Collaboration, A. Abramowski et al., *Constraints on axionlike particles with H.E.S.S. from the irregularity of the PKS 2155-304 energy spectrum*, Phys.Rev. **D88** no. 10, (2013) 102003, `arXiv:1311.3148 [astro-ph.HE]`.

[89] The H.E.S.S. Collaboration, Abramowski, A., Acero, F., et al., *Simultaneous multi-wavelength campaign on PKS 2005-489 in a high state*, A&A **533** (2011) A110.

[90] HESS Collaboration, Acero, F., Aharonian, F., et al., *PKS 2005-489 at VHE: four years of monitoring with HESS and simultaneous multi-wavelength observations*******, A&A **511** (2010) A52.

[91] F. Aharonian, A. G. Akhperjanian, K.-M. Aye, et al., *Discovery of VHE gamma rays from PKS 2005–489*, A&A **436** no. 2, (2005) L17–L20.

[92] F. Aharonian, A. G. Akhperjanian, A. R. Bazer-Bachi, et al., *Detection of VHE gamma-ray emission from the distant blazar 1ES1101-232 with HESS and broadband characterisation*, A&A **470** no. 2, (2007) 475–489.

[93] F. Aharonian, A. G. Akhperjanian, U. Barres de Almeida, et al., *Discovery of VHE γ-rays from the distant BL Lacertae 1ES0347-121*, A&A **473** no. 3, (2007) L25–L28.

[94] HESS Collaboration, F. Aharonian, A. Akhperjanian, U. Barres De Almeida, et al., *New constraints on the Mid-IR EBL from the HESS discovery of VHE gamma rays from 1ES 0229+200*, Astronomy and Astrophysics **475** (2007) L9–L13. 5 pages, 4 figures; PTA/07-44, APC-07-107.

[95] Y. Uchiyama, T. Takahashi, and F. A. Aharonian, *Flat Spectrum X-Ray Emission from the Direction of a Molecular Cloud Associated with SNR RX J1713.7-3946*, Publications of the Astronomical Society of Japan **54** (2002) L73–L77, `astro-ph/0208049`.

[96] F. Aharonian, A. G. Akhperjanian, A. R. Bazer-Bachi, et al., *A detailed spectral and morphological study of the gamma-ray supernova remnant RX J1713.7–3946 with HESS*, A&A **449** no. 1, (2006) 223–242.

[97] HESS Collaboration Collaboration, F. Aharonian, A. G. Akhperjanian, A. R. Bazer-Bachi, et al., *HESS Observations of the Galactic Center Region and Their Possible Dark Matter Interpretation*, Phys. Rev. Lett. **97** (2006) 221102.

[98] H.E.S.S. Collaboration Collaboration, A. Abramowski, F. Acero, F. Aharonian, et al., *Search for a Dark Matter Annihilation Signal from the Galactic Center Halo with H.E.S.S.*, Phys. Rev. Lett. **106** (2011) 161301.

[99] F. Aharonian, A. G. Akhperjanian, K.-M. Aye, et al., *A New Population of Very High Energy Gamma-Ray Sources in the Milky Way*, Science **307** (2005) 1938–1942, `astro-ph/0504380`.

[100] F. Aharonian, A. G. Akhperjanian, A. R. Bazer-Bachi, et al., *The H.E.S.S. Survey of the Inner Galaxy in Very High Energy Gamma Rays*, The Astrophysical Journal **636** no. 2, (2006) 777.

[101] J. R. Mattox, R. C. Hartman, and O. Reimer, *A Quantitative Evaluation of Potential Radio Identifications for 3EG EGRET Sources*, The Astrophysical Journal Supplement Series **135** no. 2, (2001) 155.

[102] M. Tsuboi, T. Handa, and N. Ukita, *Dense Molecular Clouds in the Galactic Center Region. I. Observations and Data*, The Astrophysical Journal Supplement Series **120** no. 1, (1999) 1.

[103] H. E. S. S. Collaboration, :, and F. Aharonian, *Very high energy gamma rays from the direction of Sagittarius A**, ArXiv Astrophysics e-prints (2004), `astro-ph/0408145`.

[104] Aharonian, F., Akhperjanian, A. G., Anton, G., et al., *Spectrum and variability of the Galactic center VHE γ-ray source HESS J1745–290*, A&A **503** no. 3, (2009) 817–825.

[105] F. Acero, F. Aharonian, A. G. Akhperjanian, et al., *Localizing the VHE γ-ray source at the Galactic Centre*, MNRAS **402** (2010) 1877–1882, `arXiv:0911.1912 [astro-ph.GA]`.

[106] Aharonian, F., Akhperjanian, A. G., Barres de Almeida, U., et al., *Simultaneous HESS and Chandra observations of Sagitarius A* during an X-ray flare*, A&A **492** no. 1, (2008) L25–L28.

[107] M. Pivk and F. R. Le Diberder, *Plots: A statistical tool to unfold data distributions*, Nuclear Instruments and Methods in Physics Research A **555** (2005) 356–369, `physics/0402083`.

Résumé:

L’expérience High Energy Stereoscopic System (H.E.S.S.) est un réseau de cinq télescopes à imagerie Čherenkov atmosphérique, localisé dans l’hemisphère sud, ayant pour but principal l’étude de rayons cosmiques couvrant une gamme d’énergie de quelques dizaines de GeV à plusieurs dizaines de TeV. La technique de détection Čerenkov ainsi que les spécificités de la méthode de reconstruction employée par H.E.S.S. I (première phase de l’expérience H.E.S.S.), sont décrites dans ce document. Après plus de dix ans d’activité, l’expérience H.E.S.S. a enregistré une quantité de données importante. En plus des régions d’intérêts sondées par ces détecteurs, où des sources astrophysiques ont déjà été dévoilées, l’étude d’événements collectés permet d’améliorer la compréhension de leur environnement sous-jacent. En effet, des émissions diffuses encore non-comprises se superposent aux rayonnements provenant de sources actives. Elles sont pourtant d’un intérêt significatif en astrophysique, physique des particules, cosmologie et même dans certains domaines de physique au-délà du modèle standard, tel que la recherche de nouvelles particules à trouver dans le cadre de l’étude de la nature de la matière noire. Les émissions diffuses et leurs précédentes études sont présentées dans ce document, ainsi que leurs possibles origines, depuis les mechanismes d’accelération de rayons cosmiques jusqu’à la production de rayon gamma dans les sources actives ou encore par des processus secondaires impliquant les interactions de rayons cosmiques avec le milieu interstellaire.

Dans ce travail, des outils pour étudier les émissions diffuses ont été développés et mises en œuvre. L’approche choisie permet de distinguer les différentes composantes dans les données étudiées et d’extraire une estimation de leur proportions et de leur poids dans le spectre. La méthode se base sur des fonctions de densité de probabilité construites à partir de variables discriminantes. L’étude et le traitement préliminaires nécessaires des variables discriminantes sont égalemment détaillées. Les concentrations resultantes pour chaque type de particule sont présentées, ainsi que la première détermination d’une limite supérieure sur le flux de l’émission diffuse gamma extragalactique au TeV. Une source astrophysique connue est utilisée comme référence pour l’analyse; en utilisant la modélisation de la morphologie du signal détecté pour estimer son intensité, la capacité de discrimination de la méthode développée peut être évaluée. Pour finir, deux façons de reconstruire le spectre des électrons et hadrons diffus sont expliquées et les résultats discutés.

Mots-clés: astroparticules, astronomie gamma de très hautes énergies, émissions diffuses, H.E.S.S., méthode de "unfolding", technique d’imagerie Čerenkov atmosphérique

Abstract:

The High Energy Stereoscopic System (H.E.S.S.) experiment is an array of five Imaging Atmospheric Čerenkov Telescopes (IACT) located in the Southern Hemisphere, whose primary goal is the study of cosmic gamma-rays in the few tens of GeV - tens of TeV energy range. The detection technique used by IACT as well as the specificities of the reconstruction method of H.E.S.S. I (first phase of the H.E.S.S. experiment) are fully described in this document. After more than ten years of activity, the H.E.S.S. experiment has registered a large amount of data. In addition to the regions of interest that its detectors probe and where astrophysical sources were unveiled, many events collected provide useful information on their surrounding environment. Indeed, acting as a background to the active sources, one can find the diffuse emissions, which are not well understood and yet are of significant interest for astrophysics, particle physics, cosmology and even physics beyond the standard model, such as the search for new particles in the framework of the study of the nature of dark matter. The diffuse emissions and their previous studies are presented in this document, as well as their possible origin, starting from the acceleration of cosmic-rays mechanism and the gamma-ray production in the active sources or from secondary process involving cosmic-rays interactions in the interstellar medium.

In this work, tools to investigate the diffuse emissions were developed and implemented. The approach aims at disentangling the different components of the studied data so as to extract an estimation of their proportion and their weight in the spectrum. The method is based on probability density functions built with discriminant variables. The necessary preliminary study and treatment of the discriminant variables is also detailed. The resulting concentrations of each type of particle are presented, in addition to the first estimation of an upper limit on the extragalactic diffuse gamma-ray emission flux at TeV energies. A well known astrophysical source is used as benchmark for the analysis. Indeed, through the modelization of its reconstructed image and the subsequent estimation of its intensity, the developed method's capability to disentangle particles can be evaluated. Lastly, two ways of reconstructing the diffuse electrons and hadrons spectra are explained and the results discussed.

Key words: astroparticle physics, very high energies gamma-ray astronomy, diffuses emissions, H.E.S.S., unfolding method, atmospheric Čerenkov imaging technique